INVESTIGATION INTO FLY ASH PRODUCTION DURING CO-FIRING OF BIOMASS WITH PULVERIZED COAL

Nkongolo Muanza

A dissertation submitted to the Faculty of Engineering and the Built Environment, University of the Witwatersrand, Johannesburg, in fulfilment of the requirements for the degree of Master of Science in Engineering

Johannesburg, 2009

DECLARATION

I declare that this dissertation is my own unaided work. It is being submitted for the degree of Master of Science in Engineering in the University of the Witwatersrand, Johannesburg. It has not been submitted before for any degree or examination to any other university.

(Signature of candidate)

---------- day of ---------- year----------

ABSTRACT

This dissertation considers the behaviour of particulate fly ash produced during co-combustion experiments of biomass materials with pulverized coal in a 1 MW_{th} pilot-scale combustion test facility (PSCTF). Particular attention is generally given to fly ash particles of diameters less than 10 and 2.5 microns (namely PM_{10} and $PM_{2.5}$). These small particles have the potential for affecting human health and forcing climate change because of their ability to scatter and absorb light and also to act as cloud condensation nuclei. South African coal has high ash content that consequently affects the ash burden and the efficiency of ash removal system. Previous research work reports increase of the concentration of fine particles during the co-firing of biomass with coal, thus limiting the amount of biomass co-fired.

Coal and two types of biomass, grass and sawdust, were used in this study. The coal chosen was representative on the basis of the annual average calorific value of coals burned at ESKOM'S coal-fired power stations. For each biomass, the ratios of biomass to coal used on an energy basis were 10%:90%, 15%:85% and 20%:80%, resulting in a total of seven different tests including coal alone. Seven tests with similar fuels were also carried out using a drop tube furnace (DTF) to determine their reaction kinetics for the combustion simulation.

The experimental results revealed that the grass and sawdust blends showed decreases of PM_{10}, and $PM_{2.5}$ particles percentages compared to the coal baseline. The grass because of its high content of alumina-silicate showed considerable agglomeration whereas sawdust blends gave minor increase of PM_{10} under high pressure condition inside the combustion chamber. The pulverised-coal fineness, flue gas temperature and excess air were found to affect the particulate matter behaviour. The fly ash samples collected were also analysed by scanning electron microscope and spectrometry; alkali metals released were observed to react with the alumino-silicate phase. The fine sulphate enriched particles formation during combustion process was

modelled based on the Glarborg-Marshall mechanism using CFD tool. The simulation results were validated by the experimental data from the pilot-scale combustion test facility.

DEDICATION

To

My future loving wife,

My progeny,

My ever brave and beautiful family

ACKNOWLEDGEMENTS

I would like first to thank God for His love and merciful grace upon my life.
My deep gratitude goes then to the following persons and institutions:

- My supervisor: Professor Thomas John Sheer for his tremendous constant guidance, helpful discussions on this project, support and encouragement.
- My lovely immense family, parents, brothers and sisters for sharing with me joyful and difficult moments together.
- The Eskom Research and Innovation Department for all facilities provided to us, research training and financial support to this project.
- Palo Pokothoane for his constant scientific guidance, inputs and assistance.
- Bonny Nyangwa for his technical input in this work.
- Mike Lander for his remarkable project leadership to always get this work on track.
- Dr Mark van der Riet for initiating this entire project.
- All my friends and colleagues within the Schools of Aeronautical, Industrial & Mechanical Engineering.
- All the staff members of the School of Aeronautical, Industrial and Mechanical Engineering for their assistance to issues related to this project.
- University of the Witwatersrand for allowing me to undertake this project.
- Oscar Asumani for his advice and spiritual support.

TABLE OF CONTENTS

LIST OF FIGURES

Chapter 2 **Page**

Chapter 3

Chapter 4

Chapter 5

LIST OF TABLES

Chapter 3 **Page**

Chapter 4

Chapter 5

LIST OF ABBREVATIONS

APCD	Air Pollution Cleaning Devices
BSE	Backscattered Electron Imaging
CSIRO	Commonwealth Scientific and Industrial Research Organization
CFD	Computational Fluids Dynamics
CCSEM	Computer Controlled Scanning Electron Microscopy
CSIR	Council for Scientific and Industrial Research
EDC	Eddy Dissipation Concept
EIA	Environmental International Agency
ERID	Eskom Research and Innovation Department
FPM	Fine Particle Model
GCV	Gross calorific Value
GDE	General Dynamics Equation for Aerosols
ICP-MS	Induced Coupled Plasma-Mass Spectrometry
IC	Ion Chromatography
MDE	Moment Dynamics Equation
PSD	Particle Size Distribution
PM	Particulate Matter
PM_{10}	Particulate Matter less than 10 microns
$PM_{2.5}$	Particulate Matter less than 2.5 microns
$PM_{1.0}$	Particulate Matter less than 1 micron
PSCTF	Pilot-Scale Combustion Test Facility
SEM-EDS	Scanning Electron Microscopy-Energy Dispersive X-ray
U.S. EPA	United States Environmental Protection Agency
XRD	X-ray Diffraction
XRF	X-ray Fluorescence

LIST OF SYMBOLS

ΔH_0^f	Enthalpy of formation of compound at temperature T_o (J/kg.K)
$\Delta H_{rxn}(T)$	Enthalpy of reaction at temperature T (J/kg.K)
R	Universal gas constant (J/kg.mol)
Re	Reynolds number
Mol	Mole
P	Pressure (Pa)
S_P	Mass source in the system (kg)
p	Static pressure (Pa)
S_u	Momentum source
$(\mu\nabla\vec{u})$	Stress tensor
μ	Dynamic viscosity (Ns/m^2)
S_H	Energy source due to species (J)
S_Y	Energy source due to chemical reactions (J)
R_f	Energy source due to radiation (J)
T	Local temperature (K)
m_i	Mass fraction of the *i*th species
M_i	Molecular weight of the *i*th species
C_μ	Dimensionless constant
$C_{1\varepsilon}$	Dimensionless constant
$C_{2\varepsilon}$	Dimensionless constant
C_μ	Dimensionless constant
σ_ε	Dimensionless constant
k	Turbulent kinetic energy (m^2/s^2)
ε	Turbulent kinetic energy rate of dissipation
I	Radiation intensity ($W \cdot m^{-2}$)
s	Position (m)
Ω	Solid angle (sr)
σ_s	Stefan-Boltzmann constant ($W \cdot m^{-2} \cdot K^{-4}$)

Φ	Phase function
q_r	Radiation flux ($W \cdot m^{-2}$)
a_p	Equivalent absorption coefficient
E_p	Equivalent emission of the particle
m_p	Particle mass (kg)
$m_{p,0}$	Initial particle mass (kg)
$f_{v,0}$	Initial volatile fraction
A	Pre-exponential factor ($kg/m^2/s/atm$)
E_a	Activation energy (kJ/mol)
$\nu'_{i,r}$	Stoichiometric coefficient for reactant *i* in reaction *r*
$\nu''_{i,r}$	Stoichiometric coefficient for product *i* in reaction *r*
M_i	Symbol denoting species *i*
$k_{f,r}$	Forward rate constant for reaction *r*
$C_{j,r}$	Molar concentration of species *j* in reaction *r*
$\eta'_{j,r}$	Rate exponent for reactant species *j* in reaction *r*
$\eta''_{j,r}$	Rate exponent for product species *j* in reaction *r*
A_r	Pre-exponential factor ($kg/m^2/s/atm$)
β_r	Temperature exponent
E_r	Activation energy for the reaction (kJ/mol)
$k_{f,r}$	Forward rate constant for reaction *r*
$\hat{R}_{i,r}$	Molar rate of creation/destruction of species *i* in reaction *r*
C_ξ	Volume fraction constant equal to 2.1377
ν	Kinematic viscosity ($m^2 \cdot s^{-1}$)
ξ^*	Length fraction of the fine scales
τ^*	Time scale (s)
C_τ	Time scale constant
Y^*_i	Fine-scale species mass fraction after reacting over the time

$D_{i,m}$	Diffusion coefficient for oxidant in the bulk (m^2/s)
Y_{ox}	Local mass fraction of oxidant in the gas
ρ	Density (kg/m^3)
A_p	Surface area of the particle (m^2)
F_x	Additional force (N)
$F_D(u-u_p)$	Drag force per unit particle mass (N)
C_D	Drag coefficient
n	Temperature exponent rate

NOMENCLATURE

Biomass: all kinds of materials that are directly or indirectly derived not too long ago from contemporary photosynthesis reactions, such as plant matter and its derivatives such as wood fuel, wood derived fuels, fuel crops, agricultural and agro-industrial by-products, and animal by-products.

Bioenergy: energy issued from biomass in the form of energy carriers such as charcoal, oil, gas, or as heat and electricity by both thermochemical and biochemical conversion technologies.

Coal: solid fossil fuel formed millions of years ago characterized by a mixture of organic matter and inorganic matter containing solid (fixed carbon, ash), liquid and gaseous phases (volatile matter and moisture) from distinct geological origins.

Char or charcoal: carbonaceous material obtained by heating coal or other organic matter in the absence of air or at the first stage of combustion.

Co-firing or co-combustion: refers to the practice of a simultaneous combustion of a supplementary fuel, for example petroleum coke, with a base fuel such as coal in a boiler.

Fouling: deposition on the heat recovery surfaces, essentially sulphate salts primarily due to the mineral contents of the fuels and subsequent mechanisms and reactions occurring in the flue gas.

Inertinite: Type of maceral considered equivalent to charcoal and degraded plant material.

Liptinite: Type of maceral, with low reflectance and high hydrogen-to-carbon ratios, are derived from plant spores, cuticles, resins, and algal bodies.

Maceral: dehydrogenated plant fragments observed under petrographic microscopy of coal.

Particulate matter (PM) is the sum of all solid and liquid particles suspended in air, many of which are hazardous. This complex mixture includes both organic and inorganic particles, such as dust, pollen, soot, smoke, and liquid droplets.

Slagging is the formation of hard or molten deposits on boiler tubes, usually due to the presence in the fuel of fluxing elements (silicon, alkali metals, etc.) and sulphur.

Vitrinite: type of maceral of a shiny appearance resembling glass, derived from woody tissue of the plants from which coal was formed and chemically composed of polymers, cellulose and lignin.

Vitrinite reflectance: method of identification of the vitrinite measuring its sensitivity to temperature ranges that largely correspond to those of hydrocarbon generation and indicator of maturity in hydrocarbon source.

CHAPTER 1. GENERAL INTRODUCTION

1.1 INTRODUCTION

The worldwide use of coal as a dominant source of energy since the last century has led to a serious air pollution problem, which has to receive serious consideration, in terms of not only carbon dioxide (CO_2), nitrogen oxides (NO_x), sulphur oxides (SO_x), but also suspended particulate matter (SPM) in the air and heavy metals emission. Several efforts have been introduced to mitigate greenhouse gases for prevention of global warming, particularly the Kyoto Protocol in 1997 committing developed countries to reduce greenhouse gas emissions by an average of 5.2% by 2012. These pollution issues justify the growing need for new "green" energy technologies that can replace conventional coal combustion in power stations. Moreover South Africa is currently a party to more than forty international environmental treaties, the country is required to report on national emissions and is encouraged to consider air pollution and climate change issues in domestic social, economic, and environmental policymaking (Environment International Agency, 2007).

Airborne particulate matter (PM) associated with ambient levels of fine particles affects human health, by causing asthma and cardiovascular diseases. The most important particle sizes related to human health are those less than 2.5 µm ($PM_{2.5}$) and less than 1.0 µm (aerosol). Fine particles also play an important role in climate forcing because of their ability to scatter and absorb light and also because they act as cloud condensation nuclei (Goodarzi, 2006; Lipsky et al., 2002; Chengfeng et al., 2005; and Yoo et al., 2005). The particulate matter emissions from the combustion of coal during power generation mainly depend on the ash content of the coal, coal type, type of boilers used and pollution control equipment. Their size distribution, composition, and morphology vary significantly in space and time (Wang et al., 2007; Sengupta, 2007; Environment International Agency, 2004).

The diversity of coals present around the world is related to its geological origins. Low grade coals are characterized by very high ash contents compared to other coal grades. Therefore, low-grade coals are generally expected to result in large quantities of fine fly ash downstream of the fly ash removal system typically installed on combustion systems.

Within the research framework for environment-friendly power generation, co-firing biomass with coal, directly into existing coal-fired boilers, has been regarded as a form of renewable energy source. Biomass combustion follows the reverse of the photosynthesis reaction for tree growth, and therefore in this respect it is a 'CO_2 neutral' fuel in the entire life cycle. Substituting feed coal with biomass pronouncedly reduces the net CO_2 release from coal-fired power generation (Ninomiya et al., 2003). Though combustion of fuel blends has recently attracted considerable attention, the predicted combustion behaviours are non-linear and difficult to predict (Backreedy et al., 2005).

Despite the simplicity of the co-firing concept, its application in pulverized fuel boilers is still associated with many technical issues including flame stability, ash deposition, gaseous emissions (NO_x, SO_x, and CO_2), particulate matter, corrosion, and the mineral transformation. However, emission of PM in co-combustion was reported to increase considerably in the finer range, the reasons for which have not been clarified yet (Wang et al., 2007; Diaz-Somoano et al., 2006; Ninomiya et al., 2004).

The effectiveness of fly ash removal systems such as bag filters and electrostatic precipitators in collecting particles is size dependent. These devices effectively remove coarse mode particles, and are less effective at controlling submicron particles ($PM_{2.5}$) (Lipsky et al., 2002).

Hence, an investigation of the fly ash size distribution during co-combustion of coal and biomass is a necessary part of a preliminary study to evaluate the feasibility of

biomass co-firing, if such technology is to be implemented in future in South African power stations. This dissertation describes experimental and modelling results of sequential co-combustion tests of coal/biomass blends with respect to particulate matter behaviour at pilot-scale. It is a product of collaborative work of the TSI/Eskom Research and Innovation Department and the School of Mechanical, Industrial and Aeronautical Engineering of the University of Witwatersrand under the project PRJ07-00640900-3177. The research problem addressed under this research contract was to obtain fundamental experimentally-based information on the principal effects in the combustion process of co-firing biomass with coal. These effects are basically ignitability, particulate and gaseous emissions (CO_2, SO_2, and NO_x), and ash deposition. The influence of fuel proportions, composition and operational conditions are presented and conclusions are drawn.

1.2 International research on particulate matter behaviour

Co-combustion of coal with biomass (sewage sludge) was carried out in a laboratory-scale drop tube furnace in Japan to understand the interaction between these different fuels. Two types of sewage sludge and various combustion conditions were selected to assess the influence of the fuel's composition, atmosphere, and residence time. The coal/sewage sludge co-firing ratio was kept at 50:50 (wt% to wt %), and four fuel pairs were selected based on the mineral association (Ninomiya et al., 2004). Ninomiya and co-workers studied the interaction between included and excluded minerals from coal and biomass materials and investigated the production of particulate matter during the co-combustion. They concluded that mineral transformation and PM emission correlate closely with the fuel characteristics. For the sludge that contained a high proportion of minerals inclusions, the coarse-excluded mineral grains of coal interacted with included minerals because of the collision between the ash shell of sludge and the excluded minerals of coal. The chemical species formed inside underwent transformations, and much more alkali, trace elements and fine droplets escaped from the char. Its PM emission was

increased accordingly. A similar phenomenon took place for the coal enriched with fine excluded particles where the fine minerals reacted with the ash shell to form more large particles in the ash. On the other hand, the coal with high included minerals content showed little interaction with sludge. Strong interaction was also recorded when both fuels were enriched with excluded minerals; much more agglomerated ash particles were subsequently formed, and less PM was emitted due to the deposition of vaporized elements on the surface of melt ash.

Apart from precisely elucidating low-rank coal ignitability and NO_x emission during its combustion in mixtures with biomass using an electrically heated Drop Tube Furnace, Gani et al. (2005) also investigated its ash formation characteristics. Burning biomass with coal shifts the particle size distribution from fine particles to coarse particles, with the observations from a Scanning Electron Microscope (SEM) suggesting that ash particles produced from biomass combustion seem to be captured by ash particles from coal. These fly ash particles are easily captured by dust collection systems.

The report of the work carried out under contract by Future Energy Solutions as part of the DTI Carbon Abatement Technologies Program (DTI, 2005), expresses that in scarce cases particulate emissions have also been seen to increase slightly during co-firing trials. This report summarizes full scale experiences from all ongoing biomass co-firing activities in the UK up to 2005. In relevant cases where particulate matter emission has been monitored, it has remained within the tolerance band allowed under the WHO standard (50 mg/Nm^3) for electrostatic precipitators of high collection efficiency (> 99.7%). Hence, they concluded that the impact of co-firing biomass on boiler particulate emission levels was not a serious issue.

The sometimes slight increase was attributed to the variation in the composition of the underlying coal, and increased carbon content of the incident dust size distribution. In many cases this was seen with significantly increased levels of

potassium and phosphorus oxides in the co-fired ashes for raw fuels enriched in those elements (DTI, 2005).

Wang et al. (2006) investigated the emission characteristics of particulate matter of aerodynamic diameter less than 10 µm (PM_{10}) during coal/biomass co-combustion carried out in a laboratory drop tube furnace. Two different atmospheres, N_2/O_2 = 4:1 and 1:1, were tested. The coal/biomass ratio was kept at 75:25 (wt %), and four types of coal/biomass blends were selected as fuels in these experiments. The results show that the particle-size distribution of PM_{10} from the co-combustion of coal and biomass is bimodal, with one peak at about 4.3 µm and the other at about 0.1 µm. They evaluated the influence of the oxygen ratio on the particle size distribution. With the increase of the oxygen ratio, the total concentration of PM_{10} rose and the percentage of $PM_{1.0}$ in PM_{10} diminished greatly, while that of $PM_{1.0+}$ (particle size between 1.0 – 10 µm) increased. The increase of oxygen concentration within the system caused a higher sulfation of alkali metals present in $PM_{1.0}$. This was measured by the ratio of S/Cl and translated by an enrichment of $PM_{1.0}$ with alkali, sulphur, and chlorine.

1.3 Objectives of dissertation

A review of research around the world indicates unknowns and uncertainties in the reasons for the increased emissions of particulate fly ash during the co-combustion of biomass with coal. Against this background, the research problem addressed in the overall project, of which this dissertation forms part, is to obtain fundamental experimentally-based information on the principal effects in the combustion process of co-firing biomass with coal under Eskom conditions. This information is a prerequisite for any further feasibility studies into the use of biomass as a supplementary fuel for power generation in pulverized-fuel boilers.

The main purpose of the present study is to determine at pilot-scale the effects of two specific types of biomass materials: ligneous (‘sawdust’) and herbaceous (‘grass’), on the production of particulate matter during co-firing with a typical South African power station low-grade coal at ratios of 10:90, 15:85, and 20:80 biomass/coal on an energy basis.

The information about to the resulting fly ash particulates sampled from experiments, includes particle size distribution ($PM_{>10}$, PM_{10} and $PM_{2.5}$), microstructure, morphology and chemistry characteristics. Due to the particularity of the coal, a distinct particle size distribution could be expected. Therefore, this research work addresses the following major issues:

- Analyse the physical microstructure of fly ash particles for each co-firing combination of biomass with coal and under various combustor operating conditions.

- In order also to understand the mechanism responsible for the formation of fine particles issued from gas phase-to-solid phase transformation in combustion systems, investigate the possibility of modelling by computational

fluid dynamics (CFD) the complex thermochemical conversion under experimental conditions and validate with experimental measurements from the 1 MW Eskom combustion test facility (PSCTF).

These issues represent the main objectives that were to be achieved at the end of this study.

1.4 Methodology

The Eskom Research and Innovation Department (ERID) has a down-fired pilot scale combustion test facility of 1 MW thermal output used for these experiments, operating with a single low-NO_x burner at atmospheric pressure. The combustion gases (CO_2, O_2, CO, NO, SO_2, etc.) and solid particles travel down the furnace through turbulent flow towards the heat exchangers and into the fabric filters. The radiant section bears sampling ports for fly ash collection, ash deposition measurements, temperature, and flue gas composition analysis. The facility was designed to simulate conditions as close as possible to those encountered in a commercial boiler, with respect to flame behaviour near the burner and in-situ temperature and residence time histories (DTI, 2002).

The research focused on experimental results from a series of tests with two biomass materials, herbaceous (“grass”) of medium chlorine, and high potassium and silica contents, and ligneous (“sawdust”) low-chlorine type biomass, blended on an energy basis at ratios of 10%, 15%, and 20% with a typical low-quality coal. The testing facility provided a highly controllable combustion environment that allows safe sampling of gaseous and particulate emissions.

The particulate matter was sampled isokineticaly through the ports along the radiant section during the experiment in accordance with the U.S. EPA Method 5 (U.S. EPA Method, 2000). The maximum collection efficiency of fly ash particulates of all sizes

was achieved regardless of the velocity and direction of the air stream entering the sampling device by the isokinetic sampling method.

The solid samples were analysed for their chemical composition and morphology and the results were compared to that of 100% coal (Baseline test). Induced coupled plasma and absorption emission spectrometry, ion chromatography, laser Malvern sizer, and scanning electron microscopy energy dispersive x-ray techniques were employed to elucidate the phenomenon of particulate ash matter formation.

In order to obtain more insight into the mechanism of production of aerosol particles, numerical differential-equation-solving techniques were used to simulate the simultaneous chemical processes during combustion. Based on the reaction kinetics parameters obtained from the drop tube furnace experiments performed, and the existing fine particles models, a simplified multi-reaction mechanism was modelled using CFD methods and the results were interpreted and compared to some extent to experimental data.

1.5 Outline of the dissertation

In this work, the information on the principal effects of co-firing biomass with coal from the pilot-scale experiment on the particulate matter is addressed and CFD tools for the modelling of sources of fine potassium sulphate particles are used to predict the risk levels of each test. Variables such as co-firing ratios, biomass types, and chemical characteristics are considered in this investigation. A qualitative analysis of the fly ash samples is also presented, including the morphology, chemistry, and size distribution.

In Chapter 2, a survey of basic concepts in combustion and a literature review of fly ash formation mechanisms is carried out, and theoretical discussions are presented of

the fate of alkali metals during co-combustion of biomass with coal, on which fine particle modelling is based.

Chapter 3 describes the experimental section: fuels preparation and properties, operating conditions, sampling method, analysis techniques and results of the test programme.

Chapter 4 provides details of the models used for combustion simulation, together with fine particulate modelling, using a CFD package, and the results.

Chapter 5 presents the discussion of the experimental and modelling results

In Chapter 6 the final conclusions of the experimental work and modelling work are presented. Recommendations for future work are also given.

In Appendix A fly ash PSD from port 21are given for the different test series.

In Appendix B the CFD homogeneous turbulent combustion sub-models used for the sulphate formation simulation are illustrated.

In appendix C the results of Drop Tube Furnace experiments using batch blends of coal with either sawdust or grass are presented.

In appendix D the PSCTF experimental results for combustion efficiencies and temperature profiles are presented.

In Appendix E calculation of the Potassium, Sulphur and Chlorine splits through different species during devolatilisation is presented for Potassium Sulphate formation modelling.

In Appendix F the radiant section residence time and velocity magnitude of the flue gas are given for the different test series.

In Appendix G the chloride deposition tendency onto fly ash particles is presented.

In Appendix H ICP and IC analysis on fly ash samples are given for all the tests series.

In Appendix I Co-firing coal and biomass – clinkers QEMSCAN photographs are displayed.

In Appendix J additional SEM-EDS spectra of fly ash samples extracted from port 21 are given for the different test series.

In Appendix K the comparison between experiment and modelling is presented of carbon dioxide concentrations in the PSCTF for different test series.

CHAPTER 2. LITERATURE REVIEW

2.1 Types Of Biomass Co-Firing Technologies

Co-firing of biomass with coal (subsequently referred to as co-combustion) represents a partial substitution of fossil fuel to take advantage of both fuel types in traditional coal-fired boilers (Van Loo et al., 2003, Foster Wheeler, 1999).

There are several ways to engineer the co-firing of biomass, and the best approach is usually site specific. At present power generation from biomass has mostly been successfully practiced, tested, and evaluated for different boiler technologies across Europe, Australia, and the USA. Little or no significant loss in total efficiency has been found, implying that the effective partial substitution of coal with biomass has become a substantial opportunity for power generation (DTI, 2005).

The qualitative and quantitative analysis of boiler technologies (stoker fired boilers, pulverized fired boilers and fluidized bed boilers) have shown that pulverized fired boilers offer more advantages compared to other types of boilers (Broek et al., 1995).

Existing pulverized coal-fired technologies used to combust biomass are categorized as follows (Van Loo and Koppejan, 2002; Foster Wheeler, 1999):

- Direct co-firing: Blending the biomass with coal and transporting the mixture to the boiler through the coal feeding system (silos, crushers and mill), or pneumatically separate feeding of the pre-processed biomass to the boiler furnace without impacting coal system;

- Indirect co-firing: Gasifying the biomass and firing directly the gas either in the boiler furnace or in a combined cycle power plant;

- Parallel combustion: Combusting the biomass in a separate boiler and feeding the generated steam upstream of the coal-fired plant turbine.

The majority of these methods exist already on a commercial scale, and each displays its own pluses and minuses. Van Loo and Koppejan (2002) point out that the fuel, costs, technical issues, and site factors define the basic selection criteria of these schemes.

2.2 Coal, Biomass, And Particulate Matter

2.2.1 Coal

Fundamental chemical classification of coal is based on the organic matter defined by standard proximate analysis (fixed carbon, volatile matter, moisture and ash contents), ultimate chemical analysis (carbon, hydrogen, oxygen, nitrogen and sulphur contents), and maceral contents. The abundance of fixed carbon classifies the rank of the coal whereas the amount of ash in the coal defines its type (Liu et al., 2005). Macerals are subdivided into inertinite, vitrinite and liptinite.
Difficulties to ignite and completely burn pulverized coal in boilers are essentially attributed to the maceral constituents (Cloke et al., 2002). Maceral maturity can be estimated by vitrinite reflectance. The reactivity of vitrinite varies with its reflectance and the inertinite content is considered a poor combustor, depending upon the geological origin of the coal. Southern hemisphere coals are more likely to contain a large quantity of inertinite of lower reflectance than northern hemisphere coals. Cloke and associates (1999) revealed a correlation between the coal combustion behaviour and its total reflectance existed and not with its maceral composition. Inorganic matter contains various mineral classes (van Alphen, 2005):

- Silicates: quartz, kaolinite, illite, chlorite, muscovite, montmorillonite, feldspars, etc;

- Carbonates: siderite ($FeCO_3$), calcite ($CaCO_3$), dolomite ($CaCO_3$. *x* $MgCO_3$), and ankerite ($CaCO_3$. *x* $MgCO_3$. *y* $FeCO_3$);
- Pyrite (FeS_2);
- Apatite;
- Chamosite;
- Rutile, etc.

These mineral species are organized into associations of included and excluded mineral grains. The later are produced during crushing, grinding and milling processes and dispersed among pulverized coal particles. Included minerals refer to the discrete mineral grains organically embedded to the matrix whereas excluded grains are out-of-coal particles with more or less nonexistent association with the matrix (Liu et al., 2007).

In the recently-developed mechanistic models, the Computer Controlled Scanning Electron Microscope (CCSEM) has been mainly used to identify and classify mineral grains into included and excluded minerals from the coal and their composition by image analysis (van Alphen, 2005).

Since many research works have linked mineral grains transformation to the ash formation mechanisms during coal combustion (van Alphen, 2005; Raask, 1985; Unsworth et al., 1987; Canadas et al., 1990; Charon, 1990) as discussed later in this chapter, the inorganic matter must be regarded as responsible for slagging, fouling, and particulate matter emissions.

There are three processes occurring during combustion of coal, namely: drying (heating), devolatilisation (pyrolysis), and volatile matter and char combustion. They are characterised by reaction kinetic parameters. The charcoal yield of initial pyrolysis softens and forms porous spherical particles (Smith, 1980).

2.2.2 Biomass fuels

Van Loo et al. (2003) defined four thermochemical biomass conversion technologies for energy purposes: pyrolysis, gasification, (co) - combustion, and liquefaction. Co-combustion of biomass with coal was the focus in the present research.

a) Utilization status of biomass in South Africa

Honsbein (2006) and Goosen (2008) cited the following sectors of utilization of biomass as sources of energy in South Africa:

- Primary production of charcoal from forest waste material and briquettes from the fines debris of charcoal for barbecue purposes and silicon industry;
- Slow pyrolysis for high quality charcoal production used in metallurgical processes;
- Wood for the pyrolysis to volatilise oils and gases for combustion;
- Wood-oils and wood-acids (light and heavy pyrolysis liquids) for energy or other relevant purposes;
- Agricultural residues and bagasse in the sugar industry for the gasification or partial combustion with steam;
- Pulp and paper waste from commercial forestry (Mondi Paper Ltd., Sappi, etc.) for the traditional direct combustion with air to produce steam to drive turbines;
- Sugarcane (molasses, sugar solids, crop residues) as bioenergy crop for ethanol, methane and fertilizer production, or as fuel briquettes for steam and electricity generation;
- Manure and other wastes.

Often combined heat and power (co-generation), are also linked to existing industrial operations.

b) Physical and chemical characteristics of biomass fuels

Due to the biomass diversity and complexity, studies of the physical and chemical compositions of biomass fuels are still ongoing though some databases are available on the internet (Van Loo and Koppejan, 2002).

The following is an overview of the most important characteristics used in practice as described in the literature.

i) Physical characteristics

Fuel size grading, moisture content, bulk density, gross calorific value, are important physical characteristics for biomass fuels (Van Loo et al., 2003):

- Size grading determines the appropriate fuel-feeding system into the boiler and the combustion technology;
- coal particle diameter distribution was used as input in a CFD code for combustion modelling;
- Moisture content influences the adiabatic temperature of combustion thus the efficiency of the boiler;
- Bulk density defines the fuel-feeding rate as well as the gross calorific value (GCV).

ii) Chemical characteristics (Van Loo and Koppejan, 2002):

Proximate analysis generally revealed that the volatile matter content for biomass materials was higher than that of coal resulting in relatively higher vaporization before the homogeneous gas-phase combustion reactions. The amount of volatiles therefore strongly determined the combustion behaviour

of biomass particles. As for coal, the remaining solid carbon (char) also underwent heterogeneous combustion reactions.

Ultimate analysis usually determined the fuel C, H, O, N and S contents. C in biomass was partly oxidized, which explained the low GCV of biomass fuels. Subsequently, the exothermic reactions of formation of CO_2 and H_2O from C and H released less energy. At high temperatures, fuel-bound N promoted NO_x formation during combustion processes.

Furthermore, organically bound S transformed into gaseous compounds SO_2 and by sulphation reactions, SO_3, and alkali sulphates that condensed on the fly ash particles towards low temperature zones of the boiler.

Biomass fuels had high chlorine contents which vaporized almost completely during combustion, forming HCl, Cl_2 and alkali chlorides. Part of Cl would be bound as alkali and earth alkaline chlorides on fly ash particles or on the heat exchanger surfaces; the rest would be emitted as HCl in the flue gas.

The biomass fuel consisted of lignocelluloses (collection of cellulose, hemicelluloses and lignin) behaving practically the same as the maceral did for coal. The proportion of these molecules dictated the process taking place during combustion from both physical and chemical reactions points of view. Lignin was much less reactive, similarly to inertinite, whereas cellulose compares to vitrinite (Backreedy et al., 2005).

The combustion process of biomass materials followed the stages of drying, devolatilisation, homogeneous and heterogeneous oxidation reactions, which are functions of the environmental conditions inside the system. Unlike bituminous coal, biomass particles retained their initial form that was irregular in shape during devolatilisation (Backreedy et al., 2005).

c) Biomass fuel selection criterion

The different chemical structures and organic bonds of biomass fuels fixed the quantity of volatile matter released while heated. This gave a remarkable devolatilisation signature as a function of temperature. Hence, the choice of types of biomass materials, like woody and herbaceous, took consideration of merits and disadvantages that each type could offer apart from their availability within the region, such as pre-treatment, composition, heating value, density, porosity, size, active surface area, and ash sintering temperatures (van Loo and Koppejan, 2002).

2.2.3 Particulate matter

In electricity generation by pulverized coal combustion, materials that remain after coal has burnt out are coarse particles (bottom ash and boiler slag) settling to the bottom of the combustion chamber, and the fine portion (fly ash) carried by the flue gas, which is effectively removed by APCD (American Coal Ash Association, 2007).

Particulate matter varies greatly in size, composition, and origin. It has irregular shapes and the aerodynamic behaviour is expressed in terms of the diameter of an equivalent sphere. The sampling and description of particles is based on this aerodynamic diameter, which is usually simply referred to as “particle size” (GreenFacts, 2007). Fly ash size distribution, composition, and morphology can vary significantly in space and time (Lipsky et al., 2002).

Particulate matter was reported to be responsible for reduction in visibility, mainly caused by fine particles formed from gas-phase reactions in the atmosphere. Coarse particulate matter can settle on painted surfaces, clothing and possibly cause corrosive damage to metals depending upon the composition of the adsorbed chemical by inert particles and its physical state. The combination of emitted fly ash particles and other gaseous pollutants affect vegetation growth by reduction of gas exchange, increased leaf surface temperature, and reduction in photosynthesis because of dust deposited directly onto leaf surfaces. Indirectly the coarse particles falling onto plants are enriched in heavy metals such as mercury, arsenic, or fluorine and these can also affect the biodiversity (Miller, 2005).

Based on the aerodynamic diameter, the particulate matter includes both fine and coarse particles. These particles can be inhaled, accumulated within the respiratory system and cause heart and lung disease such as asthma, increased respiratory symptoms and disease, decreased lung function, and even premature death. The elderly, individuals with cardiopulmonary disease and children represent the groups at high risk (Miller, 2005; Green Facts, 2007).

The US EPA regulated the concentration of particulates up to 10 µm in diameter. Studies, however, indicated that it was the smaller particles, diameter less than 2.5 µm ($PM_{2.5}$) that are largely responsible for the health effects of greatest concern and for visibility impairment. Based on this information, the EPA has issued regulations of the particulate matter standards for 24-hour exposure to $PM_{2.5}$ as 35 µg/m³. The 24-hour standard for coarser particles ranging from 2.5 to 10 µm (PM_{10}) has a recommended maximum of 70 µg/m³ urban exposure (U.S. Environmental Protection Agency, 1996). Hence, the fly ash particle size distribution is an important parameter that affects emission control strategy and the toxicity of the resulting PM emissions (Chengfeng et al., 2005; Yoo et al., 2005).

2.2.4 Particulate matter formation model during combustion of coal

Particulate matter mechanistic models have been developed these past years to illustrate the ash formation mechanisms. As a result an understanding of the chemical transformations for the majority of minerals in coals has been established. Information on mineral-organic association was also extremely important since mineral matter might experience different temperature-time histories resulting in different physical-chemical transformations, thus generating ash particles of different sizes and chemistry. Fragmentation, coalescence, evaporation, and subsequent condensation are the physical transformations that play an important role during ash formation (Liu et al., 2005; Liu et al., 2007).

The fusion of char during combustion caused the outer surface to shrink while the inner surface remained unchanged. The coalescence of inorganic mineral grains enriched in coal particles forms the coarse mode of particles that constituted the majority of fly ash (Lipsky et al., 2002, Field et al., 1967). Coal combustion could for instance produce particulates having diameters ranging from 0.03 to 100 µm (Liu et al., 2007, Ninomiya et al., 2006).

The transformation of ash, constituted of inorganic phases such as refractory elemental oxides in the boiler, produced coarse particulates of similar composition to the inherent minerals in the coal. The smaller particles often tended to have less SiO_2, Al_2O_3 and Na_2O but more Fe_2O_3, CaO, MgO and P_2O_5 (Chengfeng et al., 2005).

The coalescence of two or more of the included minerals, elemental oxides and the presence of large excluded minerals grains were major sources of fly ash formation during thermochemical conversion (Yoo et al., 2005; Ninomiya et al., 2006).

Ultra-fine particulates were the yield of high-temperature vaporization, nucleation, coagulation, and condensation mechanisms. The vaporized inorganic matter (K, Na and refractory elements Ca, Mg, Si and Al, including heavy metals), elemental carbon, organic carbon and sulphates and nitrates, within the high-temperature combustion region underwent homogeneous condensation to generate particle nuclei. The generated nuclei coagulate with each other by driving forces such as Brownian motion and/or turbulent shear and differential sedimentation. This vaporized inorganic matter, driven by saturation partial pressures, had a higher probability of condensing on the surfaces of existing particles (Baxter, 1992; Yoo et al., 2005).

The Computer-Controlled Scanning Electron Microscope (CCSEM) technique has been a useful tool to measure the abundance of mineral grain types in pulverised coal particles. It advanced the characterisation of these mineral particles as included and excluded minerals and this has improved the understanding of ash formation mechanisms during pulverised-coal combustion. Consequently, three different fly ash generation models were developed to predict ash size and chemical composition by many authors (Yan et al., 2000; Yan et al., 2002):

- Full coalescence scheme which assumed that all included mineral particles present in a char particle coalesced to produce a single fly ash particle (Field et al., 1967);

- No-coalescence scheme considered that one mineral particle evolved into a single fly ash particle;

- Both of the above schemes were qualified as extreme because Monroe (1982), and Yan et al. (2002) advocated the existence of a partial coalescence scheme that lies in between these two extreme schemes and which gives more reliable predictions.

The partial coalescence scheme defined an extensive included minerals coalescence function of char structure (shell thickness of char cenosphere) (Bailey et al., 1990) depending itself upon combustion conditions (Canadas et al., 1990) and nature of the maceral in the coal (Unsworth et al. 1987; Yan et al., 2000).

Bailey et al. (1990) showed that the char structure may be organised in three groups, characterised by the shell thickness of char cenosphere; the proportions are 5, 25, and 45% of char outer diameter respectively for groups I, II and III. Extensive research investigated successively the influence on ash formation mechanisms of the char surface pressure, temperature, morphology and coal properties. Canadas et al. (1990) also studied the effect on final ash distribution of the included mineral grains fusion temperature in comparison to the final particle combustion temperature. Full coalescence was expected for a final combustion temperature greater than the melting point of included matter and rather partial coalescence of mineral matter in the opposite case. An included mineral grain transformed differently from an excluded mineral grain because of differences in particle temperature, local atmosphere, and proximity to other included mineral grains (Benson et al., 1993).

Other researchers identified links between the petrographic composition and the ash formation mechanisms. First of all, in the work of Shibaoka (1969), it was noted that low reflectance inertinite materials devolatilise and form open char structures. Unsworth (1987) argued that inertinite-rich particles did not change their size and shapes at lower temperatures and subsequently inhibited coalescence, whereas vitrinite-rich particles yielded thin shell char resulting in fragmentation and large-sized char cenosphere.

Van Alphen (2005) argued in his thesis that the high proportion of low melting point mineral inclusions and absence of char fragmentation favoured the coarse “full coalescence” scheme. Hence, extensive char fragmentation and/or a high

proportion of high melting point mineral inclusions that did not coalesce would favour the “no coalescence” approach. The pair of minerals residues in contact coalesces alongside the char outer surface.

With the development in Australia of a powerful analytical technique (QEMSCAM) to characterize the mineral matter in coal particles, mineral distributions measurements are no longer random (van Alphen, 2007). These results were converted into CCSEM-like format compatible with CCSEM-based ash formation models to predict size and chemistry of fly ash. Liu et al. (2005) again used the random mineral distribution model to uniformly distribute all the mineral grains into randomly selected coal particles. The poor fly ash distribution outputs were attributed to the randomness approach resulting in less chance given to all included mineral grains to coalesce.

2.2.5 Particulate matter formation model during co-firing with biomass

Several studies on co-combustion including thermodynamic calculation and bench-scale experiments have reported considerable increase in particulate emission. No clarification of this phenomenon has yet been stated (Wayne et al., 2002; Ninomiya et al., 2004).

The addition of biomass to the coal burning process also created problems related to slagging and fouling within the coal-fired boiler, attributed to the different ash properties of biomass compared to coal (Heinzel et al., 1998). The composition and quantity of combustion residues were the primary factors determining the fly ash formation behaviour and its mineral transformation.

As for pulverized coal particles, biomass particles were also enriched with included and excluded mineral matter. Ninomiya et al. (2004) combined the mineral transformation and PM emission results of the co-combustion of coal with sewage sludge to implement a physical model describing the influence of the

fuel mineral matter and its common interaction. They successively reported for each following case:

- For high proportions of excluded minerals in both fuels: the interaction between the excluded minerals of coal and biomass caused agglomeration. Consequently the particle size of fly ash shifted to large aerodynamic diameter.

- For high proportions of included minerals in both fuels: no significant interaction between the included minerals was noticed. Therefore, the co-combustion result was the arithmetic average of the single fuel combustion results.

- Coal with high excluded minerals content and sewage sludge of high included minerals content: there was interaction between included minerals of the biomass and excluded minerals of the coal. Collisions of excluded minerals of the coal with agglomerated included minerals of the biomass produced particles of comparable size to pure biomass combustion.

Although biomass ash contents were reported low compared to fossil fuels, research has shown that Si in combination with K could lead to the formation of low-melting silicate compounds in fly ash particles (Raask, 1985). Alkali metals in combination with silica and sulphur were primarily responsible for melting or sintering at relatively low temperatures. This undesirable process was facilitated by the presence of chlorine (Cherney, et al. 2006).

Because fine particles were enriched in K, S, Cl, and Na, mainly in the form of sulphates or chlorides, there was an agreement that they were formed by nucleation/condensation of volatilized mineral matter, in a similar path to that described for coal combustion. Some developed models pointed that K_2SO_4

nucleates first, KCl formed and condensed later onto those nuclei (Jimenez et al., 2005; Christensen et al., 1998). Coagulation was most efficient for large numbers of particles, and condensation was most efficient for large surface areas. Therefore the efficiency of both coagulation and condensation decreased as particle size increases, which effectively produced an upper limit such that particles did not grow by these processes beyond approximately 1 µm (ACAA, 2007).

Ninomiya et al. (2004) showed (Fig. 2.1) a comparative diagram of the transformation of minerals during coal combustion, biomass combustion (sewage sludge) and co-combustion processes.

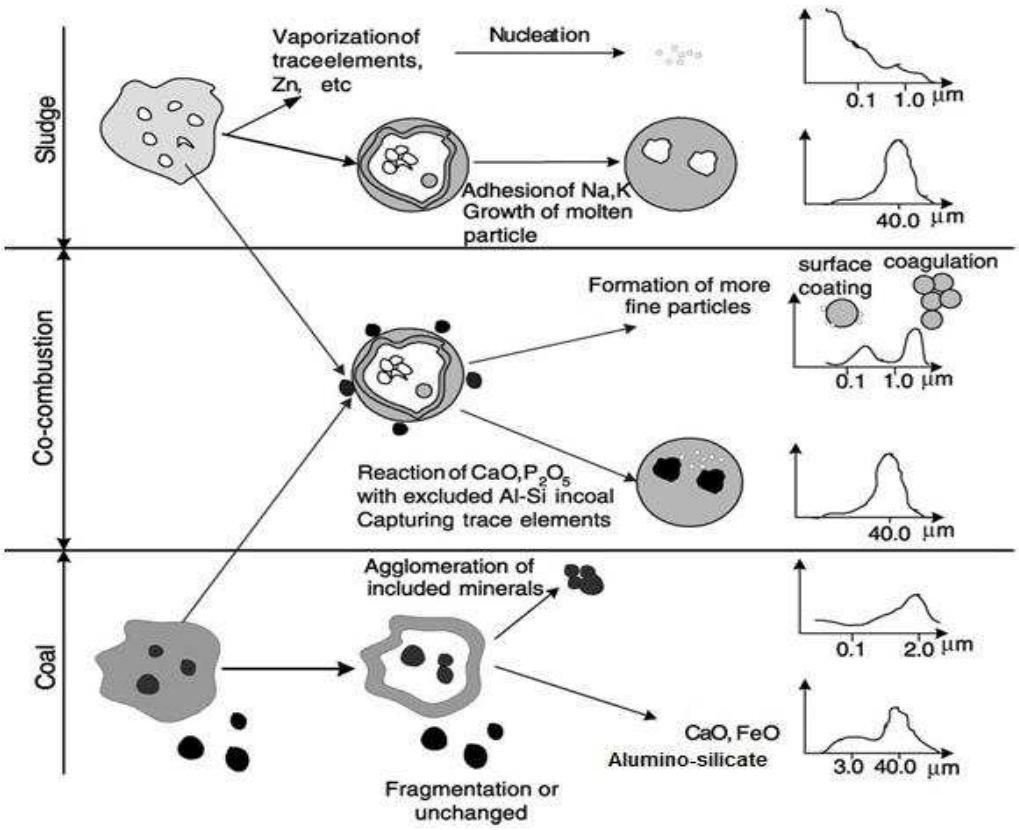

Fig. 2. 1 Schematic diagram of the transformations of minerals and PM formation during co-combustion (Ninomiya et al., 2004)

Wang and co-workers (2007) investigated the properties of PM_{10} from the co-combustion of coal with biomass and the effect of oxygen content on the emission behaviour of $PM_{1.0}$ and $PM_{1.0+}$. The majority of alkalis, sulphur, and chlorine were enriched in $PM_{1.0}$. Meanwhile, the alkali content in $PM_{1.0}$ decreases, and a significant increase was found in $PM_{1.0+}$. These results were very useful to the understanding of PM formation during co-combustion of coal and biomass. $PM_{1.0}$ was formed by vaporization and subsequent condensation of these volatile elements and $PM_{1.0+}$ by included mineral coalescence, char and excluded mineral fragmentation. However, the molten large coal ash particles were expected to capture very fine PM from the combustion of coal and biomass at higher oxygen concentration (high temperature), resulting in the decrease of $PM_{1.0}$ in PM_{10}.

A number of authors in the last decade have also proclaimed the fact that in biomass combustion coarse particles essentially followed the fragmentation ash formation model and retained the fuel's original mineral matter characteristics.

The above overview of ash formation models during mixture combustion was the prerequisite to the overall fly ash particle size distribution models that constituted to some extent the major question of this investigation: What was the effect of co-firing coal with biomass on the fly ash particle diameters?

2.2.6 Particle size distribution (PSD)

Any particulate matter size distribution prediction needs to take into account the fly ash generation models already discussed in this chapter. The PSD is one of the most important physical characteristics of particulate matter (Chengfeng et al., 2005) and is used as input for other models to evaluate ash behaviour such as slagging, fouling, erosion, heat transfer or effectiveness of the cleaning devices (Liu et al., 2005).

Basically, particulate matter emissions from coal combustion typically have a bimodal distribution (Lipsky et al., 2002). Further research showed a tri-modal PSD in the coal combustion process with particle size of the finest mode under 0.1 µm (Yoo et al., 2005; Linak, 2002). Wang and co-workers (2007) showed a bimodal size distribution for PM_{10} with two peaks at around 4.3 and 0.1 µm respectively.

PSD mathematical models have generally been based on numerical methods, using statistical algorithms to randomly distribute the measured CCSEM-derived mineral composition and sizes between different coal size classes. The number of offspring mineral grains from the fragmentation of a parent grain was random in nature (Yan et al., 2002).

Charon et al. (1990) used a random mineral distribution approach to simulate included mineral distribution for a US bituminous coal. The Monte Carlo method was used to randomly disperse mineral inclusions classified from 1 to 60 µm among simulated coal particles of 10 – 170 µm in steps of 10 µm (Charon et al., 1990; Yan et al., 2002).

A probabilistic method (‘urn method’) based on Poisson statistics developed by Barta et al. (1993), cited by van Alphen (2005), provided a random coalescence model for the fly ash size and the chemical composition of mineral inclusions measured by CCSEM.

Moderate advances have been achieved to investigate mineral transformation, especially ash formation mechanisms by several authors (Yu et al., 1993; Helbe, 1990; Srinivasachar et al., 1989; Baxter et al., 1992). They aim to predict realistically fly ash distribution and chemical composition, compared to the models described earlier developed by many researchers such as Loedhen et al. (1989); Zygarlicke et al. (1991); Wilemski et al. (1992) and Van Alphen (2005).

These authors all made an assumption of a partial coalescence scheme during combustion of pulverised coal.

A mechanistic model for ash formation developed by Yan et al. (2002) for high-rank coal, but still requiring CCSEM data, attempted to improve other existing models. Included and excluded minerals were treated separately regarding their transformation behaviour in the course of coal combustion and the influence that the char structure has on the fly ash size and compositional distribution. Based on the coal particle size distribution, mineral inclusions were randomly dispersed between coal particles. The model reflects the combined effect of partial coalescence for included minerals and fragmentation for excluded minerals. The partial coalescence scheme of included minerals was related to the char structure of coal and the simulation using the random Poisson statistical method of excluded minerals. Experimental results for an Australian bituminous coal were compared with the particle size distribution and chemical composition predicted by the Yan Model (Yan et al., 2002). Concerns about the parent coal petrography and combustion conditions have also been raised by Yan and co-workers for future development of the model.

The Yan model consisted of three sub-models addressing the mineral distribution, the included minerals transformation and excluded minerals transformation respectively (Yan et al. 2002).

- Mineral distribution sub-model: random distribution of mineral grains into a coal particle because the CCSEM data could not reflect the real mineral-coal association. The Monte Carlo method for example dispersed included minerals one by one among randomly selected high-rank coal particles.

- Included mineral transformation sub-model: A shrinking model of char combustion within a diffusion-controlled regime was assumed in this work.

Consequently, the oxidation of carbon matter was assumed to occur only on the external surface of a char cenosphere. Similarly to Monroe (1989) this model computationally summarized the coalescence behaviour of included minerals as a function of the cenosphere shell thickness, percentage of outer diameter, coal particle size, mineral grain size and mineral volume fraction.

- Excluded mineral transformation sub-model: Excluded mineral grains behaved quite differently compared to the included minerals during combustion. The important mechanism associated with excluded mineral transformation was fragmentation, which contributed to particle size variation towards the fine direction. The probability of the original mineral grain to fragment into segments was defined by a Poisson distribution. The literature review indicated fragmentation in high-temperature processing of calcite and pyrite. Under typical pulverised-coal boiler combustion conditions no major fragmentations of quartz, illite, other silicates, siderite and ankerite were reported.

The particulate size distribution determines the effectiveness of the cleaning devices and subsequently the coal-fired power plant efficiency (Lipsky et al., 2002). Mechanical collectors (electrostatic precipitators, fabric filters, and scrubbers) are used to control particle emissions from pulverized coal-fired boilers since cyclone technology is a less efficient method according to emission control standards (Goodarzi, 2006). These collectors effectively retain coarse mode particles, but their effectiveness at controlling submicron particles is arguable (Lipsky et al., 2002; Ylatalo et al., 1998).

The coal quality, combustion technology, boiler size, operating conditions, electrical generating capacity, and also types of APCD are major parameters for the release of particulate matter into the atmosphere as a result of coal combustion (Smoot et al.. 1980; Damle et al., 1982; Del Monte et al., 1983).

2.3 Fine Particle Formation In Coal And Biomass Combustion

2.3.1 Alkali metals, chlorine, and sulphur species in coal and biomass

Alkali metals in coal occur chiefly as alumina-silicates expressed as K_2O or Na_2O associated with minerals of chemical formula such as: $Na_2O.Al_2O_3.6SiO_2$, $K_2O.2Al_2O_3.6SiO_2.H_2O$ (muscovite) or $K_2O.Al_2O_3.6SiO_2$ (illite) (Raask, 1985). During thermochemical conversion, the non-volatile silicate alkalis mainly remain dissolved in the particle but partly escape in the vapour phase. However, alkalis were also found to be organically bound as carboxylic cations or as other inorganics like sodium chloride (NaCl) dissolved in the pores of coal (Glazer, 2007). Some discussions assumed that sodium was ionically bound to the coal shell independently of chlorine and released as hydrogen chloride (HCl) at lower temperatures during certain tests. Raask (1985) suggested that the liberation of HCl was due to the successive reaction of the released NaCl with the kaolin present in coal and with sulphur.

Sulphur exists in coal as organic sulphur, pyrite and sulphates. During the combustion process, coal sulphur is oxidized to SO_2 and SO_3, portions of which gases condense on the particles, with formation of sulphuric acid or further sulphates. Their contribution to particulate emissions, acid rain, and corrosion of boiler components was already mentioned previously. Chlorine is present in the form of sodium chloride as included or excluded mineral grains or in ionic form in the coal structure (Raask, 1985).

The way alkalis, sulphur, and chlorine are bound in the biofuels appears to differ from coal. Alkalis occur either as water soluble or with ionic exchangeable links and sometimes bond to oxygen not having functionalities within the matrix according to other authors (Glazer, 2007). The organically bound alkalis were believed to be easily released during combustion. Nevertheless, it is important to emphasize the higher proportion of potassium in biomass compared with coal, whereas sodium often

accounts for similar values as that found in coal (Glazer, 2007). Potassium chloride (KCl) was also a reported major mode of occurrence in biofuels. Chlorine and sulphur species exist generally in biomass in anionic forms (Glazer, 2007). Like in sugar cane, and straw, grass was characterized by high quartz that helps to strengthen the plant structure. The typical vaporized inclusions present in the biomass and coal ashes and their transformation are illustrated respectively in Figures 2.2 and 2.3.

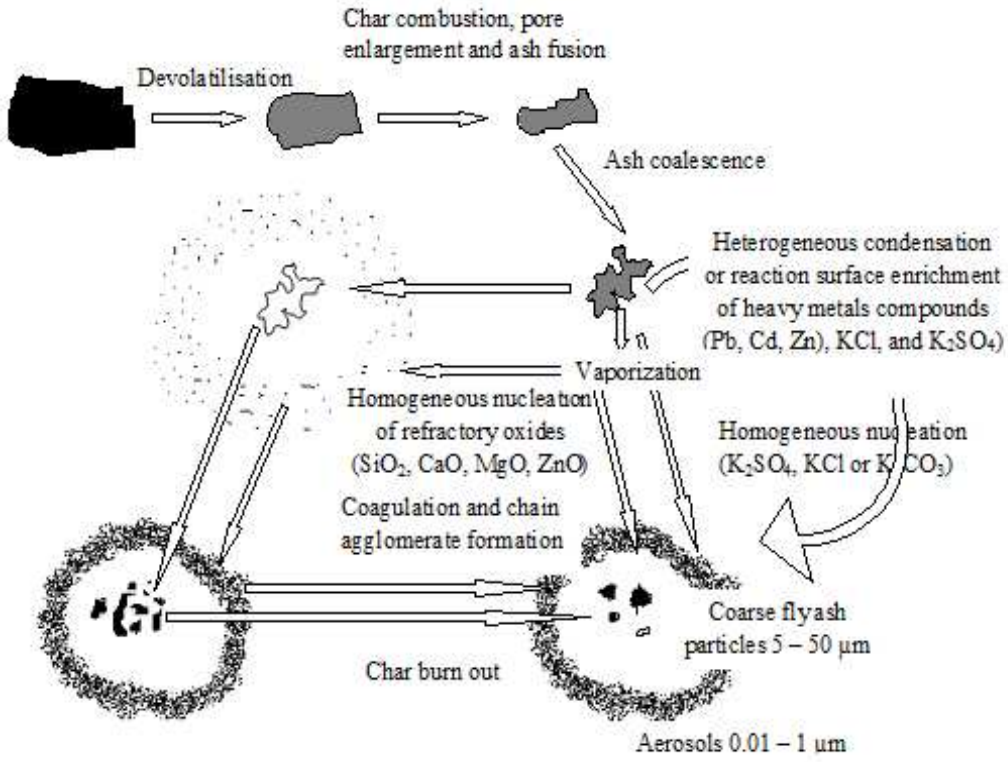

Fig. 2. 2 Particle formation mechanism during biomass combustion (adapted from Van Loo and Koppejan, 2002)

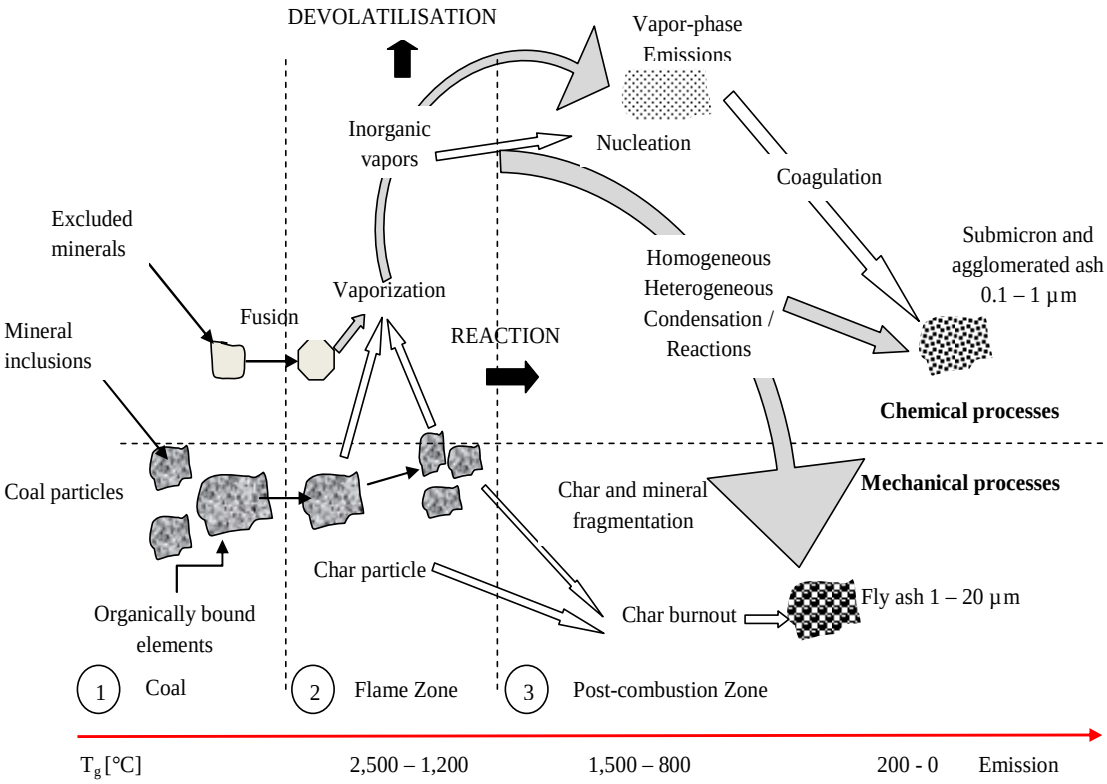

Fig. 2. 3 Particles formation mechanism during coal combustion (adapted from Wayne et al., 2002)

2.3.2 Release of Alkali metals, Chlorine, and Sulphur during Co-firing of Biomass with Coal

During coal combustion, a small fraction of alkali metals escape the glassy phase into the vapour phase. On the other hand, sodium was mainly released as NaCl or independently of Cl as Na. The behaviour became different when biomass was associated to the combustion system. Recent laboratory tests of combustion of pure straw have shown that the release of alkalis, Cl, and S was related to the chemistry of the combustion process (Knudsen et al., 2004). Experiments conducted with circulating fluidized combustors revealed that high potassium biofuels lower the SO_2 release whereas silica decreased the release of potassium that was in fact function of the chlorine content rather than the fuel's potassium content (Westberg et al., 2003). Muller et al. (2007) examined the release of K, S with interactions of straw and coal

blended at varying ratios under oxidizing conditions using High Pressure Mass Spectrometry for hot gas analysis. Their release was strongly dependent upon silicon, chlorine, and the type of binding. Therefore, the mechanism of potassium release during biomass combustion is still a subject of debate. The presence of chlorine in the biofuels plays a role of shuttle for the devolatilisation of alkali metals (Baxter et al., 1998). At the early stage of devolatilisation, the potassium escapes as chloride and hydroxide. Knudsen and co-workers (2004) advocated that high chlorine content biofuels such as straw tended to form chlorides while low chlorine content fuels form hydroxides. Most of the experiments at that date were performed under low heating rates, raising doubt about the validity of the results under pulverized-fired boiler conditions with higher heating rates (Ma et al., 2007).

Moreover, Miller (2003) observed at 1100 °C that the amount of SO_2, K, and Cl species released during the combustion of pure coal and straw did not reflect the initial values. The release of KCl and HCl was influenced more by the fuel's chlorine content. From the changes of behaviour of the emissions for the blend cases, a proposed scenario assumed potassium capture by clay minerals of the coal:

$$2KCl + H_2O + xAlSi_yO_z = \text{K-aluminosilicate} + 2HCl \qquad (2.1)$$

At a low temperature of 800 °C, the release of SO_2 decreased and on the other hand KCl and HCl stayed in the same order of magnitude as at high temperature. Miller (2003) concluded that the influence of fuel interactions was stronger than at 1100 °C.

Hald (1994) found that the amount of alkali metals liberated to the gas phase during thermochemical conversion was dependent upon:

- Increase of the temperature,
- Increase of the chlorine content in the fuels,
- Decrease of the pressure,
- Increase of the sulphur content if the conditions are oxidizing.

2.3.3 Formation of Alkali Sulphate Fine Particles in Biomass Co-firing with Coal

The alkali metals released as chlorides during the combustion of biomass or biomass/coal blends discussed in the previous section were responsible with the SO_2, originating from the sulphur in both fuels, for the formation of alkali sulphates. The mechanism described by the reaction (2.2) led to reduction of SO_2 emissions and increase of fouling deposition together with KCl transport in the system.

$$2KCl + ½\ O_2 + SO_2 + H_2O = K_2SO_4 + 2HCl \qquad (2.2)$$

Some authors argued that the mechanism was principally homogeneous in the gas phase yielding firstly gaseous potassium sulphate that would nucleate and condense onto coarse particles in the low temperature zones. Though, Glarborg and Marshall (2004) disagreed that the mechanism was kinetically very demanding and proposed a detailed homogeneous sulphate formation mechanism. However, Schofield (2003) contested that the low vapour pressure of potassium sulphate is insufficient to trigger the nucleation process but defended more the idea of a rapid heterogeneous formation of K_2SO_4 at the surface of coarse fly ash particles. On short time scales, the sulphation of solid and molten ash KCl by SO_2, and O_2 was estimated too slow though precursors gave better results. Christensen et al. (1998) also argued for a gas-to-particle conversion issuing from homogeneous nucleation of K_2SO_4 particles. But the oxidation of SO_2 to SO_3 was suggested in both cases by Christensen and Livbjerg (1996) as the limiting step to the overall reaction mechanism kinetic.

2.3.4 Reactions of Alkalis with Silicate Impurities in Combustion Flames

Due to the scarcity of available data and literature on the fate of alkali metals during combustion of biomass/coal in pulverized-fired boilers, the majority of observations were based on low heating rate systems such as fluidized bed combustors. Pyrolysis alkalis were in most cases reported to be sequestered by aluminium silicates under the conditions prevailing in fluidized bed reactors (Zheng, 2003). The corresponding reaction (2.1) implied more gaseous HCl while fuel ashes were enriched in kaolin or aluminium phases. Nevertheless this corrosion disadvantage may be compensated for by less deposition on heat transfer surfaces. Raask (1985) among other authors explained that the alkalis transformed into condensed potassium and sodium silicates from interaction with SiO_2 and Al_2O_3 species were stable at the temperature range of 800 °C – 900 °C. These alkali compounds are distributed between the bottom ash, the fly ash, and the flue gas as illustrated by Figure 2.4 below.

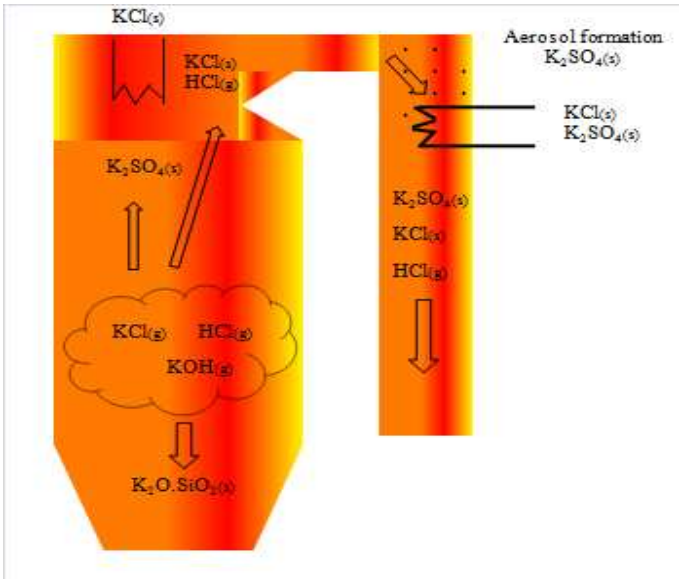

Fig. 2. 4 Path of potassium within combustion systems (adapted from Nielsen, 1998)

Whenever alkali metals are present in the combustion system due to the use of biofuels, it should be expected that they generate profound structural transformation of the alumina-silicate compound, lowering its melting point (Miles et al. 1996).

2.4 Summary

Coal and biomass materials have physical and chemical features that affect differently their respective behaviour during combustion. Though the conversion processes remain analogous during combustion, the interaction of mineral grains and the ash content might influence significantly not only gaseous emissions but the fly ash formation, particle size distribution, composition and morphology during co-firing. This raises the issue of the adverse effect of fine inhaled particulate matter ($PM_{2.5}$) on human health likely to escape from power stations' cleaning apparatus.

The prediction of fly ash size distribution has been achieved by using CCSEM data and currently-developed ash formation models. Considerations of the combustion conditions (especially particle temperature) quantified by CFD simulation, should lead to better results.

The mechanisms of increased emissions of fine particulate matter have been mentioned within this chapter. The resulting particulate fly ash size distribution during both biomass combustion and co-combustion with coal were generally reported bimodal with one peak originating from the mechanical process (mineral inclusions coalescence) and the other peak resulting from the chemical process of homogeneous nucleation, condensation and coalescence of vaporized alkali compounds.

However, several works revealed different behaviours of fly ash, results likely influenced by the combustion technologies and operating conditions. This was to some extent linked to the reduction of the amount of fine particles escaping from the flue gas cleaning devices normally mounted on the system, the efficiency of which still needed improvement. The focus given by many authors to comprehend and model the key process responsible for the aerosols formation was a step forward towards mitigation of particulate emissions during biofuels combustion.

The next chapter presents the experimental results of the set of tests operated on the pilot-scale combustion facility.

CHAPTER 3. EXPERIMENTAL INVESTIGATIONS AND RESULTS

3.1 Introduction

This dissertation is based on a pilot-scale experimental programme into the effects of co-firing biomass (of two types) with typical South African power station coal using a pulverised-fuel burner.

Tests were carried out using both herbaceous (grass) and ligneous (sawdust) types of biomass. For both types tests and simulations were carried out following the experimental programme shown in Table 3.1 for three co-firing ratios, namely with 10%, 15% and 20% of biomass in the fuel blend, on an energy basis.

Table 3. 1 Planned co-firing tests

Test (Eskom No.)	Fuel blend	Biomass to Coal Ratio (on Energy Basis)
	Tests done with the PSCTF:	
11	Coal alone (baseline coal A)	0%:100%
13	Sawdust and coal A	10%:90%
14	Sawdust and coal A	15%:85%
15	Sawdust and coal A	20%:80%
16	Grass and coal A	10%:90%
17	Grass and coal A	15%:85%
18	Grass and coal A	20%:80%
	Tests done with the DTF:	
1	Coal alone (baseline coal A)	0%:100%
2	Sawdust and coal A	10%:90%
3	Sawdust and coal A	15%:85%
4	Sawdust and coal A	20%:80%
5	Grass and coal A	10%:90%
6	Grass and coal A	15%:85%
7	Grass and coal A	20%:80%

A particular objective for this dissertation was to investigate, using standard sampling and detailed analysis methods, the effect of biomass on the production of fly ash in the range of less than 10 µm and to determine the most favourable type of biomass based on the percentage of PM_{10}.

3.2 Combustion Test Facility

The Pilot Scale Combustion Test Facility (PSCTF), illustrated in Fig. 3.1 and 3.2, located within the Eskom Research and Innovation Department (ERID) is a 1.19 x 1.19 x 6.66 m refractory lined, vertical down-fired flow furnace (radiant section). The thermal output for combustion experiments is 1 MW_{th} and operates with a single low-NO_x burner at atmospheric pressure. The facility includes milling, dosing and blending devices for different coal types. The installation is equipped with a gravimetric (weight-loss) type of feeder controlled for variable feeding rates capable of feeding 100-250 kg/h of coal or alternative fuels. During normal operation the feeder continually weighs itself and adjusts the revolutions per minute of the feed auger to maintain the desired feed
rate.

Fig. 3. 1 Eskom/ERID combustion test facility, Rosherville

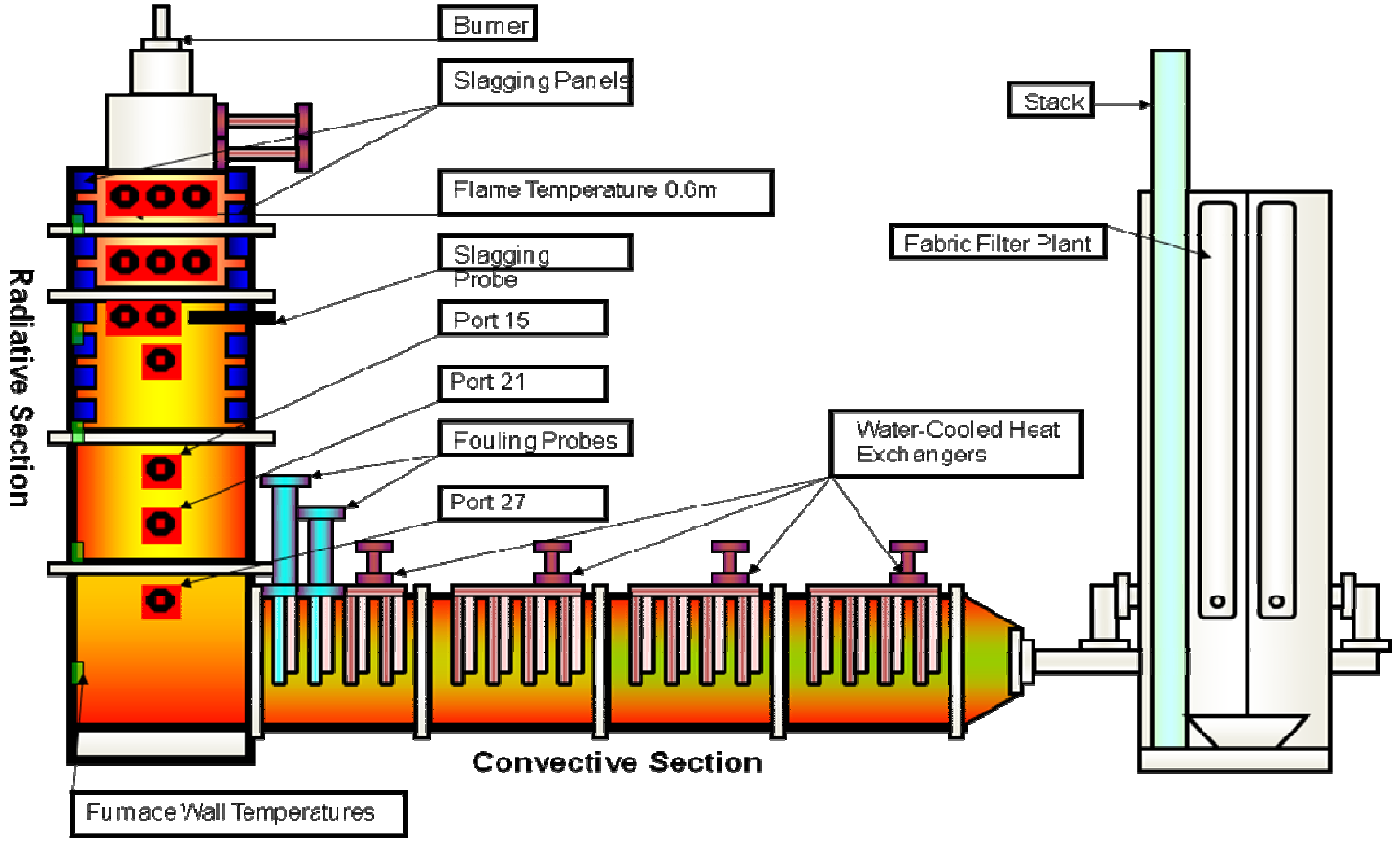

Fig. 3. 2 Eskom/ERID Pilot-scale Combustion Test Facility (TSI, 1998)

To feed the biomass into the furnace, a diesel lance which runs through the centre of the burner was removed to make room for the biomass vibratory feeder (Fig. 3.3). The furnace pressure had to be subsequently decreased to prevent biomass blow out through the feeding pipe because of its low density. The combustion air, split into primary and secondary air for the furnace (Fig. 3.4), was supplied by an air compressor. The coal conveying primary air temperature was specified to be heated up to a peak temperature of 130 °C. The variable secondary and tertiary airs, independently injected with swirl, are heated up to a maximum temperature of 400 °C. The primary and secondary air temperatures and flow rates going to the feeder and burner were monitored and controlled. The average furnace operational temperatures were between 1400 °C and 1200 °C for the radiant section with a maximum level of 1200 °C at the convective pass inlet. The flue gas was cooled down to 150 °C through a combination of water-cooled heat-exchangers and air-cooled fouling probes. An induced draft fan accounted for the necessary draft for the negative pressure operation.

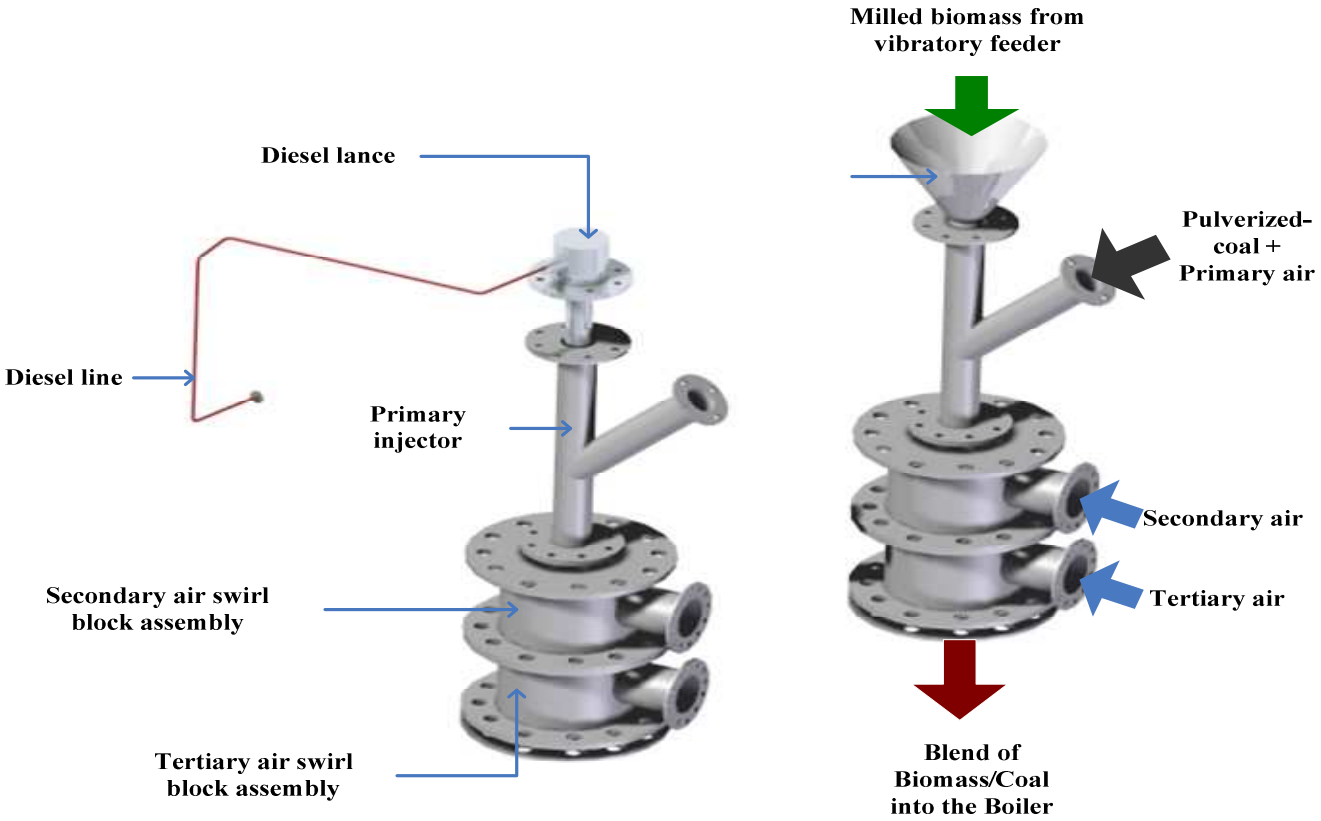

Fig. 3. 3 Burner assembly modified configuration

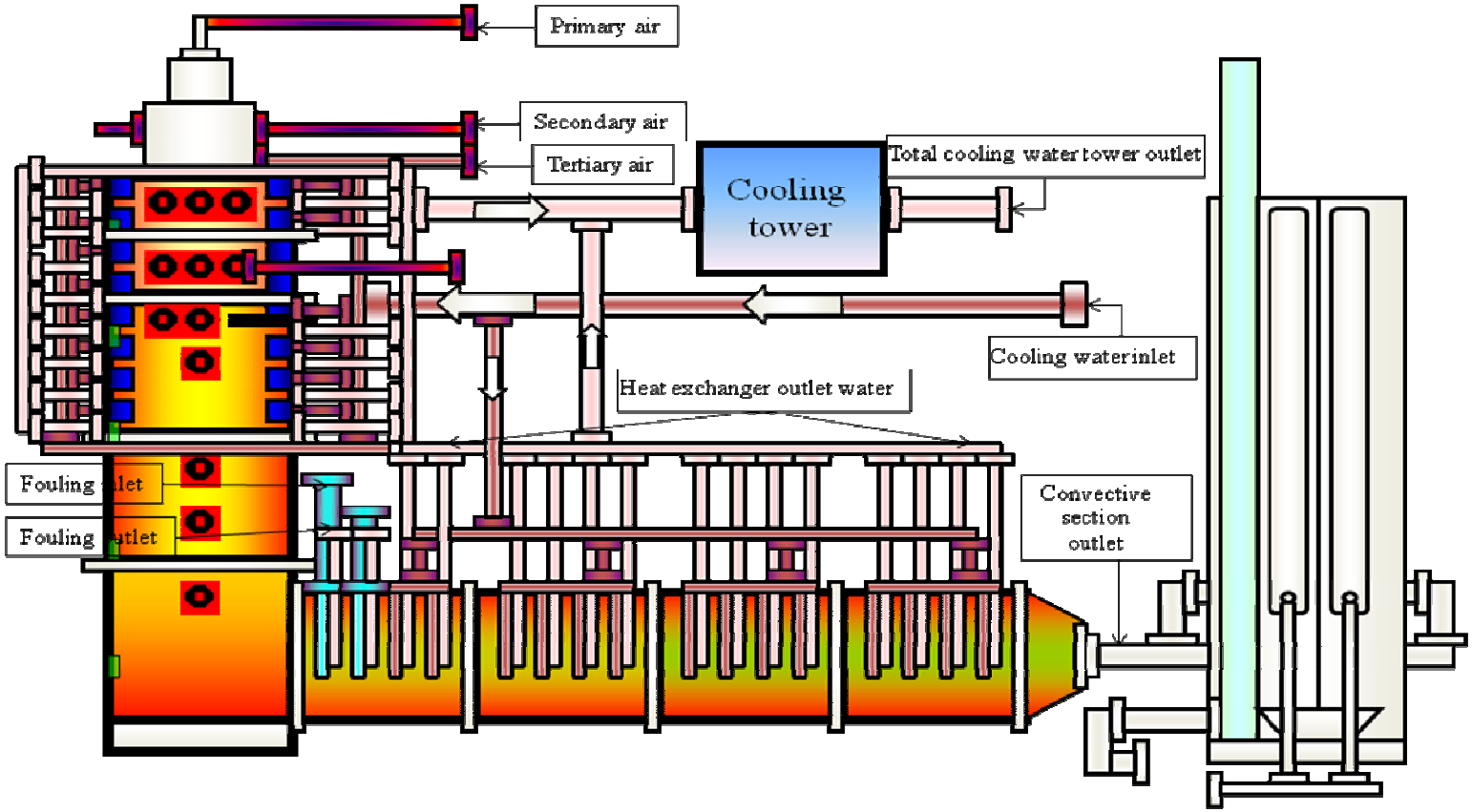

Fig. 3. 4 PSCTF Process and Instrumentation Diagram (TSI, 1998)

This combustor was designed (TSI, 1998) to reproduce the time/temperature histories and complex particle interactions of commercial-scale boilers with residence times of 3 s and 5 s respectively in the radiant and convective sections. The steady-state combustion conditions are nearly achieved by diesel injection into the furnace to heat it up until the fuel auto-ignition temperature is reached.

The radiant unit is equipped with multiple optional sampling ports at different heights for fly ash collection, ash deposition measurements, and flue gas composition analysis (Fig. 3.2).

Combustion gases and solid particles travel down the furnace in turbulent flow towards the flue gas coolers (heat exchangers) and into a bag-house. O_2, CO_2, CO, NO, SO_2, and NO_2 gas species may be analysed on-line. Further upstream, on the same row but opposite to the top sampling ports, the installation is equipped with an optical view port/sight glass for checking the flame stability.

3.3 Sampling And Analysis Techniques

The very low velocity of the flue gas inside the convective pass of the combustor caused fly ash particles of previous experiments to settle inside this section. This suggested that there would be contamination of fly ash samples, in the case where samples were collected at the convective section outlet. Therefore, suitable fly ash sampling could only be achieved upstream from ports at different heights on the furnace chamber. Recently, Van Alphen (2005) studied the variation of the major phases of fly ash with the furnace height, from the boiler wall to the centre. He recommended the important precautions and methodology during the sampling period. The sampling probe shown in Figure 3.5 was therefore kept inserted at three distinct levels in the radiant section (Fig. 3.6) to a specific depth to reduce the error that might result from segregation of particle size as depth increases. The sample was sucked by compressed air through the pipe into a jar.

Depending on the types of blends tested, the sampling could start only after stabilisation had been reached, to negate possible abnormalities of the samples.

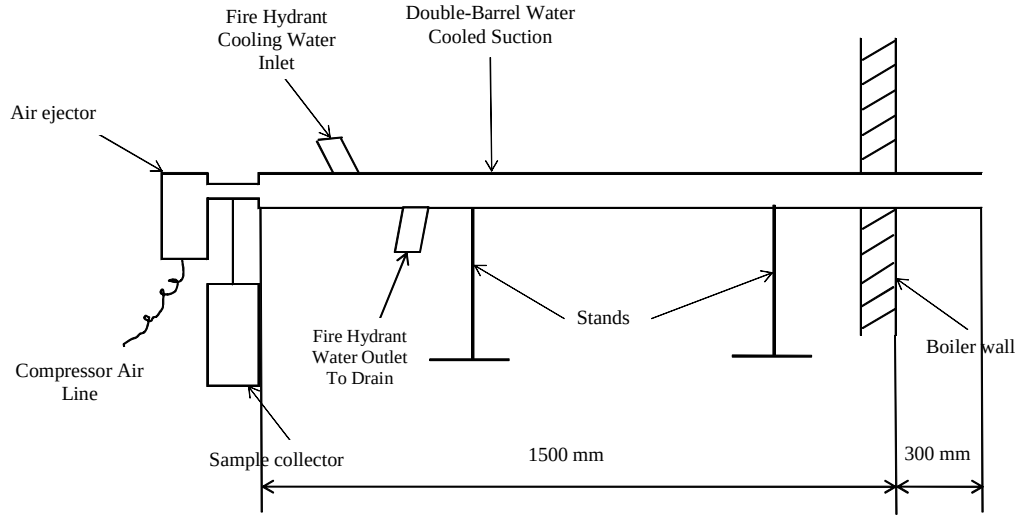

Fig. 3. 5 Suction pyrometer (adapted from van Alphen, 2005)

Fig. 3. 6 Back end of the Suction pyrometer inserted at port 9 of the PSCTF

3.4 Experimental investigations

3.4.1 Fuels and Tests Program

Due to the limited number of tests scheduled, only one type of coal was used. This coal was chosen to be as representative as possible of the coals burned in Eskom coal-fired power stations for the year 2006, based on the monthly average calorific values. The average value was found to be 19.64 MJ/kg, as indicated in Table 3.2.
The use of coal for power generation is responsible for carbon dioxide (CO_2), nitrogen oxides (NO_x), and sulphur dioxide (SO_2) emissions, and slag deposition. Carbon dioxide is a greenhouse gas while NO_x and SO_2 form acid rain, destroy ground level ozone and create smog. Hence, apart from the objective of this present work, other research aspects were being investigated such as impact of co-combustion of biomass with coal on the gaseous emissions, slag deposition and possible ignitability improvement (Pokothoane, 2009). For the latter reason, the coal had to have poor ignition properties in order to show the effect, if any, that biomass would have on ignitability. It also needed to be a coal with low propensity to foul and slag. A choice was made between five selected possible coals whose properties are indicated in Table 3.3 and coal A was chosen for the tests.

Table 3. 2 Calorific values of coals from various Eskom power stations (TSI, 1998)

Power Station	**Calorific value (MJ/kg)**
Arnot	21.81
Camdem	20.03
Duvha	20.87
Hendrina	20.79
Kendal	18.58
Kriel	20.98
Lethabo	14.22
Majuba	20.56
Matimba	18.74
Matla	19.05
Tutuka	20.46
Total/Average	**19.64**

Previous work done by the CSIR and Eskom on a South African renewable database in 1996 (Pokothoane, 2009) needs an update to classify the types of biomass as opposed to the blanket distribution it had adopted. But also based on the physiology and morphology attributes of plant species, two different types of biomass materials were selected: herbaceous (grass) and ligneous (sawdust) (see Fig. 3.7), characterized by their very high alkali metal contents. The common thatching grass “Hyparrhenia Hirta” and sawdust (mixture of municipality trees), both originating from South Africa, were used. The chemical composition of the fuels, the ash composition, with the ratios of certain elements characterizing propensity to fouling or slag deposition during combustion processes, are given in Tables 3.3 and 3.4.

(a) (b)

Fig. 3. 7 Raw biomass: a) Grass; b) Sawdust

Table 3. 3 Properties of selected possible coals

TESTS	COAL A	COAL B	COAL C	COAL D	COAL E
Proximate Analysis					
Moisture	2.4	6.6	3.4	3.5	3.3
Volatiles	20.2	22.4	22.2	20.4	21
Ash	28.8	20.8	18.1	32.2	26.3
FC	48.6	50.2	56.3	43.9	49.4
Total	100	100	100	100	100
Ultimates					
C	55.28	57.08	64.59	51.77	58.2
H	2.65	2.18	3.04	2.5	3.24
O	4.49	10.56	8.28	6.31	6.29
N	1.32	1.37	1.6	1.18	1.34
S	1.73	1.22	0.74	0.78	0.92
CO3	3.33	0.19	0.25	1.76	0.41
Moisture	2.4	6.6	3.4	3.5	3.3
Ash	28.8	20.8	18.1	32.2	26.3
Total	100	100	100	100	100
CV	21.25	21.18	25.34	19.64	22.00
Ash Elementals XRF % Composition					
Ti02	1.4	1.7	1.8	1.6	1.6
Al2O3	24.3	30	40.3	30.5	28.7
SiO2	44.8	41.2	46.9	50.1	47.7
Fe2O3	10.6	11.8	5.5	4	4.3
CaO	11.8	5.5	0.9	8.1	8.7
MgO	2.4	0.2	0.2	1.4	1.6
Na20	0.01	0.01	0.01	0.01	0.01
K20	0.3	0.4	0.7	0.6	0.5
SO3	3.5	8.2	0.6	3.3	4.6
MnO	0.06	0.03	0.01	0.07	0.06
Total	99.17	99.04	96.92	99.68	97.77
Base/Acid Ratio	0.35617	0.24568	0.08213	0.17165	0.19372
Iron Index	3.77540	2.89901	0.45174	0.68662	0.83299
Iron and Calcium	22.40000	17.30000	6.40000	12.10000	13.00000
Iron/Calcium	0.89831	2.14545	6.11111	0.49383	0.49425
Hydrogen/Carbon ratio	0.04794	0.03819	0.04707	0.04829	0.05567
Slagging Assessment	No Slagging	No Slagging	No Slagging	No Slagging	No Slagging
Fixed carbon/Volatile ratio	2.40594	2.24107	2.53604	2.15196	2.35238
Ignition Assessment	Poor Ign.	Good Ign. No slag	Poor Ign.	Good Ign. No slag	Poor Ign.
Slagging Index B/A*% S(dry)	0.631326299	0.320908346	0.062919022	0.138746643	0.184302495
Slagging Assessment	Medium	Low	Low	Low	Low
Silica Ratio	64.36782	70.18739	87.66355	78.77358	76.56501
Slagging Assessment	High	Medium	Low	Low	Low
Fouling Index	0.110412766	0.100728395	0.05831573	0.104709246	0.098796154
Fouling Assessment	No Foul.	No Foul.	No Foul.	No Foul.	No Foul.

Table 3. 4 Chemical and Physical Properties of Fuels and Ashes (Air-dried basis)

PROXIMATE ANALYSES		COAL A	COAL B	SAWDUST	GRASS
Volatile Matter	%	20.2	19.6	72.3	71.2
Fixed Carbon	%	48.6	47.5	17.3	14.55
Ash	%	28.8	30.3	1.35	6.35
Moisture	%	2.4	2.6	9.05	7.9
ULTIMATE ANALYSES					
Carbon	%	55.28	55.91	46.13	43.73
Hydrogen	%	2.65	2.73	4.49	4.27
Oxygen	%	4.49	5.44	35.61	37.07
Nitrogen	%	1.32	1.16	3.09	0.35
Sulphur	%	1.73	0.88	0.04	0.09
Carbonates	%	3.33	0.98	0.24	0.24
GROSS CALORIFIC VALUE	MJ/kg	21.25	21.7	17.7	16.7
NET CALORIFIC VALUE	MJ/kg	20.61	20.61	16.5	15.5
BULK DENSITY	kg/m3	1300	1300	400	350
ASH ANALYSES					
$Ti0_2$	%	1.40	1.80	39.60	0.02
Al_2O_3	%	24.30	26.00	4.40	0.70
SiO_2	%	44.80	60.80	15.20	81.70
Fe_2O_3	%	10.60	3.40	8.20	0.84
CaO	%	11.80	1.40	19.20	3.51
MgO	%	2.40	0.70	0.62	2.10
Na_20	%	0.01	0.10	1.10	0.10
K_20	%	0.30	0.20	4.50	6.87
SO_3	%	3.50	1.70	2.97	1.21
MnO	%	0.06	0.70	1.27	0.13
P_2O_5	%	0.83	0.08	1.58	1.19
Cl	%	-	-	0.03	<0.01
Fuel Ratio (FC/VM)		2.410	2.42	0.25	0.20
Molar Ratio H/C		0.580	0.59	1.43	1.41
Silica Ratio		64.00	0.917	35.00	93.00
Base/Acid Ratio		0.356	0.065	0.568	0.163
Iron Index		3.780	0.223	4.660	0.14
Iron and Calcium		22.40	4.800	27.40	4.35
Iron/Calcium		0.898	2.429	0.427	0.239
Slagging Index		0.631	0.058	0.025	0.016
Fouling Index		0.110	0.020	3.18	1.135
ASH FUSION					
Deformation Temperature	˚C	1310	1550	1250	1380
Softening Temperature	˚C	1320	1550	1280	1390
Hemisphere Temperature	˚C	1330	1550	1300	1410
Flow Temperature	˚C	1340	1550	1330	1430

The coal to be used was received as crushed and sieved and, from the sampling of pulverised coal done upstream of the weigh feeder on the PSCTF, was 212 µm top size.

The biomass fuels, namely sawdust and grass, were milled using a swing mill and sieved through a 2 mm sieve. This process was very slow due to the low output of the swing mill. Grass in particular was difficult to mill. It was first hammer-milled to reduce its particle size to that appropriate for then milling it with the swing mill. Eventually four drums of grass and 3½ drums of sawdust were prepared. Table 3.5 shows the size grading for each of the two types of biomass. Figure 3.8 illustrates the sawdust size grading after the milling with the swing mill.

Table 3. 5 Biomass size grading

	Mass fraction	
Diameter range	**SAWDUST**	**GRASS**
+ 6 mm	0	0
6 – 4.75 mm	0	0
4.75 - 3 mm	0	0
3 - 1 mm	14.6	14.7
1 - 0.5 mm	25.7	21
500 - 212 µm	37.3	39.3
212 - 106 µm	14.5	8.8
106 - 75 µm	3.1	5.9
- 75 µm	4.5	9.3
Total	99.6	99.5

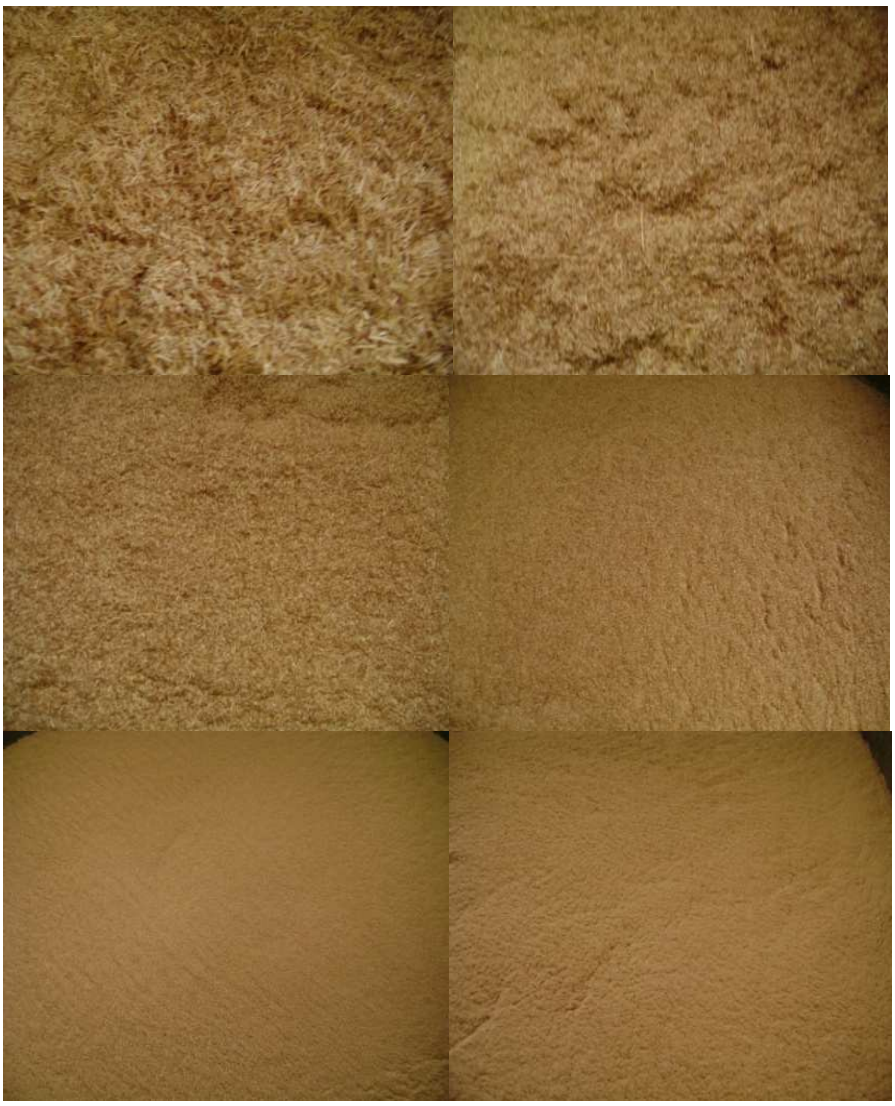

Fig. 3. 8 Sawdust fractionated into size grades respectively 3 – 1 mm, 1 – 0.5 mm, 500 – 212 µm, 212 – 106 µm, 106 – 75 µm, and – 75 µm from top to right.

The contents of each drum of biomass were mixed using the splitter shown in Figure 3.9 in order to ensure uniform test samples. Size grading was then carried out on a representative sample of each biomass type and it was then milled to -212 µm and split into two portions, one of which was used for chemical analyses and the other for Drop Tube Furnace (DTF) tests. The DTF portion was further milled to -150 µm and dried at 60°C in a vacuum oven. The coal was simply crushed, milled, sieved to -150 µm and dried in the sucking oven at 105 °C. Each of the biomass types was then

mixed with coal in a batch process in order to prepare blended samples (about 500g) for the DTF according to the co-firing ratios.

Fig. 3. 9 The splitter used to mix or subdivide samples

The chemical and physical analyses such as proximate, ultimate and calorific values in Tables 3.3 and 3.4 were used to calculate air and fuel flow requirements for the tests on the Pilot Scale Combustion Test Facility. The data were also used in the simulation of the combustion process presented in Chapter 4.

3.4.2 Fuel kinetics characterization with the DTF

The DTF used was a down-fired furnace as shown in Fig. 3.10. It has a height of 2,032 mm and an inner diameter of 50 mm. The furnace simulates the conditions of temperature, residence time and oxidizing environment during pulverized fuel firing. It consists mainly of a variable feeder syringe pump, a ceramic reaction tube, electric resistance heaters, and a water-cooled sampling probe. The temperature is distributed uniformly along the reaction domain and can be adjusted. The fuel particles are pneumatically transported at low feed rate through an insulated and water-cooled injector into the tube. The residence time was estimated to be about 1.8 s under nitrogen atmosphere. Gas species concentrations of NO_x, O_2, CO_2, CO, etc. were simultaneously monitored, using a continuous analyser. Temperature data were traced along the furnace axis during combustion, using a movable thermocouple.

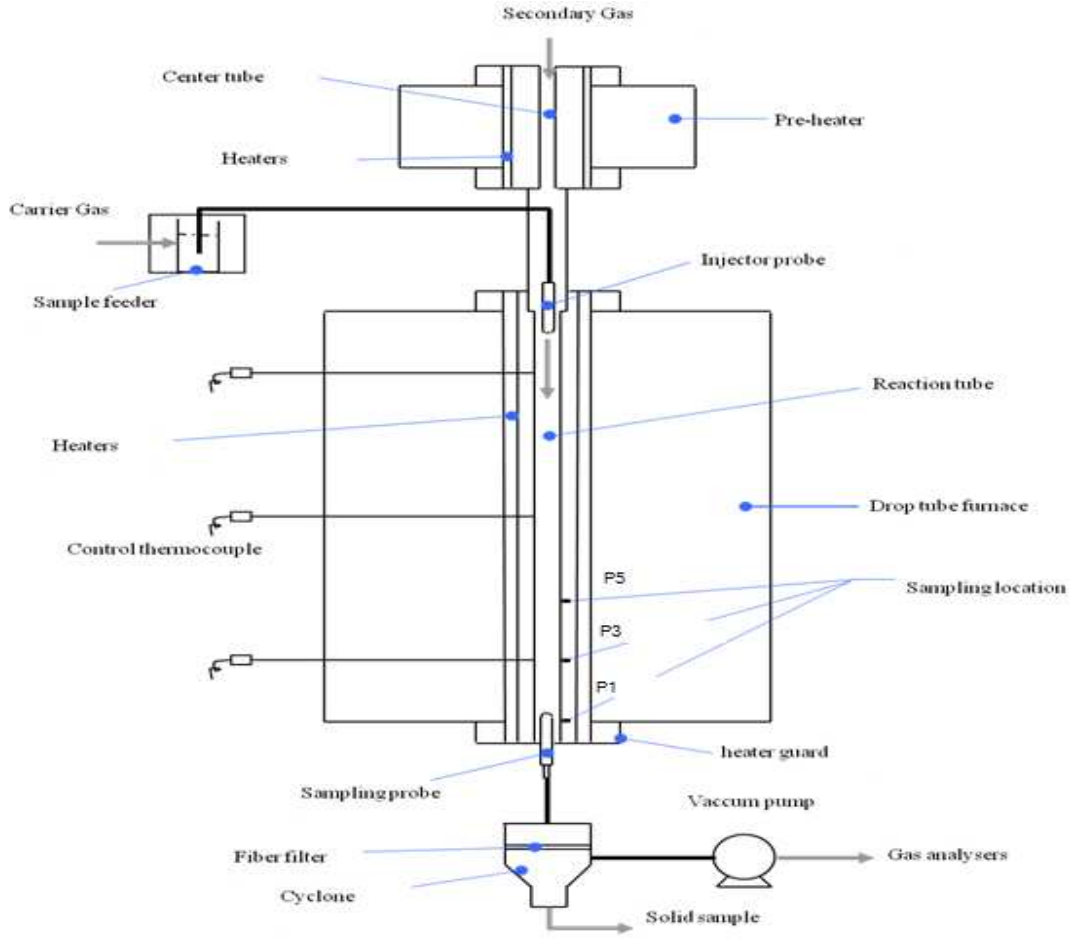

Fig. 3. 10 Eskom/ERID Drop Tube Furnace System (adapted from TSI, Power Systems, 1985)

The chars derived from the coal and its respective biomass blends (Table 3.6) were combusted in a 3% oxygen environment at 1000 °C, 1200 °C and 1400 °C. For 1000 °C partially reacted char was collected at positions P3 and P1, while for the other two temperatures partially reacted char was collected at positions P5, P3 and P1 (Fig. 3.10). Distances of each position from the injection probe were P5 = 52 cm, P3 = 92 cm and P1 = 132 cm. Carbon burnout was expected to be least at P5 and maximum at P1.

Table 3. 6 Chemical properties of the mixture fuels and ashes used on the DTF

PROXIMATE ANALYSES		COAL A	10% SAWDUST	15% SAWDUST	20% SAWDUST	10% GRASS	15% GRASS	20% GRASS
Inherent Moisture	%	2.8	3.3	3.5	3.6	3.2	3.4	3.5
Ash	%	28.9	25.4	24.0	22.3	26.0	24.3	23.1
Volatile Matter	%	20.4	26.4	30.2	33.0	30.9	26.6	33.8
Fixed Carbon	%	47.9	44.9	42.3	41.1	39.9	45.7	39.6
Fuel Ratio (FC/VM)		2.3	1.7	1.4	1.2	1.3	1.7	1.2
ULTIMATE ANALYSES								
Carbon	%	54.75	53.81	53.45	53.26	53.53	52.69	56.41
Hydrogen	%	2.41	2.72	2.93	2.89	2.98	2.87	2.29
Nitrogen	%	1.30	1.42	1.48	1.45	1.35	1.08	1.48
Sulphur	%	1.47	1.28	1.24	1.12	1.27	1.22	1.17
Carbonates	%	3.96	2.77	2.42	2.53	2.60	2.61	2.31
Oxygen	%	4.41	9.30	10.98	12.85	9.07	11.83	9.74
GROSS CALORIFIC VALUE	MJ/kg	21.00	20.46	20.41	20.32	20.46	20.41	20.17
ASH FUSION TEMPERATURES								
Deformation Temperature	˚C	1340	1350	1350	1320	1340	1320	1330
Softening Temperature	˚C	1360	1360	1360	1330	1360	1340	1350
Hemisphere Temperature	˚C	1380	1380	1380	1350	1370	1360	1360
Flow Temperature	˚C	1400	1390	1390	1360	1390	1380	1380

3.4.3 Fuels Mineral Matter Characterization

The characterization of mineral matter in coal particles has been a recent application of a powerful mineralogical methodology tool previously designed by CSIRO, Australia for precious, base metals and industrials minerals called QEMSCAN. QEMSCAN operated like a SEM-EDS with an automated image analysis system that uses backscattered electron (BSE) and energy dispersive x-ray signals from the SEM to create digital images in which each pixel corresponds to mineral species in a small region under the electron beam (Van Alphen, C., 2007).

The prepared mixtures of pulverized fuel samples with molten carnauba wax, and fly ash with epoxy resin, in 30 mm moulds were respectively allowed to set and cure. Once an individual exposed particle on the polished sections has been located from the BSE image, the SEM beam was positioned at predefined points across a particle. At each point a 1-20 millisecond X-ray spectrum was acquired. The elemental proportions were used to identify the mineral at each point (Liu, Y. et al., 2004; Van Alphen, C., 2007).

Table 3.7, given by van Alphen (2008) shows that the sawdust was characterized by a high proportion of calcite, rutile and muscovite or illite. K was a common organically bound element in biomass, and it was unlikely that there were any K-bearing minerals (muscovite/illite and microcline) in the sawdust. Grass was characterized by a high quartz and corresponding high proportion of K-bearing minerals (Table 3.7). Quartz and kaolinite are common constituents of soil and would account for the comparatively high ash content of the grass. Potassium was probably organically bound and was unlikely to be in the form of K-bearing minerals.

Table 3. 7 Calculated normative mineral percentages based on chemical analysis

Estimated Mineral proportions	Formula	Coal A	Sawdust	Grass
Pyrite	FeS_2	2.9	0.08	0.09
Calcite	$CaCO_3$	1.7	0.5	0.00
Dolomite	$CaMg(CO_3)_2$	3.4	0.00	0.7
Apatite		0.4	0.06	0.2
Microcline		0.2	0.1	0.7
Muscovite/illite		1.1	0.6	4.4
Kaolinite	$Al_2Si_2(OH)_5$	17.4	0.00	0.00
Quartz	SiO_2	2.3	0.00	4.3
Siderite/Fe-oxide	$FeCO_3$	0.00	0.1	0.00
Rutile	TiO_2	0.4	0.6	0.00
Coal matrix	C,O and H	70.2	98.15	92.28
Total mineral matter	-	29.8	1.85	7.72
Mineral volatiles	-	6.46	0.33	0.46
Ash% (DB) - calculated	-	23.34	1.53	7.26
Ash% (DB) - measured	-	23.85	1.38	6.50

3.4.4 Fly ash Analytical Chemistry Investigation

In order to better characterize the bio-fuels contents of reactive alkali metals, and organo-metal salts (chlorides, sulphates, and carbonates) soluble in water, and get more information about their fate on the fly ash composition, the raw fuels and collected samples were investigated with ion-exchange chromatography (IC), inductively coupled plasma mass spectrometry (ICP-MS) and a CHNS analyser. The IC is a process used for almost any kind of charged molecule as it works by the principle of separation of ions and polar molecules based on the charge properties of the molecules. It can be used for chloride and sulphate contents analysis.

A wide range of metals and several non-metals at concentrations below one part in 10^{12} are determined by highly sensitive ICP-MS. It is based on coupling together inductively coupled plasma as a method of producing ionization with a mass spectrometer as a method of separating and detecting the ions.

The Leco CHNS analyzer finds utility in determining the percentages of unburnt carbon in the fly ash collected based on the principle of "Dumas method" which involves the complete and instantaneous oxidation of the sample by "flash combustion". The formed CO_2 is separated from the other combustion products by a chromatographic column and detected by the thermal conductivity detector, which gives an output signal proportional to the concentration of this component of the mixture.

3.4.5 Fly ash XRD Mineralogical Investigation

Since very many materials present in the raw fuels or ashes form crystals such as minerals, metals, and salts as well as various inorganic and organic molecules, X-ray diffraction crystallography is a powerful non-destructive technique of revealing detailed information about their chemical composition and crystallographic structure.

Samples were in fact analyzed as powders with random distribution of the grains to ensure that the beam of X-rays that strikes a crystal scatters in all directions. The density of electrons within the crystal helps to estimate the mean positions of the atoms in the crystal, as well as their structure-state proportional to peak position heights and relative intensities. The X-ray spectra generated by this technique thus provides a structural fingerprint of the unknown transformations occurring during the combustion process and may be used to obtain semi-quantitative estimates of abundances and identification of main crystalline phases.

3.4.6 Fly ash SEM-EDS Investigation

To get more information about the minor or sundry undetected phases from the x-ray diffraction such as sulphate, phosphate, etc. in fly ash, which are often reported to be abundant during biomass combustion and co-combustion with coal, the samples collected near the convective section had to be analysed using the scanning electron microscope and the energy dispersive spectroscope.

The SEM system combined with various detectors provided a high resolution imaging, quantitative elemental analysis of the investigated sample and a fast elemental mapping of the area of interest with digital output. The SEM provides a high energy focused beam of electrons scanned across the surface of a sample. A high vacuum was maintained inside the microscope using turbo and ion pumps. Emissions of electrons were generated from the beam interaction with the sample; using special detectors and electronic data acquisition systems an image of the surface was created as a result.

The Energy-Dispersive Spectrometer (EDS) is a detector of x-rays from the sample excited by the high-energy electron beam interacting with the atoms of the material. Quantitative elemental analysis of the sample can be obtained with the aid of computer software by spectral comparison to known standards, because the intensity

of the individual x-ray is related to the quantity of the parent atom in the interaction volume.

The experimental data for combustion and co-combustion experiments applying the pilot scale test facility (PSCTF) are discussed in Chapter 5.

3.4.7 Fly Ash Size Distribution Investigation

The fly ash investigation techniques mentioned up to this point have been qualitative, enabling the impact of higher temperatures, reducing conditions and bio-fuels alkali metals composition to be assessed on the overall ash mineral structure. Quantitative analysis of the same samples was carried out by measurement of the particle size with Master sizer systems.

The Malvern Laser Diffraction Sizer uses the principle of light diffraction from particles in a liquid medium as the measurement means of particle diameters ranging from 1 to 1800 microns. It considers a parallel beam, produced by a low power helium-neon laser, which illuminates the sample to give a stationary diffraction pattern regardless of particle movement. A lens that that has Fourier transform property focuses this pattern onto a multi-element photo-electric detector. An analogue signal proportional to the diffracted light intensity is subsequently produced. Based on the least squares analysis method of a non-linear signal, the size distribution is curve-fitted close to the diffraction pattern. The result of the analysis is a lognormal cumulative size distribution and frequency, either by volume or weight (Malvern Instruments, 2008).

3.5 Results

The tests indicated in Table 3.1 were all carried out as planned, but the results obtained from the PSCTF tests using mixtures of sawdust with coal (nos. 13 - 15 above) appeared to be questionable. It was agreed that these three sawdust tests

should be repeated using the PSCTF only. A difficulty in doing so was that the original coal had been used up and so a new batch of coal had to be used. This necessitated a new coal-alone (baseline) test, as well as the necessary coal B analysis and preparation, and so four new tests were carried out (Table 3.8). These additional tests were finally carried out on 8 August 2008 using the coal B chemical properties shown on Table 3.4.

Table 3. 8 Repeated co-firing tests with the PSCTF

Test (Eskom No.)	Fuel blend	Biomass to Coal Ratio (on Energy Basis)
1	Coal alone (baseline coal B)	0%:100%
2	Sawdust and coal B	10%:90%
3	Sawdust and coal B	15%:85%
4	Sawdust and coal B	20%:80%

Table 3.9 below gives the summary of the fly ash samples collected from the overall set of tests. The blank cells mean that because of unexpected problems with the sampling probe fly ash could not be collected.

Table 3. 9 Overview of the collected fly ash samples from the test series

Date	Fuel	Test number	Port number	Sample I.D.
27/09/07	Coal A	11	Port 9 Port 15 Port 21	CAP09 CAP15 CAP21
27/09/07	Sawdust 10%	13	Port 9 Port 15 Port 21	SD10P09 SD10P15 SD10P21
27/09/07	Sawdust 15%	14	Port 9 Port 15 Port 21	SD15P09 SD15P15 SD15P21
27/09/07	Sawdust 20%	15	Port 9 Port 15 Port 21	SD20P09 SD20P15 SD20P21
27/09/07	Grass 10%	16	Port 9 Port 15 Port 21	GS10P09 GS10P15 GS10P21
27/09/07	Grass 15%	17	Port 9 Port 15 Port 21	GS15P09 GS15P15 GS15P21
27/09/07	Grass 20%	18	Port 9 Port 15 Port 21	GS20P09 GS20P15 GS20P21
08/08/08	Coal B	1	Port 9 Port 15 Port 21	CBP09 CBP15 CBP21
08/08/08	Sawdust 10%	2	Port 9 Port 15 Port 21	SD10P09B SD10P15B SD10P21B
08/08/08	Sawdust 15%	3	Port 9 Port 15 Port 21	SD15P09B SD15P15B SD15P21B
08/08/08	Sawdust 20%	4	Port 9 Port 15 Port 21	- SD20P15B SD20P21B

The gaseous emission values in ppm (Table 3.10) have been corrected to the standard of 6% excess oxygen for better comparison from different test results and taking into account the gaseous dilution effect. The data from the rig were usually logged in a file every minute and an average value of the measured quantity was then taken for each test. Each test took about 30 minutes. The values given in the table below are such averaged values.

The Table 3.11 below gives the char analysis results and combustion kinetics for the DTF tests that were used to set up computational fluid dynamics models for simulation, described in Chapter 4.

Table 3. 10 Summary of the data obtained from the PSCTF

Measured Quantities	Units	Coal A	Sawdust 10%	Sawdust 15%	Sawdust 20%	Grass 10%	Grass 15%	Grass 20%	Coal B	Sawdust 10%	Sawdust 15%	Sawdust 20%
Test Nos		11	13	14	15	16	17	18	1	2	3	4
Furnace Pressure	Pa	-77	-94	-130	-307	-349	-381	-289	-208.15	-184.24	-168.33	-183.76
Gas Temp Port 4	K	1604	1563	1585	1279	1429	1397	1383	1237.97	1254.19	1268.05	1283.05
Gas Temp Port 10	K	1648	1608	1646	1345	1592	1585	1570	1346.36	1367.71	1381.14	1400.29
Gas Temp Port D	K	1548	1504	1524	1226	1444	1440	1438	1216.79	1241.67	1252.76	1269.00
Gas Temp Port 28	K	1387	1349	1382	1094	1345	1349	1339	932.39	961.29	974.33	995.29
Average gas Temperature	K	1547	1506	1534	1236	1453	1443	1433	1183.38	1206.21	1219.07	1236.90
Average Wall Temperature	K	1329	1330	1328	1049	1310	1301	1298	980.88	981.39	982.49	984.87
Convective exit Temperature	K	475	484	496	240	516	522	518	170.48	177.81	180.86	187.86
Oxygen (Zirconia) wet basis	%	5.29	7.06	5.1	7.44	8.06	8.71	9.18	NM	NM	NM	NM
Oxygen (dry basis)	%	4.8	6.61	5.06	7.27	7.49	8.13	8.35	6.12	5.52	4.76	4.38
Carbon Monoxide	ppm	82	33	44	42	41	32	25	23.69	31.38	29.94	30.78
CO_2	%	14.23	12.48	14.01	11.85	11.67	11.04	10.91	12.84	13.43	14.08	14.50
SO_2	ppm	628	729	721	581	497	445	453	477.09	441.52	431.52	405.25
NO	ppm	1210	1059	1063	929	734	682	616	1302.45	1446.17	1527.38	1526.92
NO_x	ppm	1470	1286	1283	1134	901	823	744	1486.89	1642.56	1729.64	1732.59
NO_2	ppm	260	227	220	206	167	141	128	184.44	196.38	202.26	205.68
N_2O	ppm	0	0	0	0	0	0	0	0.04	0.08	0.11	0.27
Combustion Efficiency RTD Port 9	%	95.96	97.82	96.4	97.2	97.24	97.76	97.7	90.80	90.29	90.31	93.63
Combustion Efficiency RTD Port 15	%	98.72	99.52	98.61	99.22	97.46	99.2	99.09	98.43	98.40	98.27	97.82
Combustion Efficiency RTD Port 21	%	98.94	99.71	99.08	99.31	98.3	99.48	99.55	98.76	98.96	98.67	98.49
Rate of Slag Formation	g/hr	NM	NM	17.5	13.9	31.3	32.4	19.2	74.82	NM	NM	NM

NM: Not measured

Table 3. 11 Char analysis results

			COAL A	10% SAWDUST	15% SAWDUST	20% SAWDUST	10% GRASS	15% GRASS	20% GRASS
PROXIMATE ANALYSES	Inherent Moisture	%	0.2	0.4	0.2	0.4	0.2	0.4	0.2
	Ash	%	44.2	43.0	42.4	40.8	42.8	41.9	42.5
	Volatile Matter	%	0.2	0.01	0.01	0.01	0.01	0.1	0.01
	Fixed Carbon	%	55.4	56.6	57.4	58.8	57.0	57.6	57.3
	GROSS CALORIFIC VALUE	MJ/kg	20.5	19.36	19.66	20.22	19.13	20.01	20.04
IGNITION PARAMETERS	Volatiles by DTF, VMdtf	%	30.1	39.2	41.5	43.5	37.4	40.2	43.8
	CV of volatiles	MJ/kg	26.1	23.8	23.2	22.1	24.4	22.7	22
	Heat in volatiles	%	36.3	44.1	45.5	45.6	43.2	43.1	46
	Activation Energy, E_a	kJ/mol	46.6	25.1	32.3	33.5	40.2	30.9	33.7
	Energy ratio, E_r		2.9	7.3	5.9	6.1	4.4	5.9	3.4
	Pre-exponential factor A ($kg/m^2/s/atm$)		15.9	2.3	4.4	3.21	8.6	3.3	5.3
	Burnout Time	sec	1.1	2.6	2.5	1.5	2.5	2.4	1.7
ASH ANALYSES	Silicon (as SiO_2)	%	44.1	44.1	44.5	43.5	45.1	45	45.9
	Aluminium (as Al_2O_3)	%	25.4	26	26.2	25.7	25.5	24.7	24.5
	Iron (as Fe_2O_3)	%	8.4	8.3	8.5	8.3	8.1	7.8	7.8
	Titanium (as TiO_2)	%	1.4	1.6	1.7	1.7	1.4	1.4	1.3
	Phosphorus (as P_2O_5)	%	0.83	0.84	0.82	0.8	0.87	0.82	0.83
	Calcium (as CaO)	%	11.5	11.5	11.8	11.5	11.2	10.9	10.9
	Magnesium (as MgO)	%	2.3	2.3	2.4	2.2	2.3	2.3	2.3
	Sodium (as Na_2O)	%	0	0	0	0	0	0	0
	Potassium (as K_2O)	%	0.3	0.3	0.3	0.4	0.5	0.6	0.7
	Sulphur (as SO_3)	%	5.3	5.5	4.4	4.4	5.6	4.6	4.7
	Manganese (as MnO)	%	0.07	0.04	0.04	0.04	0.05	0.04	0.04

As a general trend, at 1000 °C all grass and sawdust blends showed better carbon burnout than coal alone on the DTF. The sawdust profiles at 1200 °C also revealed better carbon burnout for all its blends and sometimes identical combustion efficiency with coal. The profiles indicated delayed combustion. The situation for grass, however, was different in that it has better carbon burnout than baseline coal at two positions and nearly the same as that of baseline coal at the farthest position for all co-firing ratios. At 1400 °C sawdust profiles showed a worse carbon burnout than at the other two temperatures, with more pronounced delayed combustion behaviour. Grass burnout profiles at 1400 °C, like those of sawdust, were mainly lower than the baseline coal burnout curve, but not as far away as those of sawdust were.

The investigation of the fate of alkali on the particulate matter formation through the very low occurrence of sodium in the ash of the fuels was enabled by the potassium measurements. Since the original potassium contents in the raw fuels were known, co-firing of coal with successively 10%, 15% and 20% of high potassium biomass on an energy basis increased by replacement the resultant concentrations. Biomass materials were generally enriched in reactive potassium that would generate large numbers of fume particles within pulverized-fuel furnace.

The results of the XRD and SEM investigations of the fly ash samples, from the different tests, are shown in Figure 3.11 to Figure 3.25. As mentioned previously EDS was also performed on the samples and the results are presented in the Discussion chapter. Figure 3.11 and Figure 3.12 display respectively the scanning electron photograph and the mineral spectrum corresponding to the fly ash originated from the 100% coal combustion experiment 11. Little sign of coalescence appears from the picture of Fig.3.11 illustrating the fragmentation of large particles into finer ones.

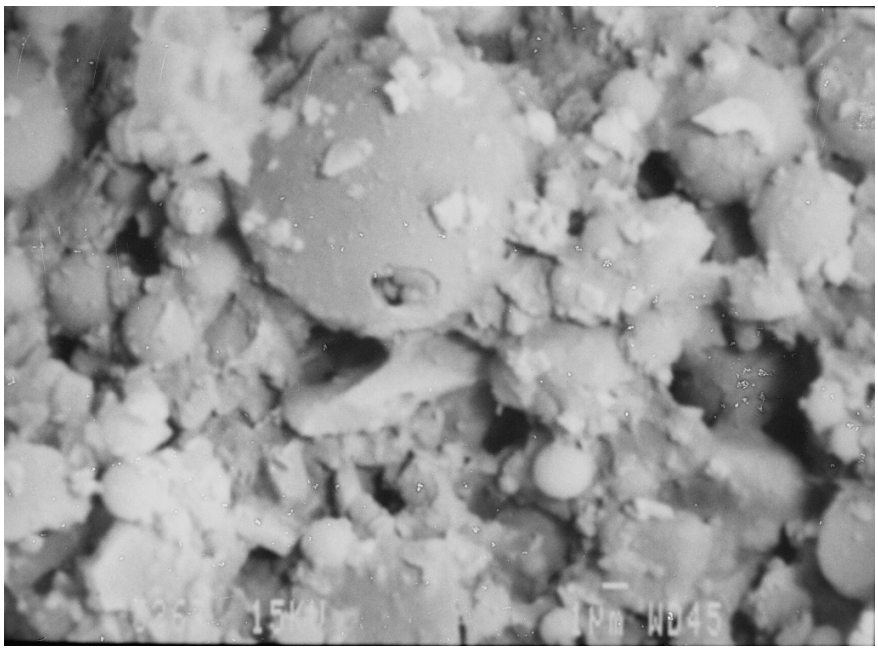

Fig. 3. 11 Fly ash collected from port 21 (experiment 11, baseline coal A, reference Table 3.8)

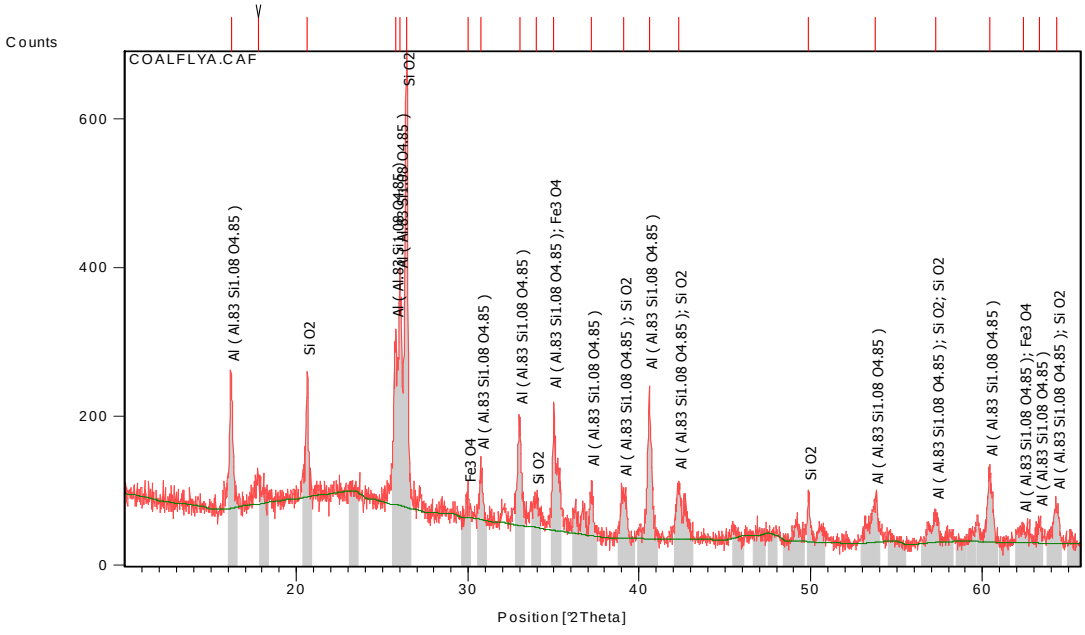

Fig. 3. 12 Flyash from port 21 mineral spectrum (experiment 11, baseline coal A reference Table 3.8)

The mineral spectrum above shows a morphology and composition of the fly ash dominant in alumina-silicate (kaolin, quartz) with a minor phase of Fe_3O_4. Co-combustion of coal with 10% (Fig.3.13), 15% (Fig.3.15), and 20% (Fig.3.17) of grass on an energy basis brought transformation of the $Al_{0.83}Si_{1.08}O_{4.85}$ compound to $Al_{4.984}Si_{1.016}O_{9.508}$ for the first two ratios (Fig. 3.14 and 3.16) and $Al_{4.95}Si_{1.05}O_{9.52}$ for the later (Fig. 3.18). This suggests that the combustion domain was under changing oxidising conditions for the net increase of oxygen concentrations in these phases with the co-firing ratios. Another important observation was the reduction of the volatilisation of Al-Si-phase (kaolinite) with the growing ratios and environment conditions.

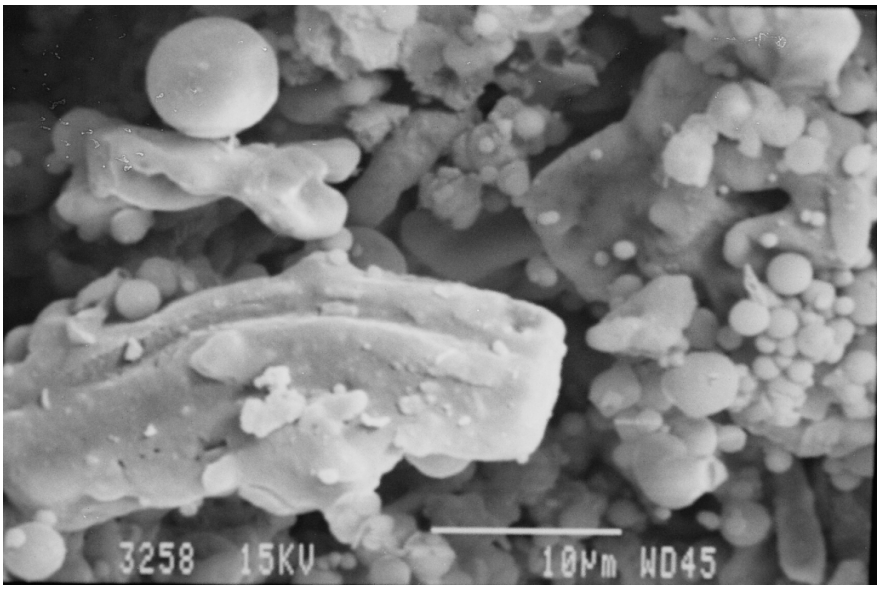

Fig. 3. 13 Fly ash collected from port 21 (experiment 16, 10% grass, reference Table 3.8)

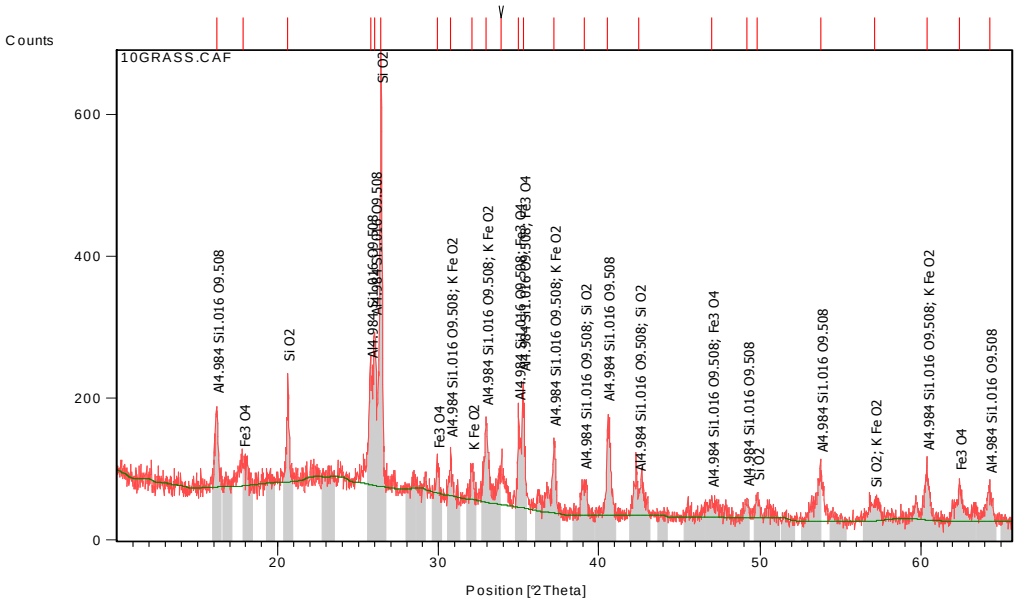

Fig. 3. 14 Flyash from port 21 mineral spectrum (experiment 16, 10% grass, reference Table 3.8)

For the 10% grass fly ash from the port 21 (Fig. 3.13), some trace of $KFeO_2$ was found (see Fig. 3.14), which spectrum was easily confused with the CaO spectrum as no logical explanations could be advanced for its absence in the remaining grass-based tests. At a magnification factor of 20 times the fused particles coalesced together and formed medium sized spherical or coarser non-spherical fly ash particles in major percentage. Similar conclusion is drawn from Figures 3.15 and 3.17 both at the scale of 1 µm emphasized the escalating coalescence effect of fused fly ash particles towards coarser mode with the augmentation of the co-firing ratio.

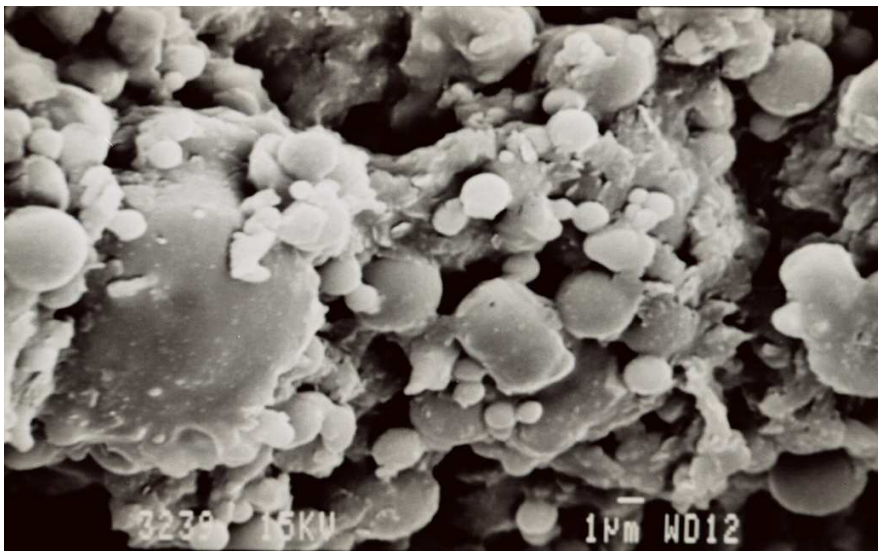

Fig. 3. 15 Fly ash collected from port 21 (experiment 17, 15% grass, reference Table 3.8)

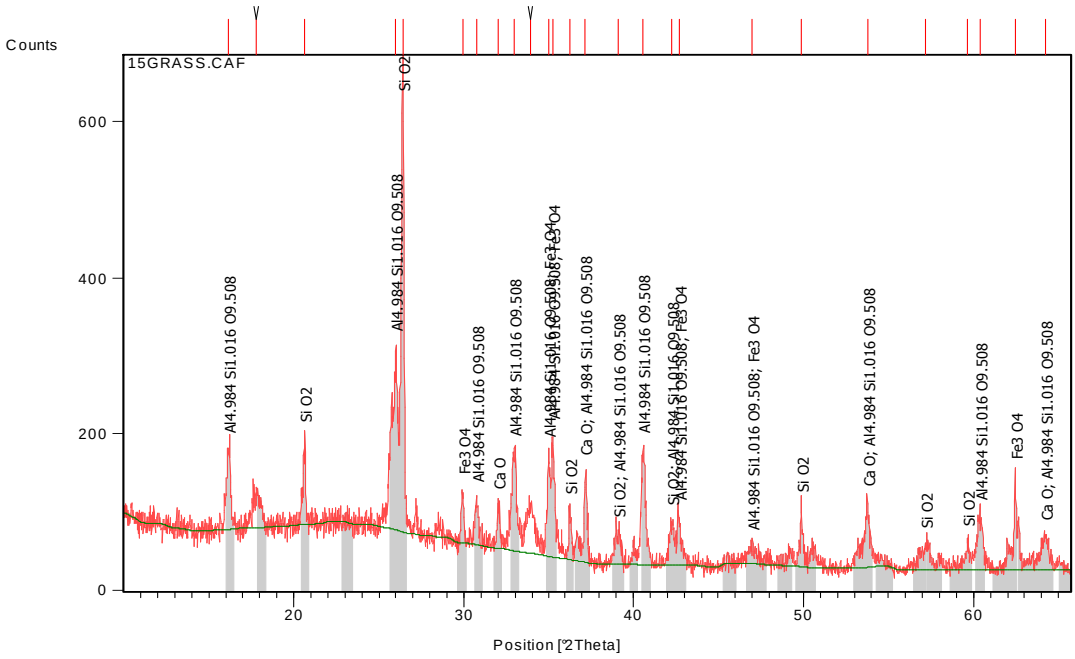

Fig. 3. 16 Flyash from port 21 mineral spectrum (experiment 17, 15% grass, reference Table 3.8)

The 20% grass (Fig. 3.17) fly ash spectrum (3.18) showed qualitatively some similarities with the first grass blend and this case is further investigated in the Discussion Chapter.

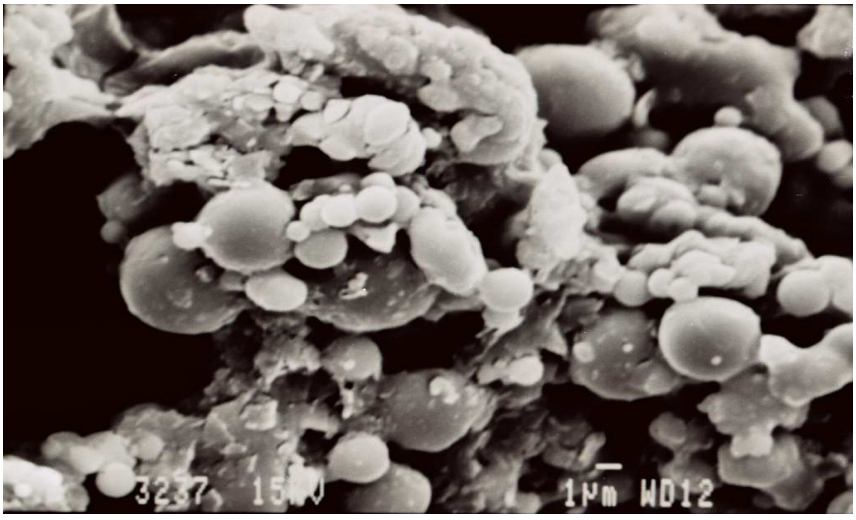

Fig. 3. 17 Fly ash collected from port 21 (experiment 18, 20% grass, reference Table 3.8)

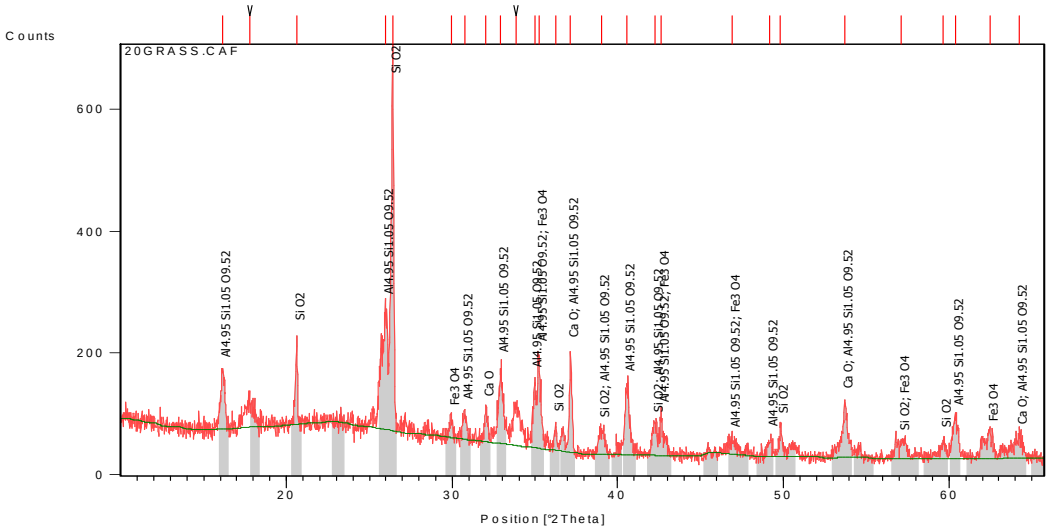

Fig. 3. 18 Flyash from port 21 mineral spectrum (experiment 18, 20% grass, reference Table 3.8)

For the sawdust/coal co-combustion tests, a remarkable phase of alkali alumina was reported in the 10% biomass blend (Fig. 3.19) fly ash spectrum (Fig. 3.20) while the remaining tests samples (Fig. 3.21 until 3.24) were formed of similar molecules like the 20% grass/coal case. As per comparison to the grass blends experiment, the fly ash particles of sawdust (Fig. 3.19 and 3.21) were finer still, spherical and abundant. This suggests the argument that the high content of reactive alkalis plays an important role on the coal major phase transformation or propensity of fly ash to coalesce and agglomerate. Test 13 (10% sawdust) fly ash spectrums shows trace of alkali-alumino-silicate phases $Na_2Al_{2x}O_{3x+1}$ (Fig. 3.20) which is more likely to fuse and coalesce. This particular phase was nowhere to be found when the ratio was increased for the tests 14 and 15 (Fig. 3.22 and 3.24) with different excess oxygen levels.

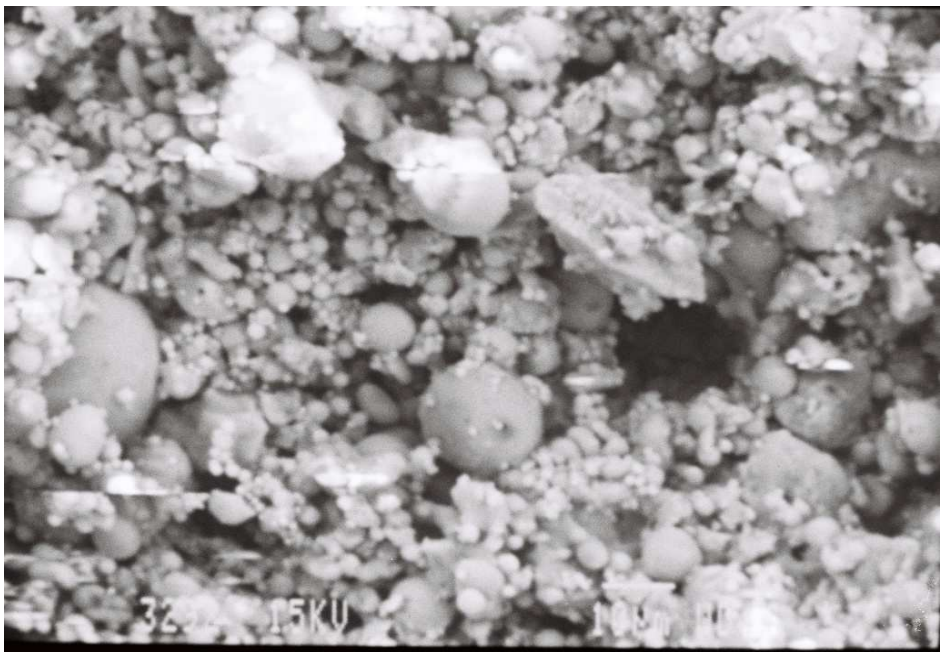

Fig. 3. 19 Fly ash collected from port 21 (experiment 13, 10% sawdust, reference Table 3.8)

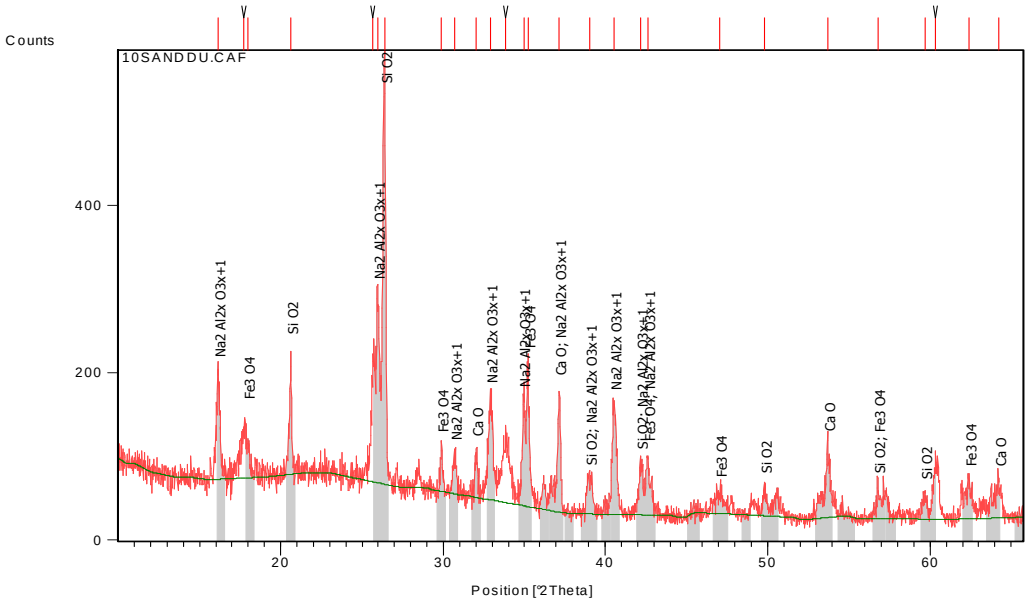

Fig. 3. 20 Flyash from port 21 mineral spectrum (experiment 13, 10% sawdust, reference Table 3.8)

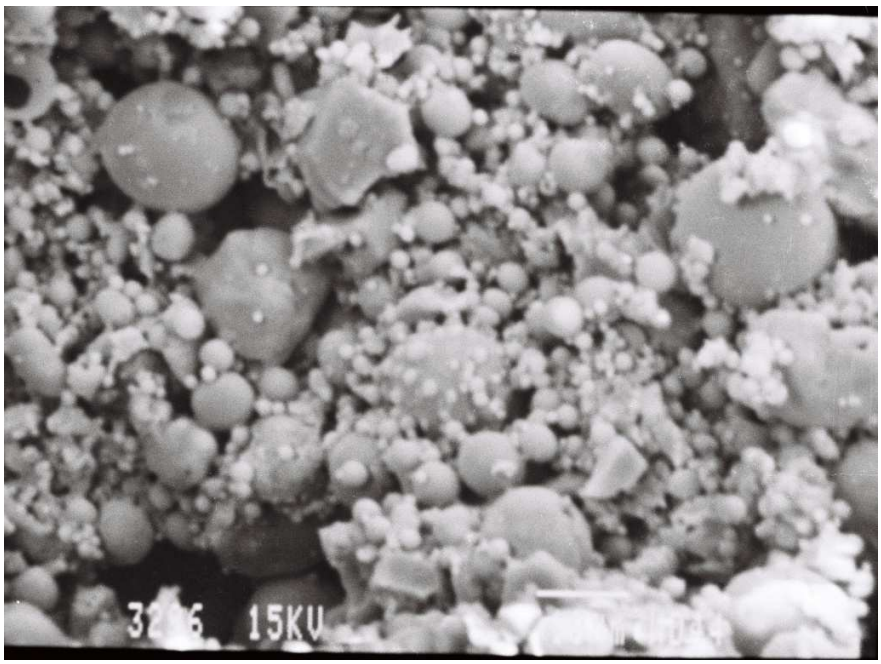

Fig. 3. 21 Fly ash collected from port 21 (experiment 14, 15% sawdust, reference Table 3.8)

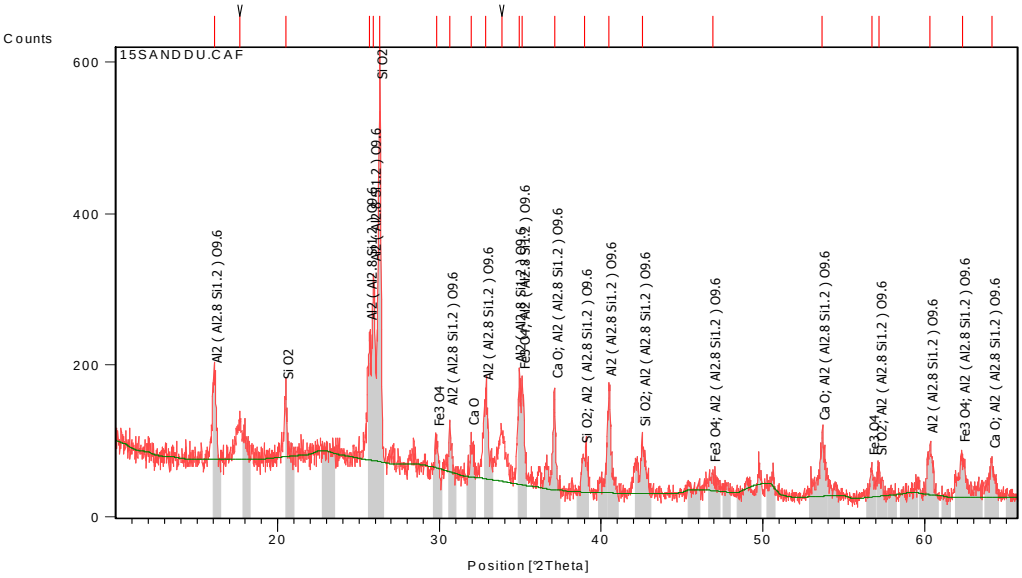

Fig. 3. 22 Flyash from port 21 mineral spectrum (experiment 14, 15% sawdust, reference Table 3.8)

There was a remarkable reduction of the finer range and concentration of fly ash particles for the Test 15, 20% sawdust (Fig. 3.23) but the spectra (Fig. 3.20 and 3.22) have remained the same.

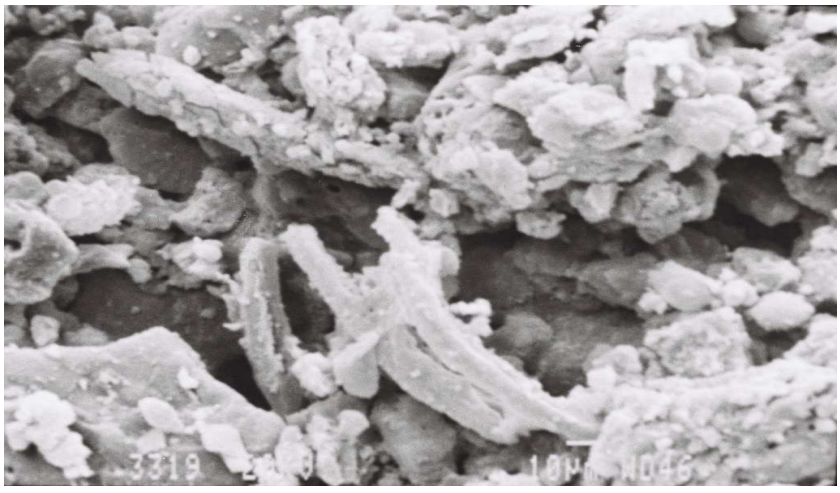

Fig. 3. 23 Fly ash collected from port 21 (experiment 15, 20% sawdust, reference Table 3.8)

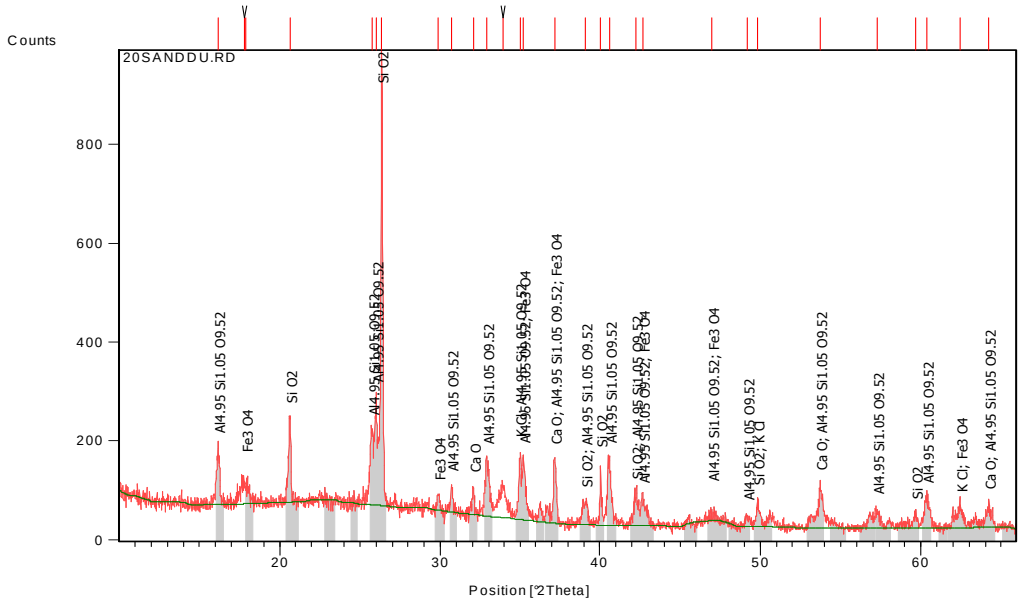

Fig. 3. 24 Flyash from port 21 mineral spectrum (experiment 15, 20% sawdust, reference Table 3.8)

The likely alkali reaction with the main alumina phase observed during 13 had to be investigated by running a new series of sawdust combustion tests (1 – 4) with a nearly similar coal B. Though there was a relatively high concentration of Na and K in the flue gas compared to the baseline, no dramatic transformations occurred to the microstructure and composition of the fly ash as shown by spectra of Figures 3.25 till 3.27. Once again the dominant aluminosilicate phase was observed without significant molecule structural changes under reducing conditions as compared to the coal B baseline test.

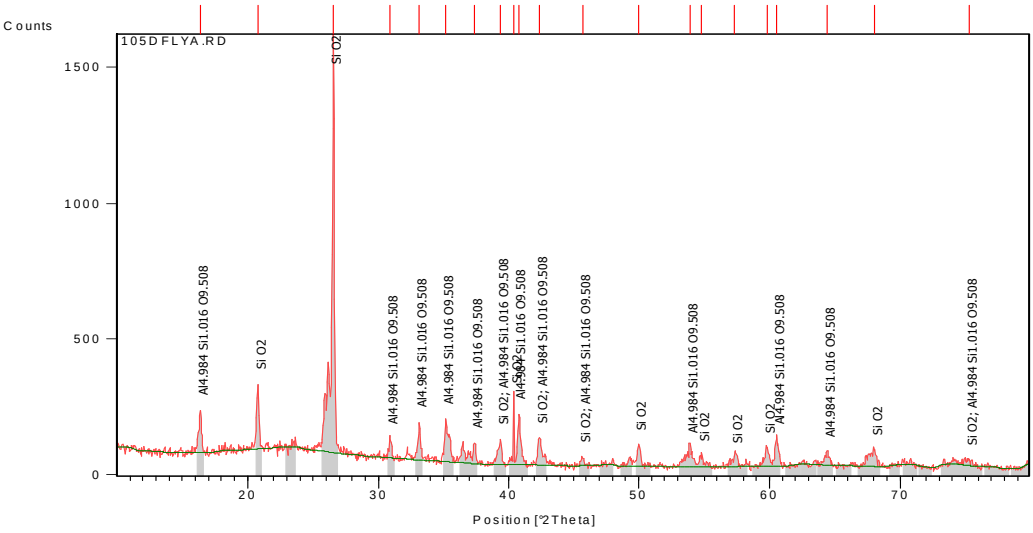

Fig. 3. 25 Flyash from port 21 mineral spectrum (experiment 2, 10% sawdust, reference Table 3.8)

It was however worthy to indicate the formation of Fe_3O_4 (Fig. 3.26 – 3.27) with the decrease of oxygen concentration inside the flue gas (see Chapter 5) while the coal/sawdust ratio increased.

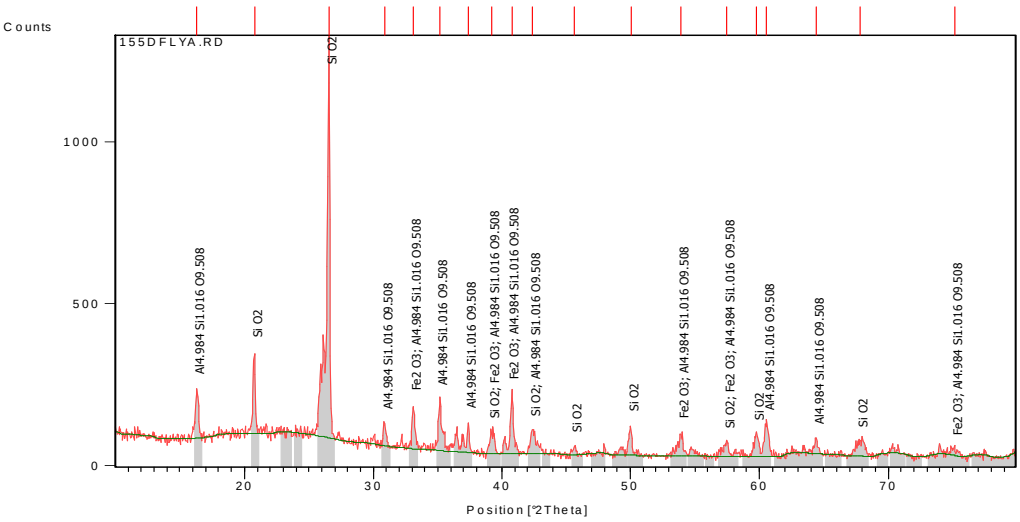

Fig. 3. 26 Flyash from port 21 mineral spectrum (experiment 3, 15% sawdust, reference Table 3.8)

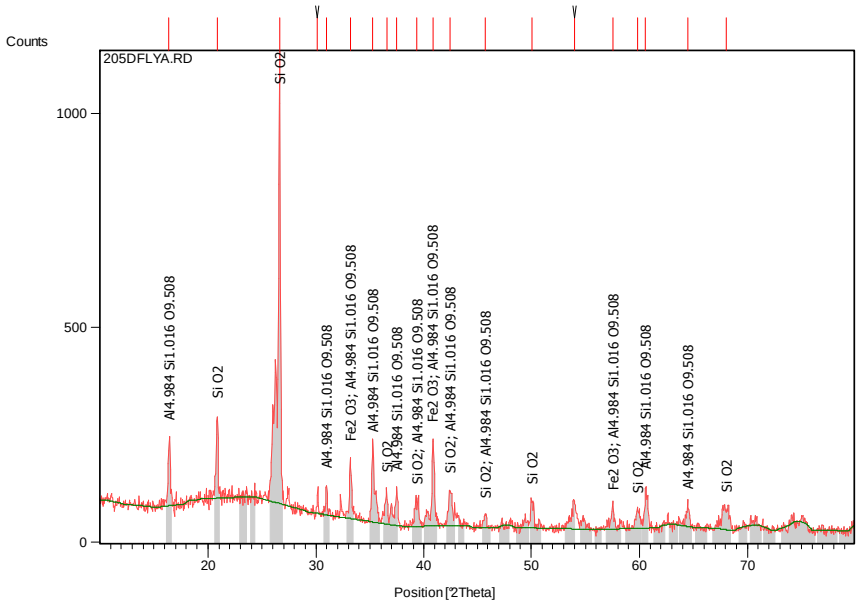

Fig. 3. 27 Fly ash from port 21 mineral spectrum (experiment 4, 20% sawdust, reference Table 3.8)

Visible variability in composition and morphology corresponding to port 21 samples characterized the set of SEM images. The chemistries of the ashes were different, as were the physical characteristics. The physical approach was probed by measurements with the Malvern sizer instrument of the particle size distribution.

Co-firing of sawdust and coal A (Tests 13 – 15) had a strong influence on PM concentration, as suggested by Fig. 3.28 by increasing the percentage of $PM_{>10}$ at the expense of PM_{10}, and PM_{10} to the benefit of finer ones ($PM_{2.5}$) as the co-firing ratio increases.

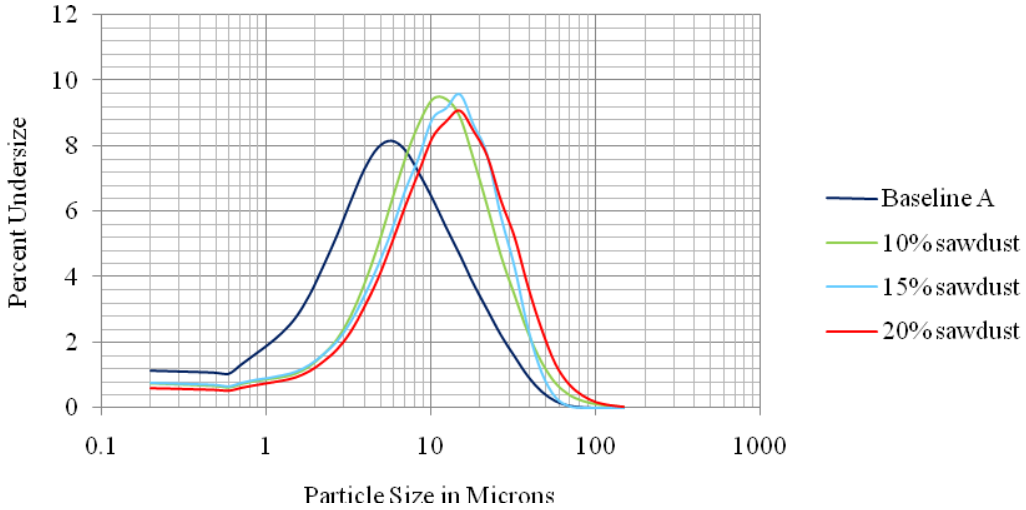

Fig. 3. 28 Lognormal PSD of fly ash for tests 11, 13 – 15 from Port 21

From the baseline coal the mean aerodynamic diameter (Appendix A) changed from 6.09 µm to 14.37 µm, 13.69 µm, and 13 µm respectively, for 10% grass, 15% grass and 20% grass (Fig. 3.29). The areas underneath the curves corresponding to the blends cases were all inferior to that of the baseline at 10 µm particle size meaning of a diminution in PM_{10} concentration.

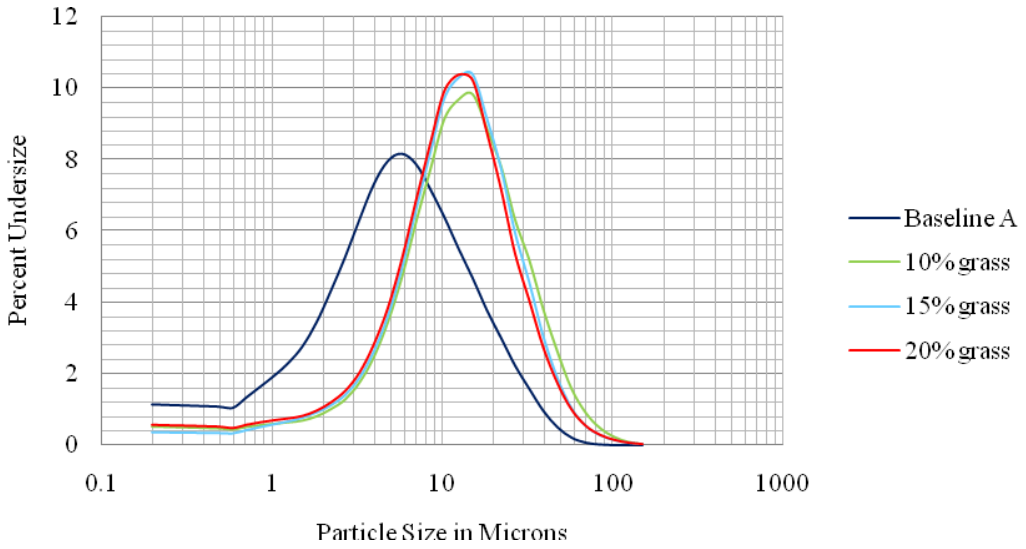

Fig. 3. 29 Lognormal PSD of fly ash for tests 11, 16 – 18 from Port 21

The particle size distribution of fly ash samples collected from Port 21 for tests 1 – 4 (Coal B) typically tended to have two or three modes, respectively located under and over 1 µm as well beyond 100 µm for the sawdust repeated case (Fig. 3.30). Closer look at this particle size graph of the repeated sawdust-based co-firing test series revealed higher diameter in the finer range compared to the previous campaign with coal A (Fig. 3.28 – 3.29).

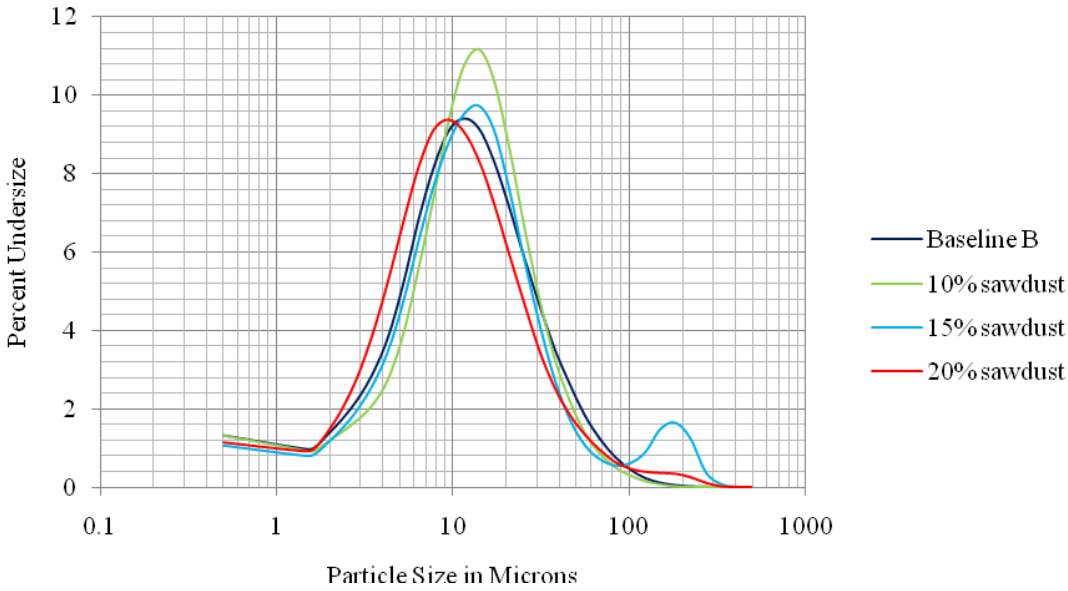

Fig. 3. 30 Lognormal PSD of fly ash for repeated sawdust tests from Port 21

Fig. 3.30 showed a relatively constant or increase of the area below the graphs at 10 µm, indicative of an increase of PM_{10} concentration as the sawdust percentage was increased during the experiment.

3.6 Summary

This chapter presents the results of morphology and composition of fly ash from tests performed on the PSCTF with two selected high and medium alkaline types of biomass respectively, grass and sawdust, burnt with an average coal at ratios of 10%, 15%, and 20% on an energy basis.

For all biomass/coal blends, the potassium retention by fly ash at position 21 of the radiant section was higher than that of the baseline coal except for the repeated sawdust blend tests under different boiler operating conditions (discussed later in Chapter 5). Furthermore, the grass potassium content was higher than that of sawdust, the fly ash of grass blends appeared to capture more potassium than that of sawdust. This suggested a pronounced reactivity with the coal particle matrix for the grass blends.

These visible variations observed by SEM of the morphology and microstructure composition of fly ash were also confirmed by the Malvernsizer measurements of the fly ash particle size distribution. The first set of sawdust blend tests revealed more susceptibilty of formation of finer fly ash particles (less than 10 µm aerodynamic diameter) in comparison with the grass tests series, but both campaigns still showed a drop of PM_{10} with a flattened tail for less than 1µm. The second sawdust tests series, in contrast, displayed a small increase of PM_{10} and a peak of $PM_{1.0}$, depending on the co-firing ratios.

In the next chapter, modelling of the potassium sulphate formation during the thermochemical transformation is described to account for the fine fly ash particles mentioned above, because sulphate is believed to be a major phase of these fine particles.

CHAPTER 4. CO-COMBUSTION COMPUTATIONAL FLUID DYNAMICS MODELLING

Computational fluid dynamics (CFD) is a computational technology that uses numerical methods and algorithms to solve and analyse problems that involve fluid flows, heat and mass transfer, moving bodies, multiphase physics, chemical reactions, fluid-structure interaction and acoustics. Computers are therefore used to build a virtual prototype of the system to be analysed, by solving simplified equations that provide approximate predictions of the performance of that particular design with images and data. Results of CFD analyses are generally relevant for conceptual studies of new designs, detailed product development, troubleshooting and redesign. The low total cost and effort involved in case testing and experiment design makes CFD codes genuine tools for quick data acquisition of complex physical simulations (Wang et al., 2008).

The finite volume discretisation method (domain discretised onto a finite set of control cells) is relatively easy in application compared to other numerical techniques for the solution of most simultaneous sets of differential equations. After the construction of the geometry, discretization constitutes the first step for calculation of the mixing and transport of chemical species solving conservation equations (convection, diffusion, and reaction sources for each species) (Dong, 2000).

Coal and biomass combustion are quite complex phenomena that combine numerous mechanisms, as described by the Figures 2.1 and 2.2, governed by chemical homogeneous and heterogeneous reactions. The Fluent suite of programs (2006) provides several models related to combustion processes such as pre-mixed, non-premixed, and species and transport models associated to sub-models concerning flow, heat transfer, gas phase and heterogeneous chemical reactions. More precise predictions of the flow, heat transfer properties, and chemical reactions characteristics could be achieved when the entry of case parameters and the use of a material data

base are correctly coordinated. The physical sub-models used here and their mathematical equations are summarized in Appendix B.

4.1 CFD homogenous turbulent combustion sub-models

4.1.1 Homogeneous gas-phase reactions sub-model (the species transport and finite rate chemistry model)

The coal and biomass devolatilisation gas species has a hydrocarbon configuration of the form CH_xO_y. Alkali metals are the most readily vaporized metals that are recognized to be released and are of greater influence than the other metal components. Ma et al. (2007) suggested that the release rate of potassium in the form of potassium hydroxide, potassium chloride or other potassium compounds during biomass devolatilisation could be considered to be the same as that of the overall volatile release.

The volatile gas combustion and additional multi-step alkali sulphate formation mechanism described later in this chapter can be modelled for chemical species to predict the local mass fraction of each species, Y_i, through the solution of the convection diffusion equation (B.4, Appendix B) for the i*th* species. The reaction rates that appear as source terms S_i are generally computed from three models related to the effect of turbulent fluctuations on the reaction kinetics (Fluent, 2006):

- Laminar finite rate model
- Eddy-dissipation model
- Eddy-dissipation concept (EDC) model.

4.1.2 Alkali sulphate formation

Based on the work of Marshall and Glarborg (2004), the mechanism of formation of condensed or solid alkali sulphates that has been advocated is that the gas-to-particle conversion occurs by the homogeneous nucleation of K_2SO_4 particles, which act as condensation nuclei for the subsequent condensation of KCl during biomass combustion. A detailed kinetic reaction of the sulphation of alkali metals is therefore proposed (Glarborg et al., 2004).

The modelling of multi-step detailed reaction mechanisms (number of reaction > 2) with the eddy-dissipation or finite rate/eddy-dissipation models produces inaccurate solutions (Fluent, 2006). The reason is that intermediate kinetically-controlled species such as radicals have Arrhenius rates different for each reaction in turbulent flows. Thus the EDC assumes that reactions occur in small turbulent structures, called the fine scales (Fluent, 2006). The length fraction of the fine scales is modelled as

$$\xi^* = C_\xi \left(\frac{\nu \varepsilon}{k^2} \right)^{1/4} \tag{4.1}$$

Where C_ξ is the volume fraction constant equal to 2.1377

ν is the kinematic viscosity

Reactions proceed over the time scale τ^*, governed by the Arrhenius rates of Equation (4-19), and are integrated numerically.

$$\tau^* = C_\tau \left(\frac{\nu}{\varepsilon} \right)^{1/2} \tag{4.2}$$

Where C_τ is a time scale constant equal to 0.4082.

The source term in the conservation equation for the mean species *i*, Equation (4-4), becomes

$$R_i = \frac{\rho(\xi^*)^2}{\tau^*\left[1-(\xi^*)^3\right]}(Y_i^* - Y_i) \qquad (4.3)$$

Where Y^*_i is the fine-scale species mass fraction after reacting over the time τ^*.

If however, a detailed reaction mechanism composed of hundreds of step-reactions is to be used (Glarborg et al., 2004), the solution of a large set of linearized algebraic equations using the EDC model, for all the chemical sources terms involved, will become CPU-expensive.

Therefore, much attention has to be paid to the mechanism reduction techniques. The elimination of the less important species and the influential reaction paths is an easy technique to reduce a long reaction mechanism provided no loss of the accuracy of predictions is recorded with further reduction (Aglave, 2007). As a fuel is also present this time in comparison with the Glarborg et al. (2004) experiments, chain branching induction will be taken into account as well as the reduced Fluent SO_x model reactions mechanism. The retained mechanism, leading to sulphation of alkali and ultimately aerosols formation, is provided by Table 4.1.

Table 4. 1 Reaction potassium species subset (Glarborg et al., 2004; NIST 2008; and Fluent, 2006)

	REACTIONS	*A*	*n*	*E_a (j/kgmol)*	*Source*
1	$O_2 + M = O + O + M^*$	36.64	0	225473.5	Fluent
2	$H_2O + O = OH + OH$	212.9	-0.57	38198.23	NIST
3	$H + O_2 = O + OH$	5.30E+16	-0.82	137173.2	NIST
4	$H_2 + O = H + OH$	1.80E+10	1	73344.06	NIST
5	$H_2 + O_2 = OH + OH$	1.70E+13	0	397051.8	NIST
6	$H_2 + OH = H_2O + H$	1.17E+09	1.3	30132.06	NIST
7	$H_2S + H = SH + H_2$	1.82E+07	0	7484.3	Fluent
8	$SH + H_2 = H_2S + H$	9375623	0	62536.6	Fluent
9	$H_2S + OH = H_2O + SH$	138.039	0	3742.15	Fluent
10	$H_2O + SH = H_2S + OH$	3.10E+07	0	121854.3	Fluent
11	$SO + OH = SO_2 + H$	1.62E+08	0	2565.926	Fluent
12	$SO_2 + H = SO + OH$	7.69E+09	0	118702.3	Fluent
13	$SH + O = SO + H$	3.55E+08	0	2687.316	Fluent
14	$SO + H = SH + O$	2.99E+09	0	169460	Fluent
15	$H_2S + O = SH + OH$	4365.16	0	13804.93	Fluent
16	$SH + OH = H_2S + O$	9.89E+08	0	60359.96	Fluent
17	$SO + O_2 = SO_2 + O$	446683	0	27032.22	Fluent
18	$SO_2 + O = SO + O_2$	1663412	0	76136.43	Fluent
19	$SH + H + M = H_2S + M^*$	1096.48	0	0	Fluent
20	$H_2S + M = SH + H + M^*$	8.67E+14	0	381946.3	Fluent
21	$SO + O + M = SO_2 + M^*$	8.71E+09	-1.8	0	Fluent
22	$SO_2 + M = SO + O + M^*$	1.91E+14	0	520736.5	Fluent
23	$SO_2 + OH + M = HOSO_2 + M^*$	7.20E+25	0	2992.68	Glarborg
24	$HOSO_2 + O_2 = SO_3 + HO_2$	7.80E+11	0	2743.29	Glarborg
25	$HO_2 + H_2O = H_2O_2 + OH$	2.90E-12	0	1330.08	Glarborg
26	$HO_2 + OH = H_2O + O_2$	4.80E-11	0	-2078.25	Glarborg
27	$Cl + HO_2 = HCl + O_2$	4.98E-17	0	0	Glarborg
28	$SO_2 + O + M = SO_3 + M^*$	3.70E+11	0	7066.05	Glarborg
29	$SO_2 + OH = SO_3 + H$	490	0	99756	Glarborg
30	$SO_2 + O_2 = SO_3 + O$	1.30E+12	0	25520.91	Glarborg
31	$K + O + M = KO + M^*$	1.50E+21	-1	0	Glarborg
32	$KO + SO_2 = KSO_3$	3.70E+14	0	0	Glarborg
33	$KSO_3 + OH = SO_3 + KOH$	2.00E+13	0	0	Glarborg
34	$KCl + H_2O = KOH + HCl$	1.70E+14	0	0	Glarborg
35	$KOH + SO_3 = KHSO_4$	1.00E+15	0	0	Glarborg
36	$KHSO_4 + KCl = K_2SO_4 + HCl$	1.00E+15	0	0	Glarborg
37	$KHSO_4 + KOH = K_2SO_4 + H_2O$	1.00E+15	0	0	Glarborg
38	$KCl + SO_3 = KSO_3Cl$	1.00E+15	0	0	Glarborg
39	$KSO_3Cl + H_2O = KHSO_4 + HCl$	1.00E+15	0	0	Glarborg
40	$KSO_3Cl + KOH = K_2SO_4 + HCl$	1.00E+15	0	0	Glarborg

**M = nitrogen, argon, oxygen*

4.2 CFD Application to co-firing Biomass with pulverized Coal an a Pilot-Scale furnace.

The simulation of gas-to-solid particle formation originating from potassium sulphate formation during co-combustion of biomass with coal as presented in Chapter 2 and following the mechanism described above must consider the fact that the combustion process and sulphate formation mechanism are simultaneous and influence one another.

Hence, an existing model of alkali sulphate formation developed by Glarborg and Marshall (2004) is used to enable predictions of potassium sulphate fractions in the flue gas that might nucleate, evaporate, and condense into fine fly ash particles emissions when coal is burnt together with a small proportion of biomass.
The numerical simulation carried out uses a commercial Computational Fluid Dynamics software package, namely Fluent© version 6.3 on a personal computer with 2 GB RAM, to predict the potassium sulphate concentration profile in the PSCTF, gaseous emissions (CO_2, SO_2, and NO_x), and certain other aspects of combustion behaviour (in-situ and wall temperature profiles). The validation of the modelling is made possible by the experimental results from the PSCTF tests (Table 3.1). Additional input data required for the simulations included reaction kinetics parameters: pre-exponential factor A and activation energy E_a, retrieved from DTF test results (Table 3.11) evaluated from combustion efficiency graphs (Appendix C).

In the PSCTF like any other practical combustion system, the flow is highly turbulent. The mixing process results in temporal fluctuations of temperature and species concentration that influence the characteristics of the flame (Fluent, 2006).

4.2.1 Temperature Profiles

Figures 4.1 to 4.11 display the predicted temperature profiles in the PSCTF furnace. These results may be compared with the measurements of temperature (Table 3.10)

inside the chamber from the ports 4, 10, 28, and D as discussed in Chapter 5. The predicted values are mass-weighted averages from the same ports, on the surface normal to the shell.

The fire ball temperature (Port 4) was predicted to reach value of 1900 K for Test 11 (coal A baseline) which differs by 20% compared with the experimental measurement (Fig. 4.1 and Table 3.10). Moreover, the short and narrow flame indicates poor ignitability of the coal, as further evidenced by analysis of the combustion efficiency and temperature graphs (see Fig. D.1 Appendix D). It is unfortunate that the high-temperature optical camera could not operate to confirm of the inclination to the left hand side of the flame, observed also in other simulations.

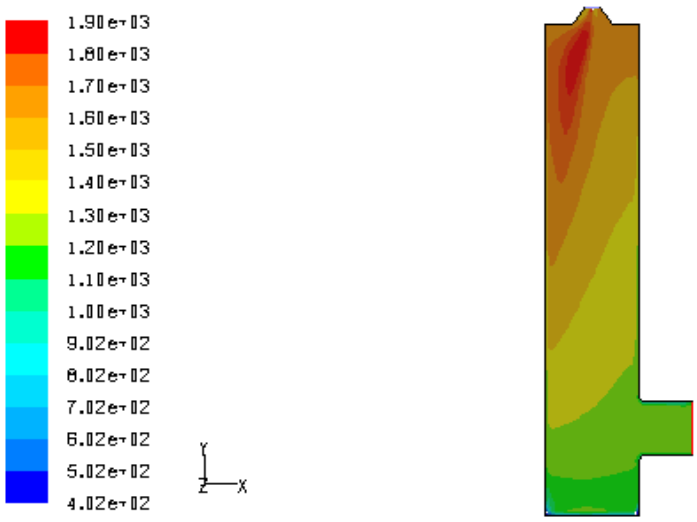

Fig. 4. 1 The predicted temperature profiles of flue gas in the PSCTF for the baseline coal A, Test 11

There is a drop of fire ball temperature for the modelling of sawdust blends Tests 13, 14 and 15 (Fig. 4.2, 4.3, and 4.4) from 1900 K to respectively 1830 K, 1830 K, and 1790 K comparable to experimental data (Table 3.10) which indicate the influence of the high moisture content of sawdust and the increased effect when the co-firing ratio increases. The flame remains tilted to the left but shows a tendency to widen in

Figures 4.2 and 4.3, interpreted as an amelioration of the ignitability of coal by great quantity of volatiles from the sawdust material.

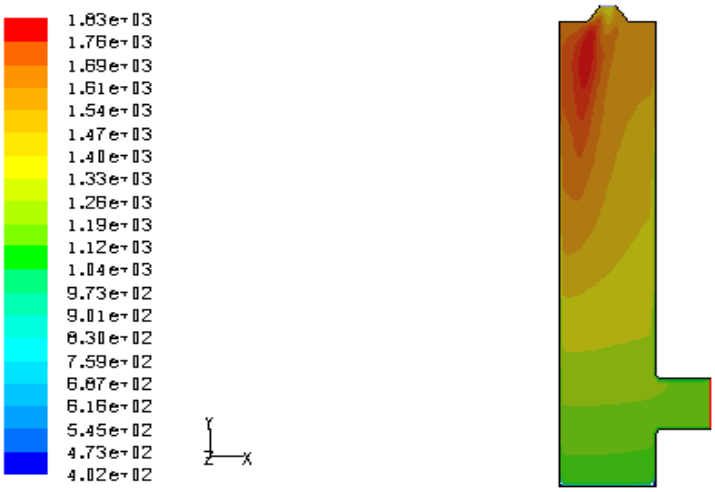

Fig. 4. 2 The predicted temperature profiles of flue gas in the PSCTF for 10% sawdust/90% coal A blend, Test 13

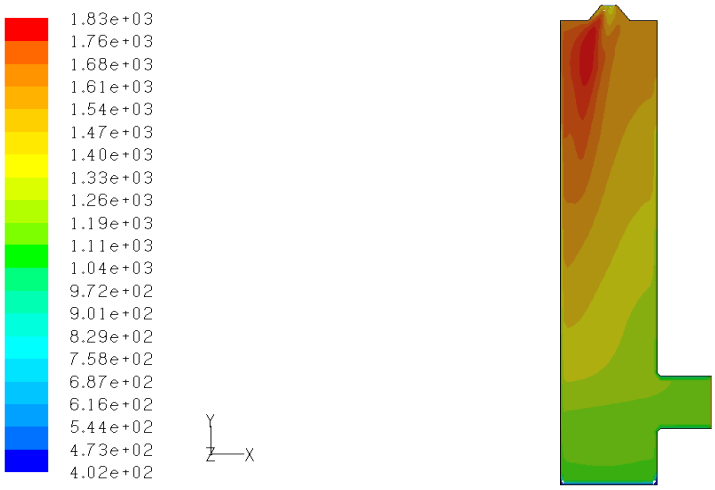

Fig. 4. 3 The predicted temperature profiles of flue gas in the PSCTF for 15% sawdust/85% coal A blend, Test 14

When the proportion of sawdust injected inside the combustion system becomes considerable and because of the very low ash content and density of sawdust materials, the flame displays a particular curved shape (Fig. 4.4). This is in fact an indication that the abundant burning biomass particles follow the flow pattern discussed later in this chapter.

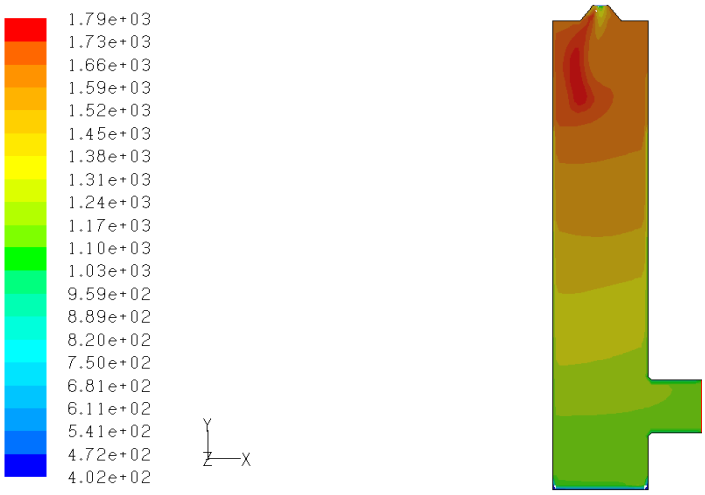

Fig. 4. 4 The predicted temperature profiles of flue gas in the PSCTF for 20% sawdust/80% coal A blend, Test 15

For the grass blend tests (16, 17, and 18) simulation, illustrated by the temperature distributions, in Figures 4.5, 4.6, and 4.7 below, apart from the inclination of the flame, the fire ball is slightly wider than with the corresponding blending ratios of coal with sawdust. Similar drops of temperature of the fire ball are also recorded but not a pronounced curvature, probably attributable to the five times higher total ash content of grass blends (though almost identical bulk density).

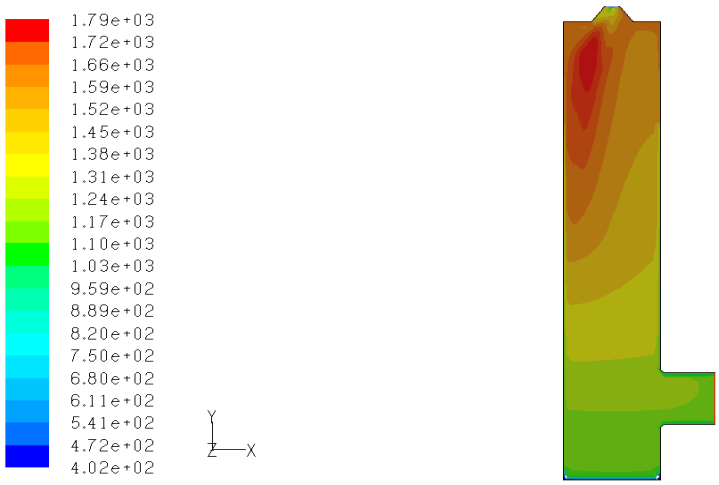

Fig. 4. 5 The predicted temperature profiles of flue gas in the PSCTF for 10% grass/90% coal A blend, Test 16

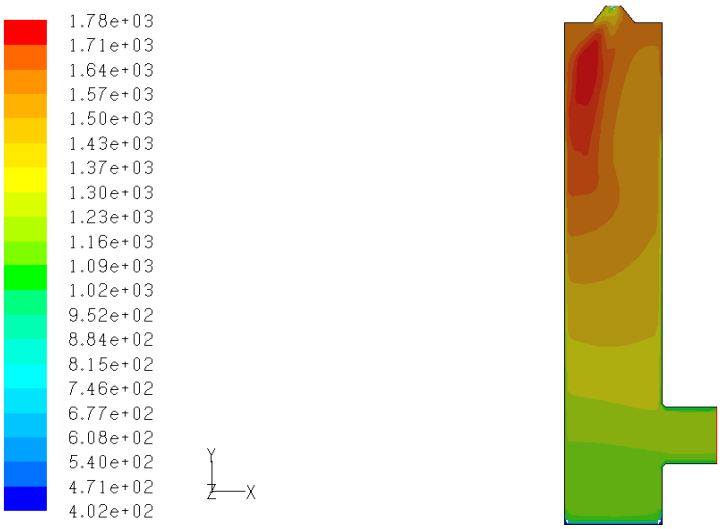

Fig. 4. 6 The predicted temperature profiles of flue gas in the PSCTF for 15% grass/85% coal A blend, Test 17

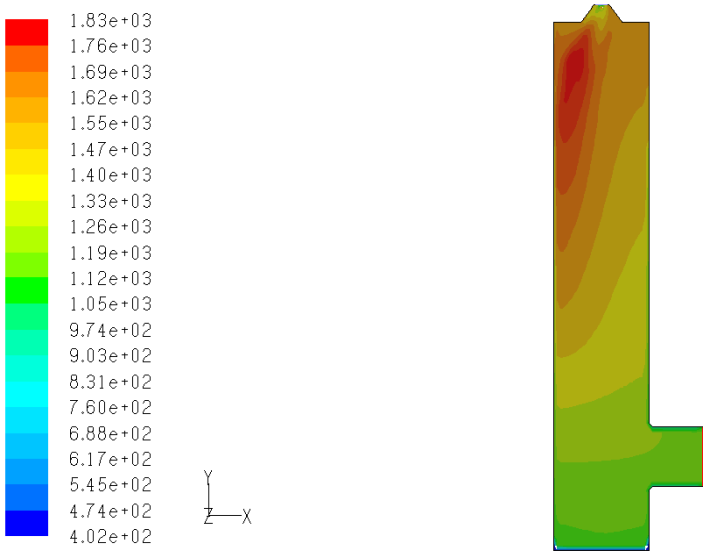

Fig. 4. 7 The predicted temperature profiles of flue gas in the PSCTF for 20% grass/80% coal A blend, Test 18

Under the boiler operating conditions during the repeated tests of sawdust blended with another coal B (Tests 1 - 4, Table 3.8), the fire ball temperatures remain unchanged for the three ratios (Fig. 4.8, 4.9, and 4.10) always with a narrow inclined flame. The main difference from the previous sawdust blend test series is that the total amount of air fed into the combustion domain was progressively increasing (Table 3.4) in the repeat tests, while it was continuously dropping in the original tests. There is every reason to correlate the amount of air to the flow field present inside the system and subsequently to the flame profile. The pf-coal fineness is however another parameter of importance that must not be neglected in the flow field behaviour during all these combustion tests (see Chapter 5).

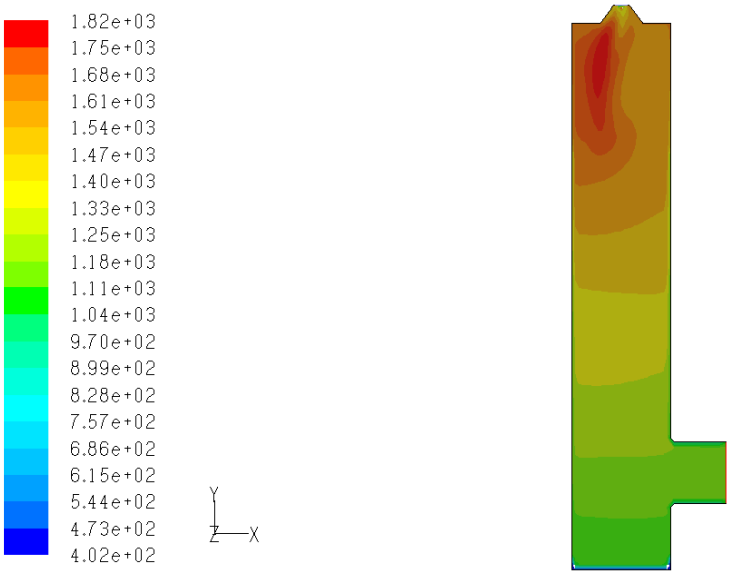

Fig. 4. 8 The predicted temperature profiles of flue gas in the PSCTF for 10% sawdust/90% coal B blend, Test 2

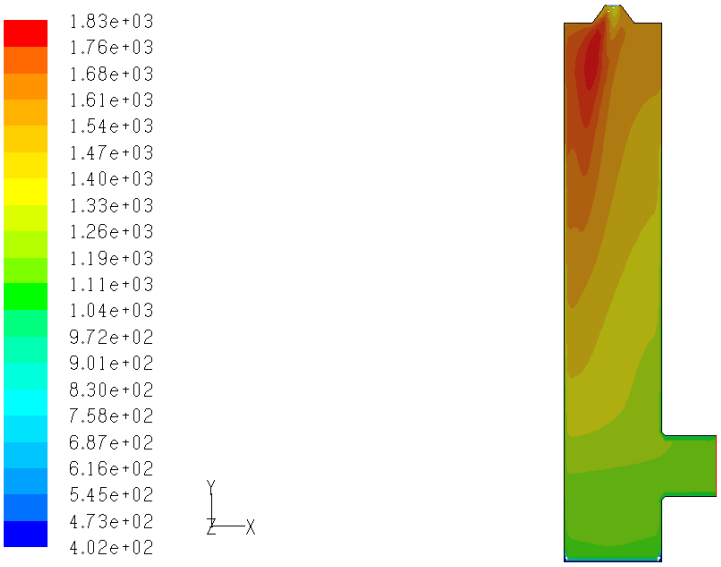

Fig. 4. 9 The predicted temperature profiles of flue gas in the PSCTF for 15% sawdust/85% coal B blend, Test 3

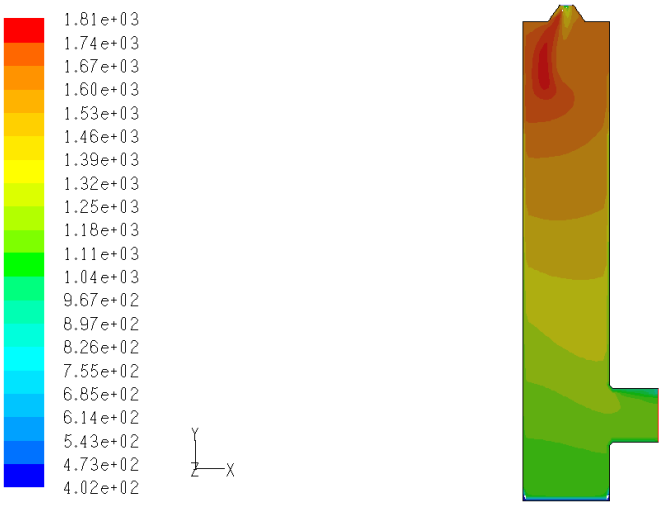

Fig. 4. 10 The predicted temperature profiles of flue gas in the PSCTF for 20% sawdust/80% coal B blend, Test 4

Further discussions based on mass-weighted averaged temperature values measured in-situ and their comparison with numerical simulations are contained, in the next Chapter, under the modelling work section.

4.2.2 Particle tracks and velocity profiles

The trajectory of the combusting particles (coal and biomass) inside the furnace are obtained from integration of the force balance (inertia, hydrodynamic drag, and gravity) on the particle, and computed using a Lagrangian approach (see Appendix B).

The flow fields and global velocities in the radiant and convective sections of the PSCTF are illustrated in Figures 4.11 till 4.17, where the different particles are tracked and coloured according to their residence within the system. The interaction of the continuous phase with the discrete phase is performed by tracking the exchange of mass, momentum and energy based on the Eulerian – Lagrangian scheme (Fluent, 2006).

The flame profiles described in Section 4.2.1 are directly linked to these trajectories and velocity profiles. The flow pattern and velocity distribution of the baseline coal A, Test 11, are demonstrated in Fig. 4.11. It is apparent that the L-shape of the reactor and the generated back-flow in the bottom pit affect strongly the flow pattern because of the asymmetric vacuum from the ID-fan. The absence of biomass particles in the baseline test and consequently less total air is responsible for the good mixing along the entire radiant region (Fig. 4.11a) while the velocity (Fig. 4.11b) grows weaker as the coal injection enters the system.

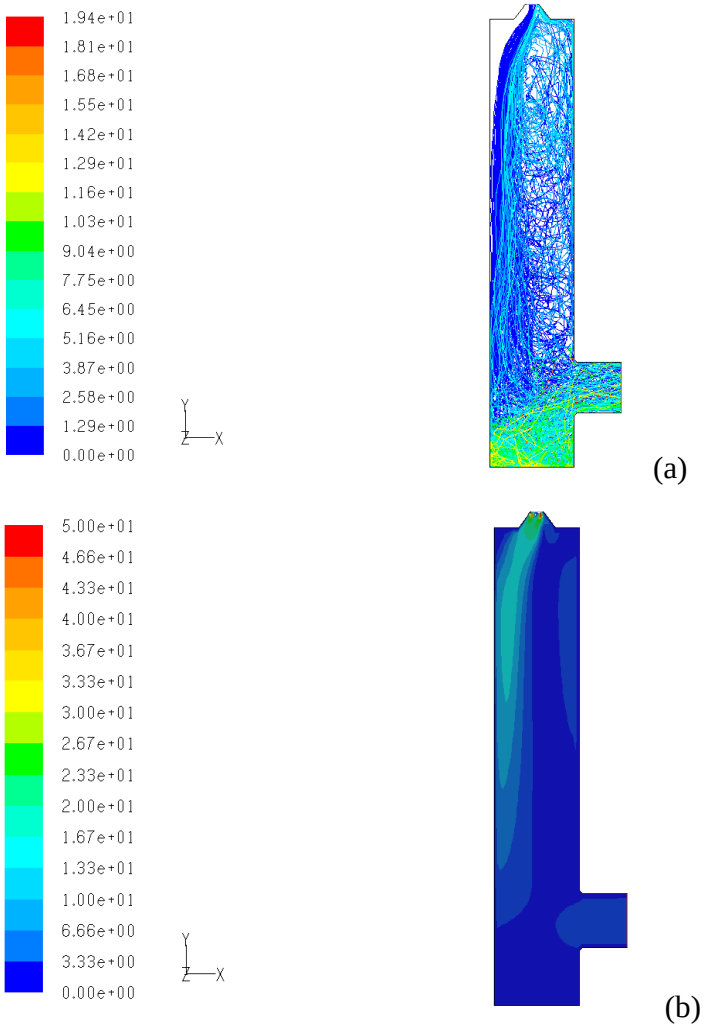

Fig. 4. 11 (a) The flow pattern and (b) velocity profiles in the PSCTF for the baseline coal A, Test 11

In the case of 10% and 15% sawdust blends (Fig. 4.12a and 4.13a) the dominant coal phase results in poor mixing along the walls and not very good mixing in the immediate central post-injection zone and bottom ash pit back-flow region. By the diffusion effect, because the ignitability of coal is improved as shown by the long flame, the flue gas velocity profiles also lengthen but have lower absolute values as a general trend (Fig. 4.12b and 4.13b).

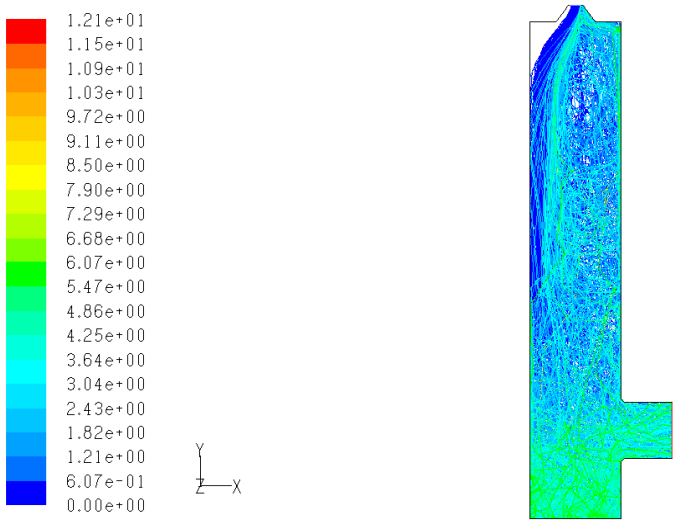

(a)

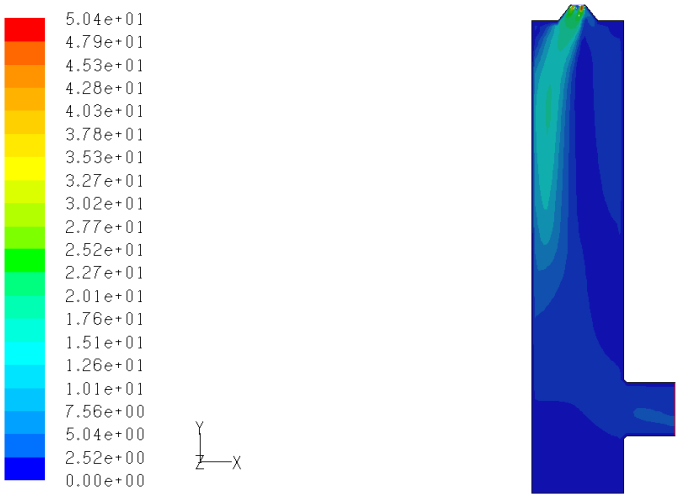

(b)

Fig. 4. 12 (a) The flow pattern and (b) velocity profiles in the PSCTF for 10% sawdust/90% coal A blend, Test 13

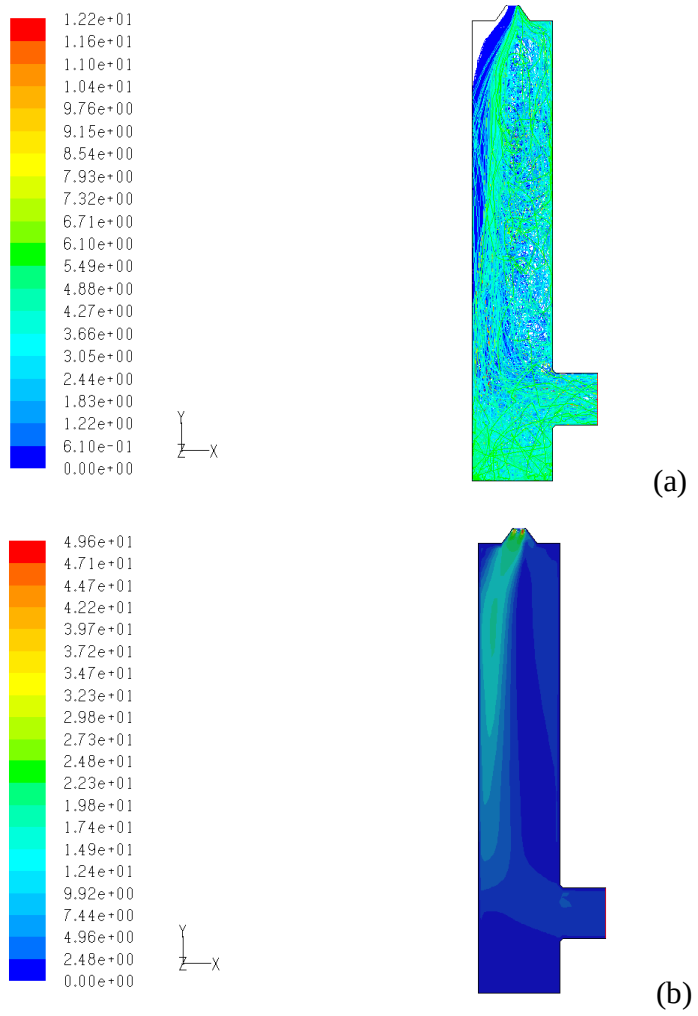

Fig. 4. 13 (a) The flow pattern and (b) velocity profiles in the PSCTF for 15% sawdust/85% coal A blend, Test 14

As for the two previous tests, the 20% sawdust blend Test 15 presents, three flow zones (Fig.4.14a): top, middle and bottom. The top central zone close to the burner illustrates more eddies or mixing because of the great percentage of lighter density and relatively lower ash content biomass particles ending in the curved shape of the flame. The middle zone shows of poor mixing and steady flow (Fig. 4.14b) while the last zone of recirculation is inclined to trap particles but still with constant flow.

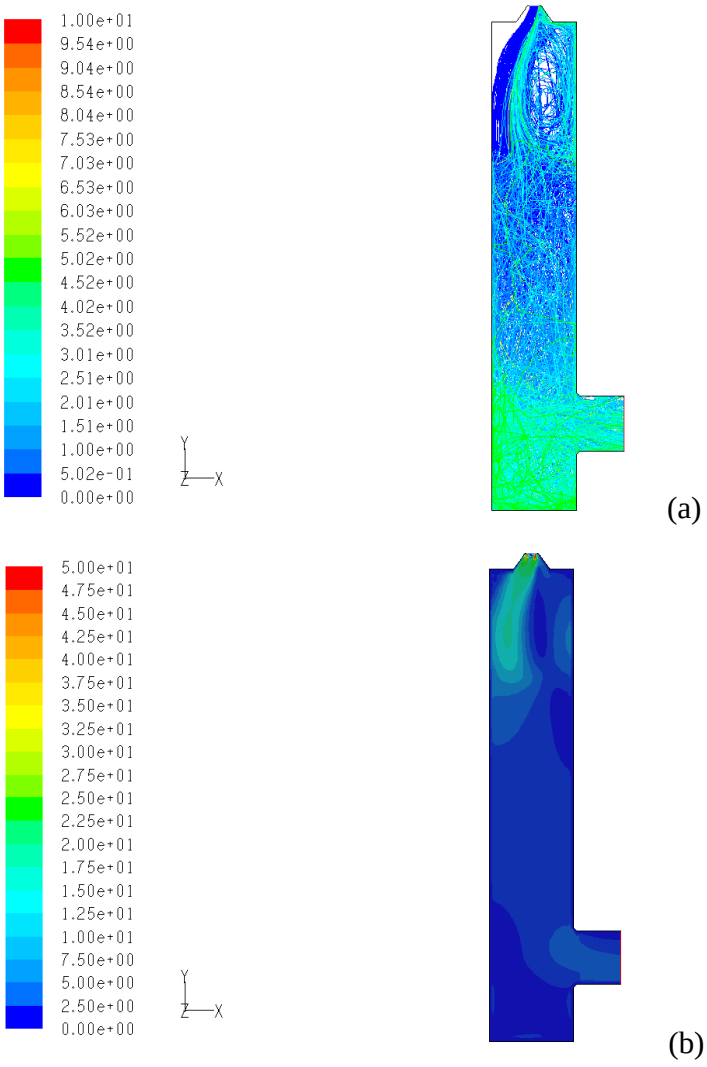

Fig. 4. 14 (a) The flow pattern and (b) velocity profiles in the PSCTF for 20% sawdust/80% coal A blend, Test 15

The flow patterns and velocity profiles for the 10% and 15% grass blends tests (Fig. 4.15 and 4.16) show the same features as in Tests 13 and 14, as noted previously.

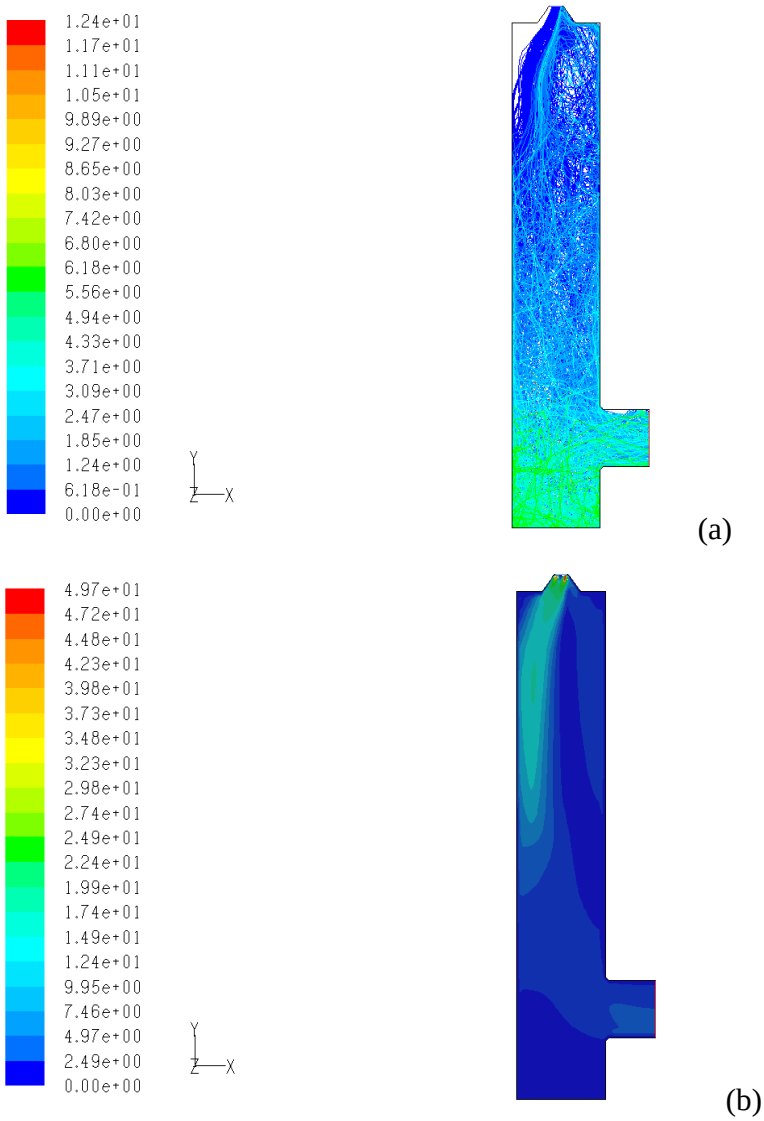

Fig. 4. 15 (a) The flow pattern and (b) velocity profiles in the PSCTF for 10% grass/90% coal A blend Test 16

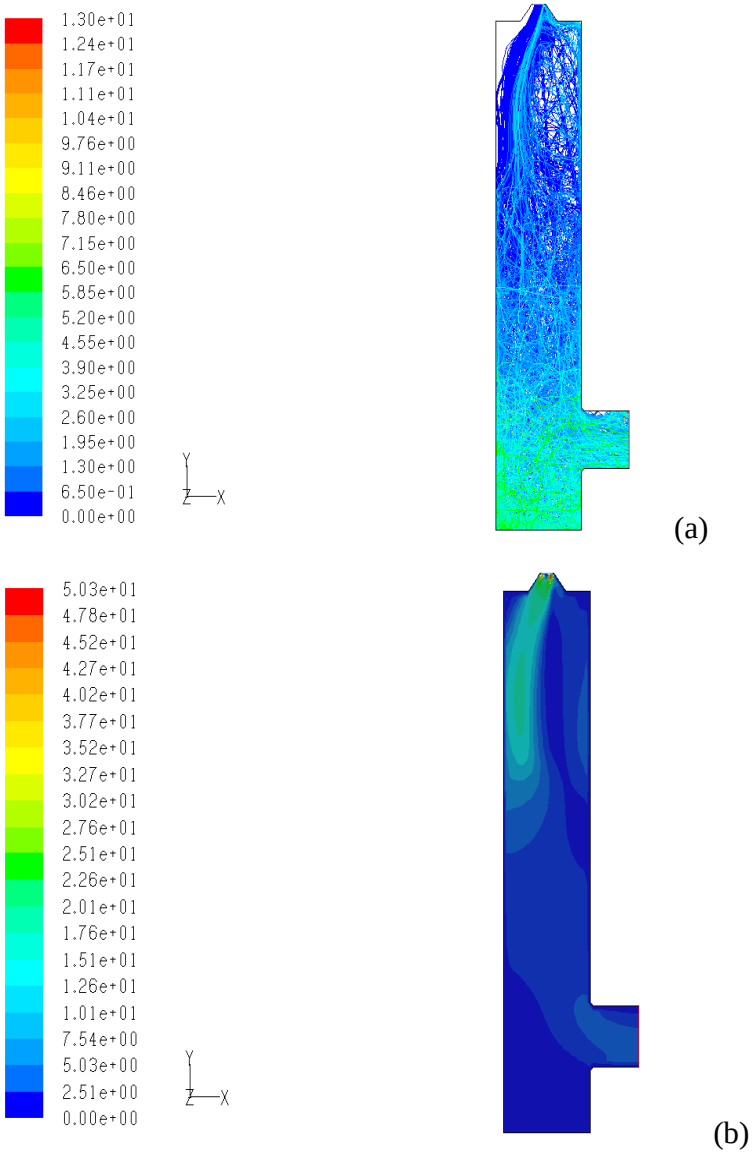

Fig. 4. 16 (a) The flow pattern and (b) velocity profiles in the PSCTF for 15% grass/85% coal A blend, Test T17

In contrast to Test 15 with 20% sawdust, the 20% grass blend test, especially, the flow pattern illustrated in Fig. 4.17a, indicates a not very good mixing zone just at the burner outlet but extremely stirred into the radiant section with lower recirculation at the bottom region. The velocity profile (Fig. 4.17b) displays a similar pattern to Test 15.

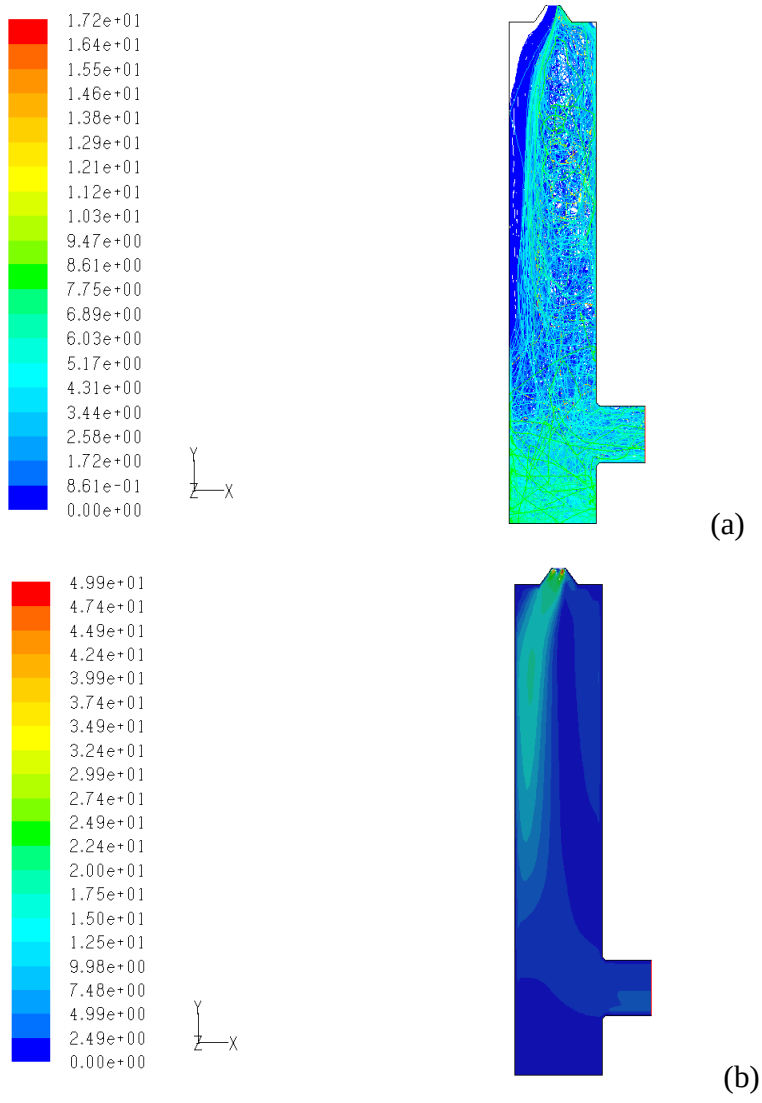

Fig. 4. 17 (a) The flow pattern and (b) velocity profiles in the PSCTF for 20% grass/80% coal A blend, Test 18

4.2.3 Potassium Sulphate, Sulphur Trioxide and Sulphur Dioxide Species Profiles

The data used for the modelling of the devolatilisation of potassium, sulphur and chlorine species involved in the alkali sulphate formation mechanism are as follows.

About 60% of atomic chlorine is released to the gas phase at 500°C for the biomass materials and the residual chlorine is released by evaporation as KCl at 700 - 800 °C and as HCl, in proportions respectively 30% and 10%, whereas potassium was liberated to the gas phase in the forms of both pyrolysis K (ICP) KCl and atomic K (30%) (Appendix E). The residual K (45 – 55% by XRF) is captured by ash. The coal behaves differently with 70% of atomic Cl, 20% KCl, 10% HCl, 35% K-ash, and the balance as atomic potassium (Ma et al., 2007).

Figures 4.18 to 4.28 show a series of predicted 2D profiles of K_2SO_4, SO_2 and SO_3 mass fractions for the entire set of tests. The profiles of SO_2 shown were estimated by using the SO_x model available with the Fluent package, while the potassium sulphate profiles were predicted using the species transport model with EDC model.

The predicted profiles for K_2SO_4, SO_2 and SO_3 in the PSCTF boiler for the coal A baseline are demonstrated in Figure 4.18. Since the total preset excess oxygen percentage was 6%, so the sulphur trioxide was consumed in the combustion chamber to form potassium sulphate and their concentrations in flue gas were very low (Fig. 4.18a and 4.18c). The flame was short and narrow and the sulphur dioxide mass fraction profile showed peak values (Fig. 4.18b) in the fire-ball region inclined to the left. There were close similarities between the SO_3 and K_2SO_4 profiles although different models were applied to simulate their formation. The relationships between SO_x formation rate, temperature, and species concentration are highly nonlinear.

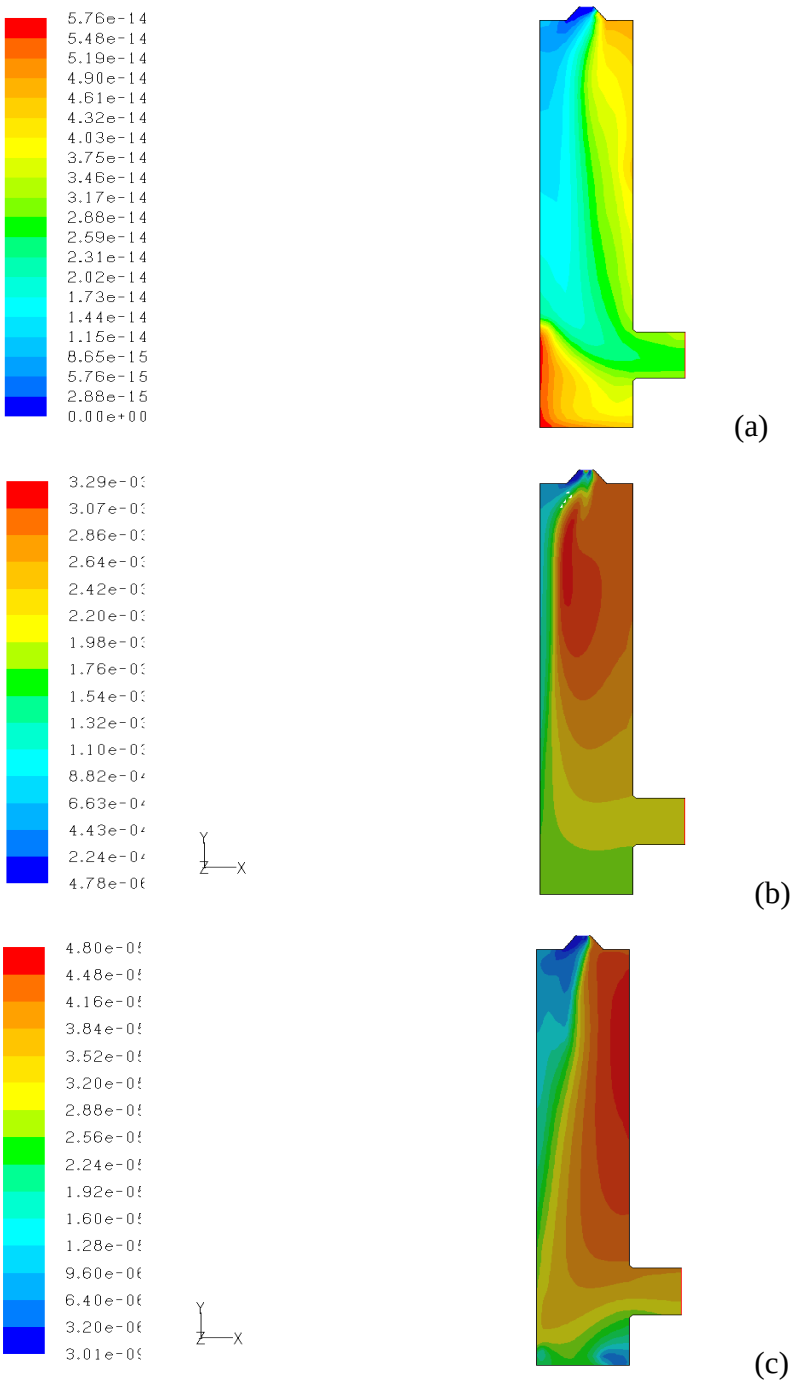

Fig. 4. 18 (a) The potassium sulphate; (b) sulphur dioxide; and (c) sulphur trioxide mass fraction profiles in the PSCTF for the baseline coal A, Test 11

The situation in the 10% sawdust blend, Test 13, was improved in terms of a reduction of the total concentration of SO_2 in the system (Fig. 4.19b). The K_2SO_4 and SO_3 mass fractions (Fig. 4.19a and 4.19c) this time were formed more outside the flame zone but still at lower proportions compared to the coal A baseline.

The cases with 15% and 20% sawdust blends show that less SO_2 is produced, not only within the flame region but also in the system. The mass fractions of sulphate and sulphur trioxide are then presented in Figs. 4.20 & 4.21.

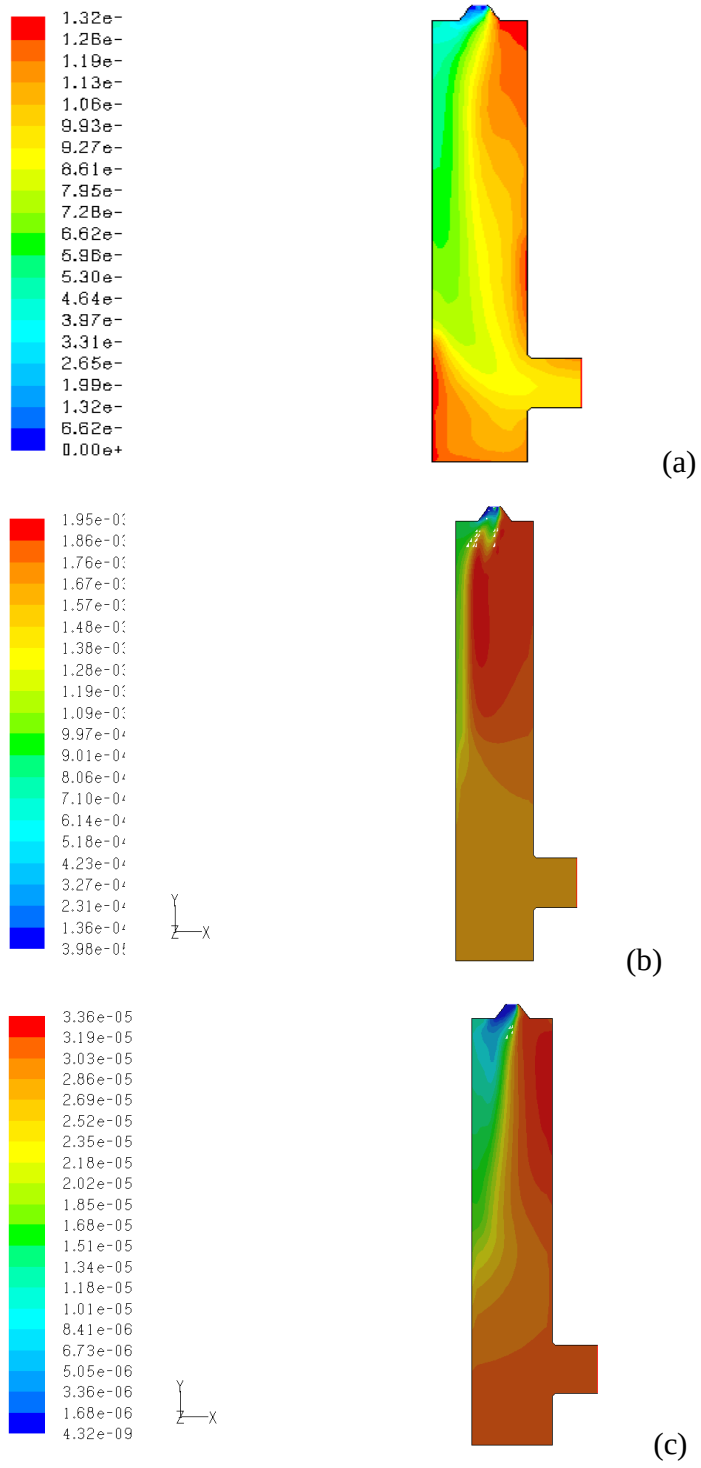

Fig. 4. 19 (a) The potassium sulphate; (b) sulphur dioxide; and (c) sulphur trioxide mass fraction profiles in the PSCTF for 10% sawdust/90% coal A blend Test 13

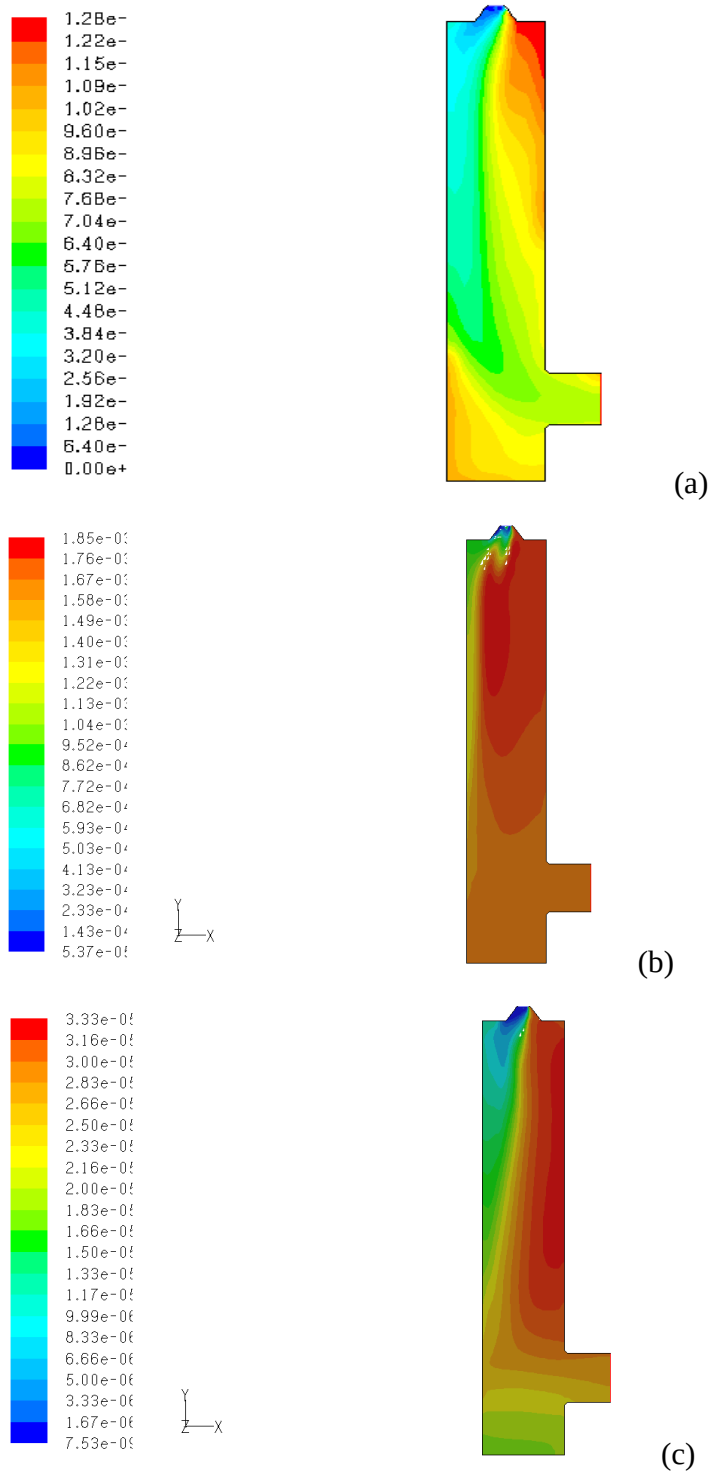

Fig. 4. 20 (a) The potassium sulphate; (b) sulphur dioxide; and (c) sulphur trioxide mass fraction profiles in the PSCTF for 15% sawdust/85% coal A blend, Test 14

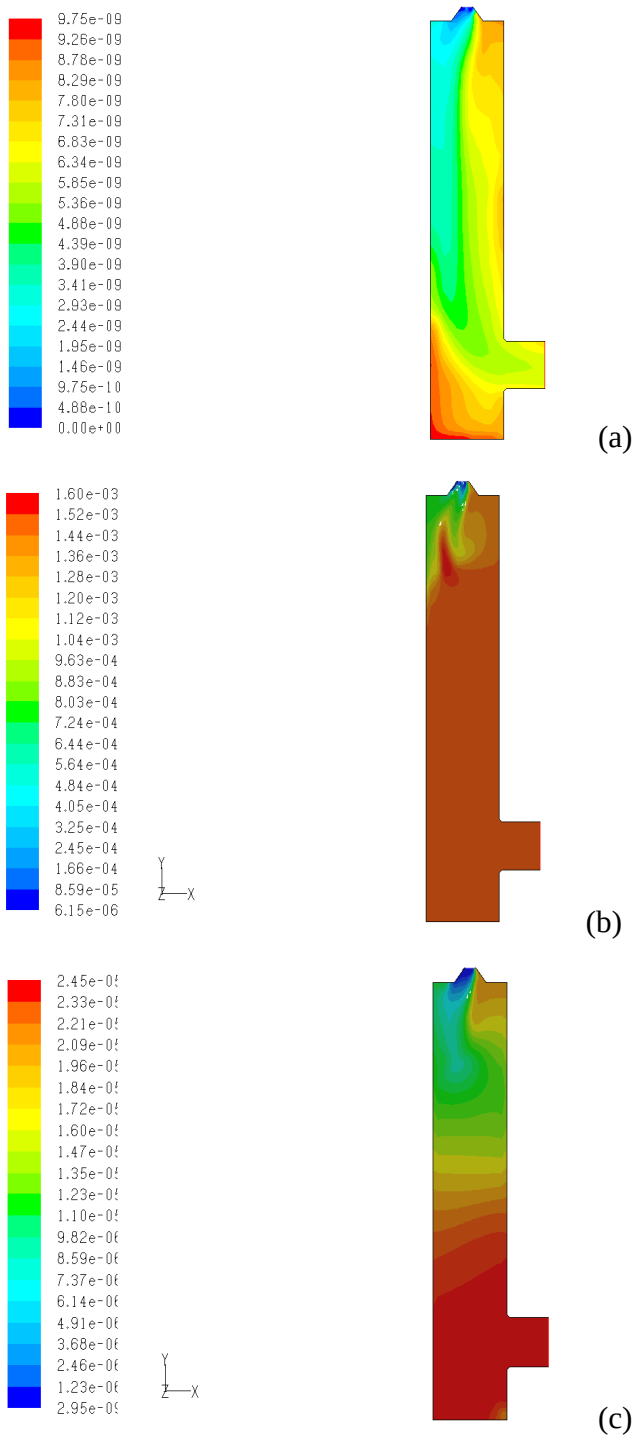

Fig. 4. 21 (a) The potassium sulphate; (b) sulphur dioxide; and (c) sulphur trioxide mass fraction profiles in the PSCTF for 20% sawdust/80% coal A blend, Test 15

The set of Figures 4.22 to 4.24 show the mass fraction profiles of K_2SO_4, SO_2, and SO_3 for the grass blend tests in the combustion system. Obviously, for the purpose of potassium sulphate formation, the grass blends seemed to generate less sulphate than sawdust blends under the PSCTF operating conditions of Table 3.4.

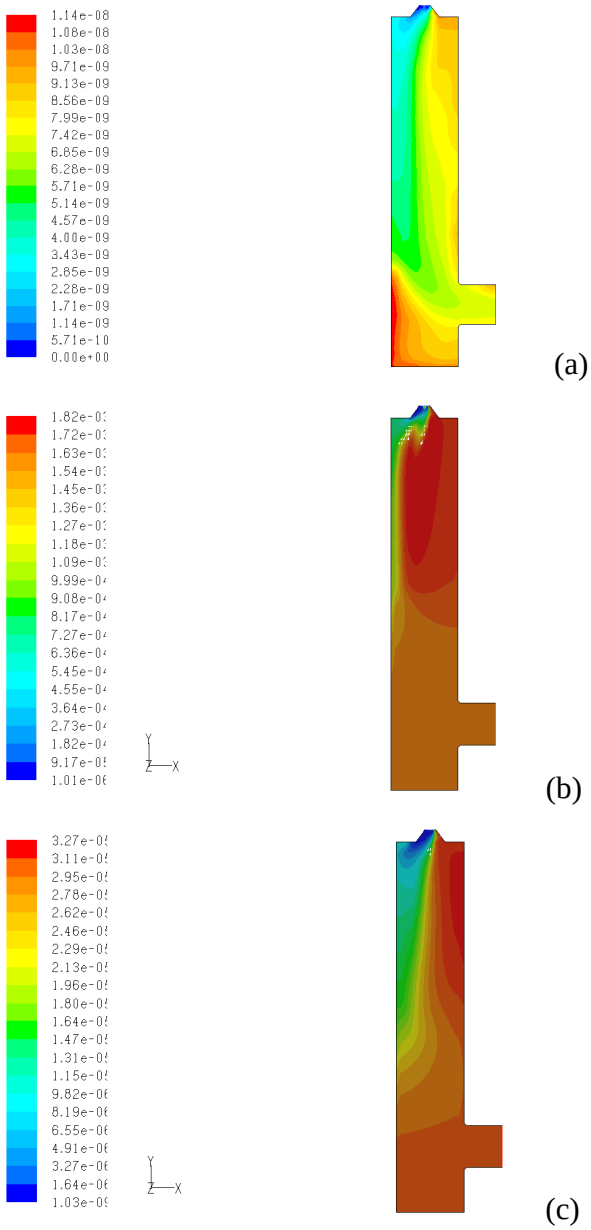

Fig. 4. 22 (a) The potassium sulphate; (b) sulphur dioxide; and (c) sulphur trioxide mass fraction profiles in the PSCTF for 10% grass/90% coal A blend, Test 16

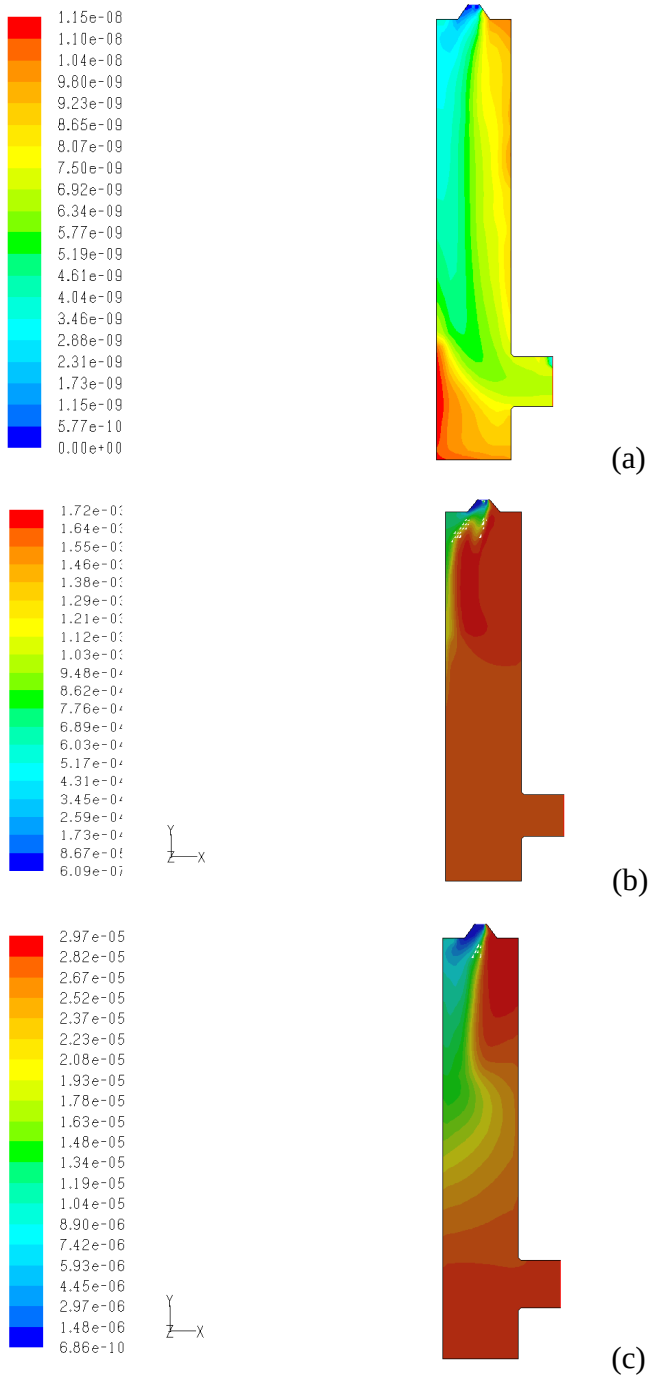

Fig. 4. 23 (a) The potassium sulphate; (b) sulphur dioxide; and (c) sulphur trioxide mass fraction profiles in PSCTF for 15% grass/85% coal A blend, Test 17

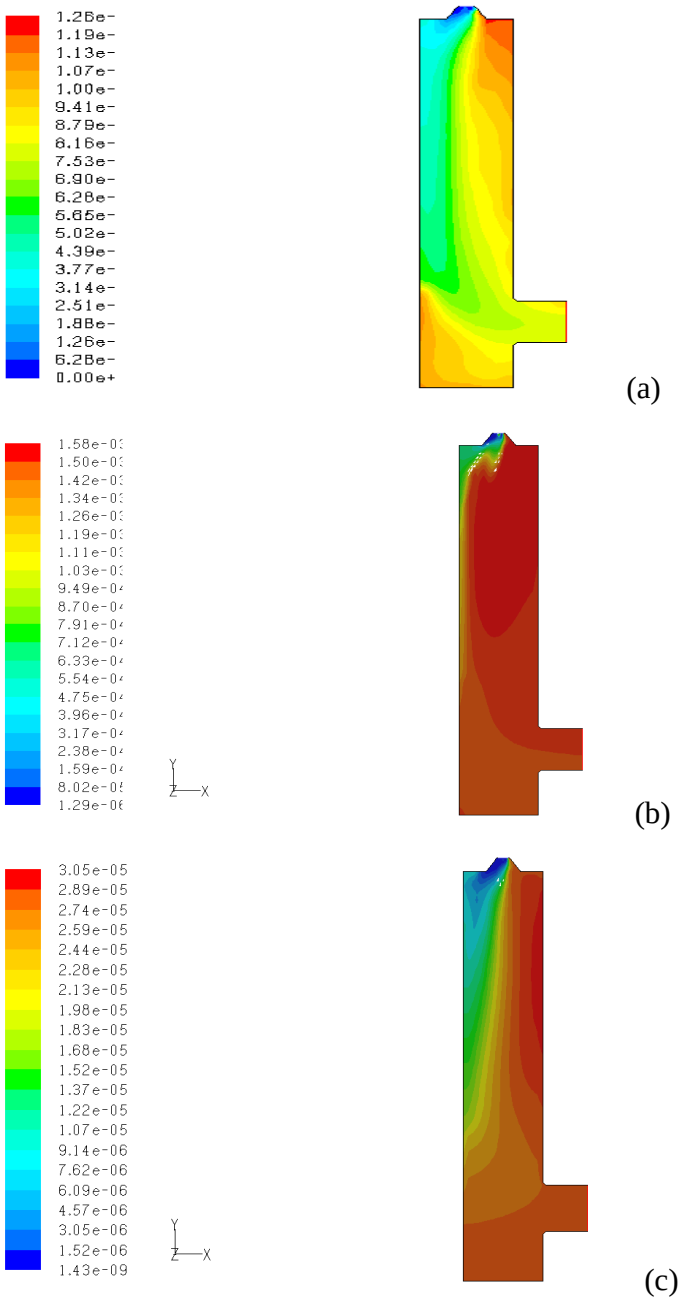

Fig. 4. 24 (a) The potassium sulphate; (b) sulphur dioxide; and (c) sulphur trioxide mass fraction profiles in the PSCTF for 20% grass/80% coal A blend, Test 18

Because coal B had approximately half the sulphur content of coal A, for which the sulphate mass fraction profile was already presented above, the profile for the baseline coal B (Fig. 4.25) displayed a reduction of the same proportion of magnitude.

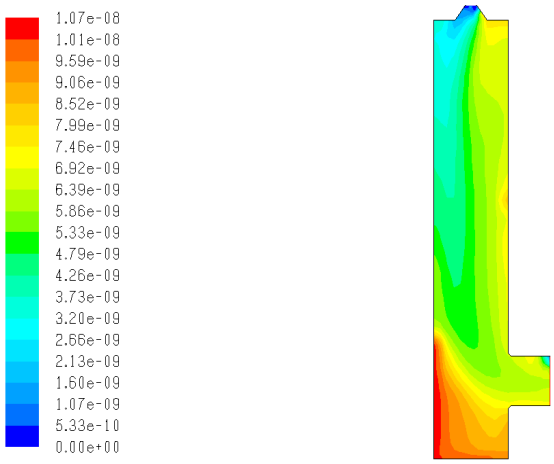

Fig. 4. 25 The potassium sulphate mass fraction profiles in the PSCTF for the baseline coal B, Test T1

The K_2SO_4 concentration was predicted (Fig. 4.26 to 4.28) to be sensitive to the excess oxygen concentration in the flue gas during the repeated sawdust blend tests when compared to the first sawdust blend test series. The decreasing excess oxygen level influenced more formation of potassium sulphate and consequently nucleated condensed and coagulated fine particles.

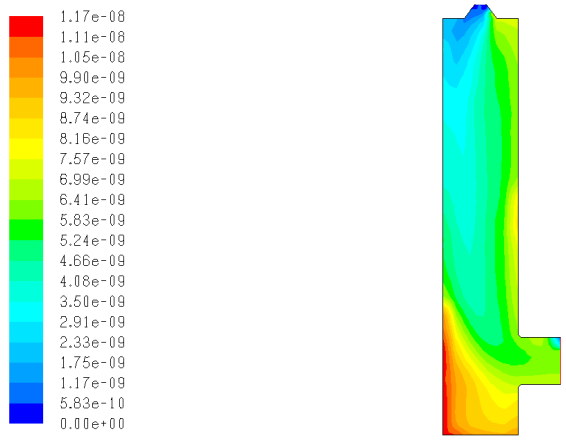

(a)

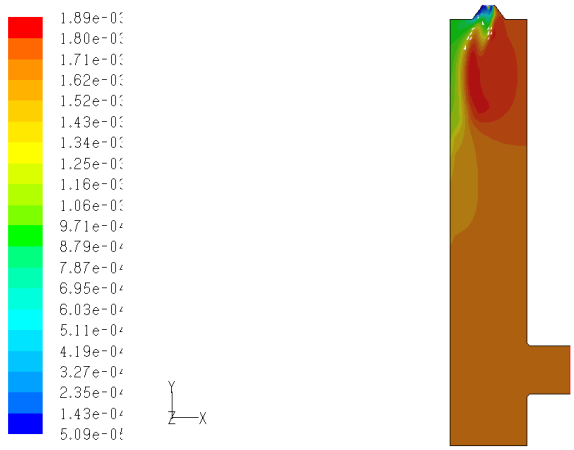

(b)

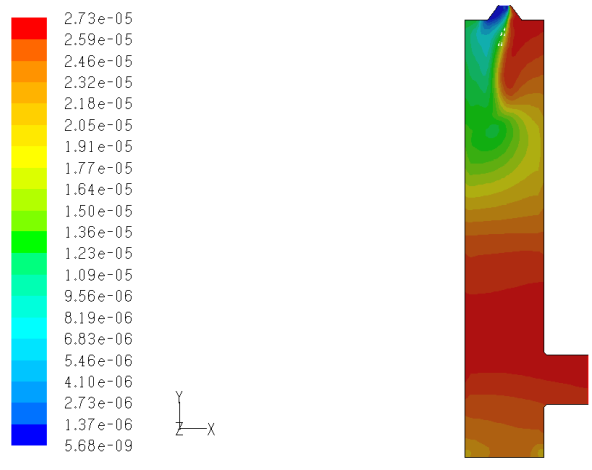

(c)

Fig. 4. 26 (a) The potassium sulphate; (b) sulphur dioxide; and (c) sulphur trioxide mass fraction profiles in the PSCTF for 10% sawdust/90% coal B blend, Test 2

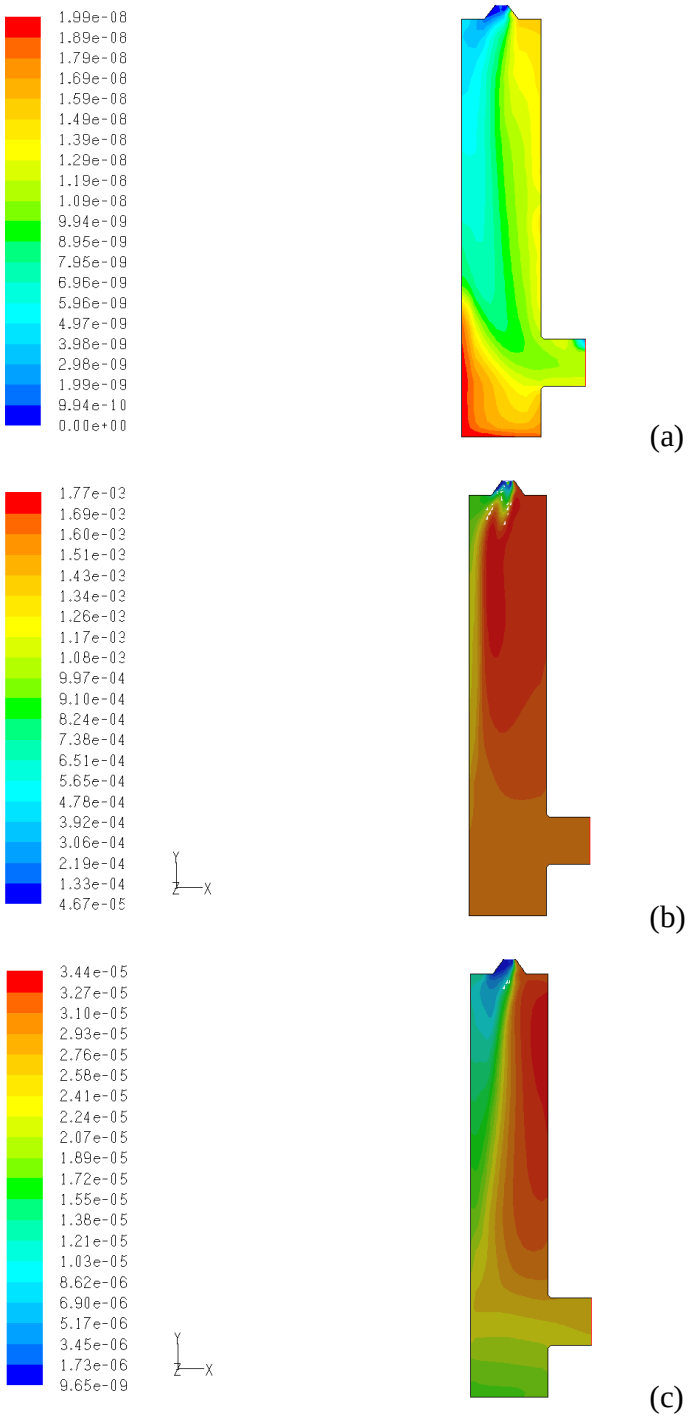

Fig. 4. 27 (a) The potassium sulphate; (b) sulphur dioxide; and (c) sulphur trioxide mass fraction profiles in the PSCTF for 15% sawdust/85% coal B blend, Test 3

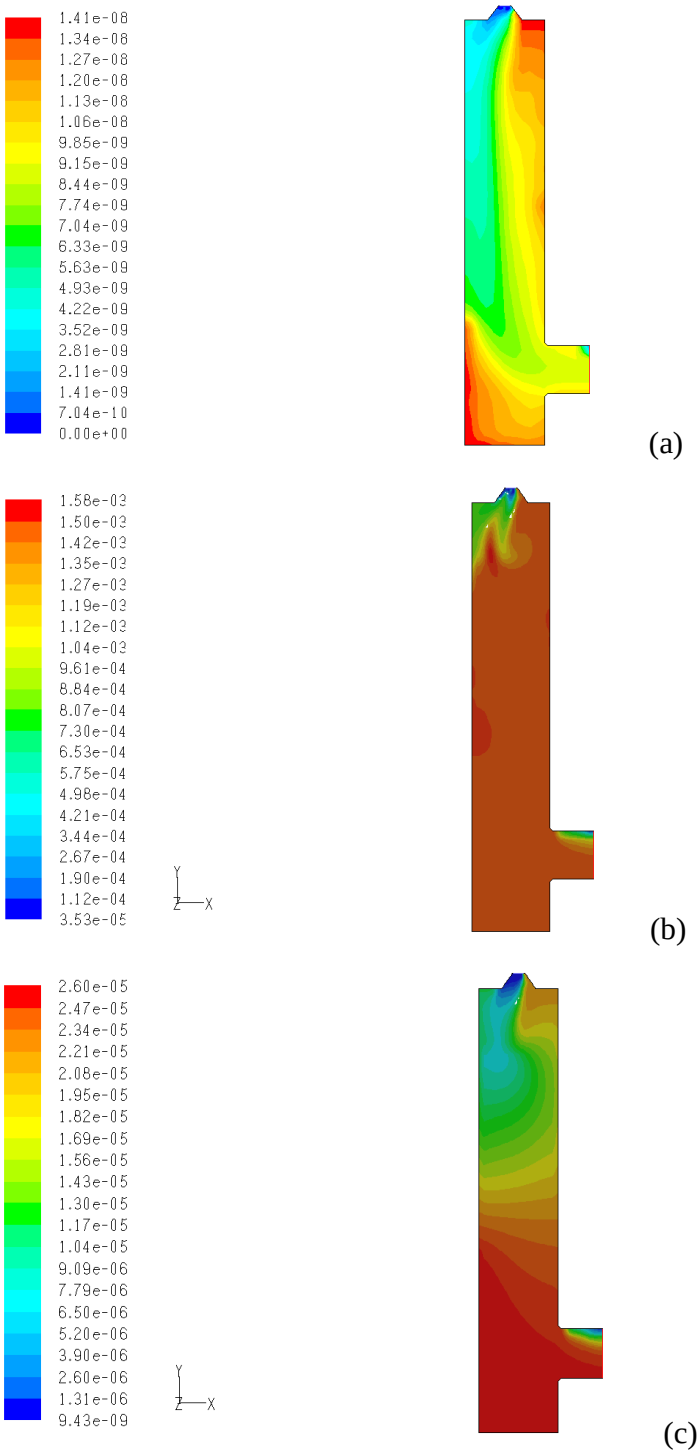

Fig. 4. 28 (a) The potassium sulphate; (b) sulphur dioxide; and (c) sulphur trioxide mass fraction profiles in the PSCTF for 20% sawdust/80% coal A blend, Test 4

4.3 Summary

The CFD technique is a proven tool around the world for the simulation of coal and biofuels combustion in commercial boilers. In this work, it has been applied to the modelling of the potassium sulphate formation during thermochemical conversion occurring from co-combustion of biomass with coal. Particle tracks and profiles of temperature, velocity, and species mass fractions are retrieved from computational solving of simultaneous differential equations describing physical models associated with the combustion process.

This chapter is a preliminary attempt based on the approach of the work of Glarborg et al. (2004) to model aerosol formation using computational fluid dynamics. Two sets of co-firing tests of coal with either sawdust or grass were investigated under certain operating conditions of a 1 MW_{th} pilot-scale down-fired combustion facility. The impact of the fuel chemical composition on the species distributions was studied for the different co-firing ratios. From the numerical simulations, it may be concluded that:

- The thermal field was to some extent in good agreement with the measured temperatures at different heights of the furnace for all the cases except in the fireball region, this error being attributed to the large encountered turbulence;
- The flow field presents information about the influence of the boiler configuration, operating conditions (pressure, air flow settings, etc) on the flow pattern and mixing rate as validated by the comparison of the particles' predicted averaged-residence times to the experimental time at the lower sampling port;
- The predicted velocity magnitude contour could be trusted for the area-averaged velocity at cross sections inside the radiant and convective zones compared with the calculations;
- Though direct in-situ measurement of the alkali sulphate concentrations inside the furnace could not be achieved, the modelling of its formation mechanism

seemed to correlate with the fly ash sulphate enrichment data at several levels of the boiler;

- Concentration of fine sulphate particles lessened as the co-firing ratio grew, with higher concentrations observed in the flue gas cooling zone. Therefore, for this particular pulverized-fuel boiler, the co-combustion technology from the modelling aspect was effective and has strong potential to decrease PM generation;
- In some cases the simulation results over-predict the SO_2 concentration by 30% on average, which is unsatisfactory. The trend however agreed quite well with that of the experimental results.

CHAPTER 5. DISCUSSION

This chapter discusses the results of spectrometry, scanning electron microscopy, and size distribution measurements performed on fly ash samples collected during the combustion test experiments as well as the comparison of modelling work with experimental data. The combustion test of 100% coal has been used for the purpose of this analysis, where the baseline is set.

5.1 Experimental work using the PSCTF

Through analysis with a Malvern sizer of fly ash samples from each test, we can ascertain the PSD of fly ash (Figs 3.28, 3.29 and 3.30) and the variation as a function of the PSCTF operating settings, and of the coal/biomass co-firing ratio.

5.1.1 Sawdust/Coal A test series

Figure 5.1, below, is derived from Figure 3.28 and shows the trend of particulate matter formed during co-firing with sawdust. During this first series of test, the proportions of fly ash particles of aerodynamic diameters less than 10 µm, 2.5 µm, and 1.0 µm drop down as the ratio of sawdust increases (Fig. 5.1).

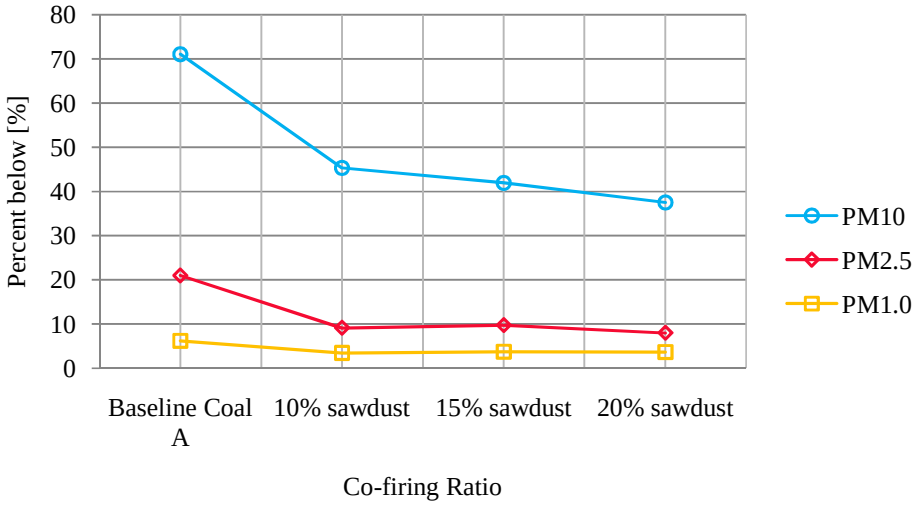

Fig. 5. 1 Sawdust blend test series (Tests 11, 13 – 15) particulate matter percentage vs co-firing ratio

5.1.1 Sawdust/coal A test series

From the Figure 5.1 it can be seen that:

- The baseline coal A (Test 11), for example, presented higher cumulative percentages of 72%, 22% and 7% respectively for PM_{10}, $PM_{2.5}$ and $PM_{1.0}$.
- The three blend tests resulted in lower values of PM_{10}, $PM_{2.5}$ and $PM_{1.0}$; these values reduced with increasing co-firing ratios. Beside, the total average particle diameter (d_{50}) figure of 6.09 µm will thus be used as the baseline.
- Test 15 (20% sawdust) showed the greatest reduction of PM.
- All the tests present similar trend of PM_{10}, $PM_{2.5}$ and $PM_{1.0}$ but with very little variation of $PM_{2.5}$ and $PM_{1.0}$ for the blends tests. Therefore, the following discussion concentrates mainly on the PM_{10} percentages.

Fly ash formation is the result of the transformation of the fuel minerals that takes place during their combustion and is a function of the mineralogy, boiler operating conditions and specific mineral reactivity. The coal A displays a high proportion of kaolinite, and a lower proportion of dolomite, quartz, and pyrite. Because of low

blending ratios utilized, the matrix of the coal/sawdust fly ash remains almost the same as for the baseline coal. As illustrated by Equation (5.1) (Raask, 1985; Muller et al, 2006; Westberg et al., 2003), alterations of the silicate structure occur during combustion and tend to define the viscosity and miscibility of sulphate and silicate phases into a eutectic mixture.

$$x\ AlSi_yO_{z\,(f)} + 2\ MCl_{(g)} + H_2O_{(g)} = \text{M-aluminosilicate} + HCl_{(g)} \qquad (5\text{-}1)$$

Where M denotes alkali metals (K, Na)

This has the general effect of lowering the ash fusion temperature and viscosity of particles as the co-firing proportion of biomass increases, equivalent to high coagulation propensity. Hence, starting from 10% sawdust, the sawdust/coal blends experiment display relatively low percentages of PM.

Fly ash particles arising from the combustion of either coal alone or blends of coal with sawdust are predominated by the coal fly ash and therefore the particle size profiles are influenced by the raw coal fineness as measured by the percent passing through a 75 µm screen (Fig. 5.2). The pulverised-coal fineness is the percentage of coal particles less than 75 µm that was used for each combustion experiment. In order to quantify the effect of co-firing pf-coal with sawdust on the fly ash PSD, focus is given to the particles less than 10 µm recorded in the Malvern sizer because not only do they have large fluctuations from one test to the other but they also include the less than 2.5 and 1.0 µm particles.

Excluded mineral grains are massively produced during crushing, grinding and milling processes and dispersed as fine pulverized coal particles. If the pulverised-coal fineness is high, the more likely the content of excluded mineral grains is high. Ninomiya et al. (2004) advanced that during co-firing of coal and biomass, high proportions of excluded minerals in both fuels provoked an interaction between the

excluded minerals of coal and biomass causing agglomeration. Consequently the particle size of fly ash shifted to large aerodynamic diameter.

The variation of PM_{10} (Fig. 5.1) highlights the possibility of a correlation in this set of tests between the PM and the fineness of pf-coal particles (Fig. 5.2); the finer the coal particle size was, the less PM_{10} was generated. As observed on Fig. 5.2, Tests 11 and 13, and Tests 14 and 15, had respectively similar fineness percentages because two different batches of milled coal were used.

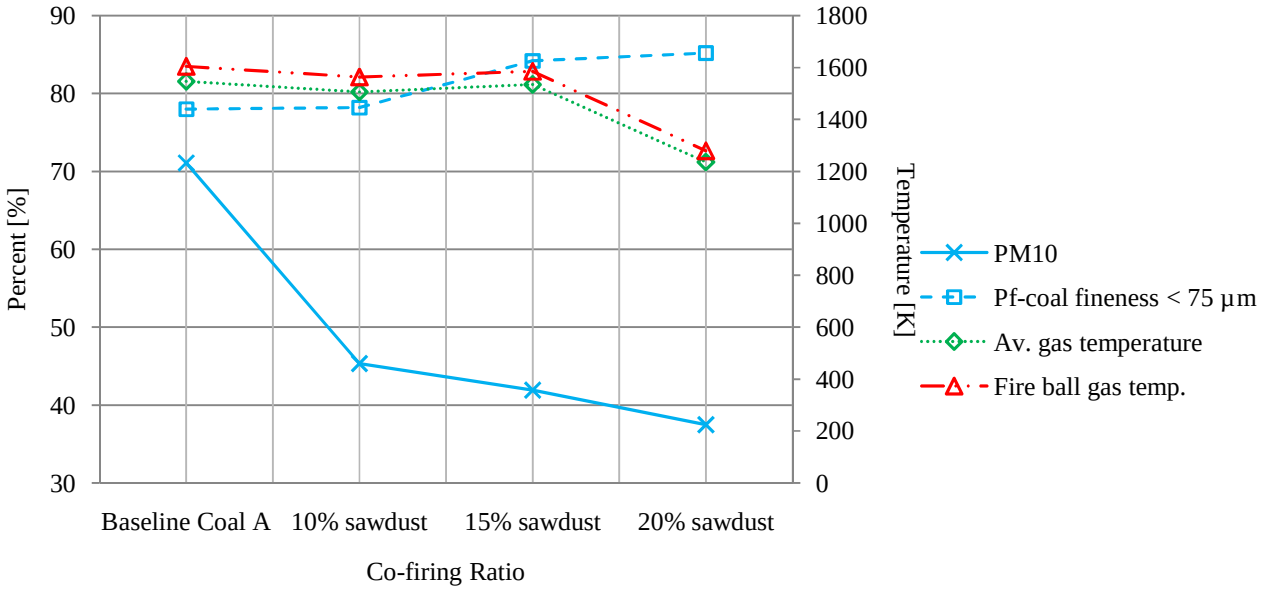

Fig. 5. 2 Correlation between pf-coal fineness, temperatures and PM_{10} based on sawdust/coal A co-firing ratios

Raask (1985) advocated that small particles, often below 1.0 µm in diameter, attained the temperature of the flame whereas large particles would be up to 200 K lower because of the difference in heat transfer by radiation. Fig. 5.3 below, for example, indicates small spherical particles, sign of molten fly ash particles formed from the reaction of the fluxing elements (Ca, Fe ...) with quartz and kaolinite at low temperatures. The above PM_{10} PSD (Fig. 5.2) results demonstrate the fact that as the

co-firing ratio increases the coagulation propensity tends also to progress, with finer particles sticking onto larger ones.

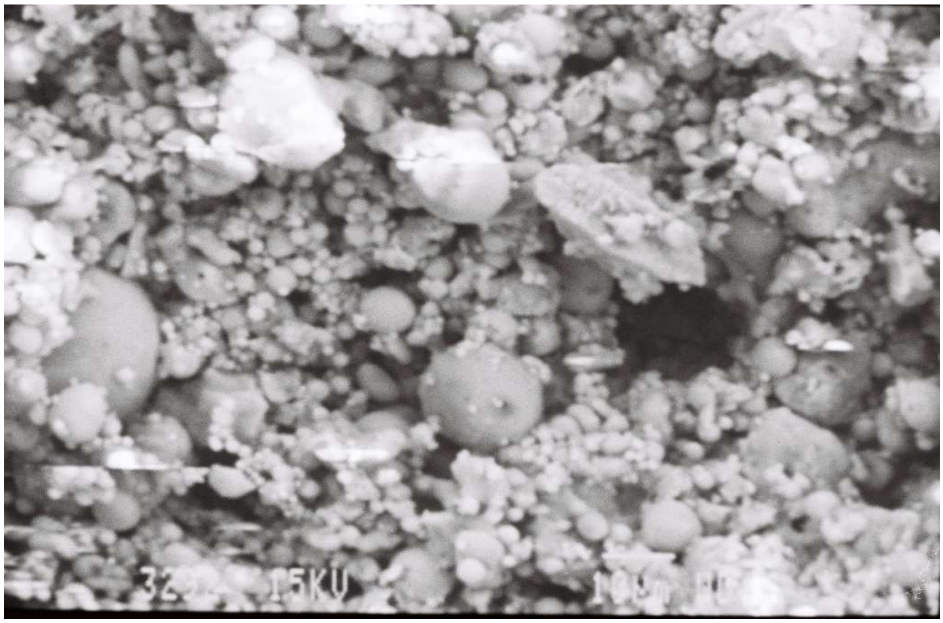

Fig. 5. 3 Fly ash collected from port 21 (Test 13, 10% sawdust) as observed by SEM

Though the drop of flue gas temperature during the blend tests is also attributed to the increase with the biomass ratio of the moisture content in the fuel (Table 3.6), another observation from the experiment to be considered is the variation of temperatures of the flue gas and fire ball with the excess oxygen mass fraction as illustrated by Fig. 5.4 below. The oxygen level is a function of the volume of flue gas in the furnace (see Total primary air in Appendix F), the higher the excess oxygen is, the lower the temperature and vice versa. This general trend has been generated using data obtained from the PSCTF test results (Table 3.10): Fire ball temperature (port 4) maximum 1604 K and minimum 1283 K. The deviation in excess oxygen level in Test 14 (15% sawdust) is not understood.

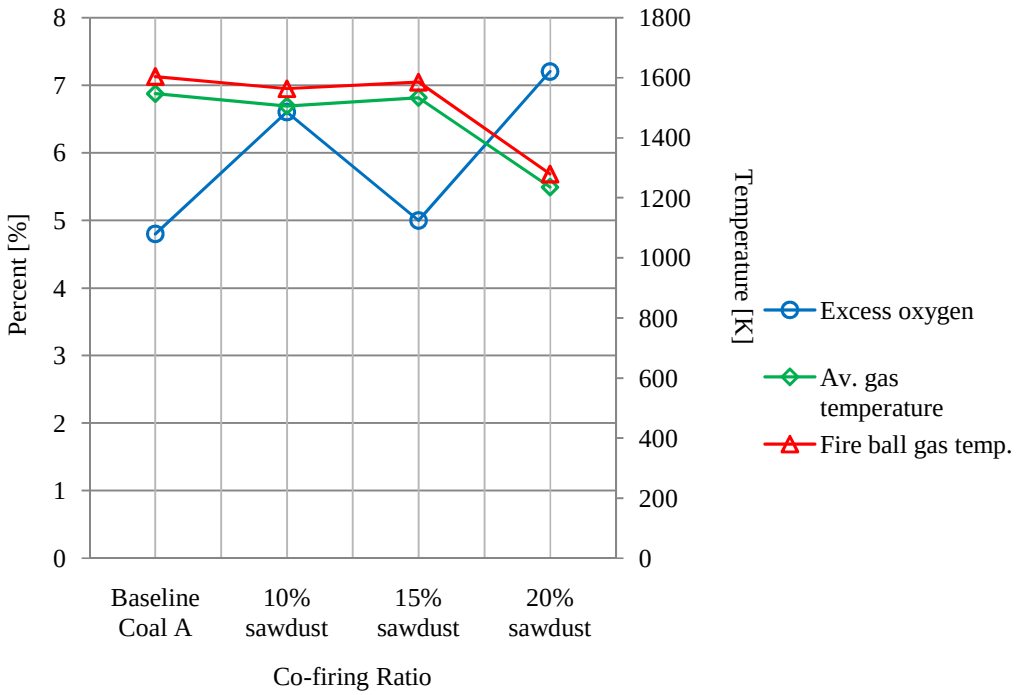

Fig. 5. 4 Temperatures and excess oxygen level in the system (Tests 11, 13 – 15) for different co-firing ratios

Hence, the influence of temperature on PM_{10} is also summarized in Fig. 5.2 where for similar pf-coal fineness from the baseline to 10% sawdust coal based tests, more coarse particles are formed. That is indicative of a high coagulation propensity of finer fly ash particles onto large ones. As can still be seen from the data in Fig. 5.2, the 15% and 20% sawdust tests are less enriched with finer pf-coal particles and show decreases of approximately 3% and 8% in PM_{10} respectively, compared with 10% sawdust.

In the case of the 10% sawdust/90% coal blend, there was an indication of a sodium alumina compound ($Na_2Al_{2x}O_{3x+1}$) that suggests significant reactivity between the volatilised sodium organically bound in the sawdust. This has facilitated the formation of fluxing element-bearing aluminosilicates.

Based on the results for the 10% sawdust blend combustion experiment, strong concentrations of alkali-bearing and fluxing calcium-bearing minerals would be expected for the 15% and 20% combustion tests. But, only calcium, iron and aluminosilicates compounds were observed, as well as a deposit issued from the crystallisation of anorthite (Ca [$Al_2Si_2O_8$]) or mullite ($Al_6Si_2O_{13}$). Since the molten fly ash is also responsible for initiation of slag deposition onto heat transfer surfaces, any particles that reached this initial molten deposit would adhere and form a clinker. Van Alphen's (2008) report on the clinker (Pokothoane, 2009) confirmed the Test 14 (15% sawdust and 85% coal) to have a high proportion of Ca-Fe bearing "alumino" and "quartz" glasses. These were unusual phases formed during the co-combustion of sawdust with coal as compared to the typical coal slagging fly ash. The normal coal-derived clinker deposit was mainly a Ca-bearing aluminosilicate. The Test 15 (20% sawdust and 80% coal) clinker deposit had phase proportions different from the other sawdust blends. There was no obvious explanation for this observation. Nevertheless, the mineralogy of the fly ash remained distinct from that of coal in terms of composition and proportions of aluminosilicates.

5.1.2 Sawdust/coal B test series

Additional PSCTF tests (Test 1 – 4) were performed subsequently with the sawdust/coal blends. These tests were performed to correct the excess O_2 level for Test 15 and to check the results of higher SO_2 and CO_2 fractions measured during Tests 13 & 14, as shown in Fig. 5.5 below, that were considered outliers in this case (Pokothoane, 2009). These latter species were expected to drop by replacement during co-firing experiments.

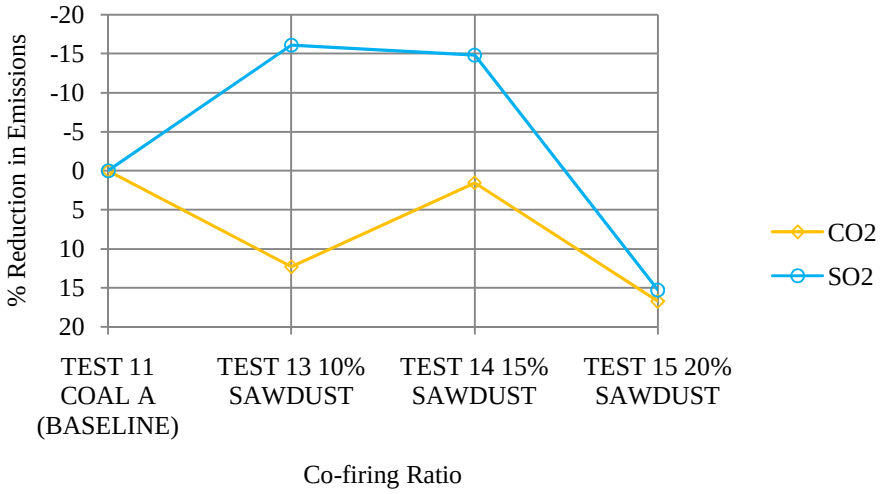

Fig. 5. 5 Effect of Sawdust on gaseous emissions from the Baseline coal A

The major differences between the first and the second series of test were the chemical composition of the baseline coals (A & B see Table 3.4), pulverized-coal percent fineness, and relatively distinct PSCTF operating conditions (temperature, turbulence, inlet velocity, etc.). The reason for two different baselines (coals A & B) is that after the first series of tests the supply of coal A was exhausted and another coal B had to be extracted from the same seam as coal A but it showed a different chemical composition (Table 3.4). Direct comparison of the fly ash PSD results for the two series of tests is therefore useful only for illustration purposes. The operating conditions are characterised by firstly the excess air, which is the amount of air required above the stoichiometric quantity to ensure complete combustion and hence better combustion efficiency. Excess air should be as small as possible to avoid significant reduction in thermal efficiency through thermal stack losses (Pokothoane, 2009). For comparison of the results from different tests, it is important to achieve as constant an excess oxygen level as possible at the PSCTF outlet. This is only achieved by setting up appropriately the flow rates of the primary and secondary air streams into the system (Appendix F). Secondly, the low-NO_x burner installed on the system must operate with respect to the recommended ratio of the primary and

secondary air velocities. The principle of operation of this burner requires the creation of a rich fuel zone in the primary combustion flame area.

During the repeat sawdust blend tests, an abundant amount of air was incorrectly allowed through the biomass inlet because of a higher pressure setting on the induced draft fan vacuum, different from that for the previous tests (Appendix F). As a consequence, a lean fuel zone was created that gave rise to higher gas temperatures, reduction in combustion efficiency (Table 3.4) and automatically to progressive increases in the NO_x emissions as co-firing ratio increased (Pokothoane, 2009).

Fig. 5.6 below shows the results of particle size cumulative distribution of fly ash collected from port 21 for the different co-firing ratios of sawdust/coal B. Results of the analysis using the Malvern sizer indicate that the mean values of the diameter of fly ash particles were 12.92, 14.21, 13.94, and 11.07 µm for 100% coal B, and the 10 up to 20% sawdust blends respectively (Fig. 3.30). This contrasting trend of PSD makes the interpretation of these results difficult compared with the previous series of tests.

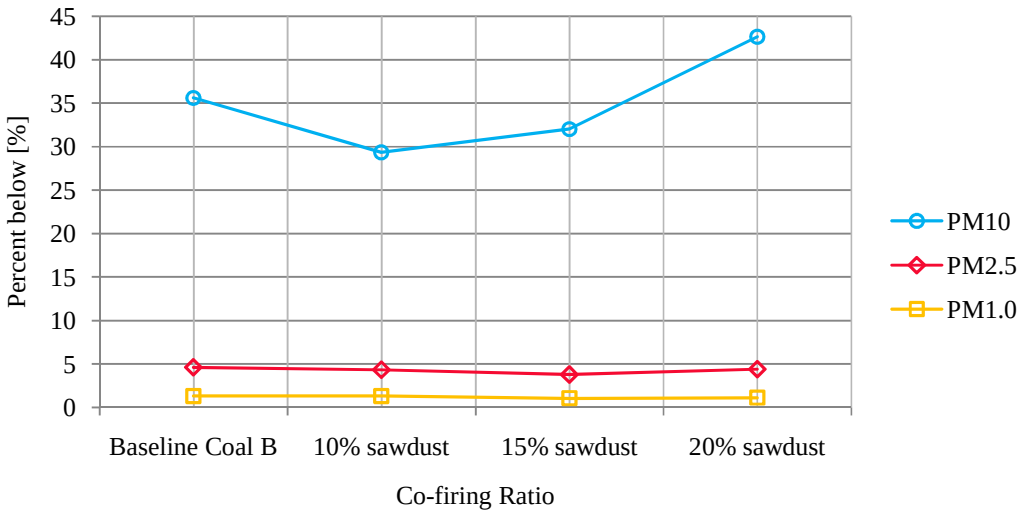

Fig. 5. 6 Sawdust blend series (Tests 1 – 4) particulate matter percentage vs co-firing ratio

The fire ball temperature of 1240 K for the baseline (Coal B) rises for the blend tests and is a function of the declining excess oxygen (Fig. 5.7) and agrees with Coal A-based sawdust tests in which, however, temperature evolves the other way round (Fig. 5.2).

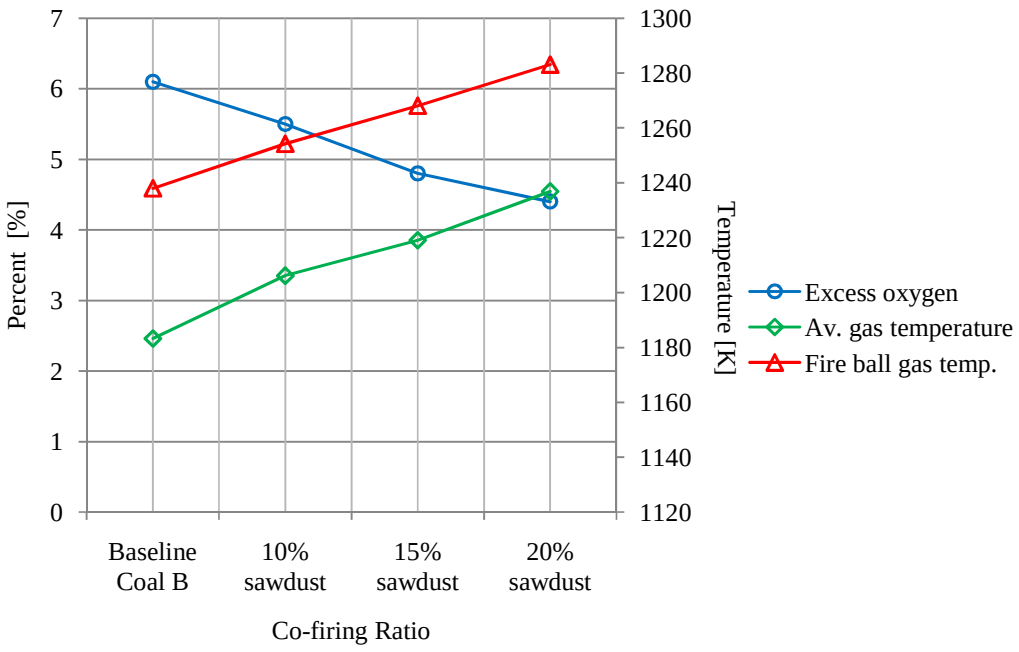

Fig. 5. 7 Temperatures and excess oxygen level in the system (Tests 1 – 4) for different co-firing ratios

According to indications from the first series of tests, considering the new temperature graph (Fig. 5.8), there should be a linear progression of PM_{10} percentage when the co-firing ratio increases, but there is an inflection at 10% and 15% (Fig. 5.8). This requires a closer look at the other parameters affecting the particulate matter behaviour by encouraging coagulation, or agglomeration of fine particles. The pf-coal fineness graph of Fig. 5.8 confirms the fact that, for nearly similar percentages of pf-coal passing through 75 µm, less PM_{10} was produced. The variation of the viscosity of fly ash particles caused by the mineralogy transformation does not

explain the increase of PM_{10} percentage during 15% sawdust/coal B test (Fig. 5.8) and the difference of this result with the 15% sawdust/coal A (Fig. 5.1). This is the reason why it is however worthy to compare the two sets of tests, despite the fact that the baseline coals are distinct.

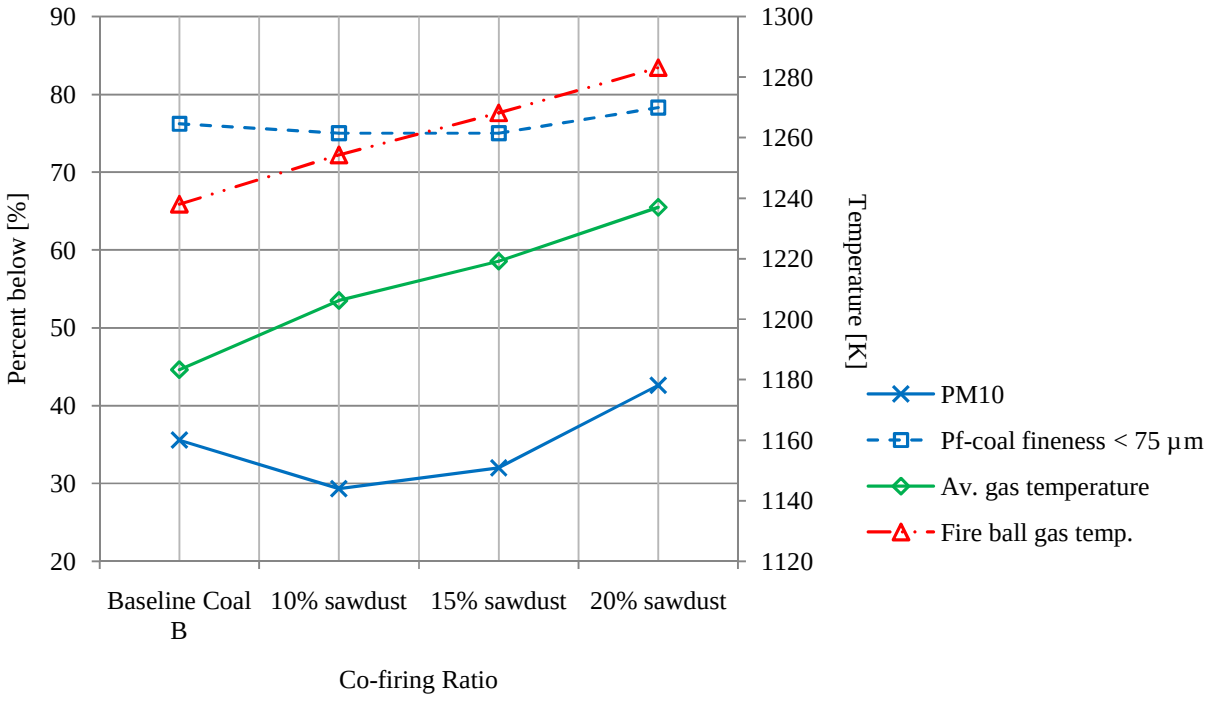

Fig. 5. 8 Correlation between pf-coal fineness, temperatures and PM_{10} based on sawdust/coal B co-firing ratios

Ninomiya and co-workers (2004) also observed a shift toward coarse PSD (Fig. 5.1) during co-combustion experiments carried out in a laboratory-scaled DTF of sewage sludge and coal at a ratio of 50:50 (wt%). They concluded that if the coal was enriched in fine excluded mineral grains and the sludge contained significant included minerals, the coal fine minerals reacted with the ash shell to form large particles inside the ash. And many more large agglomerated ash particles were formed in the case of both fuels enriched with excluded minerals because of their strong interaction; less PM was emitted due to the deposition of vaporized elements on the surface of melted ash.

Using an electrically heated DTF, Gani (2005) suggested from SEM observations that fly ash produced by straw combustion seems to be captured by ash particles from coal. Hence, burning biomass with coal shifts the PSD from fine particles to coarse particles.

Wang and co-workers (2006) also studied the composition of PM during co-combustion of biomass under DTF conditions and found that the $PM_{1.0}$ is enriched in alkali metals as sulphates or chlorides. In fact, Raask (1985) established the simplified alkali sulphation reactions [Equations (5-2) and (5-3)] during the combustion of coal. But more sophisticated multi-step mechanisms are also presented by Glarborg et al. (2005) (see Chapter 4). Because of its high content of reactive alkalis, the biomass blends should result in a greater sulphate formation which would generate after condensation, coagulation lots of $PM_{1.0}$ during co-combustion with coal. Unfortunately, $PM_{1.0}$ stays more or less constant for the blends (Fig. 5.6) and the alkali appears to react with silicates and alumina (see Chapter 2) and the emission of alkali sulphates and chlorides is lessened (Appendix G).

$$2\,MCl_{(g)} + SO_{2\,(g)} + \tfrac{1}{2}\,O_{2\,(g)} + H_2O_{(g)} = M_2SO_{4\,(g)} + 2\,HCl_{(g)} \qquad (5\text{-}2)$$

$$CaO_{(f)} + SO_{2\,(g)} + \tfrac{1}{2}\,O_{2\,(g)} = CaSO_{4\,(g)} \qquad (5\text{-}3)$$

where M represents K and Na; f: fused; g: gaseous.

It is necessary to put the graphs of pf-coal fineness and PM_{10} of the two test series on the same figure (Figure 5.9) to obtain a better understanding of the results. For close values of pf-coal fineness at both baselines and 10% sawdust tests, the PM_{10} results are far apart distant as shown on Fig. 5.9 with the first sawdust series displaying higher percentages than the second series. During the next two co-firing ratios (15% and 20% sawdust) the pf-coal fineness increases for the both series (Fig. 5.9) but especially coal A. The 15% sawdust PM_{10} results are effectively different because of the gap between the raw pf-coal used during each experiment, and because of the

coagulation effect already discussed above and the operating conditions. At 20%, the extent of the coagulation effect is estimated by comparing the two pf-coal fineness graphs. It indicates that under the operating conditions of the second series (coal B) the propensity of finer fly ash particles to condense and agglomerate onto coarser ones is more pronounced than in the first series (coal A).

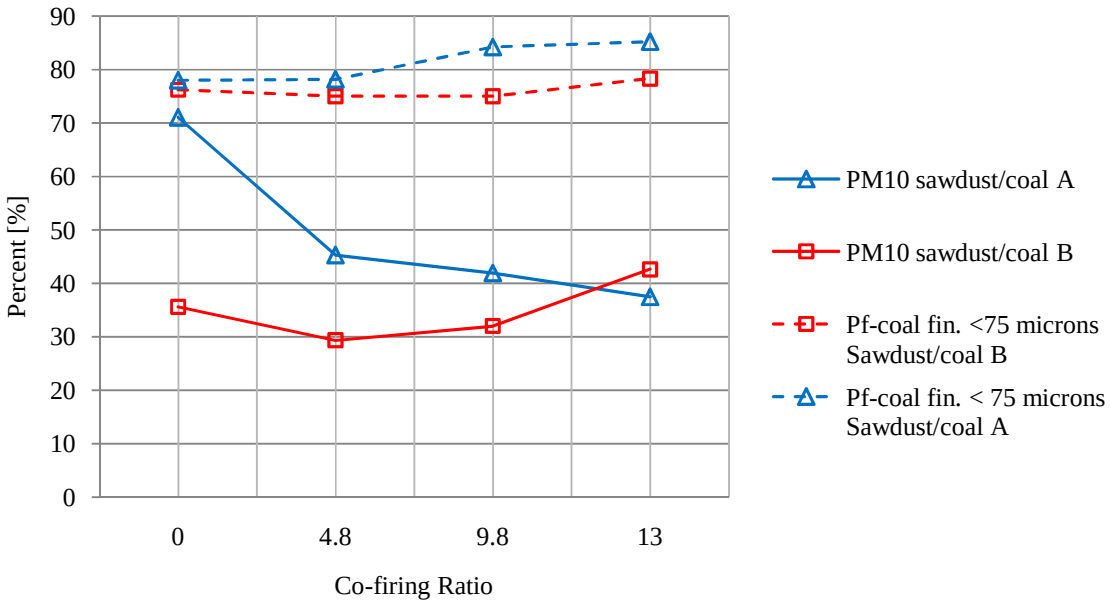

Fig. 5. 9 Comparative PM_{10} and pf-coal fineness graphs of the two sawdust test series

Observations of the flow patterns indicate that the strong turbulence effects would have to be considered; therefore the flue gas velocity inside the PSCTF on the PM_{10} is represented in Figs. 5.10 & 5.11. In general terms, slow flow of the pf-coal carrier gas (primary air mainly responsible for turbulence inside PSCTF) produces coarser modes of PM and fast air flow finer ones.

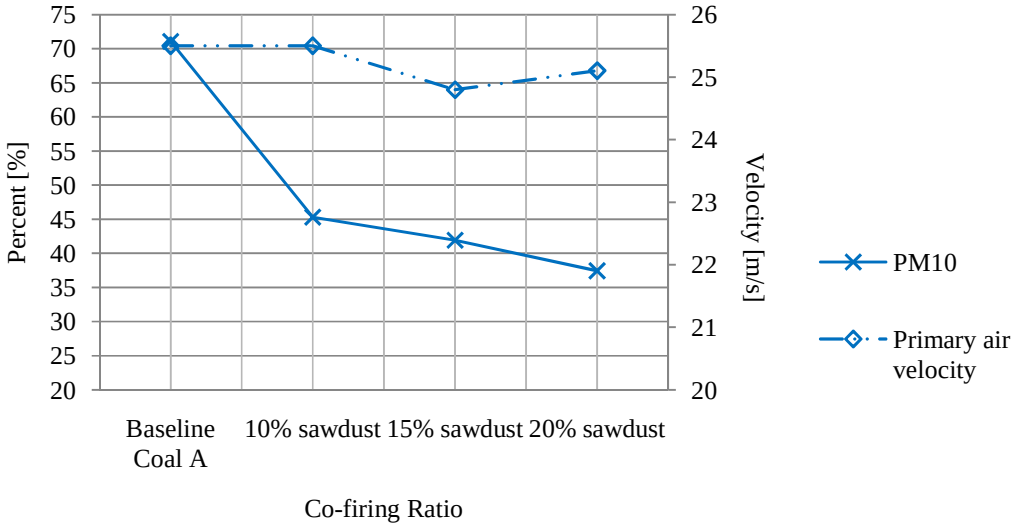

Fig. 5. 10 Primary air velocity graph vs co-firing ratio for the first sawdust test series

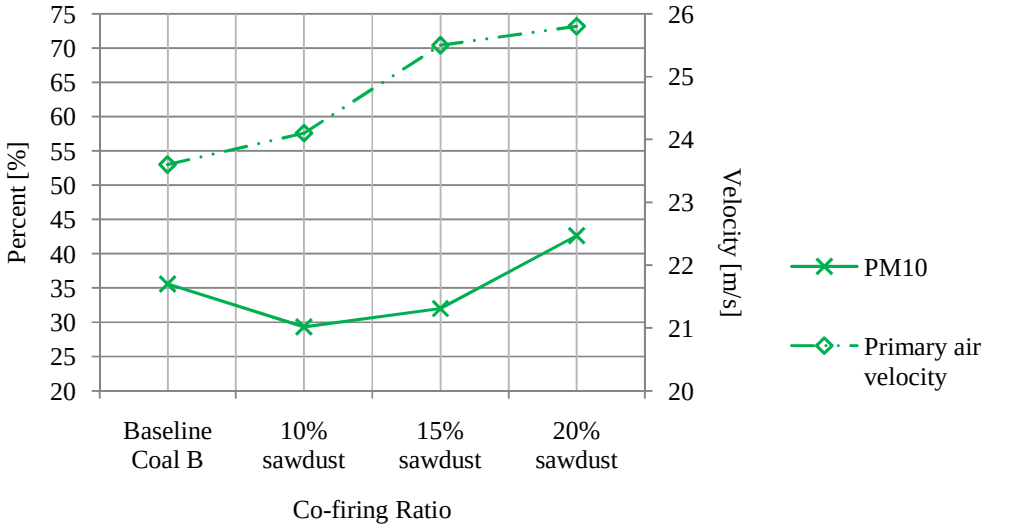

Fig. 5. 11 Primary air velocity graph vs co-firing ratio for the second sawdust test series

5.1.3 Grass/coal A test series

Figure 5.12, below, is derived from Figure 3.28 and shows the percentages of PM during the co-firing tests of coal A/Grass blends (Test 11, 16 – 18).

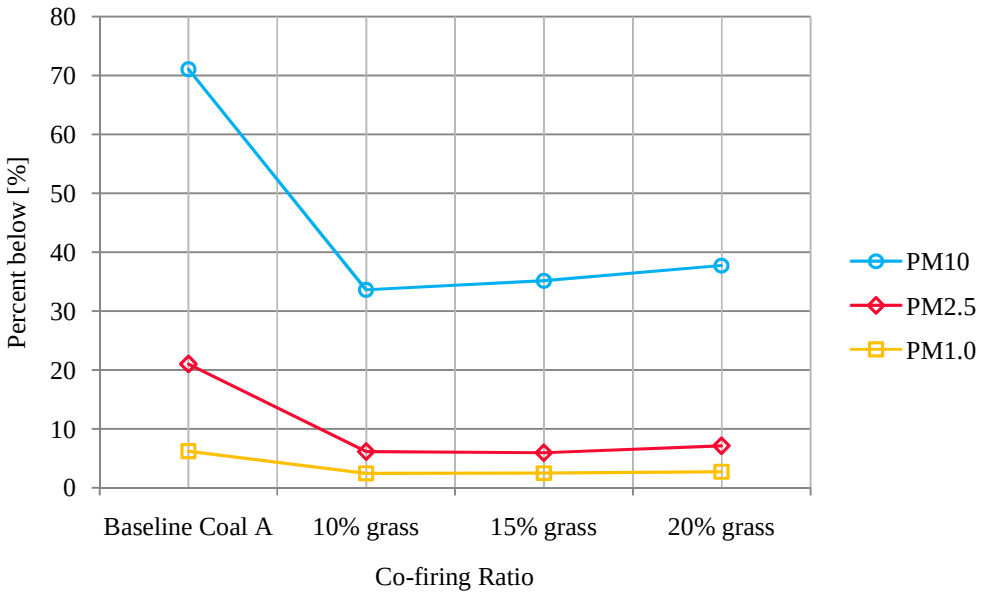

Fig. 5. 12 Grass blend series (Tests 11, 16 – 18) particulate matter percentage vs co-firing ratio

The proportions of PM_{10}, $PM_{2.5}$, and $PM_{1.0}$ vary with the grass ratio during this series of tests. Approximate average aerodynamic diameters of 14.37 µm, 13.69 µm, and 13 µm were measured from fly ash taken through port 21 for Tests 16, 17 and 18 respectively. The baseline coal A fly ash mean diameter remains 6.09 µm. Hence, Fig. 5.12 is a summary of the measurements of PSD, showing coarser modes (low PM percentages), with more or less constant $PM_{1.0}$, $PM_{2.5}$ and PM_{10} for the blends, and finer mode for the baseline test. To ensure the significance of the analysis of the data provided by the Malvern sizer and the influence of grass on the results, only the PM_{10} results are considered hereunder to account for the variation with co-firing ratio. Once again, the higher potassium and ash contents of the grass blends appear to act to encourage the alkali-bearing silicate formation responsible for the deposition of finer flying ash onto coarser particles (Fig. 5.13) for the blends. Small particles, often

below 1.0 µm in diameter, attained the temperature of the flame whereas large particles would be up to 200 K lower because of the difference in heat transfer by radiation (Raask, 1985).

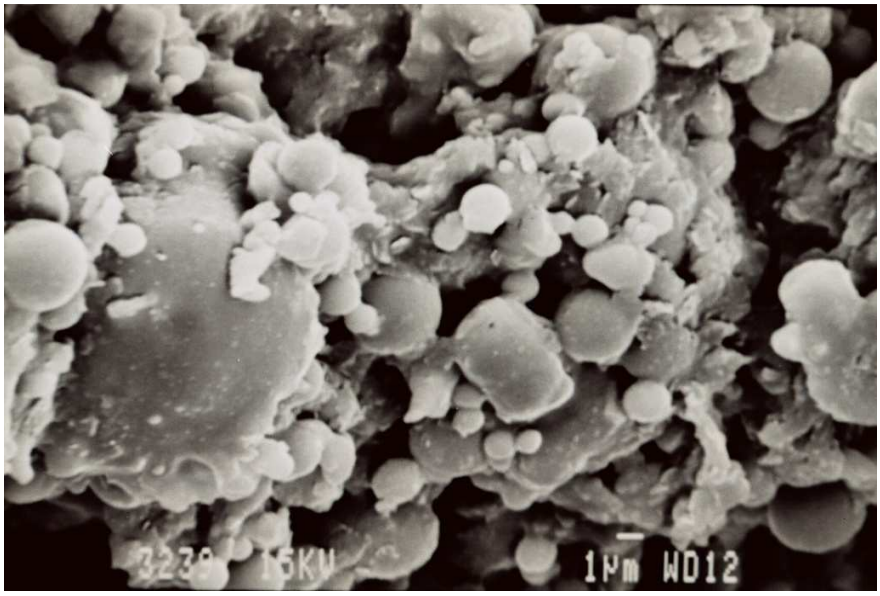

Fig. 5. 13 Fly ash collected from port 21 (experiment 17, 15% grass, reference Table 3.8)

It is clear that the major PM_{10} percentage difference between the baseline and the blend tests was firstly linked to the size of pulverised-coal particles (Fig. 5.14), the 100% coal A test had fewer finer coal particles. Collisions of excluded minerals of the coal (high fineness of pulverised-coal particles) during grass blend tests with agglomerated included minerals of the biomass produced particles of comparable size to sawdust/coal A blend combustion. Secondly, because of the above-mentioned modified mineralogy structure by alkalis during blend combustion, the pulverised-coal particles melted easily when subjected to the flue gas and fire ball temperatures (Fig. 5.14) that resulted into coarse PM ($PM_{>10}$) or less PM_{10}. The more potassium was brought into the grass/coal mixture (co-firing ratio) and the more temperatures dropped, an increase of PM_{10} was then observed as well as significant “clinker” formation or slagging (Pokothoane, 2009).

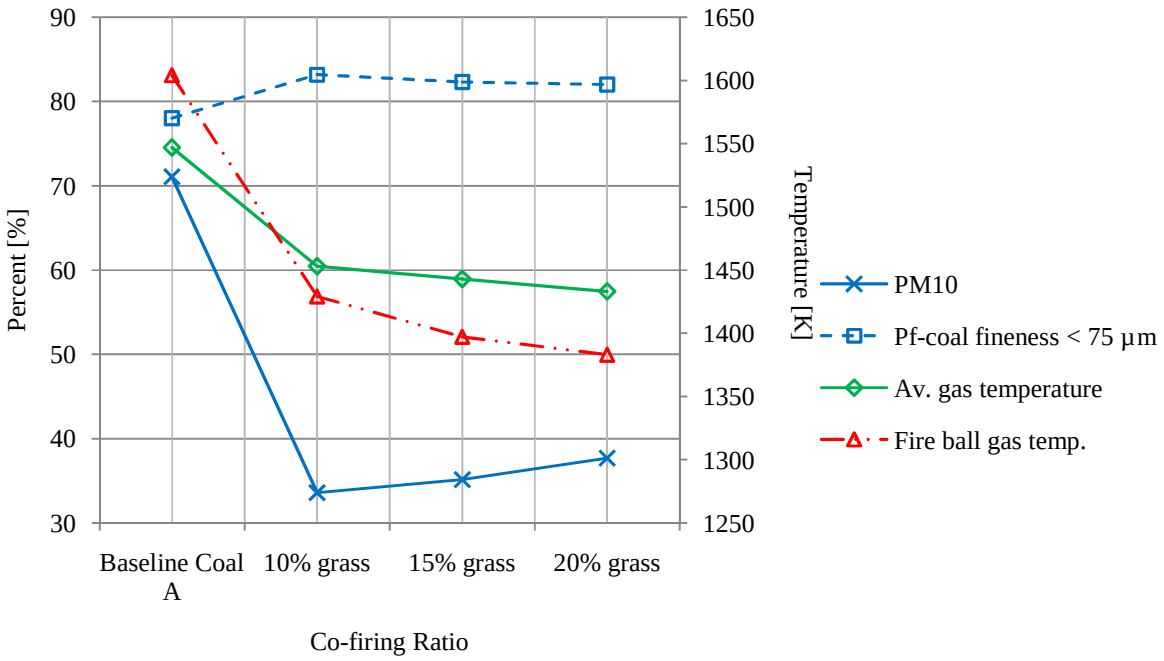

Fig. 5. 14 Correlation between pf-coal fineness, temperatures and PM_{10} based on grass/coal A co-firing ratios

The following graphs of Figure 5.14 show oxygen excess levels and temperature patterns in the PSCTF within the same range as the first sawdust test series. In fact, the operating conditions of sawdust/coal A and grass/coal A blend tests were very close. The excess oxygen level is inversely proportional to the temperatures (Fig. 5.15) as already stated for the two series of tests previously discussed in this chapter. These graphs are obtained from the PSCTF test log sheet (Table 3.10).

The thermochemical equilibrium within the very hot radiant region seemed to shift towards heterogeneous interaction of alkali metals with the alumina-silicate phase of coal leading to the formation of alkali-alumina-silicates. This explained the remarkable increase in the fly ash alkali concentration measured with ICP-MS (see Appendix H). As confirmed, with the increase of the blends biomass ratios the port 9 fly ash presented low alkali metals concentration whereas the bottom port 21 ashes

disclosed pronounced deposits of potassium (see Appendix H). Several authors have supported the assumption of the very noticeable reactivity of the biomass pyrolysis alkalis in comparison to coal. The fate of alkali metals, sulphur and chlorine for these tests was further probed by the clinker QEMSCAN conducted by van Alphen (2008) which confirmed several peaks corresponding to high proportions of Ca-Fe bearing “alumino” and “quartz” glasses for particularly Test 16.

The clinker samples of grass blends had a higher proportion of anorthite, Ca-Fe-bearing “alumino-glass” and Ca-Fe-bearing “quartz” glass. The anorthite had crystallised from the melt and the remnant glass was the Ca-Fe-bearing “alumino” and “quartz” glass (Appendix I). Discrete spherical Fe-oxide grains, angular quartz, aluminosilicate (kaolinite) and Ca-oxide/Ca-Mg-Oxide grains encapsulated in the “glass” matrix were common. These were mainly derived from coal and represent the transformation products of pyrite, quartz, kaolinite and carbonates (calcite/dolomite), respectively. The grass clinker deposits (Appendix I) had a comparatively higher proportion of Fe-oxide, Ca-oxide, Ca-Mg-oxide, quartz and aluminosilicate (kaolinite). Quartz and kaolinite is also derived from the grass. For instance, the predominant fly ash phase Al-Si-O was a product of the mineral transformation of kaolinite. Quartz represented the second abundant phase. Other minor phases might occur as a result of the interaction of kaolinite or quartz with trace concentrations of Al, Ca, Mg, Fe, Na and K during the ash formation process (Van Alphen, 2008).

This statement of dominant quartz and aluminosilicate phase was also confirmed by SEM-EDS analysis (Appendix J) of spots at several magnifications of the fly ash samples. However SEM also depicted the presence of iron, calcium and potassium of diversified origins. Pyrite, calcite, dolomite, quartz and kaolinite were common minerals in the coal (Table 3.7). Quantitative analysis with ICP-MS of port 21 fly ash revealed the presence of sulphur; chlorine and potassium in higher concentrations than for port 9 (see Appendix H). It meant not only variation of the fly ash composition and phase with height but that some compounds were adsorbed like

alkali chlorides or sulphates at the surface of the ash particles. It meant also that they might be released back to the system whenever the conditions inside the boiler changed.

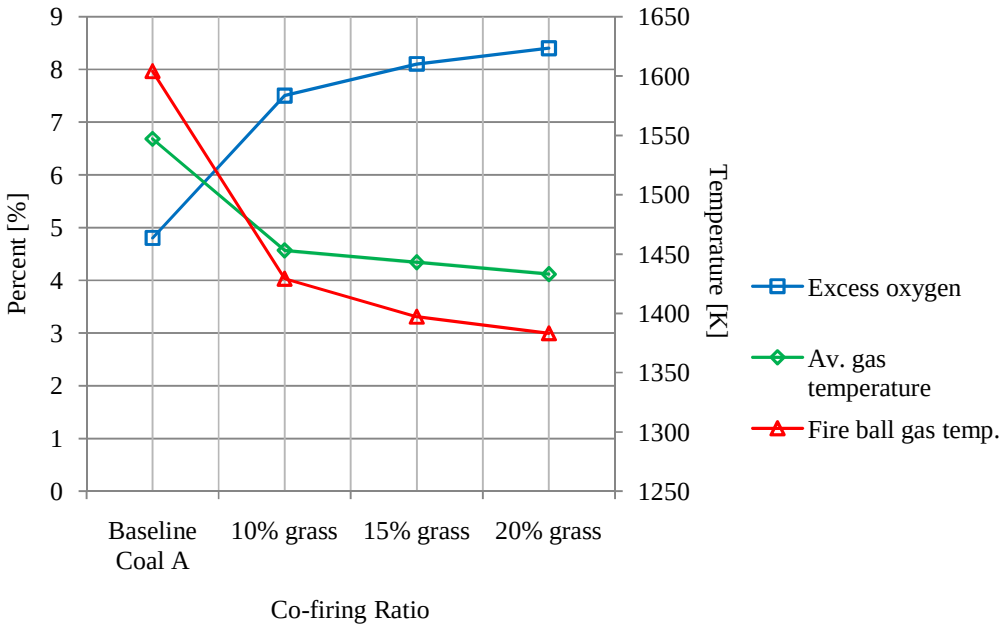

Fig. 5. 15 Temperature of the system dependency with the excess oxygen level (Tests 11, 16 – 18) vs co-firing ratio

The combination of the PSD measurements obtained from the sawdust and grass co-firing tests shown in Fig. 5.16 below reveals one side an excessive production of PM_{10} for the cases: baseline coal A, 10% and 15% sawdust coal A-based at respectively 72%, 45% and 42%. The other side 20% sawdust coal B-based blend gave an estimate percentage of 43% PM_{10}. The size distribution of raw coal being injected during each experiment varied as shown with dash-lines in Figure 5.16.

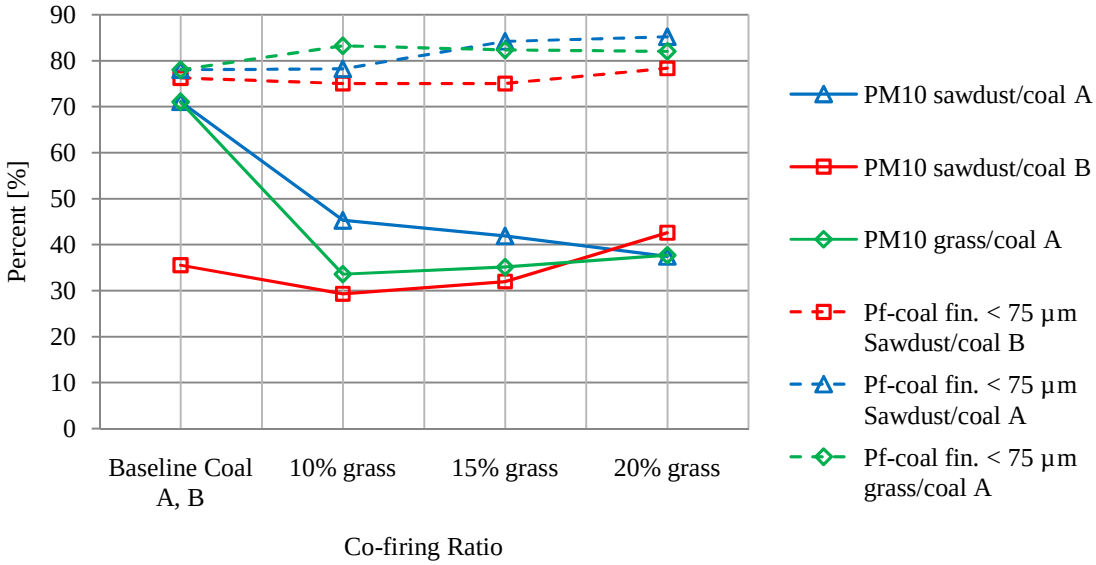

Fig. 5. 16 Comparative PM_{10} and pf-coal fineness graphs of the complete PSCTF set of tests

Briefly, the following could also be concluded from Figure 5.16:

- Though there was a general shift of particle size distribution towards a coarser mode, sawdust/coal A blends showed a relatively higher percentage of PM_{10} compared with grass for all the scenarios.
- The sawdust/coal B blend tests feature generally a very low reduction of PM_{10} relatively to its baseline (coal B) of 5% and 2 % for 10% sawdust and 15% sawdust respectively. Then there was an increase of PM_{10} percentage above 40%, for a 20% co-firing ratio, the highest value compared to the other 20% biomass blend experiments. This was due to higher turbulence inside the combustion chamber caused by the large amount of primary air admission from biomass inlet.
- The effect of grass on PM_{10} formation during co-firing with coal A tends towards reduction of the quantities of fine particles compared with the baseline test and promotes the generation of coarser particles. The coalescence mechanism responsible for the trend towards the coarse mode for grass was

due to a tendency of alkali salts formation. This tendency consequently reduced the viscosity, thus creating favourable conditions for slagging and coagulation propensities.

- Therefore, PM_{10} percentage decreases with pf-coal fineness increase.
- PM_{10} percentage decreases with co-firing ratio increase.
- Flue gas temperature decreases with O_2 excess level increase and PM_{10} percentage increases with flue gas temperature increase.

Of the two types of biomass studied, the grass was characterized by higher K content and higher chlorine content (Table 3.3). The potassium content in grass was almost 20 times greater than that of the coal A, whereas sodium was about 10 times higher. Identically to sawdust, the grass potassium was probably organically bound and was unlikely to be in the form of K-bearing minerals (microcline and muscovite/illite). Moreover, grass was characterised by a high quartz content and corresponding high proportion of K-bearing minerals (Table 3.6). It is assumed that this amorphous SiO_2 in the cell cavity, just as for sugar cane, strengthens the plant (Van Alphen, 2008).

The small difference between the results of grass and sawdust blends was also attributed to the relatively higher ash-% content of the grass compared to the sawdust and the higher proportion of “solid” ash particles (quartz, alumina-silicate, Fe-oxide and Ca/CaMg-oxide) in the “grass” slag deposits. That would effectively create a selective deposition of the different-size fly ash particles and their retention on cooled boiler tubes. The ash particles in the size range of 0.5 to 5.0 µm would be preferentially retained in the deposited ash, whereas large particles would easily escape from the deposition surface because of their sufficiently large rebound kinetic energy (Raask, 1985).

This shift of fly ash PSD towards the coarse range with co-firing could also be either attributed to the formation of cenospheres or to the agglomeration of mineral grains in the coal particles (Appendix C):

1. As previously stated, combusting coal particles react with alkalis released by biofuels and its minerals are transformed. The released volatile gases during the combustion process such as CO_2, water vapour, and SO_2 contribute to the swelling of the coal particles (Fig. 5.17) and as a result, the overall particle size (Van Alphen, 2005). Contrary to coal, biomass particles generally remained unchanged (Fig. 5.18). Consequently, in order to better comprehend the impact of possible volatiles release and alkali metals on the fly ash PSD, measurement of sulphur dioxide, and carbon dioxide was performed in the flue gas by means of an infra red analyser as presented in Figs. 5.19 & 5.20.

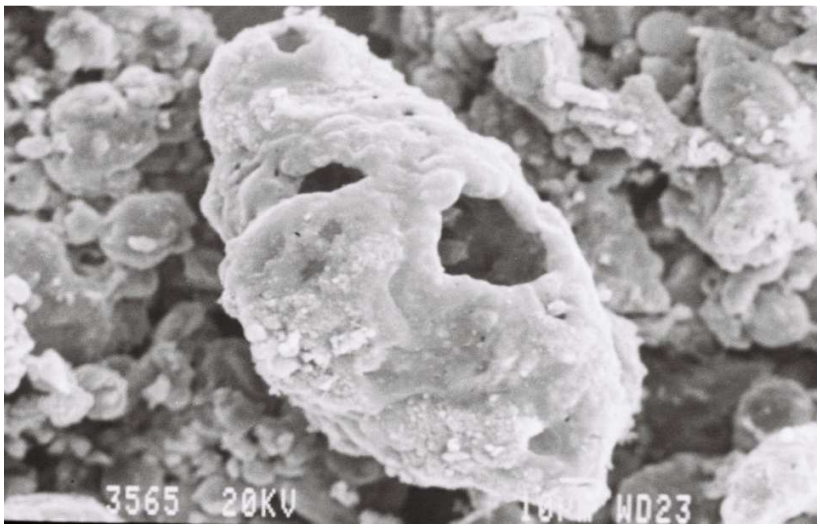

Fig. 5. 17 Fly ash collected from port 21 (experiment 15, 20% sawdust, reference Table 3.8)

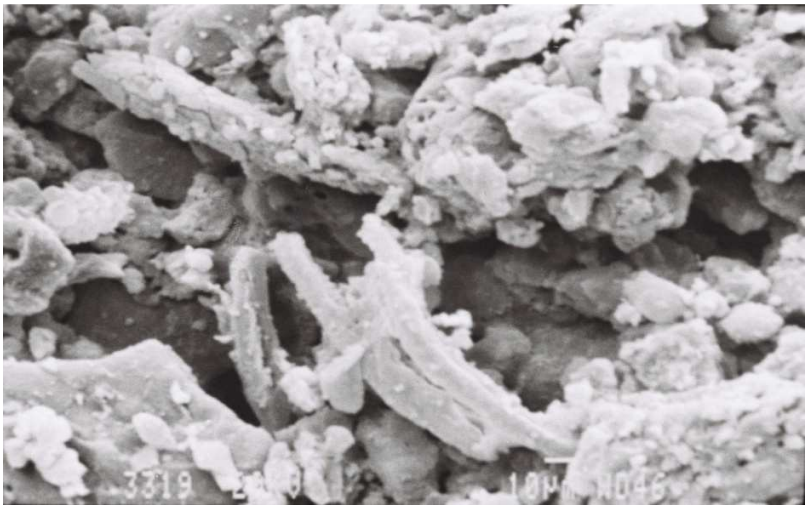

Fig. 5. 18 Fly ash collected from port 21 (experiment 15, 20% sawdust, reference Table 3.8)

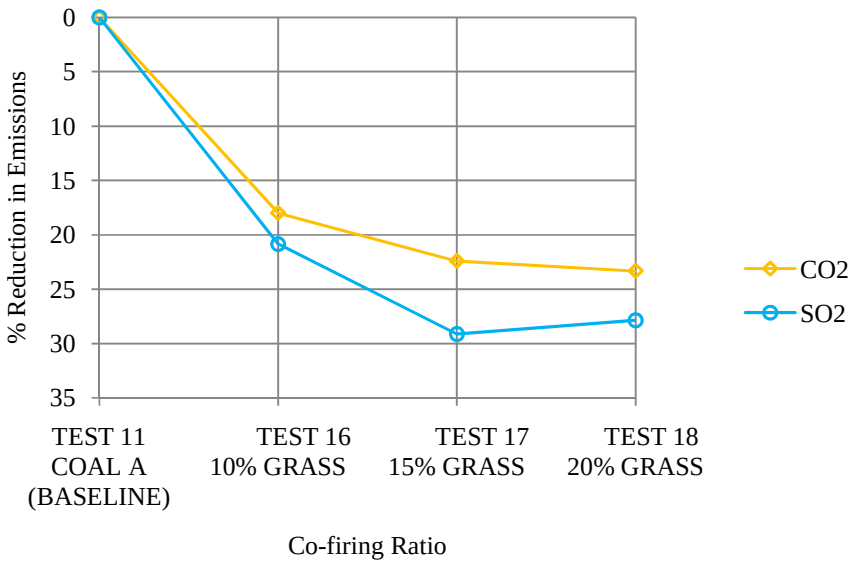

Fig. 5. 19 Effect of Grass on gaseous Emissions from the coal A-based tests

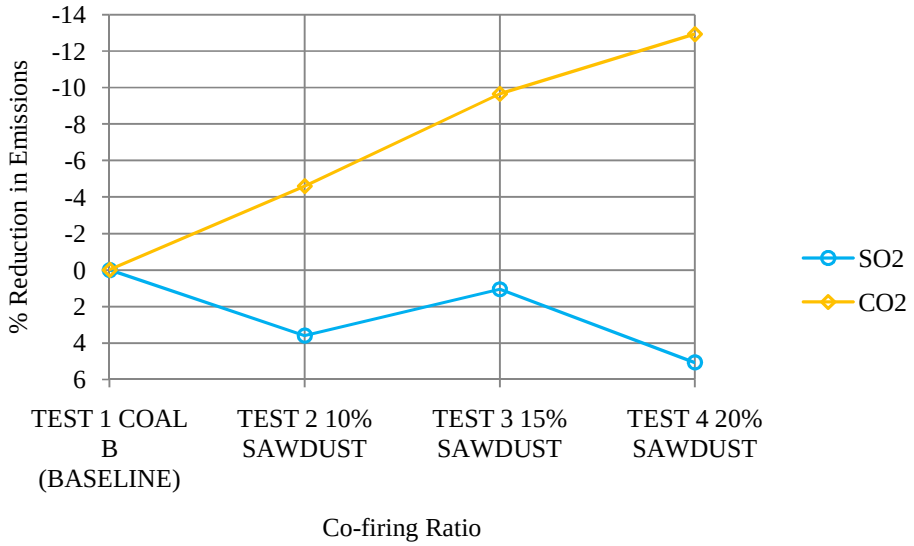

Fig. 5. 20 Effect of Sawdust on gaseous Emissions from coal B-based tests

Grass reduced SO_2 emissions by up to 30% at the co-firing ratio of 15% (Fig. 5.19). Further increase in the co-firing ratio for grass did not reduce the SO_2 emissions any further. As the amount of CO_2 and SO_2 liberated from coal particles reduced, the swelling of pf-coal particles diminished. The fly ash particles fragmented less and PM_{10} production tended to lessen. In fact because of the lower and decreasing temperatures and PSCTF in-situ pressures (Appendix F) the cenospheres did not break easily. This applies as well for the first sawdust test series (coal A-based) (Fig. 5.5), where for the first two co-firing ratios there was an increase of SO_2 mole fraction from the baseline and then a reduction down to 15% below the baseline for the last ratio. That was an incongruous result that could not be explained.

However, the PM_{10} percentage increase of coal B-based sawdust blend tests correlates with the excess oxygen level drop, CO_2 mole fractions (Fig.5.21) and temperature increases, in the flue gas as the co-firing ratio increased which reflected its influence on char breakage during combustion. Wang and co-workers (2006) also concluded in their research that the percentage of

PM_{10} rose during co-combustion experiments proportionally to the oxygen ratio and as a result the percentage of $PM_{1.0}$ diminished considerably, while that of $PM_{1.0+}$ increased.

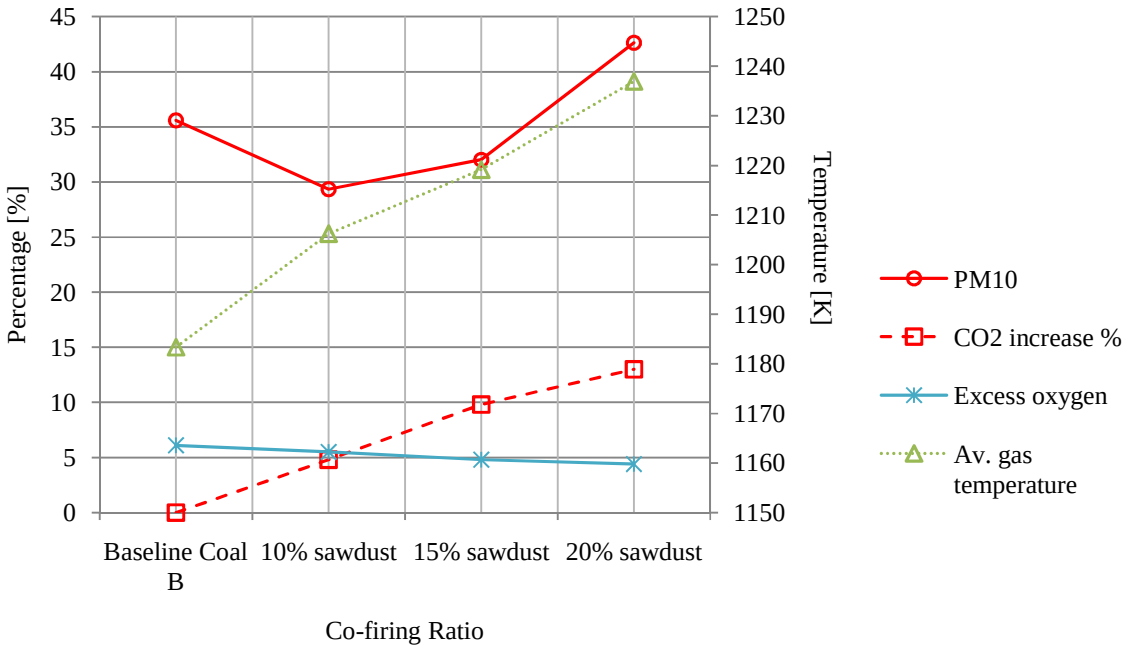

Fig. 5. 21 Combined effects of CO_2 emissions and temperature on PM_{10} formation from coal B-based tests

2. As for pulverized coal, biofuels also contain inorganic matter formed of included and excluded mineral grains (see Chapter 2). Due to the relatively high mean particle diameter of biomass achieved after milling using the swing mill compared to that of coal, it is believed that the biomass materials were more enriched with included grains that reacted with the included grains of pulverized coal as mentioned previously. The grass blends show more acute agglomeration than the sawdust blends (both coal A-based) (Fig. 5.16), probably because of their high ash content. While coarse fly ash particles essentially retained the properties of the mineral matter in the coal, fine particles were mainly composed of alkali chlorides and sulphates. The low

sulphur content of the grass and its different molecular structure compared to coal (see 2.3.1) play a major role by replacement in the reduced formation of sulphur dioxide. Another alkali metals sulphation reaction (5.2) also takes place inside the combustion chamber. Certain researchers' works advocate that Cl has more impact on the degree of alkali vaporization than the alkali concentration in the fuel itself (Muller et al., 2004; Christensen et al., 1998). But under the conditions of fly ash particle sampling, the alkali sulphate was expected to be in a vaporized form and is not likely to be detected in the two top sampling ports of the PSCTF but rather as alkali chlorides and alkali metals. For grass, very low potassium capture would have been expected as a result of its high release in the combustion process because of the high K and Cl levels.

5.2 Modelling work on the PSCTF

The flue gas temperatures were generally measured in the PSCTF with thermocouples from the ports 4, 10, 28, and D, whereas the predicted values are mass-weighted averages across the cross-section.

The modelling of baseline coal A (Fig. 5.22) displayed a short flame interpreted as weak combustion. The effect of the addition of biomass is shown in Figs. 5.23 to 5.28. The drop of temperature as the co-firing ratio increased was attributed to the relatively high moisture content of biofuels compared with coal. Table 5.1 illustrates the comparison of experimental data with results from simulation. Figure 5.23 presents the comparison between the temperature measurements at ports 4, 10, D, and 28 with those mass-averaged, across the cross-section of the PSCTF furnace for coal A alone.

Table 5. 1 Summary of comparison of experimental and predicted maxima temperatures

Test	Max temperature (measured)	Max temperature (predicted)
Baseline coal A	1648	1663
10 % sawdust/90% coal A	1608	1615
15 % sawdust/85% coal A	1646	1611
20 % sawdust/80% coal A	1579	1618
10 % grass/90% coal A	1592	1608
15 % grass/85% coal A	1593	1585
20 % grass/80% coal A	1570	1648
Baseline coal B	1346	1570
10 % sawdust/90% coal B	1368	1629
15 % sawdust/85% coal B	1381	1627
20 % sawdust/80% coal B	1400	1654

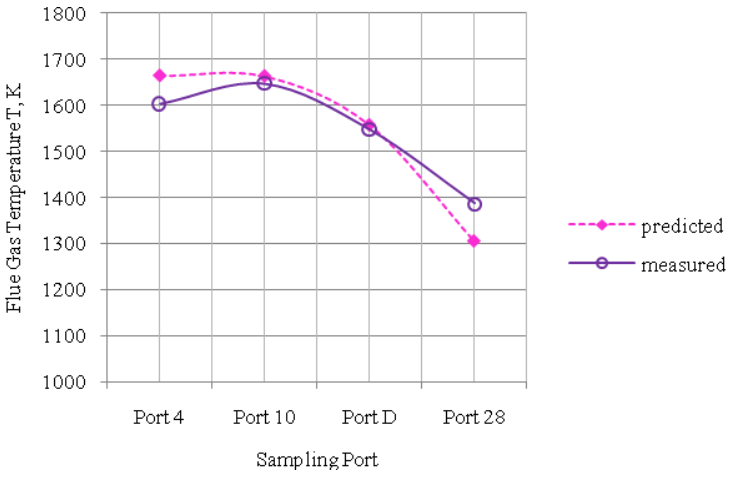

Fig. 5. 22 Comparison of temperatures of the flue gas along the height for the Baseline coal A, Test 11

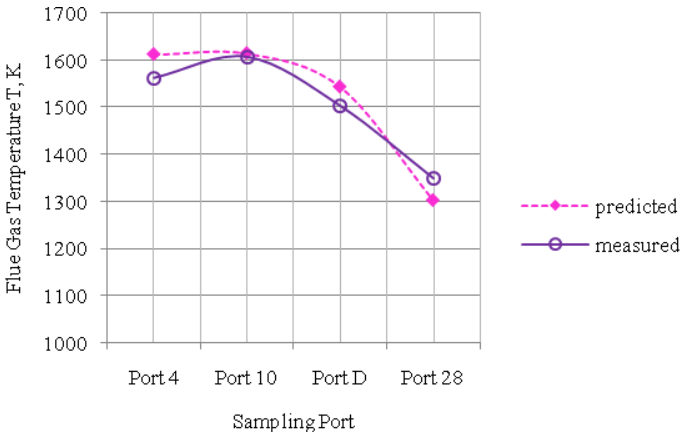

Fig. 5. 23 Comparison of temperatures of the flue gas along the height for coal A with 10% sawdust, Test 13

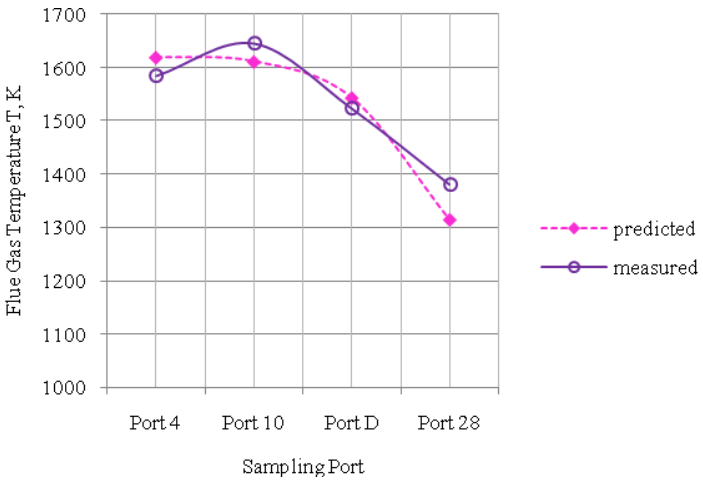

Fig. 5. 24 Comparison of temperatures of the flue gas along the height for coal A with 15% sawdust, Test 14

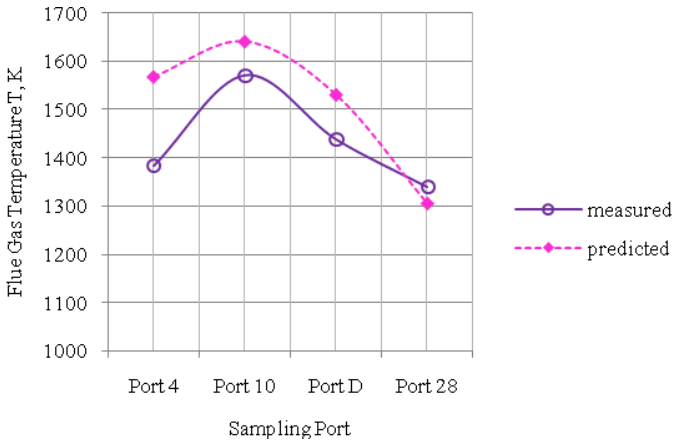

Fig. 5. 25 Comparison of temperatures of the flue gas along the height for coal A with 20% sawdust, Test 15

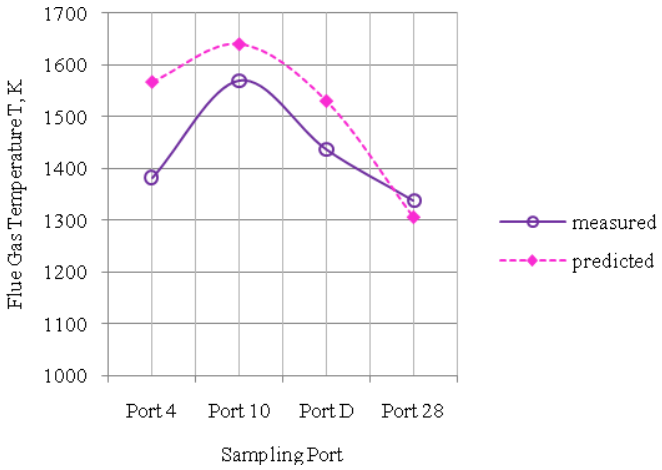

Fig. 5. 26 Comparison of temperatures of the flue gas along the height for coal A with 10% grass, Test 16

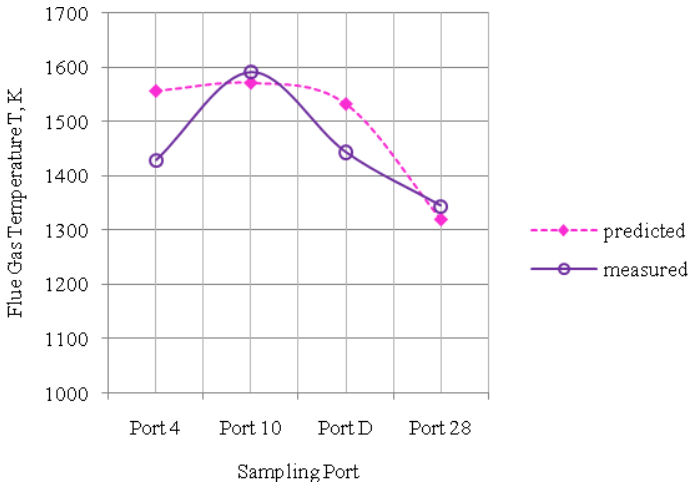

Fig. 5. 27 Comparison of temperatures of the flue gas along the height for coal A with 15% grass, Test 17

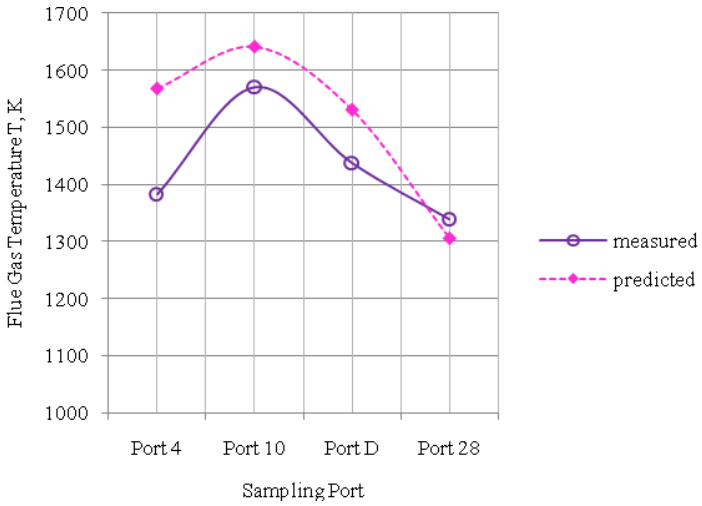

Fig. 5. 28 Comparison of temperatures of the flue gas along the height for coal A with 20% grass, Test 18

The maxima in the temperature profiles were over-predicted in most of the cases (Fig. 5.22 to 5.28), by up to 15% in the flame region, due possibly to the strongly unstable flow created by the eddies leading to inaccurate readings by instruments. However, at

lower temperatures, the predictions seemed to match the measurements well except for the baseline coal A, where the numerical prediction deviated from the measurement data at port 28 while the middle furnace points compared well. In general terms, an average error of 4% was estimated between the two sets of values, showing that the combustion modelling gives good agreement with the experiments. Because of the lack of a high temperature water-cooled camera during the test series, the flame shape and length could not be observed, and instruments were not available to monitor temperature at the centre-line of the combustion region.

The flow pattern, as demonstrated by the different eddy configurations (Fig. 4. 11a to 4.17a) depended not only on the secondary air that decreased as the coal/biomass ratio increased, but also on the furnace pressure produced by the induced draft fan. These profiles also provided important information concerning the impact that the furnace L-shape had on the inclination of both flow fields and flame, and on the recirculation of particles created by the bottom ash trap, which improved the flue gas mixing and the combustion burnout when low density particles (biomass) were added to the system.

The predicted average residence times for the tests depicted in Figure 5.29 were compared to reported experimental ones at port 27 (Appendix F) of the radiant section.

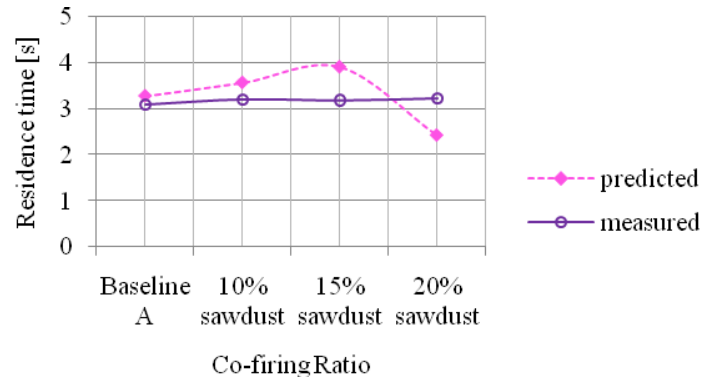

(a)

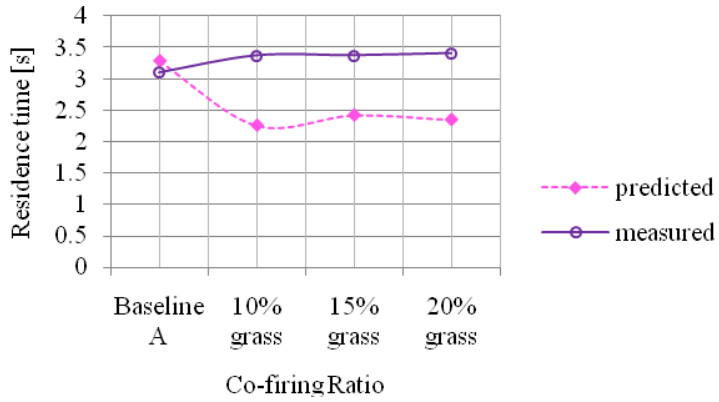

(b)

Fig. 5. 29 The residence time distribution of the different cases in the radiant section:

a) sawdust blends; b) grass blends

The sawdust blend cases had residence times of over 3 seconds, except for the 20% sawdust test that differed from the baseline figure. The grass blend tests showed shorter predicted residence times explained by the poor mixing effect present within the combustor. Although the densities of the biomass materials were slightly different, these disparate results were also influenced by the specific operating conditions of the PSCTF during each test (pressure drop, air flows, etc.). Higher residence times meant that the operating conditions were favourable to the growth of

the mixing rate. The area-averaged velocity (Figs. 4.11b to 4.11b) over the cross-sections at port 21 and at the convective section inlet are respectively compared, as shown in Fig. 5.30, to the measured velocity magnitudes along the radiant and the convective sections (Appendix K) which in fact are calculated from experimental data. It may be seen that the predicted velocities in the radiant and convective sections were considerably greater than the actual estimated values for all the cases. The uncertainty of this method of approximation of the flue gas velocities inside the radiant zone relies on the estimated density of flue gas and the flow rate of carrier air through the burner centre pipe (biomass inlet). Proper in-situ measurements of velocity would need to be provided for validation of this modelling.

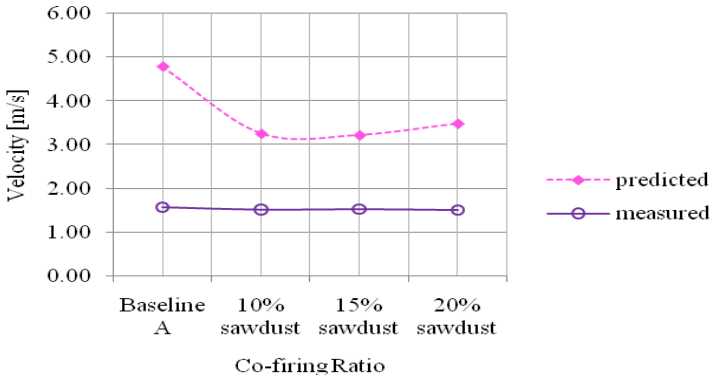

(a)

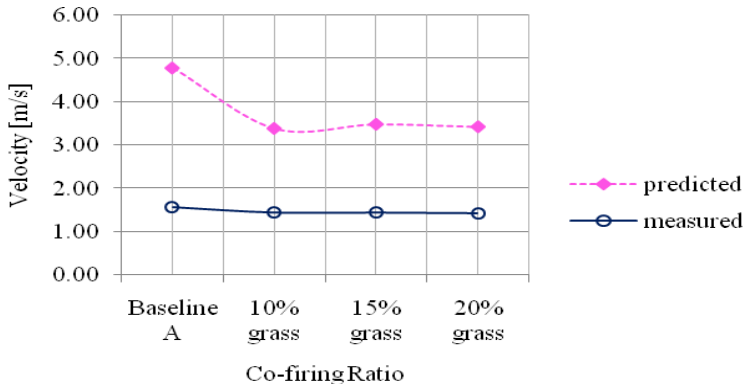

(b)

Fig. 5. 30 The radiant section velocity magnitudes of the different cases:

a) sawdust blends; b) grass blends

The predicted SO_2 profiles for sawdust in Figures 4.18b to 4.28b generally appeared to agree well with the experimental results (Fig. 5.31 (a)) but it must be borne in mind that the experimental results for 10% and 15% sawdust blends were suspect. Because the sulphur content of sawdust was less than that of coal, the overall effect should have resulted in lower progressively SO_2 emissions for the blends. If that was the case then the comparison with the model would be similar to the trends of Figure 5.31 (b) for grass. Considering the profiles for grass, it may be said that the model appeared to over-predict the SO_2 concentration by 30% on average, which is unsatisfactory. The trend however agreed quite well with that of the experimental results.

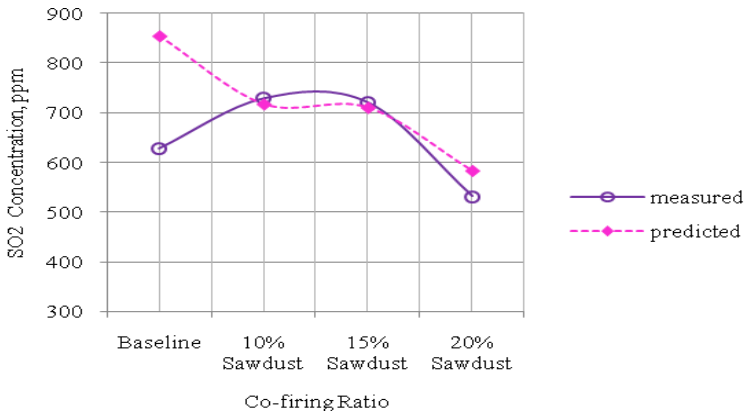

(a)

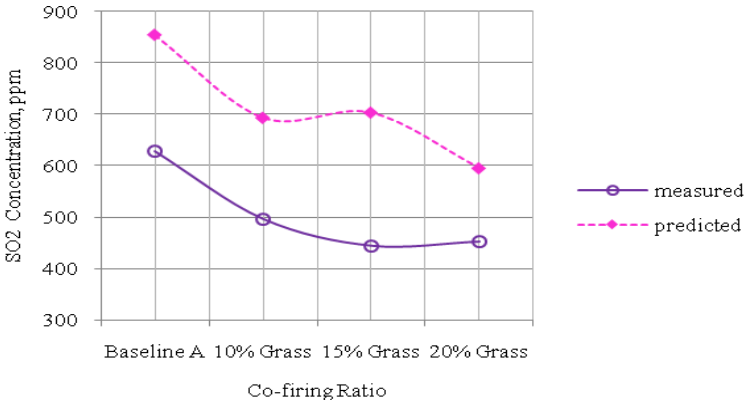

(b)

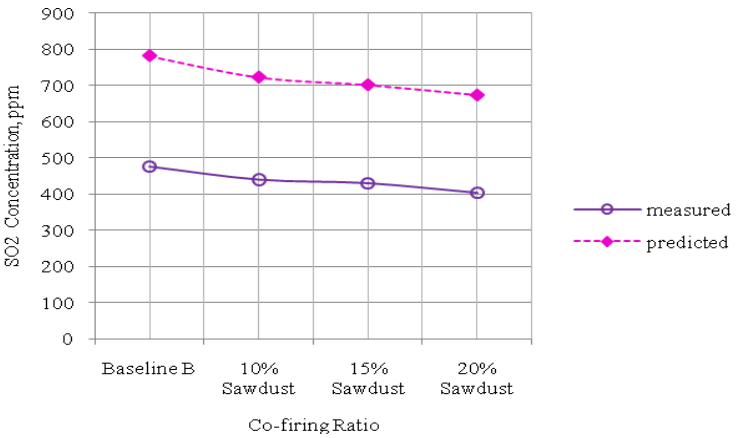

(c)

Fig. 5. 31 Sulphur dioxide concentration in flue gas at different co-firing ratios:

a) Sawdust blends; b) grass blends; c) sawdust blends repeated

An alternative interpretation based on the predicted trends of SO_2 would consider the experimental result (Fig. 5.31 (a)) for the baseline (coal A) as the outlier. The explanation might be an incorrect reading from the instrument without in this test, which the experimental measurement would otherwise have compared well with the modelling prediction in this series. As far as the gaseous emissions are concerned the modelling compared better with respect to the CO_2 results (Appendix K).

The simulated mole fraction of SO_2 for all the cases showed similar decreasing trends from 100% coal down to 80% blends with biomass. This decrease was indeed observed with the grass blends and with the repeated sawdust blends, but the first sawdust test series data (Fig. 5.31 (a)) displayed a different trend. Biomass materials are characterized by very low sulphur contents compared to the coal (Table 3.4) and by replacement the sulphur dioxide produced should naturally drop as the blending ratio grew. From this perspective the modelled test results gave reason for confidence.

SO_x emissions are produced from the oxidation of fuel-bound sulfur. During the combustion process, fuel-bound sulfur oxidizes to SO_2 and SO_3. A portion of the gaseous SO_x condense on the particles, reacting with water to form sulfuric acid, and further to form sulfates (Fluent, 2006). Wang et al. (2007) considered the measurement of sulphur trioxide concentration generated within a combustion system as equivalent to an indirect measurement of sulphate concentration.

The difference between the predicted and measured K_2SO_4 concentration inside the furnace condensed onto fly ash particles collected from the sampling port 21, as shown in Fig. 5.32 – 5.34, seemed very large. The SO_3 from the SO_x model on Fluent gives better prediction of sulphate than the described potassium sulphate model of chapter 3. Especially for the baseline Test 11 (Figs. 5.32 and 5.33), there was a good agreement between experimental data and simulation. The discrepancies of the K_2SO_4 and SO_3 mass fractions during the grass/coal A and sawdust/coal A blends tests (Fig.

5.32 and 5.33) could also be associated with the effect of its dilution by oxygen present in the flue gas.

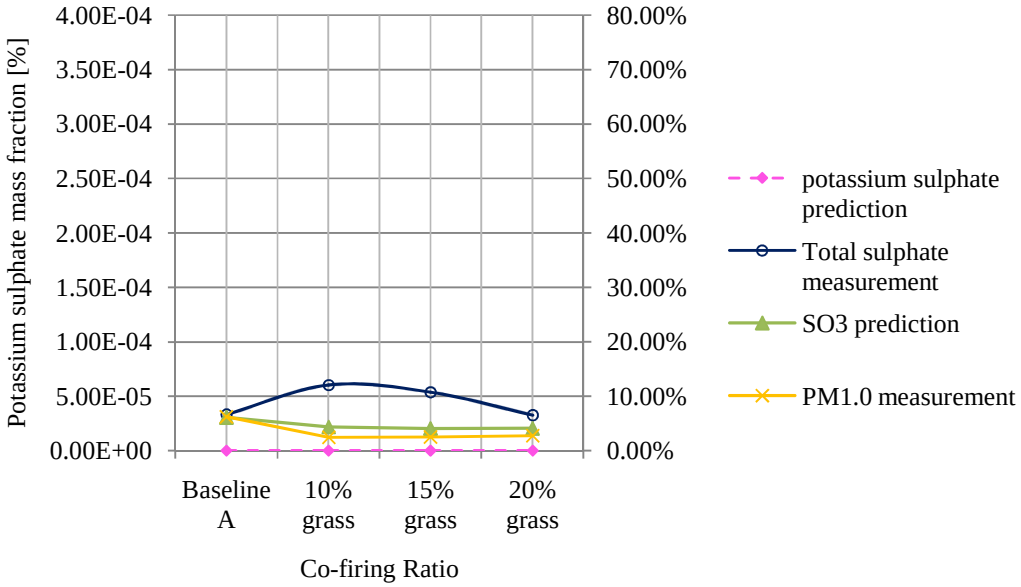

Fig. 5. 32 Potassium sulphate, sulphur trioxide mass fractions: coal-A based sawdust tests

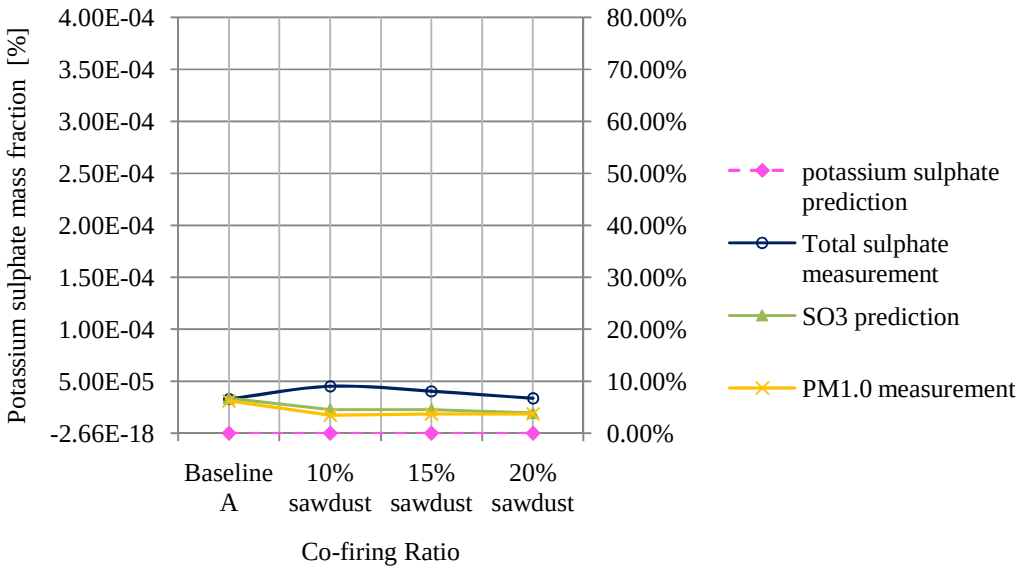

Fig. 5. 33 Potassium sulphate, sulphur trioxide mass fractions: coal-A based grass tests

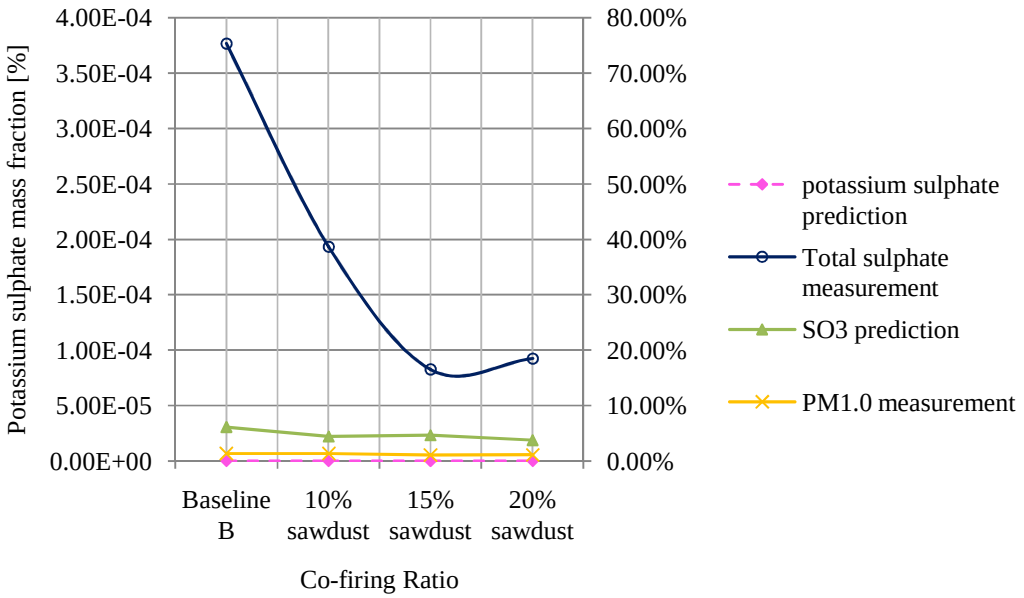

Fig. 5. 34 Potassium sulphate, sulphur trioxide mass fractions: coal-B based sawdust tests

In opposition to the modelling, measurements of sulphate generally increased during the co-combustion experiments for the 10% co-firing ratio and decreased as the co-firing ratio rose (Figs. 5.32 and 5.33). Because the potassium sulphate gas phase nucleates, condenses and coagulates to form solid fine particles, these figures compared almost correctly with $PM_{1.0}$ PSD (Fig. 5.1 and 5.12) measurements with the assumption made that sulphate was the major phase within the fine PM. These concentration ranges were very low to form aerosol particles except for the results of the repeat series of tests for sawdust (Fig.5.6 and 5.34).

Sulphur trioxide (SO_x model) (Fluent, 2006) could then be concluded to be more reliable to predict potassium sulphate concentration profiles than the species transport model of the complex alkali sulphate formation mechanism (Table 4.1). The latter assumes potassium sulphate as unique molecule in the gaseous phase leading to formation of submicron fly ash particles ($PM_{1.0}$) whereas the SO_x model considers that portion of fuel-bound sulphur forms and condenses into sulphate.

The modelling of sulphate formation verifies to some extent the experimental observations of constant percentage of $PM_{1.0}$ emitted during biomass blends combustion. The total sulphate potassium measured in the fly ash particles and shown on the above-graphs (Fig. 5.32 – 5.34) helps to check that the predicted concentration of sulphate (SO_3) remains below it.

CHAPTER 6. CONCLUSIONS, RECOMMENDATIONS AND FUTURE RESEARCH

6.1 Conclusions

In order to obtain fundamental technical information regarding fly ash particulate behaviour ($PM_{>10}$, PM_{10}, $PM_{2.5}$ and $PM_{1.0}$) for biomass co-firing with a typical pulverized South African coal, pilot-scale co-firing tests using two types of biofuels, namely ligneous (sawdust) and herbaceous (grass) fuels were conducted at co-firing ratios (biomass/coal) of 10%, 15% and 20% on an energy basis. The main objectives of this study covered in Chapter 5 were to:

- Analyse the particle size distribution of fly ash sampled from the experiments and observe its mineralogy with respect to the co-firing ratio variation;
- Compare both grass and sawdust experiments on the basis of PM PSD produced and its blending ratio with coal;
- Compare the results of fly ash particulate formation modelling by means of computational fluid dynamics methods with the experimental results from the pilot scale combustion test facility.

The experimental work on the 1 MW_{th}-PSCTF revealed with the help of a laser Malvern sizer that the percentages of PM_{10} and $PM_{2.5}$ fly ash particles generally decreased; there was a greater proportion of coarser particle, with the increase of the biomass/coal ratio.

Co-firing of both biomass materials with coal led to a reduction of up to 12% in the total fly-ash dust burden, which was due to the lower ash content of the biofuels; moreover the fly ash microstructure was enriched with alkali metals by chemical reaction or adsorption, as shown by the SEM-EDS, IC and ICP analysis. The alkali aluminosilicate compounds formed in some cases consequently lower the emissions of alkali sulphate fine particles often reported during biomass combustion alone. Effectively, the sulphur dioxide decreased correspondingly as the co-firing ratio grew

for the grass blends while the sawdust blend results have not all been satisfactorily explained.

The effect of biomass/coal co-firing on $PM_{2.5}$ and PM_{10} tended towards reduction of the quantities of these fine particles and promoted the formation of coarser particles ($PM_{>10}$) for the case of grass co-firing. Though there was a general shift of particle size distribution towards a coarse mode, sawdust showed a relatively higher percentage of $PM_{2.5}$ and PM_{10} compared with grass co-firing. The general trend was due to a tendency of alkali salts formation. This tendency consequently reduced the viscosity, thus creating favourable conditions for slagging and coagulation propensities. The grass blend tests feature generally a reduction of all PM_{10}, $PM_{2.5}$, and $PM_{1.0}$ percentages below 40%, 10%, and 3% respectively compared to the higher proportions for sawdust using the same baseline coal.

The coalescence effect of fly ash particles was caused by the low fusion point of the eutectic alkalis – alumina - silica phase resulting in slagging propensities. Consequently, biomass co-firing could reduce particulate matter pollution by decreasing the PM_{10} and $PM_{2.5}$ concentrations through a fine particle coalescence mechanism. Grass would be better than sawdust in this respect, according to the results of this particular study.

These findings compare well with other research (Ninomiya et al., 2004) which had focused on the effect of the interaction of mineral grains present in the fuels on the PM fly ash size distribution. In the present work, it is considered that since the pulverized-coal fineness is to a certain extent linked to the excluded mineral grain size distribution, fine coal excluded grains caused a shift of the fly ash PSD toward the coarse mode, and coarse coal excluded grains towards fine fly ash PSD. Hence, the blending of high ash content coal with biomass materials could be beneficial, as long as the operating conditions of the furnace, at co-firing ratios that do not exacerbate slagging and fouling, are adjusted accordingly. For example under high

pressure, the repeat sawdust set of tests on the PSCTF were characterized by a lean fuel zone created inside the primary region of the low-NO_x burner, which caused fast devolatilisation and high carbon dioxide formation which was responsible for fine PM. A $PM_{2.5}$ fly ash peak was consequently measured at the high co-firing ratio (20% sawdust) in comparison with the original sawdust test series. We also observed drops of 5% and 3% in PM_{10} for the baseline (coal B) test compared to the first experiments (grass/coal A and sawdust/coal A respectively). A dependency of fly ash PSD on the pulverized-coal PSD, flue gas temperature, primary air velocity and excess oxygen was revealed:

- PM_{10} percentage decreases with pf-coal fineness increase;
- PM_{10} percentage decreases with co-firing ratio increase;
- Flue gas temperature decreases with O_2 excess level increase;
- PM_{10} percentage increases with flue gas temperature increase.

Based principally on the work of Glarborg and co-workers (2005), the modelling of the fine sulphate particle formation mechanism involved a numerical resolution of the radiation, flows, discrete phase patterns, chemical species reactions and transport equations using a commercial CFD package (Fluent) to simulate coal/biomass blend combustion. This modelling remains computer intensive, mostly because of the complex turbulence and the variation of density of the flue gas with temperature that renders the solving of the numerical equations very lengthy.

Of the different input data required for the computer simulation, the chemical characteristics of the fuels and the combustion kinetics parameters were of great importance. Grass was rich in potassium, silica and chlorine, while sawdust was characterized by a high sodium level. Both biomass materials had very low sulphur content compared to coal. Only potassium, sulphur and chlorine were considered to devolatilise through a single rate model like the hydrocarbon species. DTF combustion tests were carried out for the evaluation of the reaction kinetics and other parameters of the coal and its blends with biomass. It is noted that sulphate and

chloride traces were measured by IC but no visible phase was detected on the XRD that suggested that they have been adsorbed with a chance of being released for instance during the flue gas cooling stage.

The results discussed in the previous chapter lead one to conclude that this simplified mechanism of sulphate formation provides moderate results under a reactor environment with presence of a fuel that normally enhances the generation of chain carrier radicals and turbulent flow. Under similar conditions and using a SO_x model, a better correlation with submicrons ($PM_{1.0}$) PSD was then achieved.

6.2 Recommendations and future work

This project is the first to report in South Africa on a pilot-scale experimental program into the effects of co-firing biomass with coal using a pulverized-fuel burner. More detailed investigation at large scale of the most promising biomass would need to be undertaken prior to implementation. However, the following recommendations are proposed, taking into account the findings of this research:

- Primarily, the operating conditions of the combustion system impacted the fine particle emissions as observed during the two sawdust test series. Further investigations should be carried out of the effect of PSCTF operating parameters (pressure, burner velocity ratio, etc.) on the formation of particles and their control to reduce fine particulate formation.
- In cooperation with the traditional industrial buyers of fly ash for the production of cement, studies would need to be undertaken to ensure that high alkali content fly ash from co-firing can be used as the same way as common coal ash.
- Very fine fly ash particles originate from the evaporation, nucleation, condensation, and coagulation of alkali sulphate produced during the co-firing process. Electrostatic precipitators are challenged at cleaning them; their

efficiency is a function of fly ash PSD. Thus, compromises have to be found on the types of suitable cleaning devices.

- In order to confirm the experimental results there is also a need for the direct measurements at the system outlet of hydrogen chloride, potassium, chlorine, and potassium sulphate in the flue gas because these play an important role in the sulphate formation mechanism (Table 4.1). These species were not monitored during the co-firing experiments due to lack of adequate instrumentation.
- There is little information about devolatilisation and char reactivity for biomass in the literature in general. For South Africa to engage in a meaningful co-firing research and development program, a reaction kinetics database for different biomass types would need to be compiled.

REFERENCES

Aglave, R. (2007), Automatically Reduced Reaction Mechanisms: A Case for Diesel Engine, PhD thesis, University of Heidelberg, Germany, unpublished.

American Coal Ash Association (ACAA) (2007), Frequently asked questions. INTERNET. www.acaa-usa.org/. Cited 22 March 2007.

Atkinson, R. ; Baulch, D. L.; Cox, R. A.; Hampson Jr., R. F.; Kerr, J. A.; Rossi, M. J.; and Troe, J. (1997), Evaluated kinetic and photochemical data for atmospheric chemistry: Supplement VI.

Backreedy, R.I., Fletcher, L.M., Jones J.M., Ma, L., Pourkashanian, M., and Williams, A. (2005), Co-firing pulverized coal and biomass: a modelling approach. *Proceedings of the Combustion Institute*, vol. 30, pp. 2955 – 2964.

Bailey, J.G.; Tate, A.; Diessel, C.F.K.; and Wall, T.F. (1990), Char morphology system with applications to coal combustion. *Fuel*, vol. 69, no 2, Feb, pp. 225-239.

Barta, L. E., Berr, J. M., Sarofim, A. F., Teare, J. D. and Toqan, M. A. (1993), Coal fouling tendency model, cited in: *Factors influencing fly ash formation and slag deposit formation (slagging) on combusting a south African pulverised fuel in a 200 MW_e Boiler*, Van Alphen, C. (Eds), PhD Thesis, 2005, University of the Witwatersrand, Johannesburg, unpublished.

Baxter, L. L. (1992), Char fragmentation and fly ash formation during Pulverised-coal combustion. In: *Factors influencing fly ash formation and slag deposit formation (slagging) on combusting a south African pulverised fuel in a 200 MW_e Boiler*, Van Alphen C., PhD thesis, unpublished.

Benson, S.A., Jones, M.L., Harb, J.N. (1993), Ash formation and deposition. In *Ash formation from excluded Minerals including consideration of Mineral-Mineral Associations;* Liu Y., Gupta R., and Wall T., Ed.; Elsevier: New York, pp. 461 – 467.

Broek, R. van den, Faaij, A., Van Wijk (1995), Biomass combustion power generation technologies. INTERNET: http://www.chem.uu.nl/nws/www/publica/95029.htm . Cited 22 March 2007.

Canadas, L., Salvador, L., and Cortes, V. (1990), Modelling of pulverised coal combustion with respect to fly ash particle size distribution. *Fuel*, vol. 69, pp. 690-695.

Charon, O., Sarofim, A. F., and Beer, J. M. (1990), Distribution of mineral matter in pulverized coal. *Prog. Energy Combustion Sciences*, Vol. 16, pp. 319-326.

Chengfeng, Z., Qiang, Y. and Junming, S. (2005), Characteristics of particulate matter from emissions of four typical coal-fired power plants in China. *Fuel Processing Technology*, vol. 86, pp. 757 – 768.

Cherney, J.H. and Baker, E.V. (2006), Ash Content of Grasses for Biofuel. INTERNET. http://www.GrassBioenergy.org. Cited 14 September 2007.

Christensen, K.A. and Livbjerg, H. (1996), A field study of submicron particles from the combustion of straw. *Aerosol Science and Technology*, vol. 25, 185-199.

Christensen, K.A., Stenlhom, M., Livbjerg, H.J. (1998), The formation of submicron aerosol particles, HCl and SO_2 in straw-fired boilers. *Aerosol Science*, vol. 29, no.4, pp. 421 – 444.

Cloke, M., Lester, E., and Thompson, A. W. (2002), Combustion characteristics of coals using a drop-tube furnace. *Fuel* vol. 81, pp. 727 – 735.

Damle, A.S., Ensor, D.S. and Ranade, M.B. (1982), Coal Combustion Aearosol Formation Mechanisms: A review**.** *Aerosol Science and Technology*, vol. 1, no.1, pp. 119-133.

Del Monte M., Braga Marcazzan G. M., Sabbioni C., and Ventura A. (1983), Morphological, physical and chemical characterization of particles emitted by a coal-fired power plant. *The eleventh annual conference of the association for aerosol research*, pp. 325 -327.

Diaz-Somoano, M., Unterberger, S. and Hein, K.R.G. (2006), Prediction of trace element volatility during co-combustion processes. *Fuel* vol. 85, pp. 1087-1093.

Dong, W. (2000), Design of Advanced Industrial Furnaces using Numerical Modeling Method, PhD thesis, Royal Institute of Technology, Sweden, unpublished.

DTI (2005), Best Practice Brochure: Co-firing of biomass (Main report), Report No. COAL R287 DTI / Pub URN 05 / 1160, unpublished.

Environment International Agency (EIA) (2004), South Africa: Energy and Environmental Issues. INTERNET. http://www.eia.doe.gov/cabs/. Cited 15 March 2007.

Environment International Agency (EIA) (2007), Country analysis briefs: South Africa. INTERNET. http://www.eia.doe.gov/ Cited 15 March 2007.

Field, M. A., Gill, D. W., Morgan, B. B. and Hawkesley, P. G. W. (1967), Combustion of pulverised coal. In: *Factors influencing fly ash formation and slag*

deposit formation (slagging) on combusting a south African pulverised fuel in a 200 MW_e Boiler, Van Alphen, C., PhD thesis, unpublished.

Fluent Inc. (2006); Fluent 6.3 User's Guide, Centerra Resource Park, Lebanon, NH 03766.

Foster Wheeler Corporation (1999), Cofiring Biomass in Coal-Fired Boilers: Results of utility Demonstrations. INTERNET. http://www.fwc.com/. Cited 22 March 2007.

Freeman, M.C., O'Dowd, W.J., Brown, T.D., Hargis Jr, R.A., James, R.A., Plasynski, S.I., Walbert, G.F., Lowe, A.F., Baptista Jr, J.J. (2000), Pilot-scale air toxics R&D assessment of creosote-treated and PCP-treated wood co-firing for pulverized coal utility boiler applications. *Biomass and Bioenergy*, vol. 19, pp. 447-456.

Gani, A., Morishita, K., Nishikawa, K., and Naruse, I. (2005), Characteristics of Co-combustion of Low-Rank coal with Biomass. *Energy & Fuels*, vol. 19, pp. 1652 – 1959.

Glarborg, P.; and Marshall, P. (2004), Mechanism and modeling of the formation of gaseous alkali sulfates, *Combustion and Flame*, vol. 141, pp. 22-39.

Glazer, M. P. (2007), Alkali metals in combustion of biomass with coal, MSc dissertation, Poznan University of Technology, Poland, unpublished.

Goodarzi, F. (2006), The rates of emissions of fine particles from some Canadian coal-fired power plants. *Fuel*, vol. 85, pp. 425 – 433.

Goosen, R. (2008), Renewable energy in South Africa: FFF Energy – Alternatives to fossil fuel. Third FFF Biofuels and Renewable Energy Conference, Johannesburg, South Africa, June 2008.

GreenFacts (2007), Particulate matter. INTERNET: http://www.greenfacts.org/glossary/ Cited 14 September 2007.

Heinzel, T., Siegle, V., Spliethoff, H., and Hein, K.R.G. (1998), Investigation of slagging in pulverized fuel co-combustion of biomass and coal at a pilot-scale test facility. *Fuel Processing Technology*, vol. 54, pp. 109 – 125.

Helble, J.J., Srinivasachar, S. and Boni, A. A. (1990), Factors influencing the transformation of minerals during pulverised coal combustion. In: *Factors influencing fly ash formation and slag deposit formation (slagging) on combusting a south African pulverised fuel in a 200 MW_e Boiler*, Van Alphen, C., PhD thesis, unpublished.

Honsbein, D. (2006), Examples of Biomass Utilisation in South Africa – Application of Slow Pyrolysis. http://www.thermalnet.inter-base.net/. Cited 14 September 2007.

Jiménez, S. and Ballester, J. (2005), Influence of operating conditions and the role of sulfur in the formation of aerosols from biomass combustion. *Combustion and Flame*, pp. 346-358.

Knudsen, J. N.; Jensen, P. A.; Dam-Johansen, K. (2004), Transformation and release to gas phase of Cl, K, and S during combustion of annual biomass, *Energy fuels*, vol. 18, pp. 1385 – 1399.

Lester, E. and Cloke, M. (1999), The characterization of coals and their respective chars formed at 1300 °C in a drop tube furnace. *Fuel*, vol. 78, pp. 1645 -1658.

Linak, W.P. (2002), Fine and ultra-fine ash particles from pulverized coal combustion. In: *Particle-Size Distributions and Heavy Metal Partitioning in Emission Gas from Different Coal-Fired Power Plants.*Yoo, J.-I., Seo, Y.-C., and Shinagawa, T. Ed.; Elsevier: New York, pp. 272 -279.

Lipsky, E., Charles, O., Stainer, Spyros, Pandis N., and Robinson, A.L. (2002), Effects of sampling conditions on the size distribution of fine particulate matter emitted from a pilot-scale pulverized coal combustor. *Energy and Fuels*, vol. 16, pp. 302 – 310.

Liu, Y., Gupta, R., Sharma, A., Wall, T., Butcher, A., Miller, G., Gottlieb, P. and French, D. (2005), Mineral matter-organic matter association characterization by QEMSCAN and applications in coal utilization. *Fuel*, vol. 84, pp. 1259 -1267.

Liu, Y., Gupta, R., and Wall, T. (2007), Ash formation from excluded minerals including consideration of mineral-mineral associations. *Energy & Fuels*, vol. 21, pp. 461 – 467.

Loedhen, D., Walsh, P.M., Sayre, A.N., Beer, J.M. and Sarofim, A.F. (1989), Generation and deposition of fly ash in the combustion of pulverised coal. In: *Factors influencing fly ash formation and slag deposit formation (slagging) on combusting a south African pulverised fuel in a 200 MW_e Boiler*, Van Alphen, C., PhD thesis, unpublished.

Ma, L.; Jones, J. M.; Pourkashanian, M. and Williams, A. (2007), Modeling the combustion of pulverized biomass in an industrial combustion test furnace, *Fuel*, vol. 86, pp. 1959 - 1965.

Malvern Instruments; INTERNET: http://www.malvern.co.uk . Cited October 2008.

Miles, T. R. Jr (1996); Experience with biomass fuel blends in combustion systems, *American Society of Mechanical Engineers, Environmental Control Division Publication, EC*, vol. 1, pp. 365-368.

Miller, B., Dugwell, D.R., and Kandiyoti, R . (2003), The influence of injected HC1 and SO_2 on the behavior of trace elements during wood-bark combustion. *Energy & Fuels*, vol. 17, 1382-1391.

Miller, B. G. (2005), Coal Energy Systems, Academic Press.

Miltner, M.; Kerschbaum, A.; Jordan, C.; Harasek, M.; and Friedl, A. (2006), Process simulation and CFD calculations for the development of an innovative baled biomass-fired combustion chamber, Vienna University of Technology, Austria.

Monroe, L.S. (1989), An experimental and modelling study of residual fly ash formation in combustion of a bituminous coal. In: *A mathematical model of ash formation during pulverised coal combustion*, Yan, L., Gupta, R.P., and Wall, T.F. (Eds) Elsevier.

Muller, M.; Wolf, K. J.; Smeda, A.; and Hilpert, K. (2006); Release of K, Cl, and S species during co-combustion of coal and straw; *Energy and Fuels*, vol. 20, no 4, pp. 1444-1449.

Ninomiya, Y., Zhang, L., Sakano, T., Kanaoka, C., Masui, M. (2004), Transformation of mineral and emission of particulate matters during co-combustion of coal with sewage sludge. *Fuel*, vol. 83, pp. 751 – 764.

NIST, INTERNET: http://webbook.nist.gov/chemistry/reac-ser.html. Cited October 2008.

Pokothoane, P. (2009), Investigation into co-firing Biomass with pulverised-coal in a pilot-scale combustion facility. School of Mechanical, Industrial and Aeronautical Engineering, University of the Witwatersrand, Johannesburg, South Africa. PhD Thesis, unpublished.

Raask, E. (1985), Mineral impurities in coal combustion: Behavior, problems, and remedial measures. Central electricity generating board technical planning and research division Leatherhead, England, UK.

Schofield, K . (2003), A new method for the direct flame calibration of nebulized additive concentrations. *Combustion and Flame*, vol. 133, 147-156.

Sengupta, I. (2007), Regulation of suspended particulate matter (SPM) in Indian coal-based thermal power plants: A static approach. *Energy Economics*, vol. 29, pp. 479 – 502.

Shibaoka, M. (2002), Investigation of Combustion Processes of Single Coal Particles. In: *Combustion characteristics of coals using a drop-tube furnace*, Cloke, M., Lester, E., Thompson, A.W., Ed. Elsevier: New York, pp. 727-735.

Smoot, L.D. and Smith, P.J. (1985), Coal combustion and gasification. New York: Plenum Press.

Srinivasachar, S. and Boni, A.A. (1989), A kinetic model for pyrite transformations in a combustion environment. *Fuel*, vol. 68, pp. 829 – 835.

Unsworth, J.F., Cunliffe, F., Graham, S.C. and Morgan, P.A.. (1987), Ash formation during pulverized coal combustion: 1: Aerodynamic influences. *Fuel*, vol. 66, pp. 1672-1679.

TSI, Power system (1985), Eskom/ERID Drop Tube Furnace. Eskom Research and Innovation Department, Johannesburg, unpublished.
TSI, Power system (1998), Pilot-Scale Combustion Test Facilities specifications and operating manual. Eskom Research and Innovation Department, Johannesburg, unpublished.

U.S. Environmental Protection Agency (1996), Air quality criteria for particulate matter. Research Triangle Park, NC: National Center for Environmental Assessment-RTP Office; report nos. EPA/600/P-95/001aF-cF.

U.S. Environmental Protection Agency Method (2000), EMTIC TM-5, Determination of Particulate Matter Emissions from stationary sources. In: *Particle-Size Distributions and Heavy Metal Partitioning in Emission Gas from Different Coal-Fired Power Plants.*Yoo, J.-I., Seo, Y.-C., and Shinagawa, T. (Eds).

Van Alphen, C. (2005), Factors influencing fly ash formation and slag deposit formation (slagging) on combusting a south African pulverised fuel in a 200 MW_e Boiler. PhD Thesis, University of the Witwatersrand, Johannesburg, unpublished.
Van Alphen, C. (2007), Automated mineralogical analysis of coal and ash products – Challenges and requirements; *Minerals Engineering*, vol. 20, no 5, pp. 496-505.

Van Alphen, C. (2008), Co-firing coal and biomass – clinkers, internal technical Eskom research and innovation department memorandum FR 021, Johannesburg, unpublished.

Van Loo, S. and Koppejan, J. (2003), Handbook of Biomass and Co-firing. Twente University Press, Enschede.

Wang, Q., Yao, H., Yu, D., Dai, L. and Xu, M. (2007), Emission Behaviour of Particulate Matter during Co-combustion of Coal and Biomass in a Drop Tube Furnace. *Energy and Fuels*, vol. 21, pp. 513-516.

Wang, Y. and Yan, L. (2008) CFD Studies on Biomass Thermochemical Conversion, *International Journal of Molecular Sciences*, vol.9, pp. 1108-1130.

Wayne, S.S., Fernandez, A., and Wendt, J.O.L. (2002), A study of fine particulate emissions from combustion of treated pulverized municipal sewage sludge. *Environment Science & Technology*, vol. 36, pp. 2772 – 2776.

Westberg, H. m.; Bystrom, M.; Leckner, B. (2003), Distribution of potassium, chlorine and sulfur between solid and vapor phase during combustion of wood chips and coal, *Energy fuels*, vol. 17, pp 18 – 28.

Wilemski, J.G., Srinivasachar, S. and Sarofim, A.F. (1992), Modelling of mineral matter redistribution and ash formation in pulverised coal combustion, In: *Factors influencing fly ash formation and slag deposit formation (slagging) on combusting a south African pulverised fuel in a 200 MW_e Boiler*, Van Alphen, C., PhD thesis, unpublished.

Whitby, E. (2005), Fine Particle model (FPM) manual for FLUENT.

Yan, L., Gupta, R.P., and Wall, T.F. (2001), The implication of mineral coalescence behaviour on ash formation and ash deposition during pulverised coal combustion. *Fuel*, vol. 80, pp. 1333 – 1340.

Yan, L., Gupta, R.P., and Wall, T.F. (2002), A mathematical model of ash formation during pulverised coal combustion, *Fuel*, vol. 81, 3, pp. 337-344.

Ylatalo, S.I., Hautanen, J., In: *Effects of sampling conditions on the size distribution of fine particulate matter emitted from a pilot-scale pulverized coal combustor*. Ed., vol., 2002, pp. 302 – 310.

Yoo, J.-I., Seo, Y.-C., and Shinagawa, T. (2005), Particle-Size distribution and heavy metal partitioning in emission gas from different coal-fired power plants. *Environmental Engineering Science*, vol. 22, no.2, pp. 271 – 279.

Yu, H., Marchek, J.E., Adair, N.L. and Harb, J.N. (1993), Characterization of minerals and coal/mineral association in pulverised coal, In: *Factors influencing fly ash formation and slag deposit formation (slagging) on combusting a south African pulverised fuel in a 200 MW_e Boiler*, Van Alphen C., PhD thesis, unpublished.

Zeuthen,J.H. (2007), The formation of aerosol particles during combustion of biomass and waste, Final Report Energinet project 6517 (FU2206), unpublished.

Zheng, L., and Furimsky, E. (IMAF Group) (2003) Quantification of chlorine and alkali emissions from fluid bed combustion of coal by equilibrium calculations; *Fuel Processing Technology*, vol. 81, no.1, pp. 7-21

Zygarlicke, C.J., Ramanathan, M. and Erickson, T.A. (1991), Fly ash particle size distribution and composition: Experimental and phenomenological approach. In: *Factors influencing fly ash formation and slag deposit formation (slagging) on combusting a south African pulverised fuel in a 200 MW_e Boiler*, Van Alphen, C., PhD thesis, unpublished.

APPENDICES

APPENDIX A FLY ASH PSD FROM PORT 21 FOR THE TESTS SERIES

T11/P21 - Townlands :Run Number 10

26/09/07

By Ali

Sample File Name: GENMETH , Record: 982
Measured on: Thu, Feb 14, 2008 4:12PM Last saved on: Thu, Feb 14, 2008 4:12PM

Source: Analysed

Presentation: 2$$D
Very Polydisperse model

Residual = 0.488 %
d (0 ,5) = 6.09 µm
D [4, 3] = 0.79 µm
Sauter Mean (D[3,2]) = 0.66 µm
Specific Surface Area = 9.1360 sq. m. / gm

Volume Result
Kill Result Low = 0 High = 26
Concentration = 0.002 %
d (0.1) = 1.46 µm
Span = 3.11

Focus = 100 mm.

Obscuration = 16.79 %
d (0.9) = 20.41 µm

Mode = 5.83 µm
Density = 1.00 gm. / c.c.

Size (Lo) µm	Result In %	Size (Hi) µm	Result Below %
0.20	1.14	0.48	1.14
0.48	1.08	0.59	2.22
0.59	1.04	0.71	3.26
0.71	1.33	0.86	4.59
0.86	1.64	1.04	6.23
1.04	1.95	1.26	8.17
1.26	2.31	1.52	10.48
1.52	2.77	1.84	13.26
1.84	3.45	2.23	16.71
2.23	4.33	2.70	21.04
2.70	5.27	3.27	26.31
3.27	6.31	3.95	32.61
3.95	7.28	4.79	39.89
4.79	7.95	5.79	47.85
5.79	8.16	7.01	56.00
7.01	7.87	8.48	63.87

Size (Lo) µm	Result In %	Size (Hi) µm	Result Below %
8.48	7.18	10.27	71.05
10.27	6.39	12.43	77.44
12.43	5.51	15.05	82.95
15.05	4.68	18.21	87.63
18.21	3.79	22.04	91.42
22.04	3.01	26.68	94.44
26.68	2.23	32.29	96.67
32.29	1.58	39.08	98.25
39.08	0.96	47.30	99.20
47.30	0.50	57.25	99.70
57.25	0.21	69.30	99.91
69.30	0.07	83.87	99.98
83.87	0.02	101.52	100.00
101.52	0.00	122.87	100.00
122.87	0.00	148.72	100.00
148.72	0.00	180.00	100.00

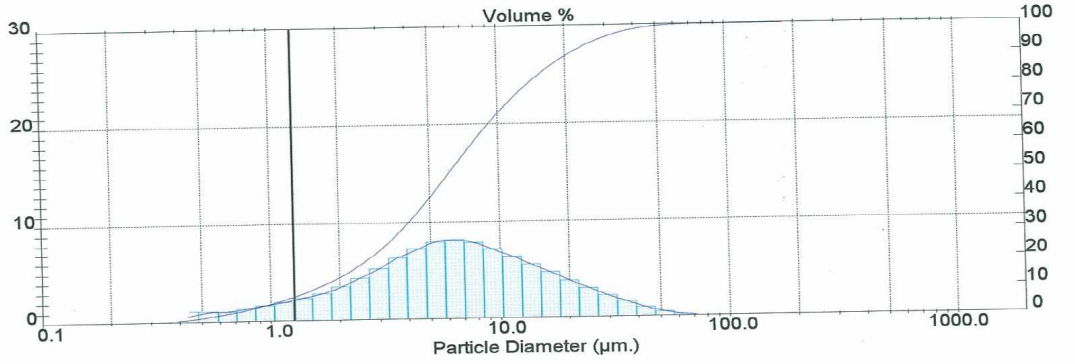

T13/P21 - 90TD/10SD :Run Number 6

26/09/07

By Ali

Sample File Name: GENMETH , Record: 978
Measured on: Thu, Feb 14, 2008 3:36PM Last saved on: Thu, Feb 14, 2008 3:37PM

Source: Analysed

Presentation: 2$$D
Very Polydisperse model

Residual = 0.278 %
d (0 .5) = 11.31 µm
D [4, 3] = 0.75 µm
Sauter Mean (D[3,2]) = 0.62 µm
Specific Surface Area = 9.6657 sq. m. / gm

Volume Result
Kill Result Low = 0 High = 26
Concentration = 0.003 %
d (0.1) = 2.94 µm
Span = 2.41

Focus = 100 mm.

Obscuration = 15.25 %
d (0.9) = 30.22 µm

Mode = 12.07 µm
Density = 1.00 gm. / c.c.

Size (Lo) µm	Result In %	Size (Hi) µm	Result Below %
0.20	0.73	0.48	0.73
0.48	0.65	0.59	1.38
0.59	0.60	0.71	1.98
0.71	0.71	0.86	2.69
0.86	0.80	1.04	3.49
1.04	0.86	1.26	4.34
1.26	0.92	1.52	5.27
1.52	1.03	1.84	6.30
1.84	1.25	2.23	7.55
2.23	1.61	2.70	9.16
2.70	2.08	3.27	11.24
3.27	2.79	3.95	14.03
3.95	3.76	4.79	17.80
4.79	4.94	5.79	22.74
5.79	6.29	7.01	29.03
7.01	7.61	8.48	36.64

Size (Lo) µm	Result In %	Size (Hi) µm	Result Below %
8.48	8.67	10.27	45.30
10.27	9.42	12.43	54.72
12.43	9.43	15.05	64.15
15.05	8.89	18.21	73.04
18.21	7.60	22.04	80.64
22.04	6.17	26.68	86.81
26.68	4.65	32.29	91.46
32.29	3.44	39.08	94.90
39.08	2.27	47.30	97.18
47.30	1.37	57.25	98.55
57.25	0.74	69.30	99.29
69.30	0.38	83.87	99.67
83.87	0.19	101.52	99.86
101.52	0.09	122.87	99.95
122.87	0.04	148.72	99.99
148.72	0.01	180.00	100.00

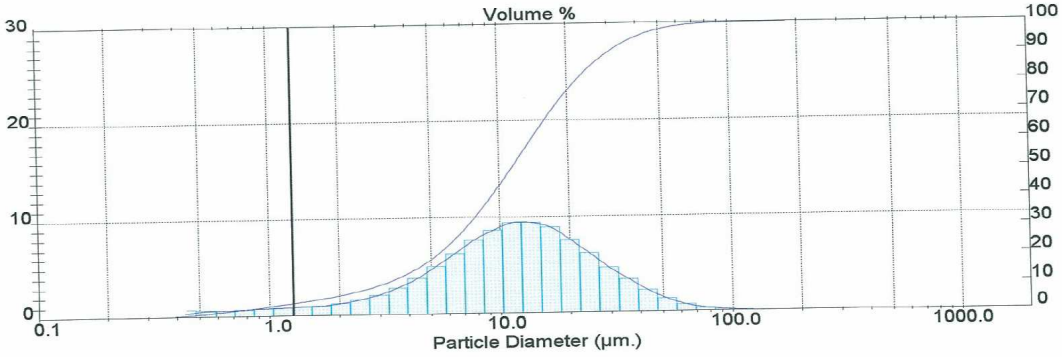

T14/P21 - 85TD/15SD :Run Number 3

26/09/07

By Ali

Sample File Name: GENMETH , Record: 966
Measured on: Wed, Feb 13, 2008 5:00PM Last saved on: Wed, Feb 13, 2008 5:01PM

Source: Analysed

Presentation: 2$$D
Very Polydisperse model

Residual = 1.700 %
d (0 .5) = 12.23 µm
D [4, 3] = 0.75 µm
Sauter Mean (D[3,2]) = 0.62 µm
Specific Surface Area = 9.6444 sq. m. / gm

Volume Result
Kill Result Low = 0 High = 26
Concentration = 0.003 %
d (0.1) = 2.77 µm
Span = 2.25

Focus = 100 mm.

Obscuration = 15.12 %
d (0.9) = 30.29 µm

Mode = 16.30 µm
Density = 1.00 gm. / c.c.

Size (Lo) µm	Result In %	Size (Hi) µm	Result Below %
0.20	0.77	0.48	0.77
0.48	0.71	0.59	1.48
0.59	0.66	0.71	2.14
0.71	0.77	0.86	2.90
0.86	0.86	1.04	3.76
1.04	0.92	1.26	4.68
1.26	1.00	1.52	5.68
1.52	1.11	1.84	6.79
1.84	1.32	2.23	8.11
2.23	1.64	2.70	9.75
2.70	2.04	3.27	11.79
3.27	2.63	3.95	14.42
3.95	3.42	4.79	17.84
4.79	4.35	5.79	22.19
5.79	5.41	7.01	27.60
7.01	6.65	8.48	34.26

Size (Lo) µm	Result In %	Size (Hi) µm	Result Below %
8.48	7.66	10.27	41.92
10.27	8.84	12.43	50.75
12.43	9.16	15.05	59.92
15.05	9.59	18.21	69.51
18.21	8.66	22.04	78.17
22.04	7.74	26.68	85.90
26.68	5.87	32.29	91.78
32.29	4.32	39.08	96.09
39.08	2.42	47.30	98.51
47.30	1.08	57.25	99.60
57.25	0.33	69.30	99.93
69.30	0.06	83.87	99.99
83.87	0.01	101.52	100.00
101.52	0.00	122.87	100.00
122.87	0.00	148.72	100.00
148.72	0.00	180.00	100.00

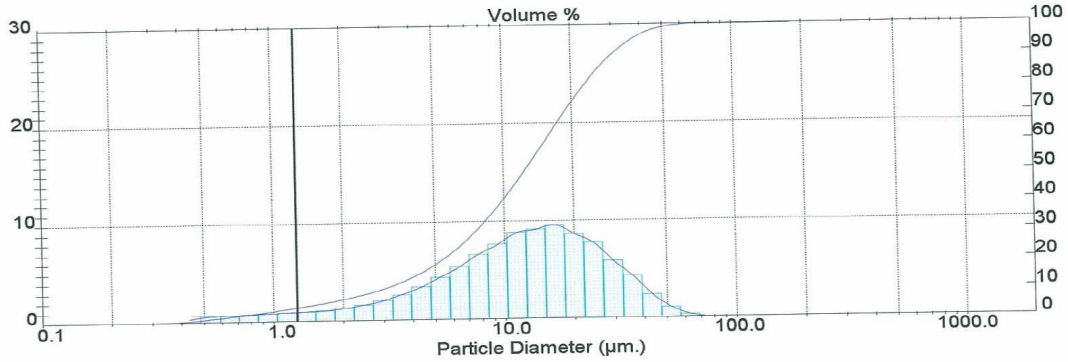

T15/P21 - 80TD/20SD :Run Number 3

26/09/07

By Ali

Source: Analysed

Sample File Name: GENMETH , Record: 975
Measured on: Thu, Feb 14, 2008 3:02PM Last saved on: Thu, Feb 14, 2008 3:03PM

Presentation: 2$$D
Very Polydisperse model

Residual = 0.517 %
d (0 .5) = 13.67 µm
D [4, 3] = 0.75 µm
Sauter Mean (D[3,2]) = 0.63 µm
Specific Surface Area = 9.5767 sq. m. / gm

Volume Result
Kill Result Low = 0 High = 26
Concentration = 0.003 %
d (0.1) = 3.33 µm
Span = 2.48

Focus = 100 mm.

Obscuration = 15.83 %
d (0.9) = 37.20 µm

Mode = 16.32 µm
Density = 1.00 gm. / c.c.

Size (Lo) µm	Result In %	Size (Hi) µm	Result Below %
0.20	0.60	0.48	0.60
0.48	0.55	0.59	1.15
0.59	0.52	0.71	1.67
0.71	0.61	0.86	2.28
0.86	0.69	1.04	2.97
1.04	0.76	1.26	3.73
1.26	0.83	1.52	4.56
1.52	0.93	1.84	5.49
1.84	1.12	2.23	6.61
2.23	1.41	2.70	8.01
2.70	1.78	3.27	9.79
3.27	2.32	3.95	12.11
3.95	3.07	4.79	15.18
4.79	3.94	5.79	19.12
5.79	5.00	7.01	24.12
7.01	6.15	8.48	30.26

Size (Lo) µm	Result In %	Size (Hi) µm	Result Below %
8.48	7.20	10.27	37.47
10.27	8.25	12.43	45.72
12.43	8.74	15.05	54.46
15.05	9.07	18.21	63.53
18.21	8.45	22.04	71.97
22.04	7.69	26.68	79.66
26.68	6.34	32.29	86.00
32.29	5.22	39.08	91.22
39.08	3.69	47.30	94.90
47.30	2.39	57.25	97.30
57.25	1.34	69.30	98.64
69.30	0.72	83.87	99.36
83.87	0.37	101.52	99.72
101.52	0.17	122.87	99.90
122.87	0.08	148.72	99.97
148.72	0.03	180.00	100.00

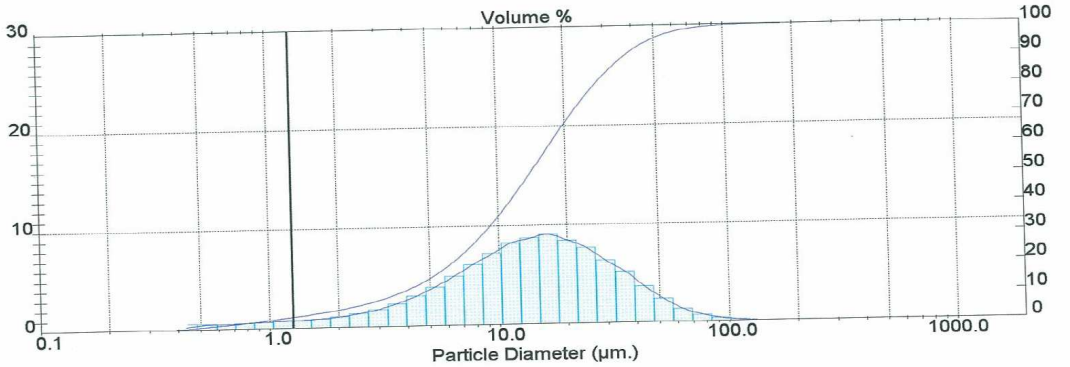

T16/P21 - 90TD/10GS :Run Number 9

26/09/07

By Ali

Sample File Name: GENMETH , Record: 981
Measured on: Thu, Feb 14, 2008 4:05PM Last saved on: Thu, Feb 14, 2008 4:05PM

Source: Analysed

Presentation: 2$$D
Very Polydisperse model

Residual = 0.556 %
d (0 .5) = 14.37 µm
D [4, 3] = 0.75 µm
Sauter Mean (D[3,2]) = 0.62 µm
Specific Surface Area = 9.6812 sq. m. / gm

Volume Result
Kill Result Low = 0 High = 26
Concentration = 0.004 %
d (0.1) = 4.26 µm
Span = 2.38

Focus = 100 mm.

Obscuration = 16.72 %
d (0.9) = 38.47 µm

Mode = 15.91 µm
Density = 1.00 gm. / c.c.

Size (Lo) µm	Result In %	Size (Hi) µm	Result Below %
0.20	0.51	0.48	0.51
0.48	0.46	0.59	0.97
0.59	0.43	0.71	1.39
0.71	0.50	0.86	1.89
0.86	0.55	1.04	2.44
1.04	0.59	1.26	3.03
1.26	0.63	1.52	3.66
1.52	0.68	1.84	4.34
1.84	0.80	2.23	5.14
2.23	1.00	2.70	6.14
2.70	1.27	3.27	7.41
3.27	1.74	3.95	9.15
3.95	2.43	4.79	11.59
4.79	3.42	5.79	15.00
5.79	4.68	7.01	19.68
7.01	6.23	8.48	25.91

Size (Lo) µm	Result In %	Size (Hi) µm	Result Below %
8.48	7.68	10.27	33.59
10.27	9.12	12.43	42.71
12.43	9.67	15.05	52.39
15.05	9.82	18.21	62.20
18.21	8.87	22.04	71.07
22.04	7.81	26.68	78.88
26.68	6.31	32.29	85.20
32.29	5.18	39.08	90.38
39.08	3.79	47.30	94.17
47.30	2.60	57.25	96.77
57.25	1.56	69.30	98.32
69.30	0.89	83.87	99.22
83.87	0.47	101.52	99.68
101.52	0.22	122.87	99.90
122.87	0.08	148.72	99.98
148.72	0.02	180.00	100.00

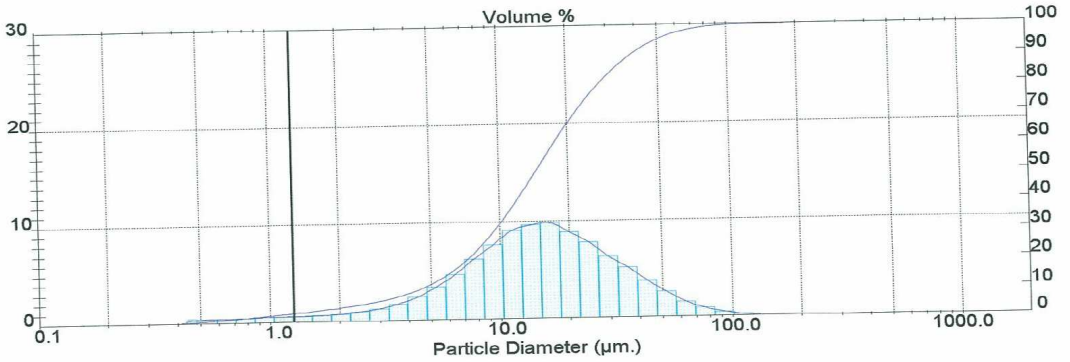

T17/P21 - 85TD/15GS :Run Number 4

26/09/07

By Ali

Sample File Name: GENMETH , Record: 967
Measured on: Wed, Feb 13, 2008 5:19PM Last saved on: Wed, Feb 13, 2008 5:19PM

Source: Analysed

Presentation: 2$$D
Very Polydisperse model

Residual = 0.535 %
d (0 .5) = 13.69 µm
D [4, 3] = 0.78 µm
Sauter Mean (D[3,2]) = 0.65 µm
Specific Surface Area = 9.1955 sq. m. / gm

Volume Result
Kill Result Low = 0 High = 26
Concentration = 0.004 %
d (0.1) = 4.21 µm
Span = 2.19

Focus = 100 mm.

Obscuration = 16.08 %
d (0.9) = 34.17 µm

Mode = 15.80 µm
Density = 1.00 gm. / c.c.

Size (Lo) µm	Result In %	Size (Hi) µm	Result Below %
0.20	0.35	0.48	0.35
0.48	0.33	0.59	0.69
0.59	0.32	0.71	1.01
0.71	0.41	0.86	1.41
0.86	0.50	1.04	1.91
1.04	0.58	1.26	2.49
1.26	0.66	1.52	3.15
1.52	0.76	1.84	3.92
1.84	0.91	2.23	4.82
2.23	1.11	2.70	5.93
2.70	1.40	3.27	7.34
3.27	1.88	3.95	9.22
3.95	2.60	4.79	11.82
4.79	3.60	5.79	15.42
5.79	4.94	7.01	20.36
7.01	6.59	8.48	26.95

Size (Lo) µm	Result In %	Size (Hi) µm	Result Below %
8.48	8.18	10.27	35.13
10.27	9.73	12.43	44.86
12.43	10.31	15.05	55.17
15.05	10.41	18.21	65.58
18.21	9.18	22.04	74.76
22.04	7.78	26.68	82.54
26.68	5.96	32.29	88.50
32.29	4.57	39.08	93.07
39.08	3.04	47.30	96.10
47.30	1.87	57.25	97.98
57.25	1.02	69.30	99.00
69.30	0.53	83.87	99.53
83.87	0.27	101.52	99.79
101.52	0.13	122.87	99.92
122.87	0.06	148.72	99.98
148.72	0.02	180.00	100.00

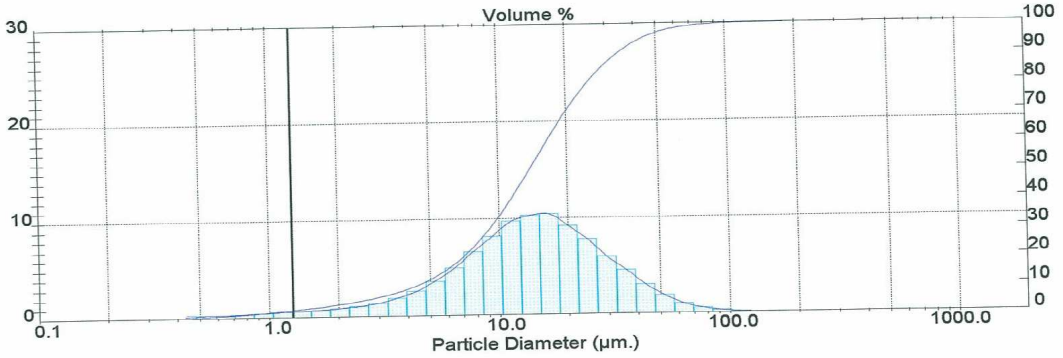

T18/P21 - 80TD/20GS :Run Number 9

26/09/07

By Ali

Source: Analysed

Sample File Name: GENMETH , Record: 972
Measured on: Wed, Feb 13, 2008 5:59PM Last saved on: Wed, Feb 13, 2008 6:00PM

Presentation: 2$$D
Very Polydisperse model

Residual = 0.510 %
d (0 .5) = 13.00 µm
D [4, 3] = 0.75 µm
Sauter Mean (D[3,2]) = 0.62 µm
Specific Surface Area = 9.6047 sq. m. / gm

Volume Result
Kill Result Low = 0 High = 26
Concentration = 0.004 %
d (0.1) = 3.74 µm
Span = 2.25

Focus = 100 mm.

Obscuration = 16.00 %
d (0.9) = 32.96 µm

Mode = 15.42 µm
Density = 1.00 gm. / c.c.

Size (Lo) µm	Result In %	Size (Hi) µm	Result Below %
0.20	0.56	0.48	0.56
0.48	0.51	0.59	1.07
0.59	0.47	0.71	1.54
0.71	0.56	0.86	2.10
0.86	0.63	1.04	2.73
1.04	0.69	1.26	3.42
1.26	0.74	1.52	4.16
1.52	0.81	1.84	4.97
1.84	0.96	2.23	5.93
2.23	1.19	2.70	7.12
2.70	1.51	3.27	8.63
3.27	2.02	3.95	10.65
3.95	2.79	4.79	13.44
4.79	3.82	5.79	17.25
5.79	5.19	7.01	22.44
7.01	6.84	8.48	29.28

Size (Lo) µm	Result In %	Size (Hi) µm	Result Below %
8.48	8.42	10.27	37.70
10.27	9.91	12.43	47.60
12.43	10.37	15.05	57.97
15.05	10.22	18.21	68.20
18.21	8.77	22.04	76.96
22.04	7.18	26.68	84.14
26.68	5.36	32.29	89.50
32.29	4.05	39.08	93.55
39.08	2.72	47.30	96.27
47.30	1.72	57.25	97.99
57.25	0.98	69.30	98.97
69.30	0.53	83.87	99.50
83.87	0.28	101.52	99.78
101.52	0.14	122.87	99.92
122.87	0.06	148.72	99.98
148.72	0.02	180.00	100.00

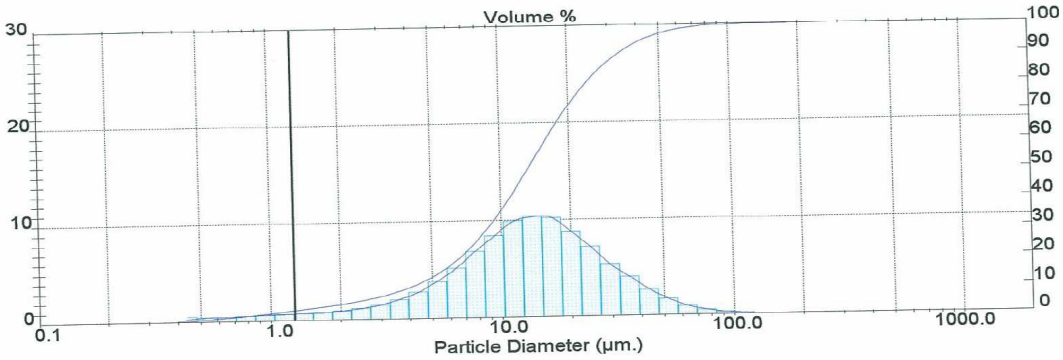

APPENDIX B CFD HOMOGENOUS TURBULENT COMBUSTION SUB-MODELS

B.1 Basic Governing Equations (Dong, 2000)

a) Conservation equations

The conservation equations of mass, momentum, energy and species are respectively shown in equations (B-1) – (B-4).

$$\frac{\partial \rho}{\partial t} + \nabla \cdot (\rho \vec{u}) = S_P \tag{B.1}$$

$$\frac{\partial (\rho \vec{u})}{\partial t} + \nabla \cdot (\rho \vec{u} \vec{u}) = -\nabla p + \nabla \cdot (\mu \nabla \vec{u}) + S_u \tag{B.2}$$

$$\frac{\partial (\rho H)}{\partial t} + \nabla \cdot (\rho \vec{u} H) = \nabla \cdot (\lambda \nabla T) + S_H \tag{B.3}$$

$$\frac{\partial (\rho Y_i)}{\partial t} + \nabla (\rho \vec{u} Y_i) = \nabla \cdot (D \nabla (\rho Y_i)) + S_Y + R_f \tag{B.4}$$

b) The state equations of a system

For a perfect gas system, the state equations can be written as

$$p = \rho RT = \rho RT \sum_{i=1}^{N} \frac{m_i}{M_i} \tag{B.5}$$

B.2 Other Physical Models

a) Turbulence Model (Fluent Inc., 2006)

Hence, the standard k-ε model is based on the Boussinesq hypothesis. Considering the generation of k by the turbulence stress and in supplement by the buoyancy, the turbulent kinetic k equation becomes:

$$\frac{\partial k}{\partial t} + U_j \frac{\partial k}{\partial x_j} = \frac{\mu_t}{\rho} S^2 - \varepsilon + \frac{\partial}{\partial x_j} \left[\frac{1}{\rho} \left(\mu + \frac{\mu_t}{\sigma_k} \right) \frac{\partial k}{\partial x_j} \right] \tag{B.6}$$

The ε equation is obtained from the Navier-Stokes equations with several undetermined quantities

$$\frac{\partial \varepsilon}{\partial t} + U_j \frac{\partial \varepsilon}{\partial x_j} = \frac{\varepsilon}{k}\left(C_{1\varepsilon} \frac{\mu_t}{\rho} S^2 - C_{2\varepsilon}\varepsilon \right) + \frac{\partial}{\partial x_j}\left[\frac{1}{\rho}\left(\mu + \frac{\mu_t}{\sigma_\varepsilon} \right) \frac{\partial \varepsilon}{\partial x_j} \right] \tag{B.7}$$

The eddy viscosity is obtained as:

$$\mu_t = \rho C_\mu \frac{k^2}{\varepsilon} \tag{B.8}$$

b) Radiation Model (Fluent Inc., 2006)

The energy source due to radiation in Eq. (B.4), S_f, can be expressed as

$$S_f = \int_0^{4\pi} \frac{dI}{ds} d\Omega \tag{B.9}$$

The radiation transfer equation (RTE) for transfer of heat due to electromagnetic waves by absorption, emission, and medium scattering can be written as:

$$\frac{dI(s,\Omega)}{ds} + (a + \sigma_s) I(s,\Omega) = a\frac{\sigma T^4}{\pi} + \frac{\sigma_s}{4\pi}\int_0^{4\pi} I(s,\Omega)\Phi d\Omega \tag{B.10}$$

Simplification of P-1 model imposes no interaction of the waves with the environment and an expansion of the radiation intensity I into an orthogonal series of spherical harmonics (P-N model). By using only four terms in the series solution, the following equation is deduced for the radiation flux q_r:

$$q_r = -\frac{1}{3(a + \sigma_s) - C\sigma_s} \nabla G \tag{B.11}$$

Combination of the transport equation for G with a simplified formulation of (B.11) gives the following equation:

$$-\nabla \cdot q_r = aG - 4a\sigma T^4 \tag{B.12}$$

The effect of dispersed second phase of particles (Discrete phase model) can also be included in the energy equation (B.3) as follows:

$$-\nabla \cdot q_r = -4\pi\left(a\frac{\sigma T^4}{T_p} + E_p\right) + (a + a_p)G \qquad \text{(B.13)}$$

c) Chemical Reactions Sub-models (Fluent, 2006)

The coal and biomass thermochemical conversions are associated to complex chemical and physical processes such as vaporization, devolatilisation, homogeneous volatile reactions, char oxidation, and transport phenomena.

- Devolatilisation sub-model (Single kinetic rate sub-model)

The single kinetic rate devolatilisation model that is used in the next chapter assumes that this rate is first-order dependent on the amount of volatiles remaining in the particle:

$$-\frac{dm_p}{dt} = k\left[m_p - (1 - f_{v,0})m_{p,0}\right] \qquad \text{(B.14)}$$

With $k = A\exp(-E_a / RT)$ (B.15)

- Volatile matter turbulent combustion

During volatile species CH_xO_y oxidation to carbon dioxide and water in the gas stream, the heat generated from the exothermic reaction is important for further release of volatiles, char ignition, and heat source to other transformation of the inorganic vapour such as alkali sulphation, etc.

$$CH_xO_y + \nu_{O2}\, O_2 = \nu_{CO2}\, CO_2 + \nu_{H2O}\, H_2O \qquad +\Delta H\ kJ/mol \qquad \text{(B.16)}$$

Hence, the relation (B.16) can be compared to the r*th* reaction written in general form as

$$\sum_{i=1}^{N} \nu'_{i,r} M_i \xrightarrow{k_{f,r}} \sum_{i=1}^{N} \nu''_{i,r} M_i \qquad \text{(B.17)}$$

For non-reversible reactions, the molar rate of creation/destruction of species *i* in reaction *r* is given by

$$\hat{R}_{i,r} = \Gamma(\nu''_{i,r} - \nu'_{i,r})\left(k_{f,r} \prod_{j=1}^{N} \left[C_{j,r}\right]^{(\eta'_{j,r}+\eta''_{j,r})} \right) \tag{B.18}$$

With the forward rate constant for reaction *r*, $k_{f,r}$, computed using the Arrhenius expression

$$k_{f,r} = A_r T^{\beta_r} e^{-E_r / RT} \tag{B.19}$$

The net source of chemical species *i* due *r* to reaction in equation (B.4) is computed as the sum of the Arrhenius reaction sources over the N_R reactions that the species participate in:

$$R_i = M_{w,i} \sum_{r=1}^{N_R} \hat{R}_{i,r} \tag{B.20}$$

- Heterogeneous char-gas phase reactions sub-model Kinetic/Diffusion surface reaction rate model) (Fluent Inc., 2006)

  $$Char(s) + S_{b\,ox}(g) \rightarrow products(g) \qquad +\Delta H\ kJ/mol \tag{B.24}$$

The diffusion-limited surface reaction rate model assumes that the surface reaction proceeds at a rate determined by the diffusion of the gaseous oxidant to the surface of the particle:

$$\frac{dm_p}{dt} = -4\pi d_p D_{i,m} \frac{Y_{ox} T_\infty \rho}{S_{box}(T_p + T_\infty)} \tag{B.25}$$

$$D_0 = C_1 \frac{[(T_p + T_\infty)/2]^{0.75}}{d_p} \tag{B.26}$$

$$R = C_2 e^{-(E/RT_p)} \tag{B.27}$$

$$\frac{dm_p}{dt} = -A_p p_{ox} \frac{D_0 R}{D_0 + R} \tag{B.28}$$

d) Particle Motion Sub-model (Discrete Phase Model: DPM) (Fluent Inc., 2006)

$$\frac{du_p}{dt} = F_D(u - u_p) + \frac{g_x(\rho_p - \rho)}{\rho_p} + F_x \tag{B.29}$$

$$F_D = \frac{18\mu}{\rho_p d_p^2}\frac{C_D \mathrm{Re}}{24} \tag{B.30}$$

Appendix C Drop Tube Furnace Experiments Using Batch Blends Of Coal And Respectively Sawdust And Grass

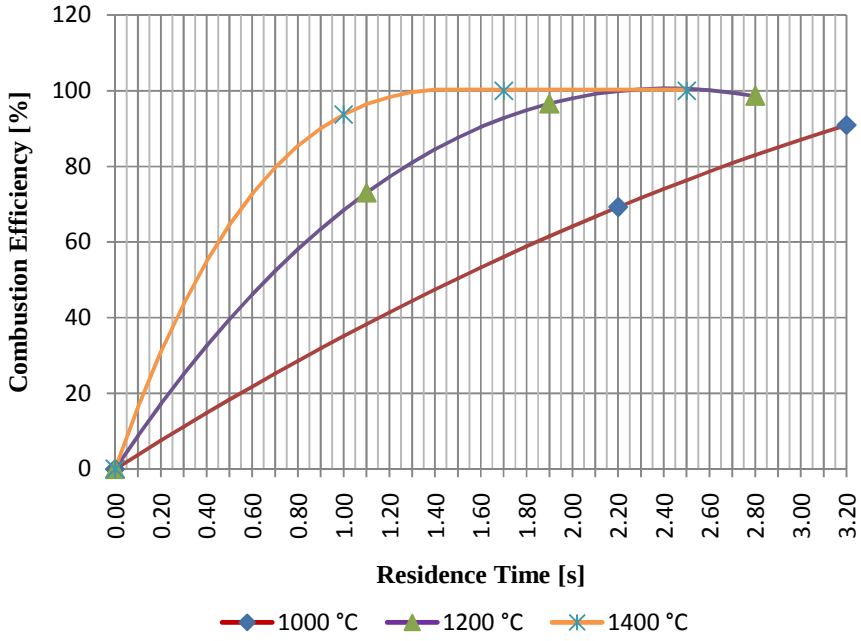

Fig. C.1 DTF Combustion efficiency profiles for 100% coal A

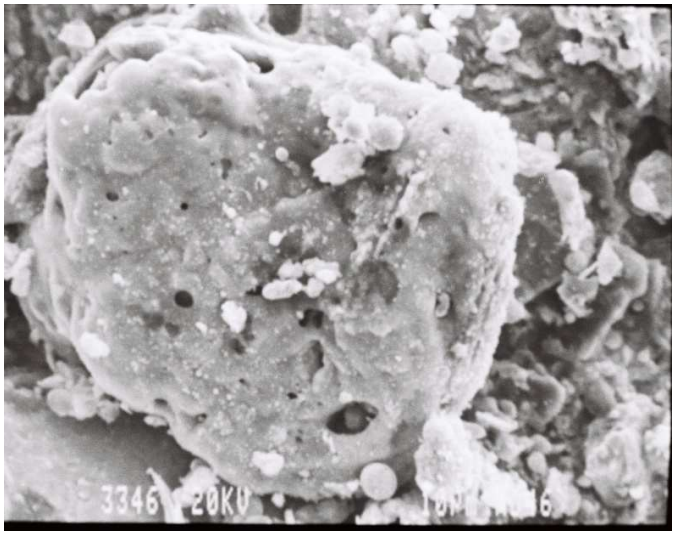

Fig. C.2 Morphologies of Coal A char particles at 1400 °C

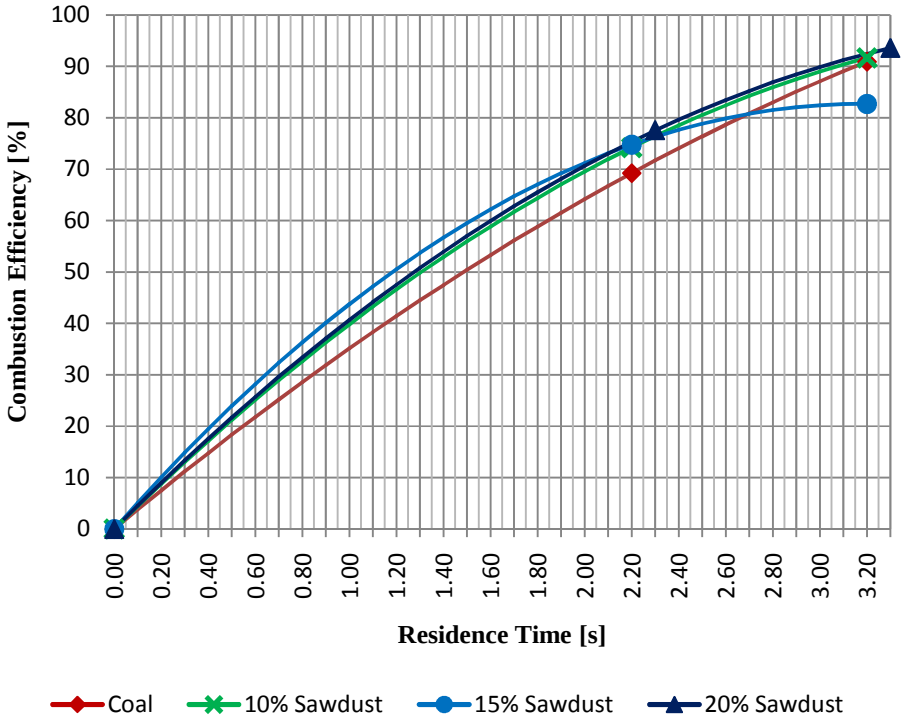

Fig. C.3 Sawdust co-firing burnout profiles from DTF at 1000 °C

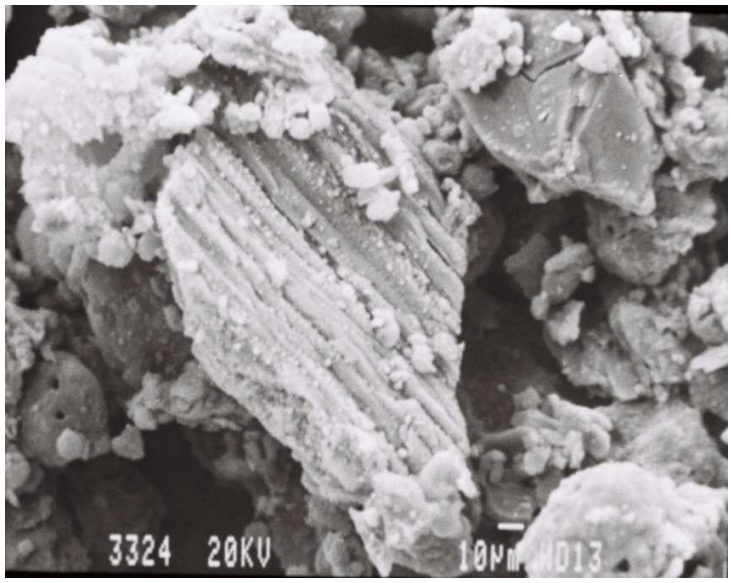

Fig. C.4 Morphologies of char particles at 1400 °C (10% grass)

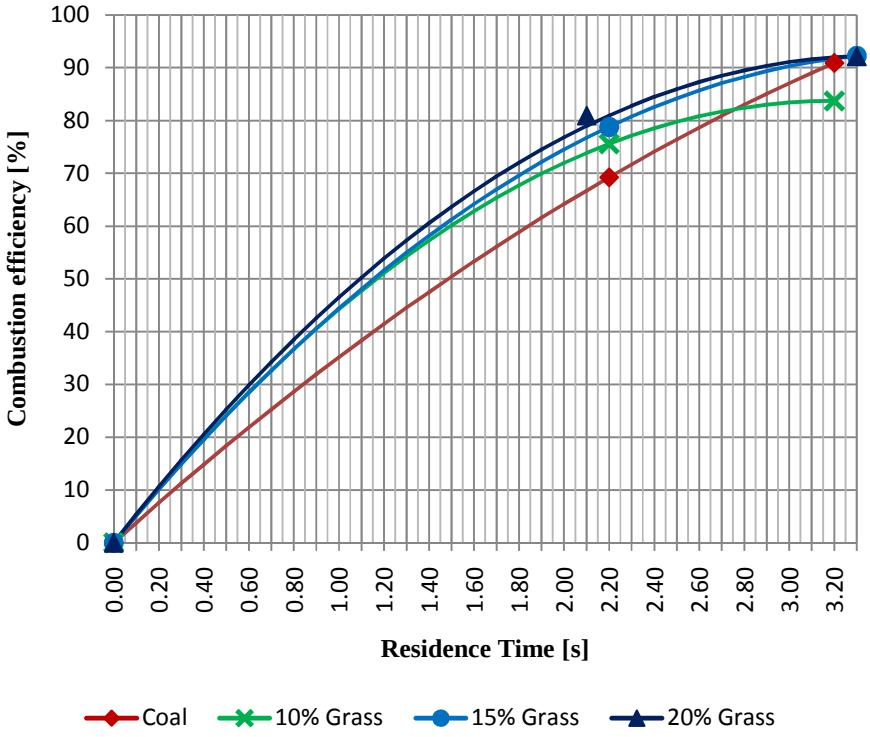

Fig. C.5 Grass co-firing burnout profiles from DTF at 1000 °C

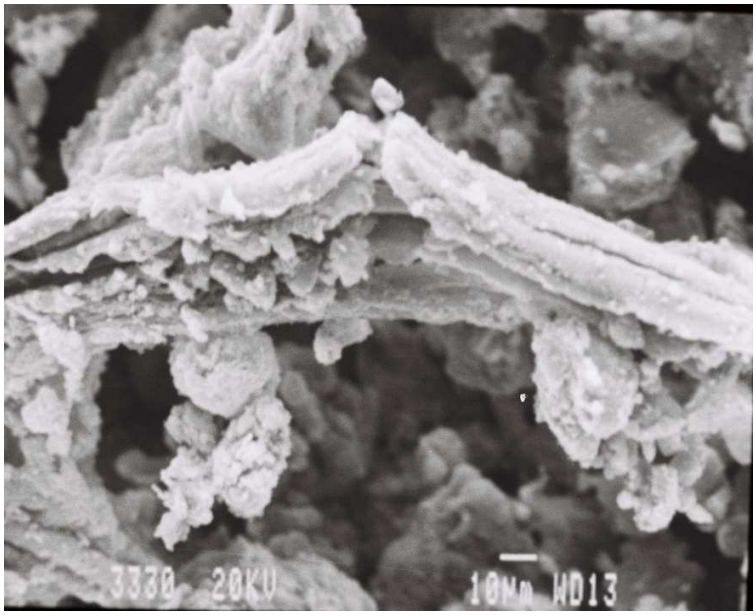

Fig. C.6 Morphologies of char particles at 1400 °C (15% grass)

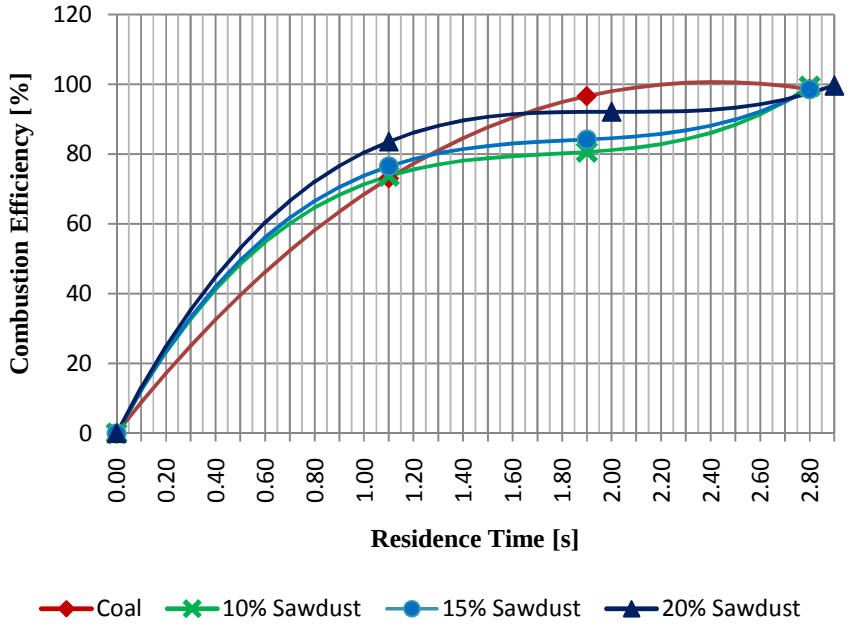

Fig. C.7 Sawdust co-firing burnout profiles from DTF at 1200 °C

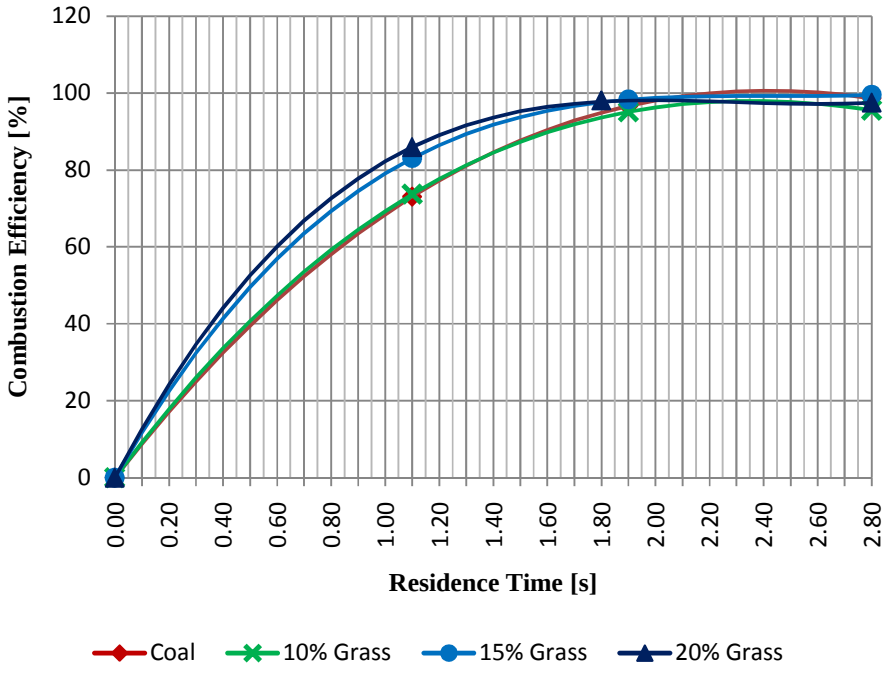

Fig. C.8 Grass co-firing burnout profiles from DTF at 1200 °C

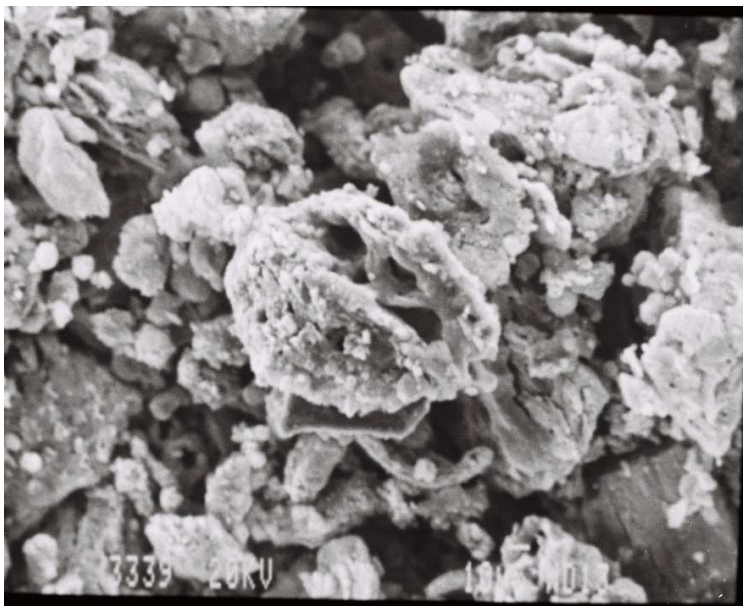

Fig. C.9 Morphologies of char particles at 1400 °C (20% grass)

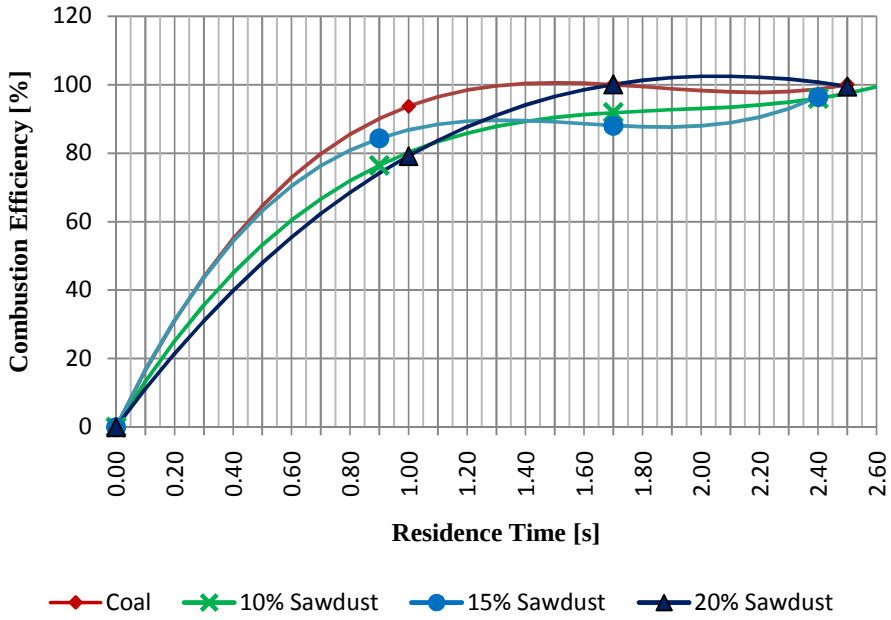

Fig. C.10 Sawdust co-firing burnout profiles from DTF at 1400 °C

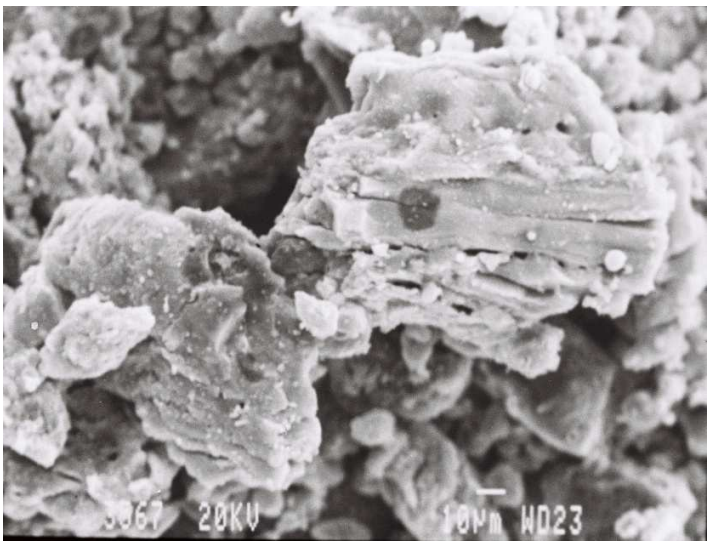

Fig. C.11 Morphologies of char particles at 1400 °C (10% sawdust)

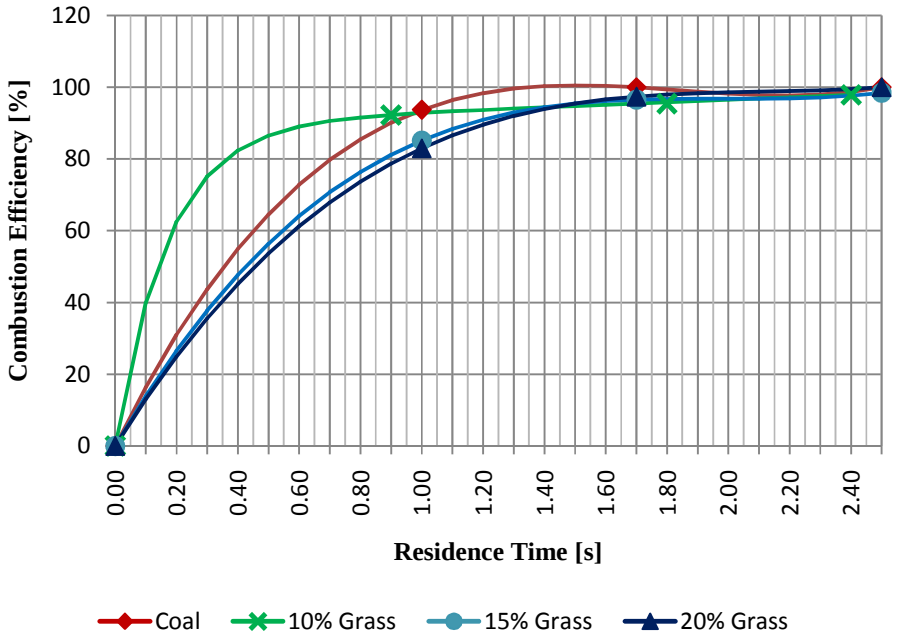

Fig. C.12 Morphologies of char particles at 1400 °C (10% sawdust)

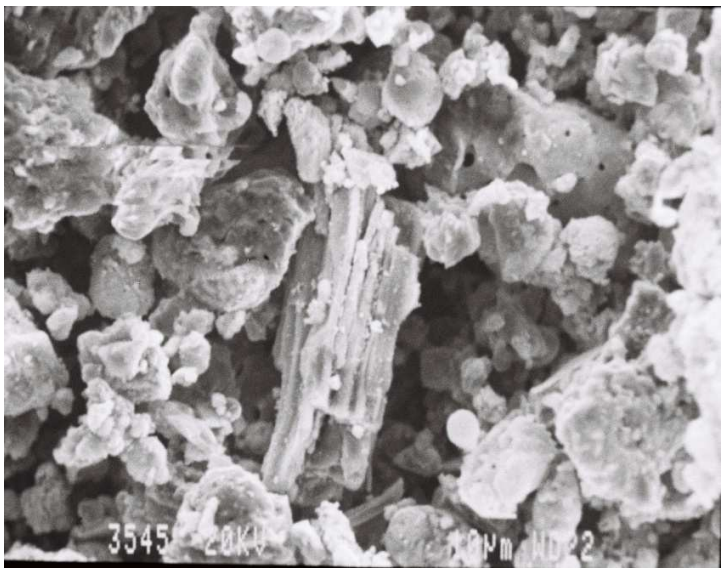

Fig. C.13 Morphologies of char particles at 1400 °C (15% sawdust)

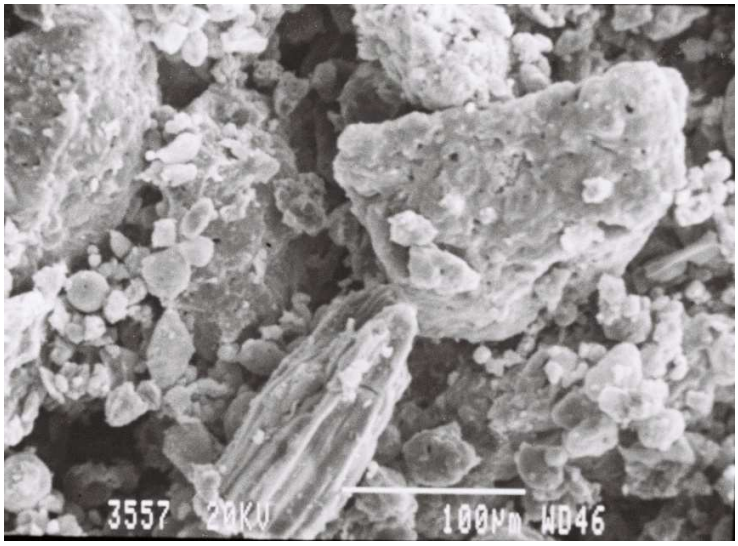

Fig. C.14 Morphologies of char particles at 1400 °C (20% sawdust)

Appendix D Psctf Experiments Combustion Efficiencies and Temperature Profiles

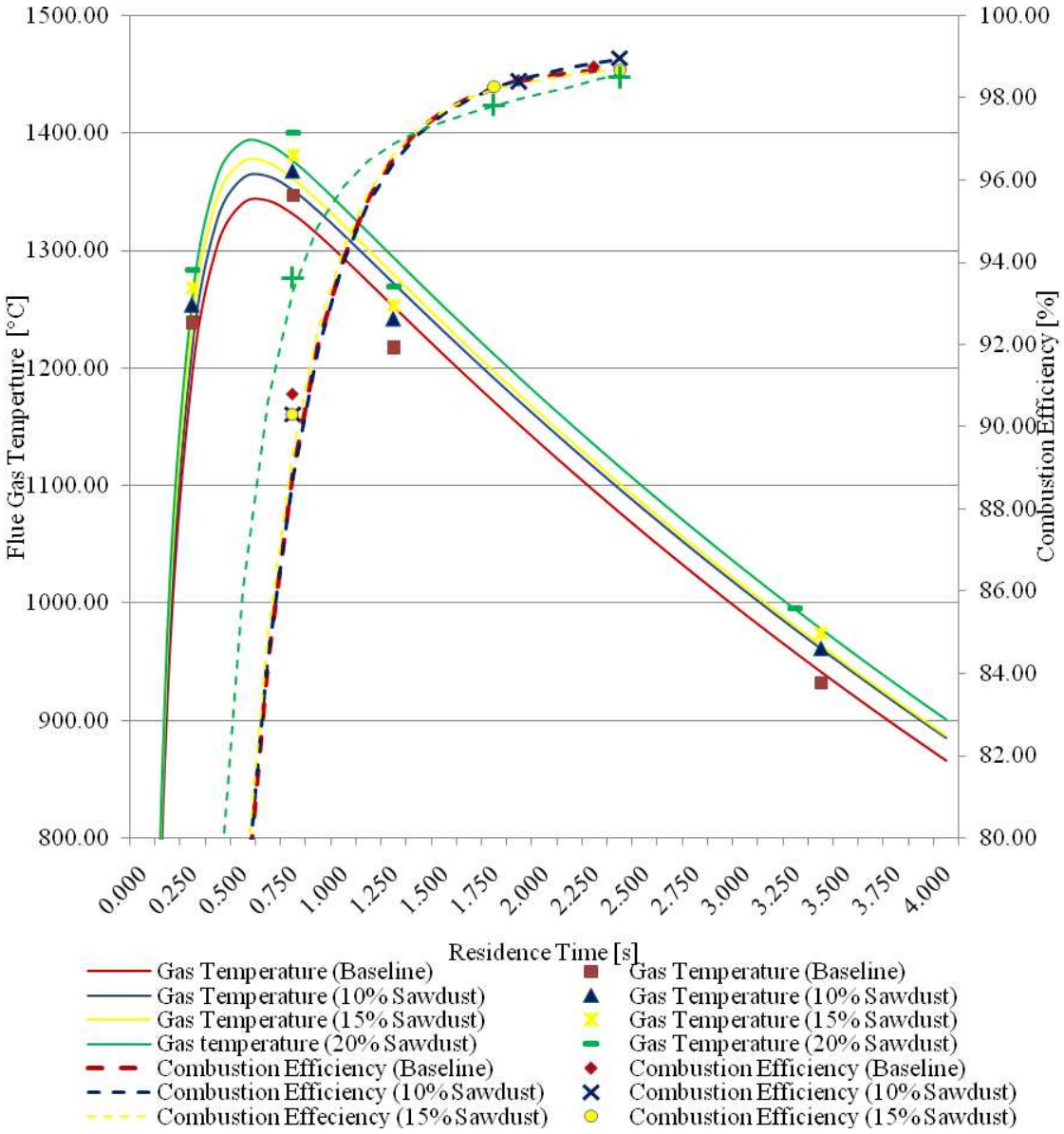

Fig. D.1 Effect of sawdust on flue-gas temperature profiles and combustion efficiency

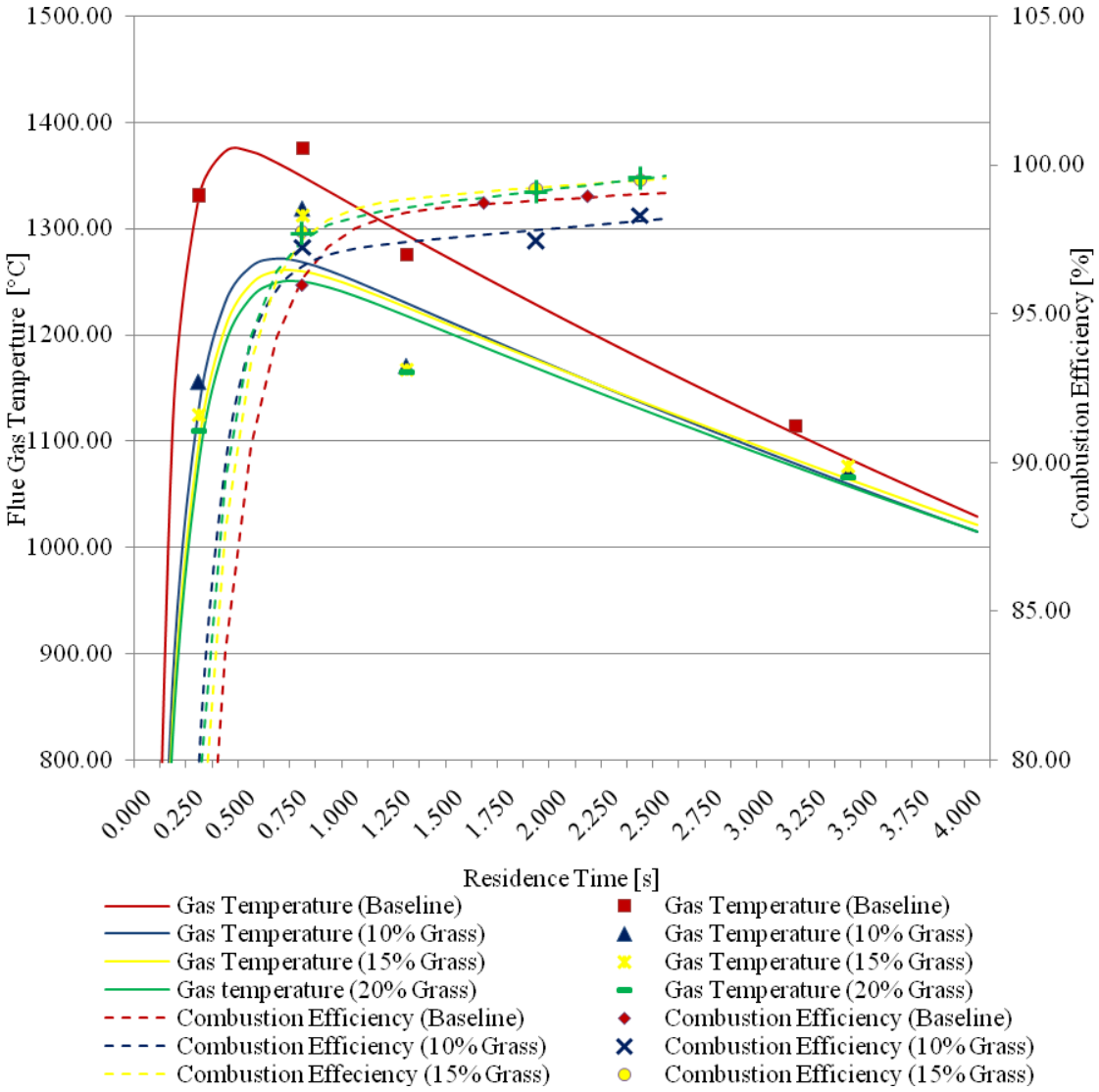

Fig. D.2 Effect of grass on flue-gas temperature profiles and combustion efficiency

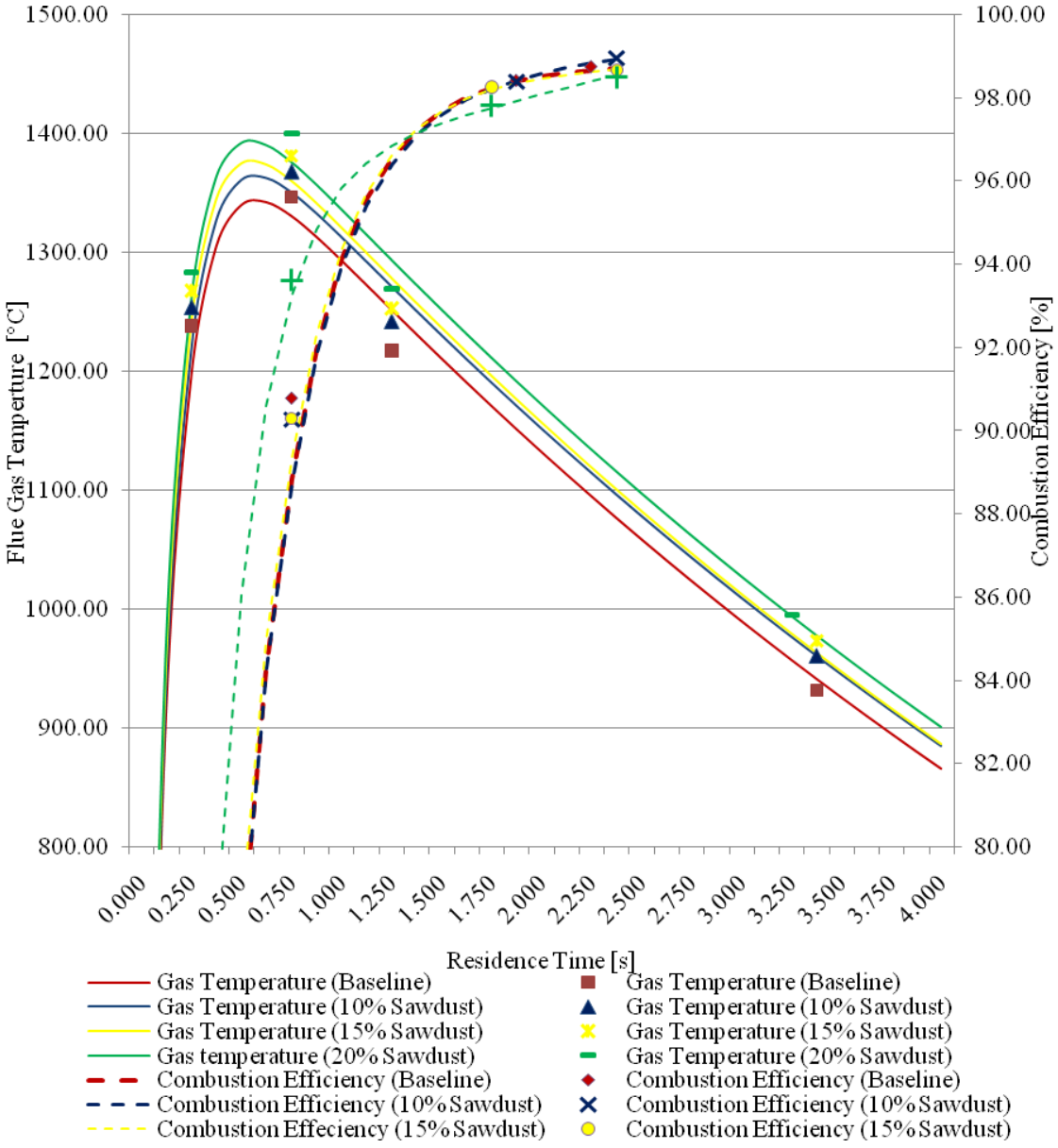

Fig. D.3 Effect of sawdust on flue-gas temperature profiles and combustion efficiency

Appendix E Calculation Of The Potassium, Sulfur And Chlorine Splits Through Different Species During Devolatilisation For Potassium Sulfate Formation Modelling

Fvol + Fchar = 1

$$\frac{P_{Xv}}{P_{Xc}} = X_{split}$$

(Fvol x PXv) + (Fchar x PSc) = TXfuel

$$P_{Xc} = \frac{TX_{fuel}}{F_{vol} \times X_{split} + F_{char}}$$

	TS_{fuel}	F_{char}	F_{vol}	S_{split}	P_{Sc}	P_{Sv}	$P_{H2S,c}$	$P_{SO2,c}$	$P_{H2S,v}$	$P_{SO2,v}$	Cl	K
Sawdust	0.00044	0.2051	0.7949	0.7	0.00058	0.0004	0.00061	0.00115	0.00043	0.00081	0.0031	0.0004
Grass	0.00098	0.2269	0.7731	0.74	0.00123	0.0009	0.00130	0.00245	0.00096	0.00181	0.0049	0.0045
Coal A	0.02642	0.7964	0.2936	0.42	0.03184	0.0134	0.03384	0.01421	0.03597	0.01511		
Coal B	0.01321	0.7064	0.2936	0.48	0.01559	0.0075	0.01657	0.03115	0.00795	0.01495	0.0022	0.0013

Where

$P_{H2S,c,v} = P_{Sc,v} \times MW_{H2S} / MW_{H2S}$

$P_{SO2,c,v} = P_{Sc,v} \times MW_{SO2} / MW_{SO2}$

MW: Molecular weight

$P_{Sc,v}$: percentage by mass of sulfur in char or volatile

$P_{H2S,c,v}$: percentage by mass of H_2S in char or volatile

$P_{SO2,c,v}$: percentage by mass of SO_2 in char or volatile

S_{split} : split of sulfur between volatiles and char

F_{vol} mass fraction of volatiles in fuel (d.a.f)

F_{char} mass fraction of char in fuel (d.a.f)

TS_{fuel}: percentage by mass of sulfur in fuel (d.a.f)

Appendix F Radiant Section Residence Time Calculation And Velocity Magnitude Of The Flue Gas

Test	**Test 11 100% Coal**
Date	26-Sep-07
Test Duration	07:39 to 08:05
Test Description	Combustion Performance
Operator	Priven Rajoo

Residence Time Calculation	SI Units	
Area		
Primary Air Area with sleeve	m^2	0.0048
Secondary Air Area	m^2	0.0090
Tertiary Air Area	m^2	0.0075
Density		
Barometric Pressure	kPa	84.4
Primary Air Temp	℃	93
Pressure in Primary Air Pipe	kPa	
Density of Primary Air	kg/m^3	0.963
Secondary Air Temp	℃	301
Pressure in Secondary Air Pipe	kPa	
Density of Secondary Air	kg/m^3	0.614
Tertiary Air Temp	℃	295.00
Pressure in Tertiary Air Pipe	kPa	
Density of Tertiary Air	kg/m^3	0.621

Mass Flows	SI Units		
Total Air (Required)	kg/hr	1610	246
Primary Air Flow	kg/hr	428	
Secondary Air Flow	kg/hr	1182	
Tertiary Air Flow	kg/hr		

Velocities at Burner Face	SI Units	
Primary Air Velocity	m/s	25.5
Secondary Air Velocity	m/s	59.3
Tertiary Air Velocity	m/s	0.0
SAV/PAV Ratio should be between 2 to 3		2.32
TAV/PAV		0.0

Furnace	SI Units	Average	Convective
Furnace Temperature	℃	1273	880
Area	m^2	1.4641	0.908
Density	kg/m^3	0.194	0.260
Massflow	kg/s	0.447	0.447
Velocity	m/s	1.576	**1.896**
Radiant Length	m	7.25	7.920
Distance sample point port 4	m	0.40	
Time	s	0.254	
Distance sample point port 9	m	1.15	
Time	s	0.729	
Distance sample point port D	m	1.80	
Time	s	1.142	
Distance sample point port 15	m	2.65	
Time	s	1.681	
Distance sample point port 21	m	3.45	
Time	s	2.188	
Distance sample point port 27	m	4.90	
Time	s	3.108	

Test	**Test 13 10%Sawdust 90%Coal**
Date	26-Sep-07
Test Duration	10:48 to 11:16
Test Description	Combustion Performance
Operator	Priven Rajoo

Residence Time Calculation	SI Units	
Area		
Primary Air Area with sleeve	m^2	0.0048
Secondary Air Area	m^2	0.0090
Tertiary Air Area	m^2	0.0075
Density	SI Units	
Barometric Pressure	kPa	84.4
Primary Air Temp	℃	94
Pressure in Primary Air Pipe	kPa	
Density of Primary Air	kg/m^3	0.962
Secondary Air Temp	℃	301
Pressure in Secondary Air Pipe	kPa	
Density of Secondary Air	kg/m^3	0.615
Tertiary Air Temp	℃	295.00
Pressure in Tertiary Air Pipe	kPa	
Density of Tertiary Air	kg/m^3	0.621

Mass Flows	SI Units		
Total Air (Required)	kg/hr	1601	246
Primary Air Flow	kg/hr	427	
Secondary Air Flow	kg/hr	1175	
Tertiary Air Flow	kg/hr		

Velocities at Burner Face	SI Units	
Primary Air Velocity	m/s	25.5
Secondary Air Velocity	m/s	58.9
Tertiary Air Velocity	m/s	0.0
SAV/PAV Ratio should be between 2 to 3		2.31
TAV/PAV		0.0

Furnace	SI Units	Average	Convective
Furnace Temperature	℃	1233	880
Area	m^2	1.4641	0.908
Density	kg/m^3	0.199	0.260
Massflow	kg/s	0.445	0.445
Velocity	m/s	1.527	**1.886**
Radiant Length	m	7.25	7.920
Distance sample point port 4	m	0.40	
Time	s	0.262	
Distance sample point port 9	m	1.15	
Time	s	0.753	
Distance sample point port D	m	1.80	
Time	s	1.179	
Distance sample point port 15	m	2.65	
Time	s	1.736	
Distance sample point port 21	m	3.45	
Time	s	2.260	
Distance sample point port 27	m	4.90	
Time	s	3.209	

Test	**Test 14 15%Sawdust 85%Coal**
Date	26-Sep-07
Test Duration	11:34 to 12:02
Test Description	Combustion Performance
Operator	Priven Rajoo

Residence Time Calculation	SI Units	
Area		
Primary Air Area with sleeve	m^2	0.0048
Secondary Air Area	m^2	0.0090
Tertiary Air Area	m^2	0.0075

Density	SI Units	
Barometric Pressure	kPa	84.4
Primary Air Temp	℃	94
Pressure in Primary Air Pipe	kPa	
Density of Primary Air	kg/m^3	0.961
Secondary Air Temp	℃	297
Pressure in Secondary Air Pipe	kPa	
Density of Secondary Air	kg/m^3	0.619
Tertiary Air Temp	℃	295.00
Pressure in Tertiary Air Pipe	kPa	
Density of Tertiary Air	kg/m^3	0.621

Mass Flows	SI Units		
Total Air (Required)	kg/hr	1582	244
Primary Air Flow	kg/hr	415	
Secondary Air Flow	kg/hr	1167	
Tertiary Air Flow	kg/hr		

Velocities at Burner Face	SI Units	
Primary Air Velocity	m/s	24.8
Secondary Air Velocity	m/s	58.1
Tertiary Air Velocity	m/s	0.0
SAV/PAV Ratio should be between 2 to 3		2.34
TAV/PAV		0.0

Furnace	SI Units	Average	Convective
Furnace Temperature	℃	1261	880
Area	m^2	1.4641	0.908
Density	kg/m^3	0.195	0.260
Massflow	kg/s	0.439	0.439
Velocity	m/s	1.537	1.863
Radiant Length	m	7.25	7.920
Distance sample point port 4	m	0.40	
Time	s	0.260	
Distance sample point port 9	m	1.15	

Time	s	0.748	
Distance sample point port D	m	1.80	
Time	s	1.171	
Distance sample point port 15	m	2.65	
Time	s	1.725	
Distance sample point port 21	m	3.45	
Time	s	2.245	
Distance sample point port 27	m	4.90	
Time	s	3.189	

Test	**Test 15 20%Sawdust 80%Coal**
Date	26-Sep-07
Test Duration	12:48 to 13:14
Test Description	Combustion Performance
Operator	Priven Rajoo

Residence Time Calculation	SI Units	
Area		
Primary Air Area with sleeve	m^2	0.0048
Secondary Air Area	m^2	0.0090
Tertiary Air Area	m^2	0.0075
Density	SI Units	
Barometric Pressure	kPa	84.4
Primary Air Temp	℃	94
Pressure in Primary Air Pipe	kPa	
Density of Primary Air	kg/m^3	0.962
Secondary Air Temp	℃	303
Pressure in Secondary Air Pipe	kPa	
Density of Secondary Air	kg/m^3	0.613
Tertiary Air Temp	℃	295.00
Pressure in Tertiary Air Pipe	kPa	
Density of Tertiary Air	kg/m^3	0.621

Mass Flows	SI Units		
Total Air (Required)	kg/hr	1588	248
Primary Air Flow	kg/hr	421	
Secondary Air Flow	kg/hr	1168	
Tertiary Air Flow	kg/hr		

Velocities at Burner Face	SI Units		
Primary Air Velocity	m/s	25.1	
Secondary Air Velocity	m/s	58.7	
Tertiary Air Velocity	m/s	0.0	
SAV/PAV Ratio should be between 2 to 3		2.34	
TAV/PAV		0.0	

Furnace	SI Units	Average	Convective
Furnace Temperature	℃	1236	880
Area	m^2	1.4641	0.908
Density	kg/m^3	0.199	0.260
Massflow	kg/s	0.441	0.441
Velocity	m/s	1.518	**1.871**
Radiant Length	m	7.25	7.920
Distance sample point port 4	m	0.40	
Time	s	0.264	
Distance sample point port 9	m	1.15	
Time	s	0.758	
Distance sample point port D	m	1.80	
Time	s	1.186	
Distance sample point port 15	m	2.65	
Time	s	1.746	
Distance sample point port 21	m	3.45	
Time	s	2.273	
Distance sample point port 27	m	4.90	
Time	s	3.228	

Test	**Test 16 10%Grass 90%Coal**
Date	26-Sep-07
Test Duration	14:21 to 14:44
Test Description	Combustion Performance
Operator	Priven Rajoo

Residence Time Calculation	SI Units	
Area		
Primary Air Area with sleeve	m^2	0.0048
Secondary Air Area	m^2	0.0090
Tertiary Air Area	m^2	0.0075

Density	SI Units	
Barometric Pressure	kPa	84.4
Primary Air Temp	℃	94
Pressure in Primary Air Pipe	kPa	
Density of Primary Air	kg/m^3	0.963
Secondary Air Temp	℃	299
Pressure in Secondary Air Pipe	kPa	
Density of Secondary Air	kg/m^3	0.617
Tertiary Air Temp	℃	295.00
Pressure in Tertiary Air Pipe	kPa	
Density of Tertiary Air	kg/m^3	0.621

Mass Flows	SI Units	
Total Air (Required)	kg/hr	1580
Primary Air Flow	kg/hr	410
Secondary Air Flow	kg/hr	1170
Tertiary Air Flow	kg/hr	

Velocities at Burner Face	SI Units	
Primary Air Velocity	m/s	24.5
Secondary Air Velocity	m/s	58.4
Tertiary Air Velocity	m/s	0.0
SAV/PAV Ratio should be between 2 to 3		2.39
TAV/PAV		0.0

Furnace	SI Units	Average	Convective
Furnace Temperature	℃	1180	880
Area	m^2	1.4641	0.908
Density	kg/m^3	0.206	0.260
Massflow	kg/s	0.439	0.439
Velocity	m/s	1.454	**1.861**
Radiant Length	m	7.25	7.920
Distance sample point port 4	m	0.40	
Time	s	0.275	
Distance sample point port 9	m	1.15	
Time	s	0.791	
Distance sample point port D	m	1.80	
Time	s	1.238	
Distance sample point port 15	m	2.65	
Time	s	1.823	
Distance sample point port 21	m	3.45	
Time	s	2.373	
Distance sample point port 27	m	4.90	
Time	s	3.371	

Test	**Test 17 15%Grass 85%Coal**
Date	26-Sep-07
Test Duration	15:16 to 15:43
Test Description	Combustion Performance
Operator	Priven Rajoo

Residence Time Calculation	SI Units	
Area		
Primary Air Area with sleeve	m^2	0.0048
Secondary Air Area	m^2	0.0090
Tertiary Air Area	m^2	0.0075

Density	SI Units	
Barometric Pressure	kPa	84.4
Primary Air Temp	℃	93
Pressure in Primary Air Pipe	kPa	
Density of Primary Air	kg/m^3	0.963
Secondary Air Temp	℃	304
Pressure in Secondary Air Pipe	kPa	
Density of Secondary Air	kg/m^3	0.611
Tertiary Air Temp	℃	295.00
Pressure in Tertiary Air Pipe	kPa	
Density of Tertiary Air	kg/m^3	0.621

Mass Flows	SI Units		
Total Air (Required)	kg/hr	1590	249
Primary Air Flow	kg/hr	419	
Secondary Air Flow	kg/hr	1171	
Tertiary Air Flow	kg/hr		

Velocities at Burner Face	SI Units	
Primary Air Velocity	m/s	25.0
Secondary Air Velocity	m/s	59.0
Tertiary Air Velocity	m/s	0.0
SAV/PAV Ratio should be between 2 to 3		2.36
TAV/PAV		0.0

Furnace	SI Units	Average	Convective
Furnace Temperature	℃	1170	880
Area	m^2	1.4641	0.908
Density	kg/m^3	0.208	0.260
Massflow	kg/s	0.442	0.442
Velocity	m/s	1.453	**1.873**
Radiant Length	m	7.25	7.920
Distance sample point port 4	m	0.40	
Time	s	0.275	

Distance sample point port 9	m	1.15	
Time	s	0.792	
Distance sample point port D	m	1.80	
Time	s	1.239	
Distance sample point port 15	m	2.65	
Time	s	1.824	
Distance sample point port 21	m	3.45	
Time	s	2.375	
Distance sample point port 27	m	4.90	
Time	s	3.373	

Test	**Test 18 20%Grass 80%Coal**
Date	26-Sep-07
Test Duration	16:05 to 16:32
Test Description	Combustion Performance
Operator	Priven Rajoo

Residence Time Calculation	SI Units	
Area		
Primary Air Area with sleeve	m^2	0.0048
Secondary Air Area	m^2	0.0090
Tertiary Air Area	m^2	0.0075

Density	SI Units	
Barometric Pressure	kPa	84.4
Primary Air Temp	℃	94
Pressure in Primary Air Pipe	kPa	
Density of Primary Air	kg/m^3	0.961
Secondary Air Temp	℃	300
Pressure in Secondary Air Pipe	kPa	
Density of Secondary Air	kg/m^3	0.616
Tertiary Air Temp	℃	295.00
Pressure in Tertiary Air Pipe	kPa	
Density of Tertiary Air	kg/m^3	0.621

Mass Flows	SI Units		
Total Air (Required)	kg/hr	1586	246
Primary Air Flow	kg/hr	416	
Secondary Air Flow	kg/hr	1170	
Tertiary Air Flow	kg/hr		

Velocities at Burner Face	SI Units	
Primary Air Velocity	m/s	24.8
Secondary Air Velocity	m/s	58.5
Tertiary Air Velocity	m/s	0.0
SAV/PAV Ratio should be between 2 to 3		2.36
TAV/PAV		0.0

Furnace	SI Units	Average	Convective
Furnace Temperature	℃	1160	880
Area	m^2	1.4641	0.908
Density	kg/m^3	0.209	0.260
Massflow	kg/s	0.440	0.440
Velocity	m/s	1.438	**1.868**
Radiant Length	m	7.25	7.920
Distance sample point port 4	m	0.40	
Time	s	0.278	
Distance sample point port 9	m	1.15	
Time	s	0.799	
Distance sample point port D	m	1.80	
Time	s	1.251	
Distance sample point port 15	m	2.65	
Time	s	1.842	
Distance sample point port 21	m	3.45	
Time	s	2.398	
Distance sample point port 27	m	4.90	
Time	s	3.407	

Test	**Test 100%Coal B (Repeat)**
Date	8-Aug-08
Test Duration	13:19 to 13:51
Test Description	Combustion Performance
Operator	Bonny Nyangwa

Residence Time Calculation	SI Units	
Area		
Primary Air Area with sleeve	m^2	0.0048
Secondary Air Area	m^2	0.0090
Tertiary Air Area	m^2	0.0075

Density	SI Units	
Barometric Pressure	kPa	84.4
Primary Air Temp	℃	93
Pressure in Primary Air Pipe	kPa	
Density of Primary Air	kg/m^3	0.964
Secondary Air Temp	℃	301
Pressure in Secondary Air Pipe	kPa	
Density of Secondary Air	kg/m^3	0.615
Tertiary Air Temp	℃	295.00
Pressure in Tertiary Air Pipe	kPa	
Density of Tertiary Air	kg/m^3	0.621

Mass Flows	SI Units	
Total Air (Required)	kg/hr	1517
Primary Air Flow	kg/hr	397
Secondary Air Flow	kg/hr	1120
Tertiary Air Flow	kg/hr	

Velocities at Burner Face	SI Units	
Primary Air Velocity	m/s	23.6
Secondary Air Velocity	m/s	56.1
Tertiary Air Velocity	m/s	0.0
SAV/PAV Ratio should be between 2 to 3		2.38
TAV/PAV		0.0

Furnace	SI Units	Average	Convective
Furnace Temperature	℃	1183	880
Area	m^2	1.4641	0.908
Density	kg/m^3	0.206	0.260
Massflow	kg/s	0.421	0.421
Velocity	m/s	1.399	**1.786**
Radiant Length	m	7.25	7.920
Distance sample point port 4	m	0.40	
Time	s	0.286	
Distance sample point port 9	m	1.15	
Time	s	0.822	
Distance sample point port D	m	1.80	
Time	s	1.287	
Distance sample point port 15	m	2.65	
Time	s	1.895	
Distance sample point port 21	m	3.45	
Time	s	2.467	
Distance sample point port 27	m	4.90	
Time	s	3.504	

Test	**Test 2 10%Sawdust 90%Coal B (Repeat)**
Date	8-Aug-08
Test Duration	14:14 to 14:34
Test Description	Combustion Performance
Operator	Bonny Nyangwa

Residence Time Calculation	SI Units	
Area		
Primary Air Area with sleeve	m^2	0.0048
Secondary Air Area	m^2	0.0090
Tertiary Air Area	m^2	0.0075

Density	SI Units	
Barometric Pressure	kPa	84.4
Primary Air Temp	℃	93
Pressure in Primary Air Pipe	kPa	
Density of Primary Air	kg/m^3	0.964
Secondary Air Temp	℃	301
Pressure in Secondary Air Pipe	kPa	
Density of Secondary Air	kg/m^3	0.615
Tertiary Air Temp	℃	295.00
Pressure in Tertiary Air Pipe	kPa	
Density of Tertiary Air	kg/m^3	0.621

Mass Flows	SI Units	
Total Air (Required)	kg/hr	1527
Primary Air Flow	kg/hr	404
Secondary Air Flow	kg/hr	1123
Tertiary Air Flow	kg/hr	

Velocities at Burner Face	SI Units	
Primary Air Velocity	m/s	24.1
Secondary Air Velocity	m/s	56.2
Tertiary Air Velocity	m/s	0.0
SAV/PAV Ratio should be between 2 to 3		2.34
TAV/PAV		0.0

Furnace	SI Units	Average	Convective
Furnace Temperature	℃	1206	880
Area	m^2	1.4641	0.908
Density	kg/m^3	0.203	0.260
Massflow	kg/s	0.424	0.424
Velocity	m/s	1.430	**1.798**
Radiant Length	m	7.25	7.920
Distance sample point port 4	m	0.40	
Time	s	0.280	

Distance sample point port 9	m	1.15	
Time	s	0.804	
Distance sample point port D	m	1.80	
Time	s	1.259	
Distance sample point port 15	m	2.65	
Time	s	1.853	
Distance sample point port 21	m	3.45	
Time	s	2.412	
Distance sample point port 27	m	4.90	
Time	s	3.426	

Test	**Test 3 15%Sawdust 85%Coal B (Repeat)**
Date	8-Aug-08
Test Duration	14:52 to 15:12
Test Description	Combustion Performance
Operator	Bonny Nyangwa

Residence Time Calculation		
Area		
Primary Air Area with sleeve	m^2	0.0048
Secondary Air Area	m^2	0.0090
Tertiary Air Area	m^2	0.0075

Density		
Barometric Pressure	kPa	84.4
Primary Air Temp	℃	93
Pressure in Primary Air Pipe	kPa	
Density of Primary Air	kg/m^3	0.965
Secondary Air Temp	℃	304
Pressure in Secondary Air Pipe	kPa	
Density of Secondary Air	kg/m^3	0.612
Tertiary Air Temp	℃	295.00
Pressure in Tertiary Air Pipe	kPa	
Density of Tertiary Air	kg/m^3	0.621

Mass Flows		
Total Air (Required)	kg/hr	1550
Primary Air Flow	kg/hr	429
Secondary Air Flow	kg/hr	1121
Tertiary Air Flow	kg/hr	

Velocities at Burner Face		
Primary Air Velocity	m/s	25.5
Secondary Air Velocity	m/s	56.5
Tertiary Air Velocity	m/s	0.0
SAV/PAV Ratio should be between 2 to 3		2.21
TAV/PAV		0.0

Furnace		Average	Convective
Furnace Temperature	℃	1219	880
Area	m^2	1.4641	0.908
Density	kg/m^3	0.201	0.260
Massflow	kg/s	0.431	0.431
Velocity	m/s	1.464	**1.826**
Radiant Length	m	7.25	7.920
Distance sample point port 4	m	0.40	
Time	s	0.273	
Distance sample point port 9	m	1.15	
Time	s	0.785	
Distance sample point port D	m	1.80	
Time	s	1.229	
Distance sample point port 15	m	2.65	
Time	s	1.810	
Distance sample point port 21	m	3.45	
Time	s	2.356	
Distance sample point port 27	m	4.90	
Time	s	3.346	

Test	**Test 4 20%Sawdust 80%Coal B (Repeat)**
Date	8-Aug-08
Test Duration	15:29 to 15:49
Test Description	Combustion Performance
Operator	Bonny Nyangwa

Residence Time Calculation		
Area		
Primary Air Area with sleeve	m^2	0.0048
Secondary Air Area	m^2	0.0090
Tertiary Air Area	m^2	0.0075

Density		
Barometric Pressure	kPa	84.4
Primary Air Temp	℃	93
Pressure in Primary Air Pipe	kPa	
Density of Primary Air	kg/m^3	0.965
Secondary Air Temp	℃	301
Pressure in Secondary Air Pipe	kPa	
Density of Secondary Air	kg/m^3	0.614
Tertiary Air Temp	℃	295.00
Pressure in Tertiary Air Pipe	kPa	
Density of Tertiary Air	kg/m^3	0.621

Mass Flows		
Total Air (Required)	kg/hr	1553
Primary Air Flow	kg/hr	433
Secondary Air Flow	kg/hr	1120
Tertiary Air Flow	kg/hr	

Velocities at Burner Face		
Primary Air Velocity	m/s	25.8
Secondary Air Velocity	m/s	56.2
Tertiary Air Velocity	m/s	0.0
SAV/PAV Ratio should be between 2 to 3		2.18
TAV/PAV		0.0

Furnace		Average	Convective
Furnace Temperature	℃	1237	880
Area	m^2	1.4641	0.908
Density	kg/m^3	0.198	0.260
Massflow	kg/s	0.431	0.431
Velocity	m/s	1.485	**1.830**
Radiant Length	m	7.25	7.920
Distance sample point port 4	m	0.40	
Time	s	0.269	
Distance sample point port 9	m	1.15	
Time	s	0.774	
Distance sample point port D	m	1.80	
Time	s	1.212	
Distance sample point port 15	m	2.65	
Time	s	1.784	
Distance sample point port 21	m	3.45	
Time	s	2.323	
Distance sample point port 27	m	4.90	
Time	s	3.300	

Appendix G Chloride Deposition Tendency Onto Fly Ash Particles

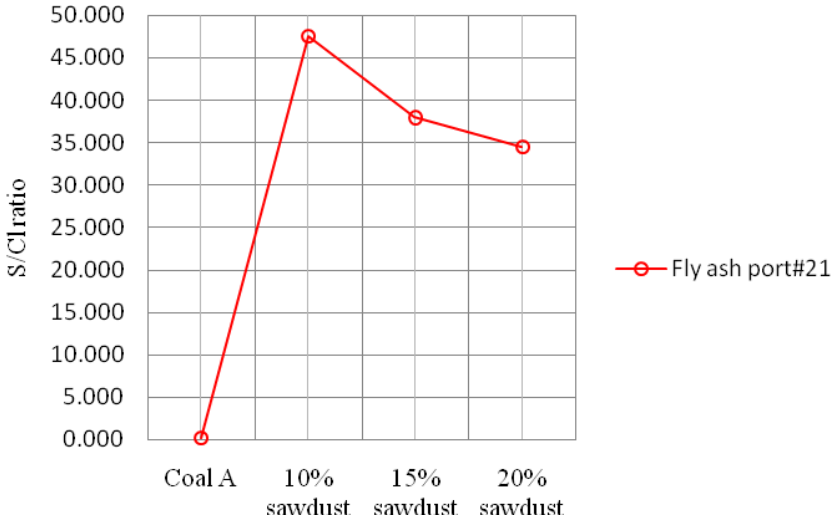

(a)

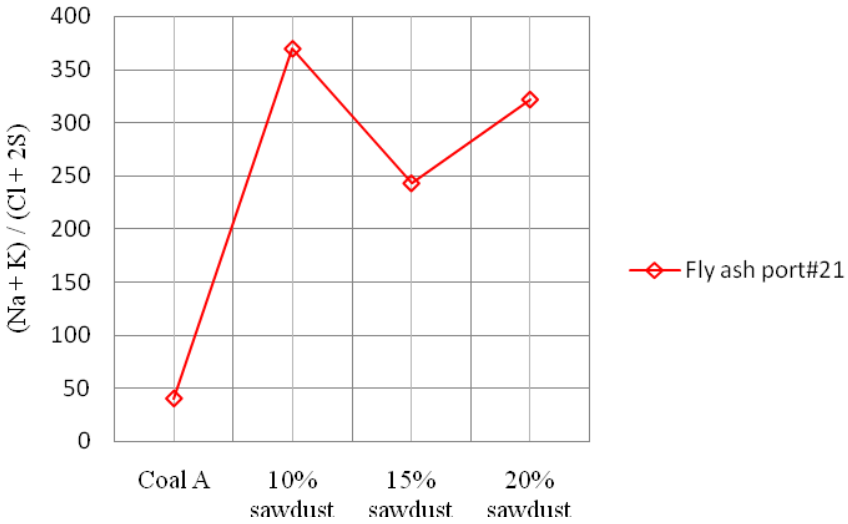

(b)

Fig. G.1 Effect of the co-combustion of sawdust with coal on: a) chlorine deposition tendency onto fly ash particles through S/Cl ratio; b) Total alkali to chlorine & sulphur ratio

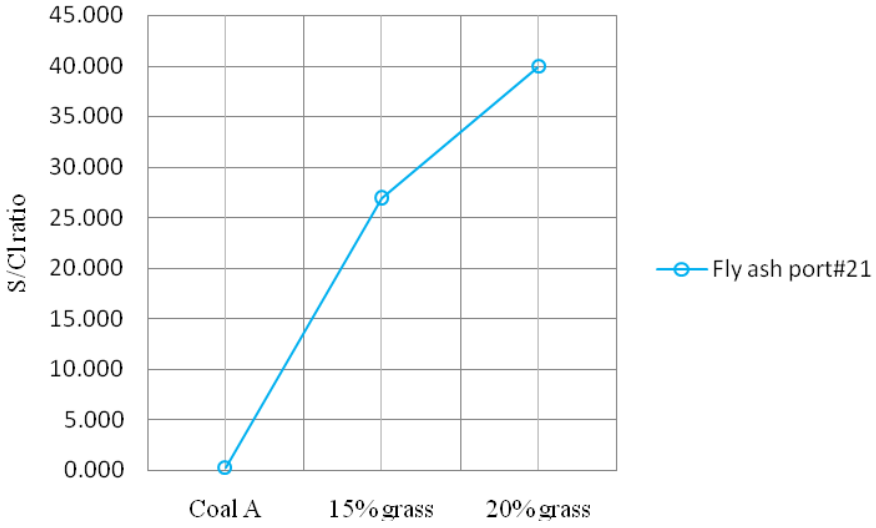

(a)

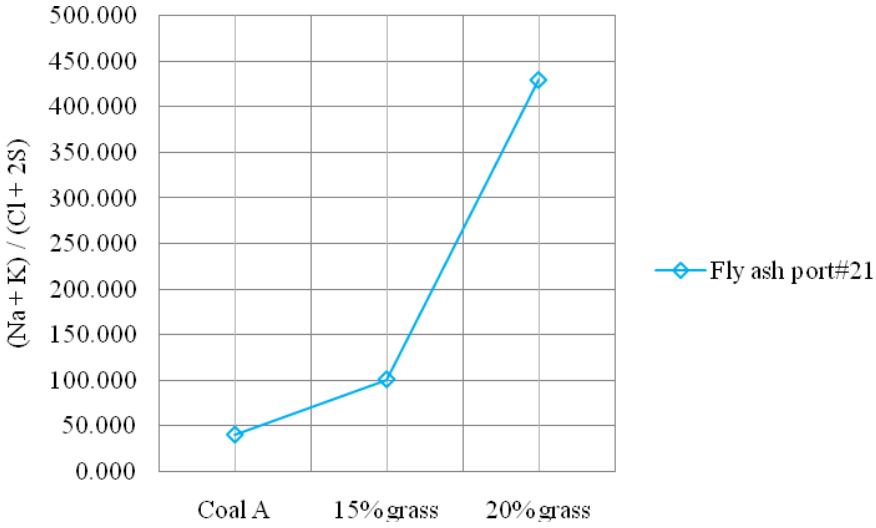

(b)

Fig. G.2 Effect of the co-combustion of grass with coal on: a) chlorine deposition tendency onto fly ash particles through S/Cl ratio; b) Total alkali to chlorine & sulphur ratio

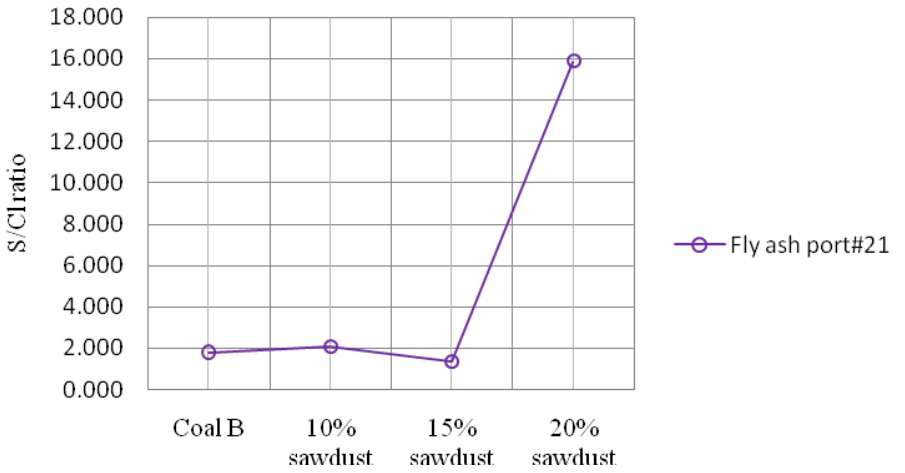

(a)

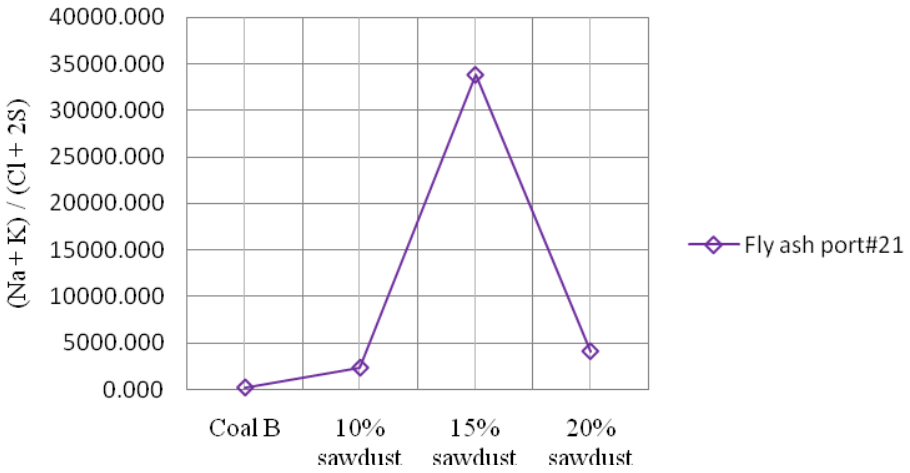

(b)

Fig. G.3 Effect of the co-combustion of sawdust with coal on: a) chlorine deposition tendency onto fly ash particles through S/Cl ratio; b) Total alkali to chlorine & sulphur ratio

Appendix H Icp And Ic Analysis On Fly Ash Samples For All The Tests Series

	Coal A	10% sawdust	15% sawdust	20% sawdust	Coal A	15% grass	20% grass	Coal B	10% sawdust	15% sawdust	20% sawdust
Na (ppm)	580	3530	2070	2520	580	840	3330	175	410	8280	270
K (ppm)	500	1720	1160	1240	500	890	1250	115	960	850	680
Sulphate (ppm)	4.658	7.025	6.558	5.756	4.658	8.401	5.264	0.452	0.232	0.099	0.111
Cl (ppm)	17.471	0.148	0.173	0.167	17.471	0.312	0.132	0.25	0.112	0.072	0.007
S/Cl	0.267	47.466	37.908	34.467	0.267	26.926	39.879	1.808	2.071	1.375	15.857
(Na + K) / (Cl + 2S)	40.318	369.770	243.058	321.945	40.318	101.087	429.644	251.300	2378.472	33814.815	4148.472

Appendix I Co-Firing Coal And Biomass – Clinkers

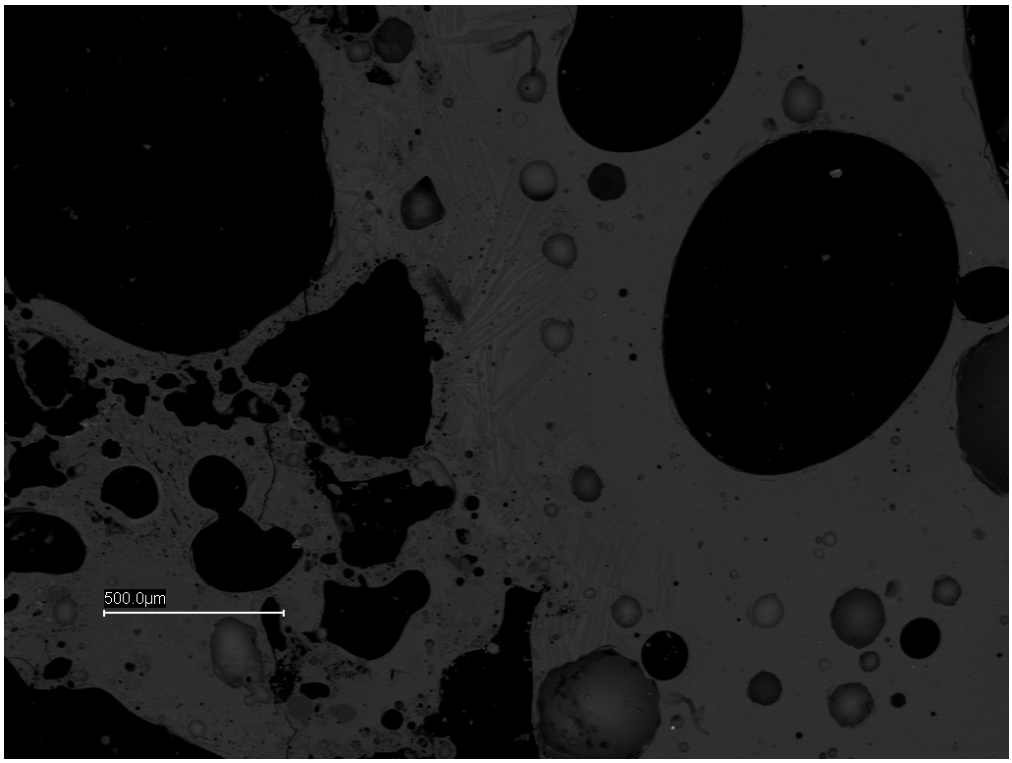

Figure I.1: Backscatter electron micrograph – T14 clinker deposit. Note the dark anorthite laths in the predominately glass matrix (light grey). Scale bar represents 500 µm.

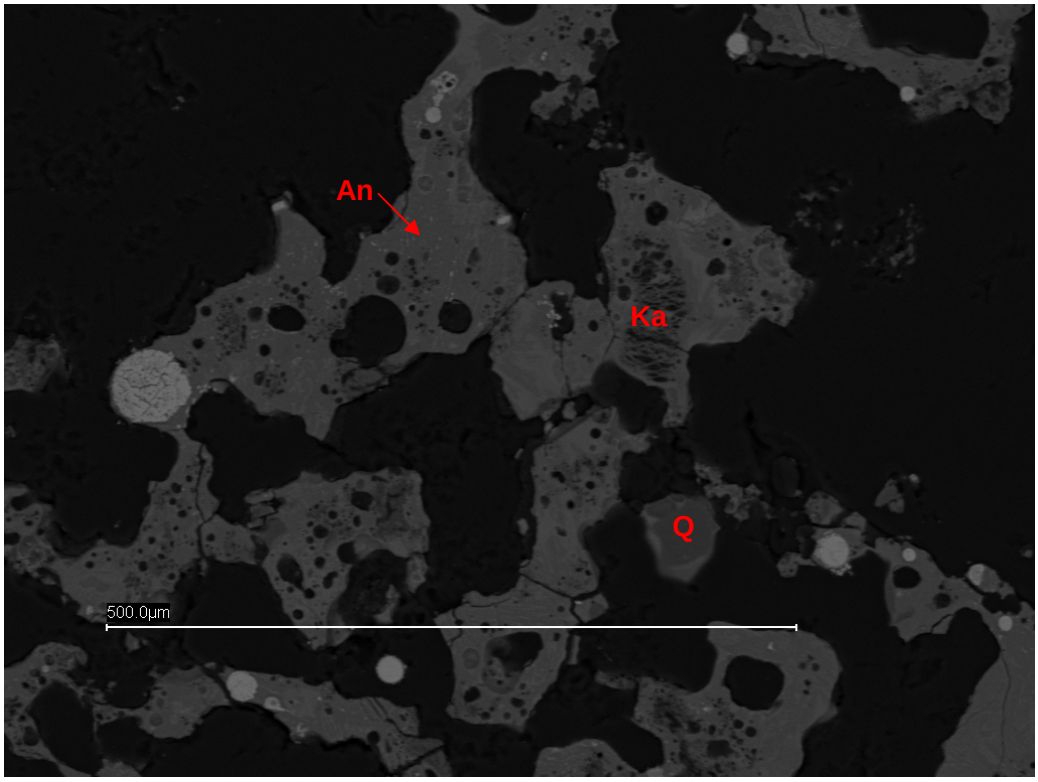

Figure I.2: Backscatter electron micrograph of T18 clinker deposit. Note the spherical Fe-oxide grains (light grey), angular quartz (Q), aluminosilicate (Ka) and anorthite laths in light grey “glass”. Scale bar is 500 µm. The dark background is epoxy resin.

Appendix J Additional Sem-Eds Spectra Of Fly Ash Samples Port 21 For The Different Tests Series

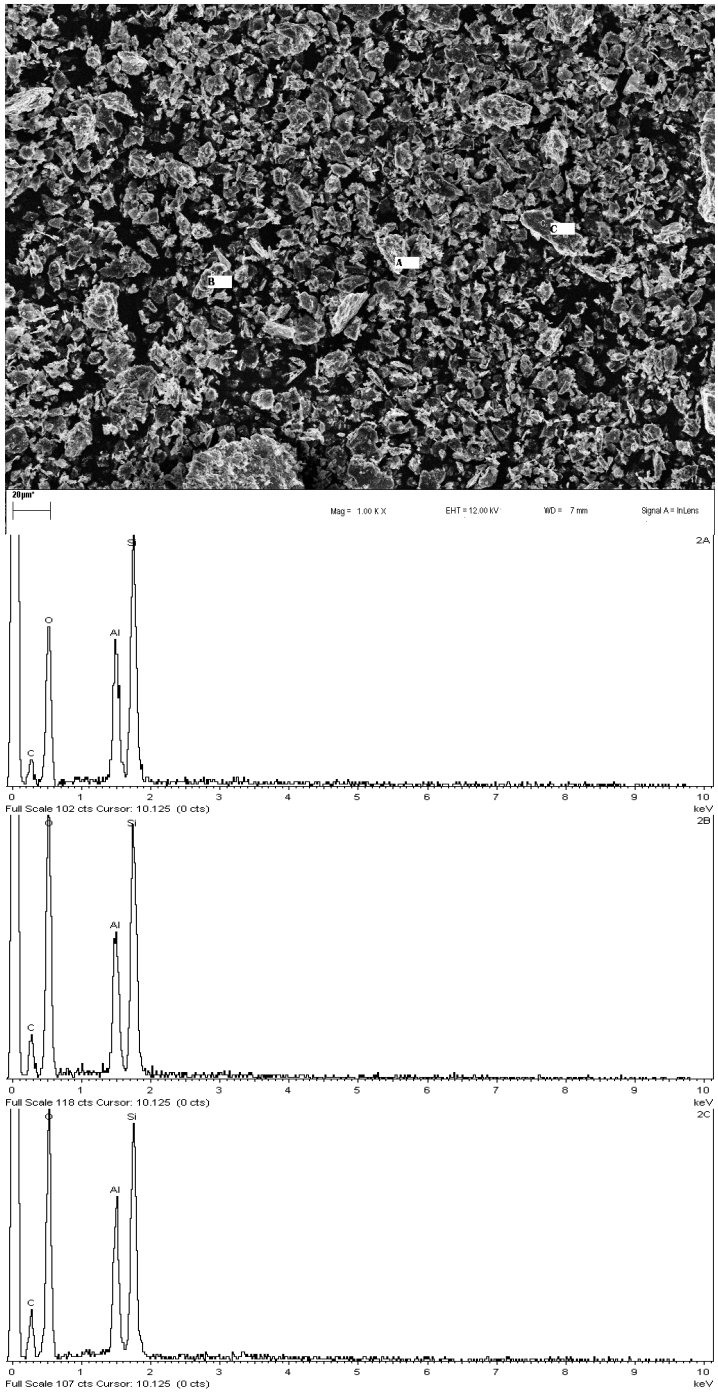

Fly ash SEM-EDX spectrum (experiment T18, reference table 4-8)

Appendix K Comparison Between Experiment And Modelling Of Carbon Dioxide Concentrations In The Flue Gas In The Psctf For Different Fuels Blends And Co-Firing Ratios

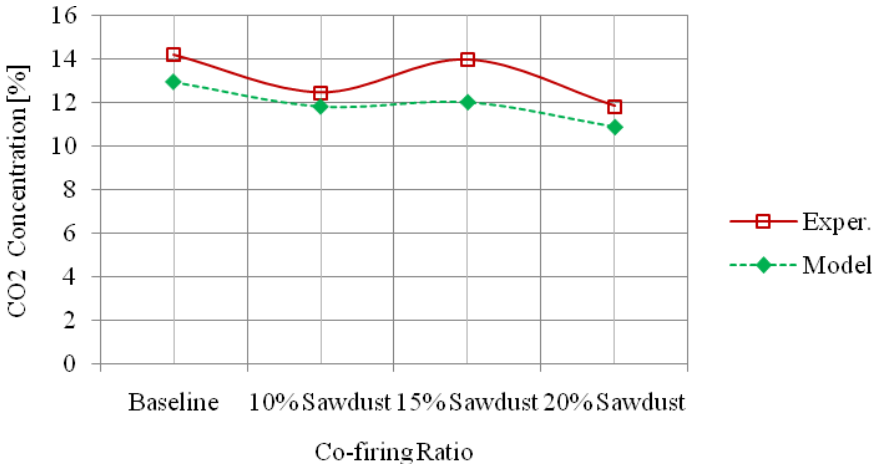

Fig. K.1 CO_2 Profiles for Sawdust test series

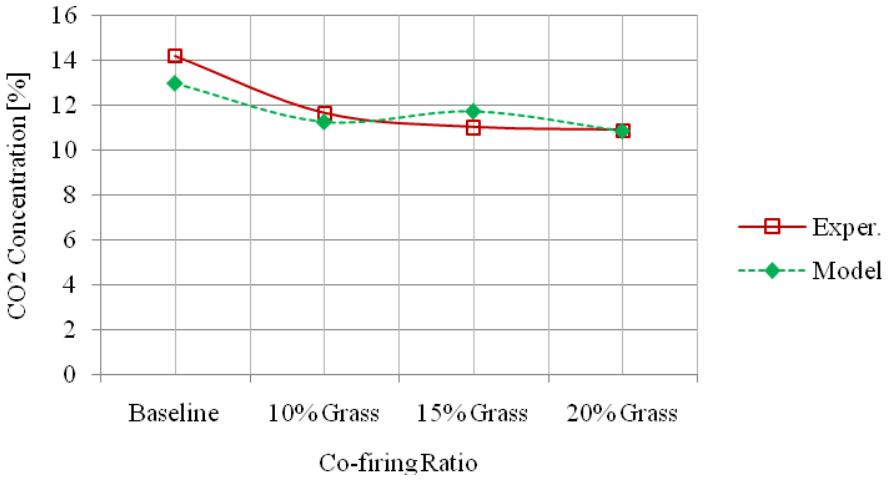

Fig. K.2 CO_2 Profiles for Grass test series